

Department of Mechanical, Materials & Manufacturing Engineering

New production methods for salient pole rotor manufacture

Thesis submitted to the University of Nottingham for the degree of Engineering Doctorate (EngD)

Aaran Sumner
STU ID: 4214755
Primary supervisor: Professor Adam Clare
Secondary supervisor: Professor Svetan Ratchev

H70Q Engineering Doctorate in Manufacturing Engineering

Abstract

The current design for a salient pole rotor consists of hundreds of laminations joined together to form a core pack, which is then pressed onto shaft. This thesis examines the possibility of using a solid cast rotor to reduce the complexity of rotor construction.

To produce a solid salient pole rotor that has the capability to match the performance of the current lamination based rotor three fundamental areas which affect rotor performance were investigated.

They are:

- The magnetic performance of cast steel and a lower saturation Fe-Ni alloy for the magnetic shielding of pole faces.
- The comparison of the performance of a solid steel rotor verses the lamination based rotor.
- The use of laser cladding to produce a soft magnetic coating to prevent eddy currents from being induced into the rotor.

Samples of cast steel were tested after various heat treatments were applied and their DC B-H curves were measured. The samples were examined, via optical microscopy, to determine the effect of heat treatments on their microstructure. The changes in their B-H curves and permeability were linked to the changes in microstructure by examination of the optical images.

A prototype of a solid rotor was produced to determine its performance compared with the lamination based rotor. The prototype rotor was produced with a Fe-Ni alloy on the rotor pole faces. The prototype rotor was found to require an average of 72% more power in the field windings to match the performance of the lamination based rotor. This was true until the generator's output reached 72kW when the Fe-Ni alloy on the rotor pole faces saturated, resulting in the air gap between the rotor and stator increasing from 2mm to 34.5mm.

After the increase in air gap the prototype rotor required an average of 188% more power to match the lamination based rotor. The point at which the Fe-Ni alloy saturates is critical, as once saturated the power in the field windings must increase sharply to bridge the larger air gap.

From this work it is clear that a cast steel with a better magnetic performance is required and that the point at which the lower saturation material on the pole shoes saturates needs to more closely match the normal operating power of the generator.

Laser cladding was used to produce a coating that can be applied to the pole faces, with a sufficient thickness to allow a controllable increase in the air gap between the rotor and the stator at predetermined field strengths. The use of laser cladding in this way enables the pole face to act as a magnetic shield stopping heating in the rotor due to induced eddy currents. The use of annealing in both inert and reactive atmospheres was examined to determine their effect on the DC magnetic properties of the deposited coating. Annealing in an inert atmosphere of argon was found to improve the saturation magnetisation of the coating 30% better than annealing in a reactive hydrogen atmosphere.

Acknowledgments

I would like to express my thanks to Professor Adam Clare and Steven Grace for giving me the opportunity to undertake this doctorate. In particular I would like to thank Professor Adam Clare and Dr Gaurang Vakil for their guidance and advice over the course of this journey.

I would also like to thank Phil Bend, Dr Neil Brown, Jhan Y Chan, Dan Fellows, and Stefano Nuzzo, who were all essential in the completion of this work.

I would like to thank my fellow EngD researchers at the MTEDC who provided support throughout the doctoral process. Not all of us hung on to the bitter end but those that left have gone on to excel nevertheless.

Finally and most importantly I would like to thank my fiancée, Jenny, for all her help, guidance, wine purchasing, and counselling, and my son, Ben, for his ability to provide perspective on the relative importance of a doctorate compared to knocking down towers of blocks and blowing raspberries.

Publications

A. Sumner, C. Gerada, N. Brown, A. Clare, “Controlling DC Permeability in Cast steels” *Journal of Magnetism and Magnetic Materials,* vol. 429, pages 79-85, May. 2017.

A. Sumner, G. Vakil, N. Brown, A. Clare, “DC magnetic properties of laser clad permalloy 80 with annealing in inert and reactive atmospheres”, *Journal of Magnetism and Magnetic Materials* – Under review

Abbreviations

CGT	-	Cummins Generator Technologies
MVA	-	Mega Volt Amps
kVA	-	Kilo Volt Amps
UoN	-	University of Nottingham
AC	-	Alternating Current
DC	-	Direct Current
REE	-	Rare earth elements
FCC	-	Face Centred Cubic
BCC	-	Body Centred Cubic
BTC	-	Face Centred Tetragonal
SMA	-	Soft Magnetic Alloy
DED	-	Direct Energy Deposition
OCC	-	Open Circuit Characteristics
SCC	-	Closed Circuit Characteristics
μ	-	Permeability
μ_r	-	Relative permeability
FACR	-	Fastest annealing cooling rate

Contents

Abstract 2

Acknowledgments 4

Publications 5

Abbreviations 6

Table of figures 12

Tables of tables 25

1 Introduction 27

1.1 Industrial context 27

1.2 Research objectives 32

1.2.1 Material characterisation for cast salient pole rotor 32

1.2.2 Prototype rotor design and testing 35

1.2.3 Laser cladding of soft magnetic material 37

1.3 Thesis structure 39

2 Literature review 40

2.1 Physics of magnetism [4] 40

2.1.1 Types of magnetism 41

2.1.2 Magnetic properties 44

2.2 Design and manufacture of generators 8

2.2.1 Rotor 9

2.2.2 Salient pole rotor 10

2.2.3 Assembled rotor 12

2.2.4 Stator 18

2.2.5 The stator core 18

2.3 Introduction to synchronous generators 21
2.3.1 Synchronous Generator 21
2.3.2 Losses 22
2.3.3 The rotor losses 24
2.3.4 The stator losses 24
2.4 Effects of material selection on performance 24
2.4.1 Hard magnetic materials [44] 25
2.4.2 Soft magnetic materials 26
2.4.3 Microstructure 32
2.4.4 Casting 38
2.4.5 Heat treatments 39
2.4.6 Additive manufacturing 40
2.4.7 Laser cladding 41
2.4.8 Powder production 42
2.5 Knowledge gaps 43
3 Experimental methods 45
3.1 Material characterisation for cast salient pole rotor 47
Samples for B-H curve analysis 49
3.1.1 Applying heat treatments 50
3.1.2 Baseline B-H curve 50
3.1.3 Annealing 51
3.1.4 Quenching and Tempering 53
3.1.5 Optical microscopy 54

3.2 Prototype rotor design and testing 59
3.2.1 Material selection for pole shoes 60
3.2.2 Prototype design 62
3.2.3 Prototype fabrication 68
3.2.4 Testing 71
3.3 Laser cladding of Ni-Fe soft magnetic alloy 77
3.3.1 Material selection 79
3.3.2 Powder production 80
3.3.3 Laser cladding 81
3.3.4 Production of samples for magnetic testing 83
3.3.5 Magnetic testing 88
3.3.6 Optical microscopy 89
3.3.7 Annealing 91
4 Material characterisation for cast salient pole rotor 92
4.1 Introduction 92
4.2 Effects of heat treatments on electromagnetic properties 92
4.2.1 Data quality 92
4.2.2 Permeability 95
4.2.3 Effects of heat treatments on B-H curve 97
4.2.4 Comparison of B-H curve at 0.5 tesla 106
4.3 Conclusions 110

5 Prototype rotor design and testing 112
5.1 Introduction 112
5.1.1 Design concepts 112
5.1.2 Cast rotor production 121
5.2 Performance of standard and prototype rotor 122
5.2.1 On-load characteristics 123
5.2.2 Open circuit characteristics (OCC) 126
5.2.3 Short circuit characteristics (SCC) 129
5.2.4 Magnetisation curve 131
5.2.5 Losses 133
5.2.6 Further testing (University of Nottingham) 134
5.2.7 Results (thermal) 136
5.3 Conclusions 139
6 Laser cladding of Ni-Fe soft magnetic alloy 142
6.1 Introduction 142
6.2 Results 142
6.2.1 Steel substrate 143
6.2.2 Deposited permalloy 146
6.2.3 Permalloy clad steel 149
6.2.4 Alloy 79 152
6.3 Discussion 155
6.4 Conclusions 158

7 Conclusions and future work 160
7.1 Conclusions 160
7.2 Future work 163
7.2.1 Material selection for main rotor body 163
7.2.2 Proposed further testing of the rotor 163
7.2.3 Concept for a multilayer magnetically shielding pole shoe 164
7.2.4 Overall concept for next generation salient pole rotor 165
References 167
Appendix A 184
Appendix B 220

Table of figures

Figure 1-1. The two main magnetic components of a salient pole generator [1]. The rotor is connected to a prime mover which provides rotational energy. The stator is static, the rotor DC magnetic field causes an AC magnetic field to be induced in the copper windings mounted in the stator.....27
Figure 1-2. A flowchart laying out the steps taken to answer the research question on the DC performance on cast steels. The results of cast steel testing will be DC magnetic performance data and optical images of microstructure. 34
Figure 1-3. A flowchart laying out the steps taken to answer the research question on the performance of a cast steel rotor verses a lamination based rotor. The effect of the use of lower saturation magnetisation pole shoes will also be shown. 36
Figure 1-4. A flowchart laying out the steps taken to answer the research questions on the performance of a laser clad permalloy. Optical image will be used to analyse the microstructure to determine why the coatings performance alters due to annealing. 38
Figure 2-1. DC magnetic characteristics of a steel sample. 44
Figure 2-2. Saturation curve of a cast steel, the blackline shows the saturation point of the material.....1
Figure 2-3. Hysteresis curve of a ferromagnetic material [11] 3
Figure 2-4. Graph of voltage and current waveforms with a unity power factor, resistive load. 6
Figure 2-5. Graph of voltage and current waveforms with the current lagging the voltage by 90º. 6
Figure 2-6. Section of a salient pole type generator [1]. As the rotor is spun by a prime mover (not shown) the DC exciter provides power to the windings on the rotor core pack. The magnetic field in the rotor core pack induces a AC current in the stators windings that produces the output of the generator. 8

Figure 2-7. (a) Non-salient pole rotor otherwise known as a cylindrical rotor due to the distributed windings the rotor cannot achieve the same power density, for the same length, as the salient pole rotor. (b) Salient pole rotors have concentrated windings that give a higher power density, for its length, than non-salient pole rotors.....9
Figure 2-8. A 3D CAD rendering of a salient pole rotor. The core pack consist of hundreds of laminations hydrologically pressed together. The core pack is then pressed onto the shaft and the Cu windings are wound onto the salient poles.....10
Figure 2-9. An assembled salient pole rotor with the Cu windings highlighted in-situ on the salient poles. 11
Figure 2-10. The core pack of a salient pole rotor with a single lamination highlighted. The rotor laminations are produced at the same time as the laminations that form the stator to reduce material waste. 12
Figure 2-11. Damper windings shorted at both ends of a complete damper winding. In salient pole rotors the damper windings are used as a crude squirrel cage rotor to spin the rotor to near synchronous speed before the field windings lock the rotor to synchronous speed.....13
Figure 2-12. The support bars are produced out of steel and are hydraulically pressed into the core pack to improve the rigidity of the core pack and support the Cu windings to stop centrifugal forces bending the windings into the stator during operation.....14
Figure 2-13. The shaft of the rotor is produced from steel billet and depending on the output power of generator can be heat treated to reduce the impact of cyclical fatigue during operation. 14
Figure 2-14. Key electromagnetic components of the rotor and stator. The rotor core and the stator core are produced out of the same electrical steel to reduce waste in the stamping process. 16

Figure 2-15. The main function of the rotor is to produce the DC magnetic field that cuts across the conductors in the stators windings to produce an induced current flow. As the rotor is rotating the amount of induce current in the stators varies over time resulting in an AC current flow. 16
Figure 2-16. The induced AC current in the stator windings generate their own AC magnetic field which is strong enough to induce currents to flow in the surface of the pole shoe. 16
Figure 2-17. A salient pole rotor with the pole shoes made of a material that is driven to saturation by the DC electromagnetic field. The induced AC magnetic field sees the saturated pole shoe as an airgap. 17
Figure 2-18. Image of a stator core with one of the laminations highlighted. The stator is produced on a fixture and then pressed to remove any oil left on the laminations from the stamping process. 18
Figure 2-19. Stator core with Cu windings and wedges used to hold the windings in their slots. The frame dampens mechanical vibrations during operation. 19
Figure 2-20. The B-H curves of multiple materials that are termed as soft magnetic materials 26
Figure 2-21. A continuous casting method for the production of electrical steel [49]. 28
Figure 2-22. Reducing the thickness of “hot band” steel to the finish thickness requirement [49]. 28
Figure 2-23. Changes in the Ni content of a NI-Fe alloy result in changes in magnetic performance [58]. 31
Figure 2-24. Phase diagram for steel [65]. The C content of electrical steels is typically below 0.03%wt resulting in a pure ferrite crystal structure. 33
Figure 3-1. A flow chart showing how the three results chapters are linked together to produce a methodology for producing a solid salient pole rotor 46

Figure 3-2. The data logger data describing the cooling rate of the furnace when it is heated to 950°C held for 20 minutes and then switched off and its cooling rate determined. 51
Figure 3-3. A summary of the permeability testing process. 53
Figure 3-4. Unaltered image (a,c,e) and altered image (b,d,f) for multiple magnifications (a) 20x magnification unaltered image, (b) 20x magnification analysed for crystal size, (c) 50x magnification unaltered image, (d) 50x magnification analysed for crystal size, (e) 100x magnification unaltered image, (f) 100x magnification analysed for crystal size. 56
Figure 3-5. SEM image of annealed sample AS4. 58
Figure 3-6. A SEM image of a single pearlite grain in the annealed sample AS4. 58
Figure 3-7. Comparison of the B-H curves of A1 cast steel in its normalised state and a Fe-Ni36 alloy 61
Figure 3-8. Main sub-components as fitted onto the shaft, the non-drive end is on the left side of the drawing with the drive end next to the cooling fan. This shaft is termed a single bearing as it only has a single bearing at the non-drive end. 65
Figure 3-9. The critical surface finishes of the single bearing shaft. The best surface finishes are for the bearing mount, exciter mount, and coupling disk mount.. 65
Figure 3-10. A single rotor lamination with keys features labelled. 66
Figure 3-11. The cast and normalised rotor ready for shipping to the machining company to be machine to its finished typology. If the rotor was going for annealing this is the stage at which it would be carried out.....69
Figure 3-12. The machined rotor is shown ready for dispatch to AlTech Ltd to have its field windings tumble wound into place. Also shown are the pole shoes that were machined by G.S. Precision Ltd and sent to Summerfield Ltd to confirm the pole shoes fitted correctly. 69
Figure 3-13. The rotor fitted with pole shoes and windings fitted, also visible are the plastic clips that were glued onto the main rotor body.....70

Figure 3-14. The completed rotor ready for insertion into a stator for testing. The aluminium fan can be seen at the bottom left of the image with the DC exciter at the top right. 71
Figure 3-15 . The DC B-H curves of the A1 grade steel that forms the main rotor body (in green) and the Invar 36 that forms the pole shoes (in red). Also shown (in black) is the B-H curve of the steel that forms the steel laminations in the standard rotor. 72
Figure 3-16. The position of the four resistance temperature detectors (RTD) on one of the poles shoes is shown. Sensor 1 is positioned on the side of the poles shoe. Sensor 2 is midway along the edge, on the underside of the shoe. Sensor 3 is on the outer set of windings. Sensor 4 is on the inner set of windings. 73
Figure 3-17. Images of the experimental setup. (a) shows the powder feeder, cladding head, shroud used to create a glove box arrangement to retain a Ar atmosphere, and (b) the x,y stage that moves the substrate during cladding. 81
Figure 3-18. EN3b substrate with six laser clad beads; (a) was obtained with a power density of 180W/mm^{-1} (b) was obtained with a power density of 360W/mm^{-1} beads c-f are all produced with a power density of 360W/mm^{-1} (c) is constructed from three beads one upon the other, (d) is six beads one upon the other, (e) is nine beads one upon the other and (f) is twelve beads one upon the other. 82
Figure 3-19. Flow chart of the procedure for testing the magnetic properties of permalloy before and after annealing heat treatments are applied. 83
Figure 3-20. Schematic of the laser cladding of an EN3b substrate. The cladding head deposits an approximately 1mm thick layer of material in a raster pattern. Once the raster is completed the cladding head raises by 1mm in the z-axis and the next raster is laid down on top of the previous raster. 85
Figure 3-21. Schematic of the raster pattern used to produce a solid block of laser clad material. The waviness on the top surface is characteristic of a laser clad coating. 85

Figure 3-22**.** A diagram of the laser cladding of an EN3b cylinder. The cladding head deposits a 1mm thick layer of material on the circumference of the cylinder. Once the circumference has been coated the x,y stage moves 1mm and the next track is laid down. When the whole surface area has been coated the cladding head raises by 1mm in the z-axis to deposit a new layer onto of the recently deposited coating. 87
Figure 3-23. Image of the raster pattern used to produce a coating of permalloy onto a steel cylinder. The laser claddings characteristic waviness of the coating runs perpendicular to the axis of the cylinder. 87
Figure 3-24. Image of the solid block of laser clad material a 5mm thick section removed to provide specimens of the laser clad blocks interior for optical microscopy. 89
Figure 3-25. Image of the cylinder of substrate with a 5mm coating of laser clad Ni-Fe. The cylinder was sectioned to provide a 5mm thick disk that was quarter to provide four specimens for optical microscopy. 89
Figure 3-26. SEM images of the non-annealed deposited permalloy which shows how the differences iin microstructure colourisation is based on the orientation of the individual crystals when sectioned. (a) shows the boundaries between visibly different crystal at 100µm, (b) shows the circled area in (a) at 50µm the change in texture between the two crystals is more evident, (c) shows the circled area in image (b) at 5µm the different surface texture between the two $FeNi_3$ crystals is apparent. The finer the surface texture the less electron scattering takes place therefore the darker the surface appears. 90
Figure 4-1 Output of B-H curve testing machine.....92
Figure 4-2, A screen grab of the combine test data from the same toroid measured twice. Showing the offset of the data due to the PID controller that controls the data acquisition of the steel test machine.....93

Figure 4-3, A comparison of the dataset outputted from the test equipment with the curve produced by a 5th order polynomial created by the LINEST excel function. 94
Figure 4-4, A graph of nine datasets, each toroid was tested three times (A,B,C). The raw data was then normalised by the LINEST excel function. 94
Figure 4-5, This graph is for the baseline B-H curve of sample AS1 with the standard deviation of the nine datasets plotted on the secondary axis. 95
Figure 4-6. The DC B-H curves of the 12 normalised steel samples supplied from the foundry, the dotted line represents the field strength that the permeability will be taken from. 96
Figure 4-7. The range of B-H curves obtain in sample AS4 with the application of different heat treatments, The best performing sample was that annealed at the FACR with the other annealed sample reducing in performance the lower the cooling rate. The quenched sample had the worst performance of the samples. ..97
Figure 4-8. The standard deviation of the datasets plotted in Figure 4-7. The smallest deviation occurs at the initial magnetisation and at the knee point that follows the linear section of the magnetisation curve. 98
Figure 4-9. (a) image of the ferrite/pearlite microstructure of the normalised A1 grade steel, (b) image of ferrite/pearlite microstructure of the annealed A1 grade steel, (c) image of the ferrite/martensite microstructure of the quenched A1 grade steel. 99
Figure 4-10. The effect of heat treatments on the B-H curve of a sample of P310 grade steel. Up until 1500A/m the annealed at a cooling rate of 6.0°C/min has the highest B-H curve after this point the initial resistance of the quenched samples martensitic structure is overcome and its B-H curve increases sharply. Aside from the 6.0°C/min cooling rate the rest of the annealed samples have very little improvement in there B-H curve. 100

Figure 4-11. The standard deviation of the datasets plotted in Figure 4-10. The smallest deviation occurs at the initial magnetisation and at the knee point that follows the linear section of the magnetisation curve. 101
Figure 4-12. (a) Graph of the B-H curve of three heat-treated samples of P310 grade steel, (b) image of the ferrite/pearlite microstructure of the normalised P310 grade steel, (c) image of ferrite/pearlite microstructure of the annealed P310 grade steel, (d) image of the ferrite/martensite microstructure of the quenched P310 grade steel. 102
Figure 4-13. The effect of heat treatments on the B-H curve of a sample of Mac 1 grade steel. The best performing heat treatments are the annealing at cooling rates of 6.0°C/min and 4.5°C/min. The quenched sample produces the lowest B-H curve until 1000A/m where the martensitic structures initial resistance to magnetisation is overcome and the normalised sample becomes the lowest B-H curve sample. 103
Figure 4-14. The standard deviation of the datasets plotted in Figure 4-13. The smallest deviation occurs at the initial magnetisation and at the knee point that follows the linear section of the magnetisation curve. 104
Figure 4-15. (a) image of the ferrite/pearlite microstructure of the normalised Mac1 grade steel, (b) image of ferrite/pearlite microstructure of the annealed Mac1 grade steel, (c) image of the ferrite/martensite microstructure of the quenched Mac1 grade steel.....105
Figure 4-16. Chart showing the twelve cast steels permeabilities before heat treatments and with heat treatments. 107
Figure 5-1. First concept design for a cast rotor with removable pole shoes.....112
Figure 5-2. First concept view of the core pack with removable pole shoes bolted into place. 113
Figure 5-3. Exploded view of first design concept of the core pack. The separate pole faces allow the use of different magnetic materials to be used to block inducted eddy currents from the rotor. 113

Figure 5-4. Second concept design for a cast rotor with removable pole shoes. 115
Figure 5-5. Second design concept of the core pack with removable pole shoes bolted into place. 115
Figure 5-6. Second design concept for removable pole shoes with removable support bars. 116
Figure 5-7. Exploded view of second design concept. 116
Figure 5-8. Third concept design for a cast rotor with removable pole shoes. ...118
Figure 5-9. Third design concept of the core pack with removable pole shoes bolted into place. 118
Figure 5-10. Exploded view of third design concept. 119
Figure 5-11. Third design concept for removable pole shoes with removable support bars. 119
Figure 5-12. An image comparing a) the original single bearing shaft b) the new two bearing shaft. 121
Figure 5-13. Outputs of resistance temperature detectors (RTD) attached to four locations on the prototype rotor. Sensor 4 is between the two sets of Cu windings so is the hottest place on the rotor. Sensor 3 is one the second first set of windings so is the second hottest. Sensor 2 is on the underside of the pole shoe midway along its length. Sensor 1 is on the edge of the pole shoe on its profile edge. 122
Figure 5-14. The current supplied to the rotor plotted against the output power of the generator. The smooth slope of the standard rotor (in green) shows that the iron of the rotor is not saturated at any point. The slope of the prototype (in red) has a distinct trough where the pole shoes saturate. 123
Figure 5-15. The current supplied to the standard rotor plotted against the output power of the generator. The three different power factors are shown with the increase in current required as the power factor moves further from unity. 124
Figure 5-16. The current supplied to the prototype rotor plotted against the output power of the generator. The three different power factors are shown with the increase in current required as the power factor moves further from unity. 125

Figure 5-17. The current supplied to the rotor and the resultant voltage generated in the stator of the standard rotor (in green) and the prototype (in red). 126
Figure 5-18. The voltage supplied to the rotor and the resultant voltage generated in the stator in the standard rotor (in green) and the prototype (in red). 127
Figure 5-19. The percentage increase of the rotor current (in green) and voltage (in red) between the standard rotor and the solid rotor. 127
Figure 5-20. The current supplied to the rotor is plotted against the current produced by the generator when the output terminals are shorted together. The green line is the standard rotor and the red line is the prototype rotor. 129
Figure 5-21. The voltage supplied to the rotor is plotted against the current produced by the generator when its output terminals are shorted together. The green line represents the standard rotor and the red the prototype. 130
Figure 5-22. The magnetisation curve of both the standard rotor, in green, and the prototype rotor, in red. The OCC of the prototype rotor can be seen to saturate at a lower output voltage, line voltage, than the standard rotor. 132
Figure 5-23. The efficiency curve of the generator equipped with a standard (in green) and prototype rotor (in red). The initial efficiency of the prototype rotor is lower than the efficiency of the standard rotor. The change in power factor results in a drop in efficiency for both rotors. 133
Figure 5-24. A graph showing the OCC of the prototype rotor from data collected at Cummins Stamford test facility and the UoN test facility. 134
Figure 5-25. A graph showing the SCC of the prototype rotor from data collected at Cummins Stamford test facility and the UoN test facility. 135
Figure 5-26. Graph of the temperature of the rotor during 5 kW increases in output power and different transient loading 136
Figure 5-27. The baseline testing of the rotor shows that the temperature increases as a result of the increasing applied load. 138
Figure 5-28. The absolute B-H curve of the electrical steel used in current rotor production alongside the A1 grade in both its normalised and annealed states. .139

Figure 6-1. A graph of the DC magnetic performance of theEN3b steel substrate samples 1 and 2 before annealing. The DC performance after annealing is also shown.....143
Figure 6-2. A graph showing the standard deviation of the datasets used to produce Figure 6-1.
.....144
Figure 6-3. A graph of the initial permeability of the steel substrate as the field strength is increased to 500 A/m. The initial permeability of the samples changes after annealing and both annealed samples show an increase in permeability when compared to the non-annealed state until 500 A/m is reach then the permeability of the Ar annealed sample drops below that of the non-annealed. 144
Figure 6-4. Images of the microstructure of the steel substrate (a) with no heat treatment applied (b) with H annealing applied, and (c) with Ar annealing applied.
.....145
Figure 6-5. A graph of the permeability of the deposited permalloy before and after annealing. Both annealing process result in the characteristically sharp initial permeability of permalloys however the Ar annealed sample has a much higher saturation magnetisation point when compared to the H annealed sample. 146
Figure 6-6. A graph showing the standard deviation of the datasets used to produce Figure 6-5 147
Figure 6-7. A graph of the initial permeability of the deposited permalloy as the field strength is increased to 500 A/m. The initial permeability of the samples changes after annealing and both annealed samples show an increase in permeability when compared to the non-annealed state. The Ar annealed sample shows a much higher permeability when compare to the H annealed sample. ...147
Figure 6-8. Images of the microstructure of the deposited permalloy (a) with no heat treatment applied (b) with H annealing applied, and (c) with Ar annealing applied. 148

Figure 6-9. A graph of the permeability of the permalloy clad steel before and after annealing. Both the non-annealed samples have low initial permeability and a very low saturation magnetisation. Once annealed both samples show an increase in both initial permeability and saturation magnetisation. 149
Figure 6-10. A graph showing the standard deviation of the datasets used to produce Figure 6-9 149
Figure 6-11. A graph of the initial permeability of the permalloy clad steel as the field strength is increased to 500 A/m. The initial permeability of the non-annealed samples improve by both H annealing and Ar annealing. The H annealing process improves the permeability of the permalloy clad steel more than the Ar annealing. 150
Figure 6-12. Images of the microstructure of the permalloy clad steel substrate (a) with no heat treatment applied (b) with H annealing applied, and (c) with Ar annealing applied.....151
Figure 6-13. A graph of the permeability of Alloy79 before and after annealing. Both the non-annealed samples have low initial permeability and a very low saturation magnetisation. Once annealed both samples show an increase in both initial permeability and saturation magnetisation, with the Ar annealed sample having a higher magnetic saturation.....152
Figure 6-14. A graph showing the standard deviation of the datasets used to produce Figure 6-13 153
Figure 6-15. A graph of the initial permeability of Alloym79 as the field strength is increased to 500 A/m.. The initial permeability of the non-annealed samples improve by both H annealing and Ar annealing. The Ar annealing process improves the permeability of the Permalloy clad steel more than the H annealing.....153
Figure 6-16. Images of the microstructure of Alloy 79 (a) with no heat treatment applied (b) with H annealing applied, and (c) with Ar annealing applied. 154

Figure 7-1. A design concept of a multilayer pole shoe with laser clad layers with differing ratios of Ni/Fe in each layer. The differing ratios would result in different saturation magnetisations for each layer producing a graduated magnetic shield on the pole face.....164

Tables of tables

Table 1-1.List of models in the Stamford range of generators. 30
Table 1-2. List of models in the HC4 generator range. 31
Table 2-1. Rotational speed and pole numbers required to produce 50 Hz. 21
Table 2-2. Rotational speed and pole numbers required to produce 60Hz. 22
Table 3-1. Composition of the twelve samples for testing. The composition of the steels was provided by the foundry that provided the steel billets for testing. The grades of steel are produced to meet thee specifications laid out in BS3100:1991[119] 48
Table 3-2 The heat treatments the steel samples chemical composition have been optimised for. the supplied billets of the steels from the foundry had these heat treatments applied before they were normalised to remove machining stress and reset their microstructure for baseline property testing. 49
Table 3-3. Results of ImageJ analysis of annealed sample AS4 at different magnifications. The software showed different crystal sizes for the same under different magnifications. 57
Table 3-4. Comparison of the amount of material machined from a billet of material to produce the core pack and to produce both the core pack and the shaft. 63
Table 3-5. ISO roughness grade with roughness value equivalent 64
Table 3-6. Composition of permalloy powder, Alloy 79, used in this study. 81
Table 3-7. Table of samples produced for magnetic testing with sample identifiers and summary of methodology 84
Table 3-8. The heating rate for the H and Ar annealing cycles of the laser clad samples is shown. 91
Table 4-1. Relative permeability of cast steel samples at a field strength of 1250A/m 96
Table 4-2. Relative permeability of normalised (Norm) verses annealed cast steel (with different cooling rates) tested at 0.5 Tesla 108

Table 4-3. B-H curve of normalised (Norm) verses quenched (then tempered) cast steel tested at 0.5 Tesla.....108

1 Introduction

1.1 Industrial context

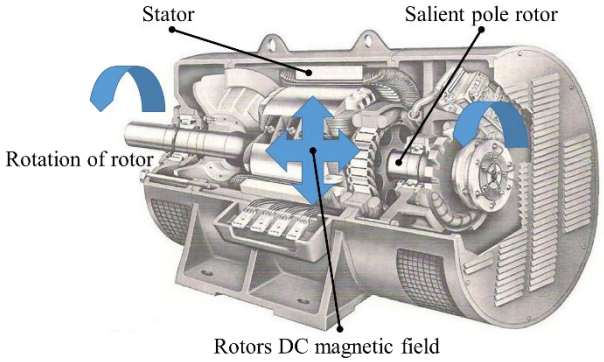


Figure 1-1. The two main magnetic components of a salient pole generator [1]. The rotor is connected to a prime mover which provides rotational energy. The stator is static, the rotor DC magnetic field causes an AC magnetic field to be induced in the copper windings mounted in the stator

In Figure 1-1 a synchronous generator is shown with the frame, in which the individual components of the generator are mounted cut away. A salient pole rotor has projections pointing outwards from the rotors shaft. The projections allow multiple turns of wire to be wrapped about them allowing for the creation of a strong DC electromagnetic field. The salient pole rotor is spun and the DC magnetic field of the rotor cuts across the copper wires mounted in the stator inducing an AC current to flow in them, this induced AC electromagnetic field is the output of the generator. The production of rotors for CGT's Stamford type generators has remained unchanged for decades. In this time most of the development work on the design has been focused on increasing the power output of the generator. As the typology has remained static the only viable way of improving the power density of the rotor is to increase the quality of the grade of electrical steel used in its construction, or increasing the cooling to allow the steel to be driven closer to saturation. All the development work on making better grades of electrical steel is carried out by its manufacturers, and so for CGT it is simply a case of comparing power density verses the cost of using a better quality electrical steel.

The use of portable generators as temporary power supplies and as permanent backup power supplies for critical infrastructure ensures that there is a sustained market for their manufacturers. The production of the generators that are coupled to diesel engines to produce generator sets is complicated by the end users' requirements to have a generator that is capable of supplying the desired load without having excess capacity. This results in a large range of generators being required to meet end user demand.

The work leading to this thesis is sponsored by Cummins Generator Technologies (CGT) who supply generators to produce generator sets. As this project is an Engineering Doctorate its scope and direction are more heavily directed by the sponsor than if it were a PhD project. This requirement results in the cost of the processes and methodologies used to produce this thesis being directed by the consideration, by the sponsor, of how cost effective they are against the cost of the methods used to produce rotors currently.

The basic design of a generator has not changed in 100 years, instead a steady improvement in the understanding of the material science of magnetic materials has seen the output power and efficiency of the generator increasing gradually over time.

The mechanical characteristics of the materials that are used in the construction of a generator are secondary to the electromagnetic properties required of the materials that make up a modern generator. The need to ensure high efficiency when converting the mechanical energy into electrical energy has limited the capability for large savings in production costs as composition and quality of the materials used in construction are strictly controlled. The assembly of a generator is predominantly carried out by hand with little automation, as the large range of generators available mean any automated assembly process will need to have a high degree of flexibility to cover the complete range of produced generators.

In this thesis a new method of producing one of the critical electromagnetic components will be introduced.

This will allow the simplification of the assembly process and allow new typologies to be used, which will in turn result in an improvement in performance of the generator.

As this project is sponsored by CGT one of their generators was selected to provide the basis for a prototype machine. Cummins produce two main ranges of generators, they are:

- The AvK range which produce between 1 mega volt amps (MVA) and 10 MVA depending on the model.
- The Stamford range which produce between 20 kilo volt amps (kVA) and 5 MVA depending on the model.

The Stamford range are produced in Stamford, UK, while the AvK range are produced in Craiova, Romania, production having recently been moved from Germany. The high cost of labour in the UK provides a good incentive to reduce the number of man-hours required to produce a completed generator. The current design of the generator and the number of series types (Table 1-1) makes the use of automation difficult. Each model has multiple sub-series resulting in a range of 151 different Stamford generators. When combined with the requirement for critical thinking during assembly, the automation of production becomes prohibitively expensive. The simplification of the method of manufacture would significantly reduce the man-hours required to build a generator as well as acting as an enabling technology to allow further simplification of production of the complete generator design.

Table 1-1.List of models in the Stamford range of generators.

Series	Model	Output power (50Hz) (kVA)	Output power (60Hz) (kVA)	Voltage range
P0	4-Pole	20	23	220-600
P0	2-Pole	20	23	220-480
S0	S0	30	36	400-480
P1	4-Pole	45	55	220-600
P1	2-Pole	45	55	220-480
S1	S1	63	75	400-480
UC	22	85	104	380-690
UC	27	250	313	380-690
HC4	HC4	400	500	380-690
HC5	HC5	675	843	380-690
HC6	4-Pole	1135	1438	346-690
HC6	6-Pole	1135	1438	346-600
P6	P6	1250	1513	380-480
P7	6-Pole	2200	2625	346-600
P7	4-Pole	2200	2625	346-690
P80	LV	3911	4464	380-690
P80	HV	3875	4750	6000-13800
P80	MV	4264	5190	3300-4160

Table 1-1 shows the different series of the Stamford range of generators, ordered from smallest to largest (output powers). Some of the series have different models associated with them. Each of the models of generator have multiple sub-types The production of the Stamford range is split into two production lines based upon the physical size of the generator models. The smaller generators (the P0 to UC series) are produced on one production line and the larger generators (the HC4 to P80 series) are produced on the second production line.

Recently the production of the smaller generators has moved from Stamford to a new production facility in Beijing, China. The reduction of production lines in the UK, reduced the possible models on which to base the prototype on.

The Stamford production facility can only carry out final assembly operations on the larger ranges.

The larger P80 generators are based on scaled up HC4 generators, so the HC4 was chosen for this thesis as a new design for the HC4 would be scalable to all of the larger generators.

Table 1-2. List of models in the HC4 generator range.

Sub-Type	Type	Output power at 380 volts (50Hz) (KVA)	Output power at 440 volts (60Hz) (kVA)
HCM434C	Marine	210	245
HCM434D	Marine	230	270
HCI444C	Industrial	250	300
HCM434E	Marine	275	325
HCI444D	Industrial	300	360
HCM434F	Marine	310	375
HCI444E	Industrial	350	440
HCI444F	Industrial	400	500

Table 1-2 shows the range of sub-types for the HC4 series. The marine type generators require extra manufacturing process when compared to the industrial type. These extra processes are related to compliance with wiring and insulation standards and do not alter the design of the electromagnetic components. The letters at the end of the sub-type code denote the core length of the generator. C represents the shortest core length and F the longest. To make prototype production costs as low as possible an industrial type C core generator, HCI444C, will be used as the basis of the prototype design.

1.2 Research objectives

The aim of this work is to carryout research at a PhD level to enable the production of a solid salient pole rotor to enable a simplification in the production process. , the solid rotor should use well understood manufacturing technologies that can be scaled easily to meet the current production volumes. Although the redesign will take the HC4 model as the basis of the redesign, the new designs must be scalable to both the smaller and larger models in the Stamford range.

The key research questions that this work answers are:

- What are the DC magnetic characteristics of a range of cast steels and how does the application of heat treatments, commonly applied during the casting process, alter the DC magnetic characteristics of the cast steels?
- How does a cast steel salient pole rotor perform when compared to a conventional lamination based rotor?
- What effect does a lower saturation material have on the airgap of the generator before and after it saturates?
- Can laser cladding produce a coating of a permalloy 80 type alloy that can match the performance of a commercially available alloy?
- What are the effects on the DC magnetic performance of the deposited coating of annealing in either an inert or reactive atmosphere?

1.2.1 Material characterisation for cast salient pole rotor

The first knowledge gap identified by the literature review was the lack of published work on the use of cast steel components in DC applications, such as the salient pole rotor of a generator. This gap lead to the research question “What are the DC magnetic characteristics of a range of cast steels?” and “what effect do commonly applied heat treatments have on these magnetic properties, and why?” Before a cast rotor can be produced a material needed to be selected that has the best magnetic properties when compared to the current M700-65A electrical steel used by CGT.

Literature on the magnetic properties of cast steel was limited to that associated with the breakdown in metastable microstructures into stable ferrite and pearlite structures and its use in determining timelines for failure in steel pipes. Chapter 4 in this thesis focuses on producing data on the magnetic characteristics of a range cast steels. Cast steels have a non-homogeneous microstructure, directly after casting, so the use of heat treatments to produce a more homogeneous microstructure are common in the casting industry. Different heat treatments have diffing impacts on the magnetic performance of the cast steel. In this chapter the two primary heat treatment methods, annealing, and quenching then tempering were carried out on cast steel samples to find which combination of steel grade and applied heat treatment would produce the best performing steel to produce a salient pole rotor.

The steel core of the rotor will not experience any AC induced eddy currents so the testing of the steel was carried out with only a DC applied magnetic field. The testing methodology to characterise the DC magnetic properties of a range of steels was set out in the standard BS EN 60404-4:1997 [2], to provide optical imaging of the changes of microstructure before and after heat treatments were applied the standard ASTM A34M-06:(2012) [3] was followed.

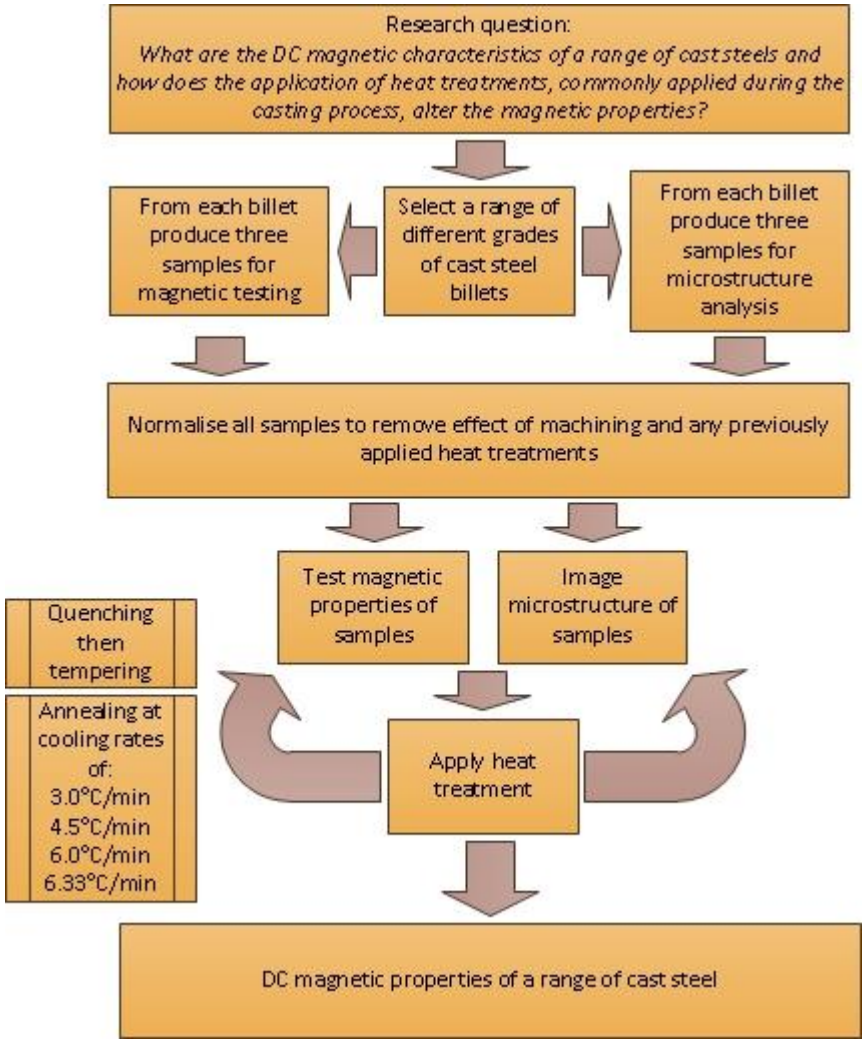


Figure 1-2. A flowchart laying out the steps taken to answer the research question on the DC performance on cast steels. The results of cast steel testing will be DC magnetic performance data and optical images of microstructure.

In Figure 1-2 a flowchart shows how Chapter 4 was produced to answer the research question on the DC magnetic characteristics of cast steels and the effect of heat treatments upon the DC magnetic performance of the samples. The changes in microstructure were optically imaged and the changes in DC performance explained with the use of these images.

1.2.2 Prototype rotor design and testing

Once a steel was selected the design of the prototype rotor was finalised. The critical characteristics of a current CGT rotor, produced out of laminations, was captured and incorporated into the solid rotor design to enable a comparison of the performance of the prototype and current CGT rotor. The main typological difference between the current CGT rotor and the prototype was the removable pole shoes, of the prototype, which allows different soft magnetic materials to be tested to see their effect on blocking harmonics and transients inducing eddy current in the main rotor body. The design was sent for approval from CGT and once changes they had requested were made, the rotor was manufactured. The testing of the rotor was carried out to match with CGT current testing methodology. The prototype rotor and the current rotor, it was based upon, were both tested in the same stator and a comparison of their performance made. The prototype rotor was shipped to (University of Nottingham (UoN), from CGT, to allow cross-calibration of the two test facilities.

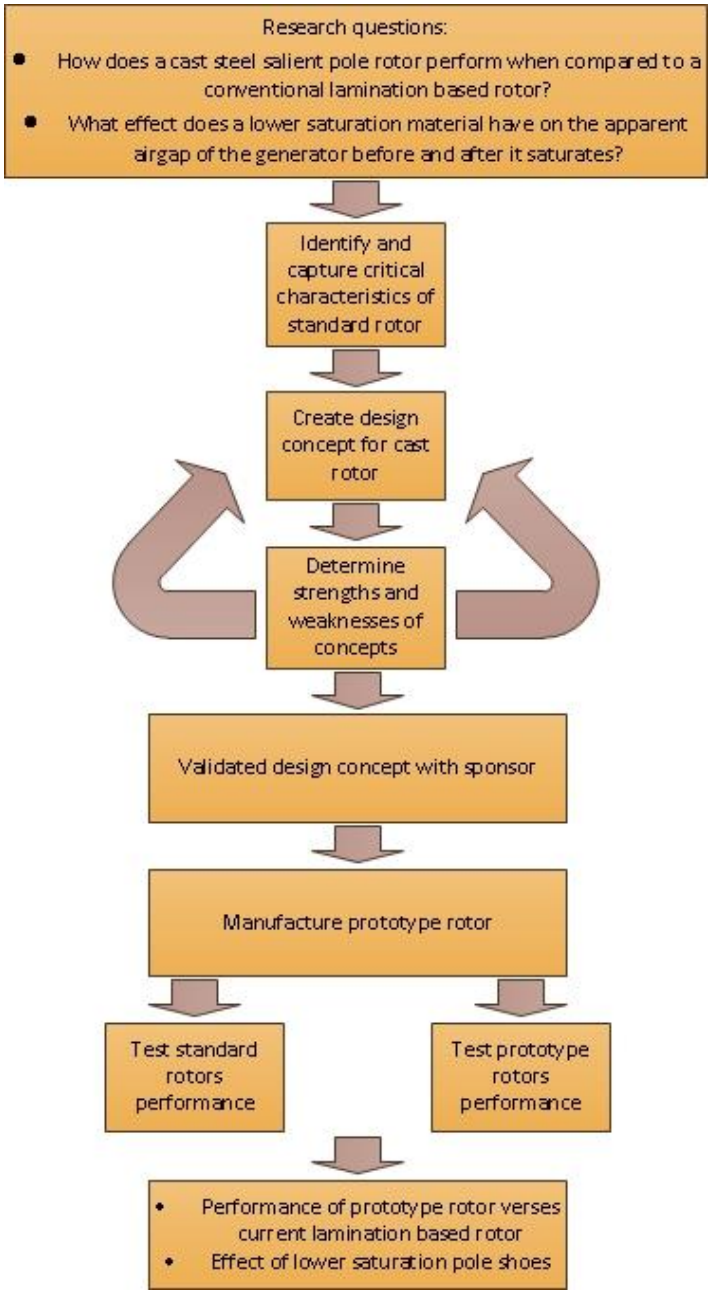


Figure 1-3. A flowchart laying out the steps taken to answer the research question on the performance of a cast steel rotor verses a lamination based rotor. The effect of the use of lower saturation magnetisation pole shoes will also be shown.

In Figure 1-3 a flowchart of the processes undertaken to answer the research questions about the performance of a cast steel rotor verses a lamination based rotor. The second research question answered in this chapter will be how the lower saturation pole shoes effect the performance of the rotor.

1.2.3 Laser cladding of soft magnetic material

The prototyping chapter has shown the effect of lower saturation pole shoes on the performance of the prototype rotor. To shield the main rotor body from harmonics and transient induced eddy currents there is a need to produce a pole shoe which can saturate at predetermined points as the generator's output power changes during operation. The change in saturation point will allow the air gap to increase and decrease depending upon the power output of the generator. The method selected to achieve this was using a technique termed laser cladding. The use of laser cladding to produce soft magnetic materials is a gap in the literature. This chapter primarily shows how laser cladding of a soft magnetic material effects its DC magnetic properties when compared to commercially produce soft magnetic material. Additive manufactured parts lack the ordered microstructure of conventionally produce materials so additional heat treatments were tested to determine which type of annealing atmosphere would resulted in the biggest improvement in DC magnetic performance.

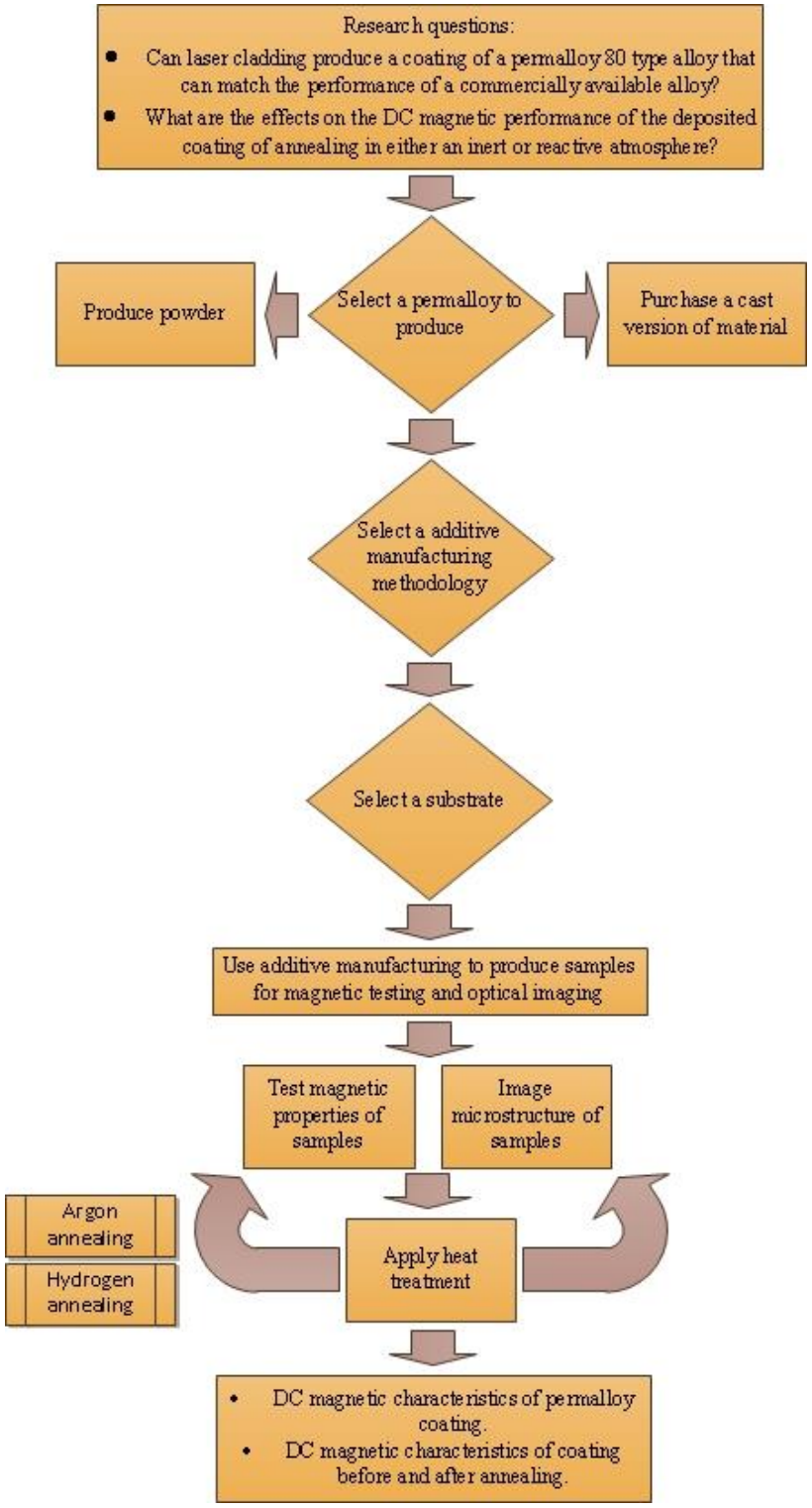


Figure 1-4. A flowchart laying out the steps taken to answer the research questions on the performance of a laser clad permalloy. Optical image will be used to analyse the microstructure to determine why the coatings performance alters due to annealing.

In Figure 1-4 a flowchart shows how the research question about the viability of a thick (>10mm) coating of a permalloy produced via laser cladding will be answered. The second research question answered in this chapter is about the effect, on the magnetic performance of a permalloy coating, of annealing in either an inert or reactive atmosphere.

1.3 Thesis structure

The thesis is ordered as follows:

Chapter 2 - A review of the current state of the art with regards to the how a generator works and how its construction enables it to function. The review will investigate what effects manufacturing methods have on the finished generator design and identify the knowledge gaps that will allow new methods of manufacturing generators.

Chapter 3 - Contains the methodologies and apparatus used, in this study, to answer the research questions that were derived from the knowledge gaps identified in the literature review.

Chapter 4 - Shows the DC magnetic characteristics of a selection of cast steels and the effect on DC magnetic performance of a range of heat treatments. The change in microstructure due to the applied heat treatments is shown optically and the magnetic changes linked to these microstructure changes.

Chapter 5 - Contains the design, production, and testing of a prototype rotor produced from the best performing steel found in the previous chapter.

Chapter 6 - Contains the use of laser cladding to produce a coating of a permalloy 80 type alloy and the effect of annealing the deposited coating in either an inert or reactive atmosphere.

Chapter 7 - Conclusions of the work undertaken, and identifies potential future work.

2 Literature review

The production method for a generator is a combination of the most efficient method of producing its constituent parts and producing parts that meet the electromagnetic requirements of the finished generator. It is not advisable to alter the production methods of any electromagnetic component without considering the effect of the alterations on performance of the generator. Accordingly this literature review, explores the current state-of-the-art materials and production methods to find gaps in the literature that can form the basis of this thesis and meet the needs of the industrial sponsor.

2.1 Physics of magnetism [4]

Coulomb found that magnets have two poles; one positive called north, and one negative called south. Poles that are alike, north to north or south to south repel each other, whereas dissimilar poles are attracted to each other. Magnets have a north and south pole meaning that they are dipoles. The force (F) of the attraction or repulsion is the product of the strength of the poles and inversely proportional to the distance separating them. Coulomb deduced that the force of attraction and repulsion is determined by separating the poles, taking one of the poles as the test pole, and the second pole as the source pole. The effect the source pole has on the test pole is represented by magnetic field strength, measured in Henrys (H). In modern international standard units (SI) the field strength is measured in Amperes per meter (A/m). Building on Coulomb's work Maxwell went on to describe magnetic induction (B) which is measured in the SI units of Tesla (T). Another name for magnetic induction is flux density. Different materials have different electron structures, this causes the materials to have a different capacity to concentrate the applied magnetic field. The ability of a material to concentrate magnetic fields is termed its permeability (μ) with the SI units of Henrys per metre (H/m) or Newtons per Ampere squared (N/A^2).

Maxwell stated magnetic induction and magnetic field strength are related by the following equation

$$B = \mu H$$

Where:

$B = Magnetic\ Induction$

$\mu = Permeability\ of\ a\ material$

$H = Magnetic\ field\ strength$

2.1.1 Types of magnetism

When a magnetic field is applied to a material it causes a magnetic moment to be induced in electrons orbiting the material's constituent atoms. In any given material the electrons have two methods of producing magnetic moments: the orbital, and spin angular momentums. Both of these properties are represented by vectors, as they have both direction and magnitude [5].

Materials produce magnetic moments when a magnetic field is applied, this is called diamagnetism. Some materials have an electron structure that causes permanent magnetic moments. If the coupling between the magnetic moments is very small or zero the material is termed to be paramagnetic. If the coupling is larger than there are three main terms for the effects of an applied field; ferromagnetic, ferrimagnetic, and anti-ferromagnetic. .

2.1.1.1 Paramagnetism [5]

In a paramagnetic material the magnetic moments of the electrons do not cancel each other out. If the material is predominantly made up of the same element the individual magnetic moments of each of the constituent atoms will be the same. When no magnetic field is applied, the magnetic moments will be aligned randomly resulting in a non-magnetic material. If a magnetic field is applied the magnetic moments will align with the applied field producing a strong magnetic moment in the direction of the applied field. The determining factor for the strength of the magnetic moment will be the thermal state of the material.

In a paramagnetic material the input of thermal energy has a large impact on the ability of the magnetic moments to align with the applied magnetic field. The temperature at which a material becomes paramagnetic varies depending upon the elements that form the majority of the material.

The temperature at which a previously ferromagnetic, ferrimagnetic, or anti-ferromagnetic material becomes paramagnetic is the Curie temperature.

2.1.1.2 **Ferromagnetic** [6]

In a ferromagnetic material the magnetic moments of each atom are coupled to the neighbouring atom and arranged in parallel. This results in a material that has the property of spontaneous magnetisation, which even in the absence of an applied magnetic field will have magnetic moments. When the magnetic moments spontaneously align they produce an area that is aligned in the same direction, this is termed a domain. Domains are separated by the crystal boundaries of the ferromagnetic materials crystal structure, any boundary between domains is termed a domain wall. The thicker the domain wall the less influence the individual domains have on each other. To overcome the domain's insulation from each other a magnetic field can be applied which causes all the domains to align in the same direction. This causes the ferromagnetic material to become magnetised. When the applied magnetic field is removed the domains retain the orientation of the applied magnetic field causing the ferromagnetic material to become a permanent magnet. If thermal energy is applied to the magnet the strength of the magnetic field will be reduced as the domains change their orientation randomly due to thermal excitation. When the material is heated to above its Curie temperature the material switches from ferromagnetic to paramagnetic. A reduction in insulation between magnetic domains results in a magnet domain which requires more thermal energy to be applied before the magnet's field strength is reduced.

There are three main elements that can be termed ferromagnetic they are; iron (Fe), nickel (Ni), and cobalt (Co). Some rare earth elements (REEs) are also ferromagnetic however they also tend to only be ferromagnetic at low temperatures. If alloyed with other ferromagnetic metals such as Fe, Ni, and Co the Curie temperature of the resultant alloys are higher resulting in greater applications for REEs.

2.1.1.3 **Anti-ferromagnetic** [7]

In a ferromagnetic material the magnetic domains align themselves with an applied magnetic field, increasing the magnetic field strength. In an anti-ferromagnetic material the magnetic domains align themselves in the opposite polarisation to the applied magnetic field. The alignment of the domains in the opposite polarity to the applied field causes a reduction in the magnetic field strength. Anti-ferromagnetic materials can be used for information storage in electronics. Transitional metals commonly form oxides that are anti-ferromagnetic in nature.

2.1.1.4 **Ferrimagnetic** [8]

A ferrimagnetic material has a majority of magnetic moments that align themselves with an applied magnetic field. The remainder of the magnetic moments align themselves opposite to the applied magnetic field. As the two opposing magnetic moments are unequal, a ferrimagnetic material with an applied magnetic field will cause increased field strength. Ferrimagnetic materials are used in oxide form in the electronics industry to produce ferrite cores for high frequency electronics.

2.1.2 Magnetic properties

2.1.2.1 Permeability (μ)

As previously stated permeability is taken as a ratio of flux density (B) measured in Tesla (T) to magnetic field strength (H), measured in ampere per metre (A/m)

$$\mu = B/H$$

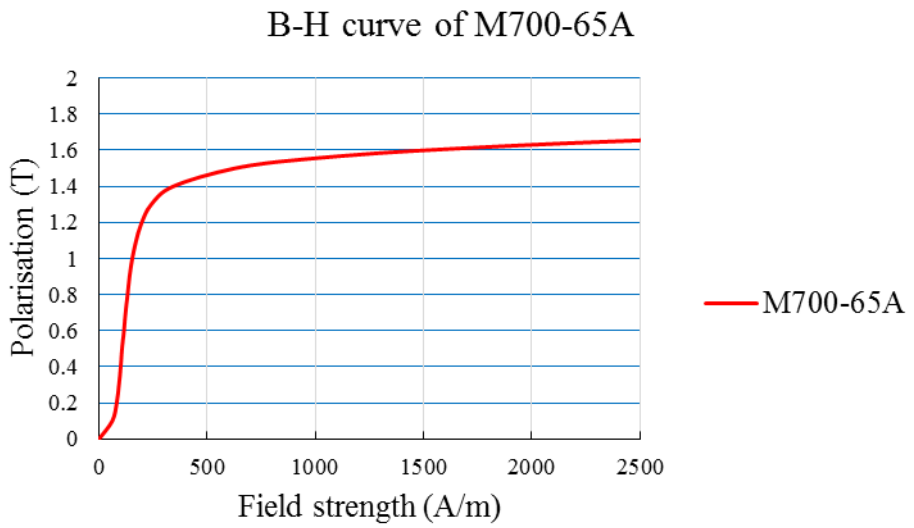


Figure 2-1. DC magnetic characteristics of a steel sample.

In Figure 2-1 the plot of Polarisation (B) in tesla against field strength (H) in A/m is shown. As absolute permeably is B/H the value for the absolute permeability over the whole plot can be defined as:

$$\mu' = \frac{dB}{dH}$$

As absolute permeability is not linear defining a single value of absolute permeability at a single point on the plot is not possible. In both academia and industry the primary method used to produce a single permeability value for a material is to take either the B or the H value at a pre-determined point. For the

manufacturers of electrical steel the permeability is given at 1.0T and 1.5T [9] however this is not the DC permeability it is the permeability at 50/60Hz.

For the samples tested in this thesis the pre-determined point will be the DC permeability at a pre-determined point which will be decided on after plots for all the samples tested have been reviewed. This will allow the selection of either a B or H value to determine the absolute permeability at a point which allows a meaningful comparison of increases or decrease in DC permeability.

As the permeability is a ratio of current density to field strength the resultant number is very small and this increases the difficult of drawing a direct comparison. To make the permeability a number that allows easier comparison it is standard practice to change the permeability to relative permeability (μ_r).

$$\mu_r = \mu/\mu_0$$

Where:

$\mu_r = Relative\ permeability$

$\mu = Permeability\ (at\ pre-determined\ point)$

$\mu_0 = Permeability\ of\ free\ space = 4\pi \times 10^{-7} N/A^2$

μ_r is a ratio between the permeability and the permeability of free space, therefore it has no units. A material with a μ_r of 1000 concentrates magnetic flux 1000 times better than free space (classic vacuum). For casting a rotor the highest possible μ_r is desirable

2.1.2.2 Saturation Magnetisation

The saturation of a ferromagnetic material represents the point at which all the magnetic spin moments, that make up the material, are all aligned with the applied magnetic field .To obtain a precise saturation point value for a material the exact atomic composition of the material needs to be known so the number of atomic moments (which varies depending upon the elemental composition) can be used to calculate the saturation point. It is extremely difficult to know the exact composition of a material. The saturation magnetisation is normally determined by measurement of the B-H curve of the material. The point of saturation is normally taken as a point after the knee of the curve. The B-H curve doesn't level out, after the knee of the curve, and stay level as the permeability of free space ensures that if the applied magnetic field increases the polarisation will also increase. The subjective point at which the saturation point is taken is not critical as just after the knee of the curve the rate of change of the polarisation due to applied magnetic field is very low.

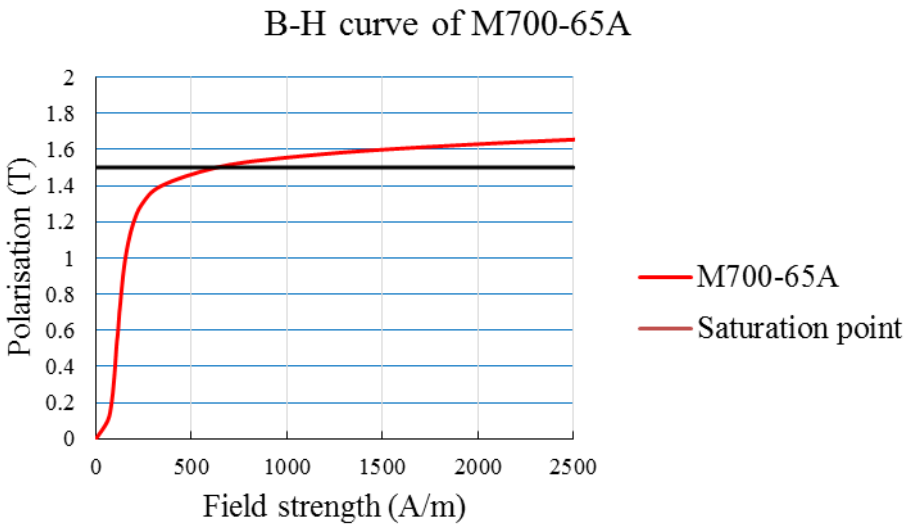


Figure 2-2. Saturation curve of a cast steel, the blackline shows the saturation point of the material

The saturation magnetisation curve (Figure 2-2) of a material shows the subjective point at which an increasing applied magnetic field no longer causes an increase in magnetisation.

The units of saturation magnetisation are Tesla (T).

2.1.2.3 Remanence

Remanence only occurs in a ferromagnetic material. It is the residual magnetisation left in a material when an applied magnetic field has driven the material to saturation and is than removed. The higher the remanence of a material the stronger the remaining magnetisation after the applied magnetic field has been removed. Material with a high remanence is used to produce permanent magnetics. The SI units for remanence are the same as flux density (B) measured in Tesla (T).

2.1.2.4 Coercivity

Coercivity, like remanence, only occurs in a ferromagnetic material. Coercivity is the strength of an applied magnetic field, with an opposite polarity, required to remove the remaining remanence from the material. If a material requires a large applied magnetic field, operating in the opposite polarity, to demagnetise the material then significant energy will be used. In applications where the polarity of the applied magnetic field changes frequently a material with a high coercivity will use much of the energy from the applied magnetic field changing polarity. This energy takes the form of heating of the material being magnetised. If a material has a low coercivity it requires less energy to change magnetic polarity. A material with a low coercivity is termed a soft magnetic material (Section 2.4.1). A material with a high coercivity is termed a hard magnetic material. Coercivity is measured by the SI units Amperes per metre (A/m).

2.1.2.5 Hysteresis [10]

Hysteresis describes how a ferromagnetic material reacts to an alternating magnetic field. The hysteresis curve is formed from the saturation curve and the remanence curve for one cycle of an alternating current. To measure the hysteresis of a material an alternating current (AC) is used to produce an applied magnetic field that reverses in polarity. When a material is subjected to the applied magnetic field the material will be driven to its saturation point, the polarity of the applied magnetic field switches and the induced magnetic field will try to keep the same waveform as the applied field. Because all ferromagnetic materials resist switching polarity, the induced magnetic field will

not follow the applied field instead the inducted magnetic field will lag behind the applied field. The applied magnetic field will need to increase to force the induced magnetic field to switch polarity.

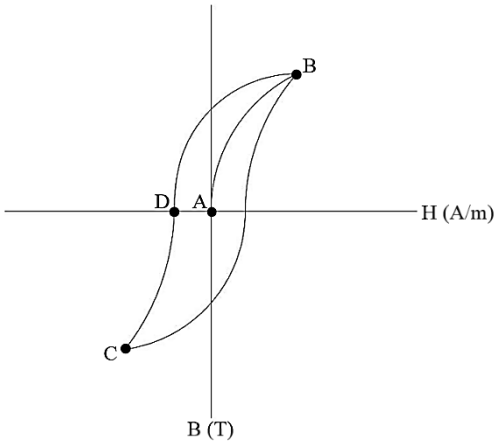


Figure 2-3. Hysteresis curve of a ferromagnetic material [11]

In Figure 2-3 an example of a hysteresis curve is shown. It shows the initial condition of the material to be tested at point A, which has no magnetisation. As the applied magnetic field (H) is increased to the material's saturation (point B) a curve is formed between the points A and B that represents the material's direct current (DC) permeability. At saturation (point B) the applied field (H) is reduced to zero. The material is then driven to saturation in the opposite polarity (point C). Once saturated at the opposite polarity the applied field (H) is reduced to zero. The applied magnetic field (H) has its polarity reversed to the original orientation and the material is driven back to saturation (point B). This results in a loop between points B and C. This loop is termed the hysteresis loop of the material and will vary depending on the materials composition. Point D is the coercivity of the material as discussed in Section 2.1.2.4.

2.1.2.6 Eddy currents [12]

Eddy currents are produced when an alternating magnetic flux induces voltages in magnetic materials. The induced voltages resist changes in flux direction, proportional to the materials coercivity, resulting in greater flux density being required to obtain a change in flux direction. Eddy currents reduce the efficiency of electrical machines such as, transformers, motors, alternators, and cause an

increase in operating temperature that results in extra cooling being required to prevent machines from overheating.

2.1.2.7 Resistivity

The physical property of a material to resist the flow of a current is known as resistance. The resistance to current flow of a material can be affected by changes in the cross sectional area and the length of a part. A long thin wire will have a higher resistance than a short thick wire, even though they both contain the same amount of material. Resistivity describes the ability of a material to resist current flow considered over a standard volume. The units of resistivity are ohms per metre cubed (Ω/m^3).

2.1.2.8 Reluctance [13]

Reluctance is the magnetic circuit equivalent of resistance in an electrical circuit. The higher the reluctance of a material the lower the flux density will be. In an electrical circuit the current will flow through the path of least resistance, in a magnetic circuit the magnetic flux will flow through the path of least reluctance. The SI units of reluctance are inverse Henrys (H^{-1}).

2.1.2.9 Magnetomotive force [14]

When trying to understand a complex electrical circuit it is common practice to reduce the circuit to an equivalent simple electrical circuit which contains three variables; voltage, current, and resistance. The same method is used to simplify complex magnetic circuits. The variables are magnetomotive force (MMF), flux density, and reluctance. MMF acts in a comparable manner to voltage in an electrical circuit. MMF causes flux density to flow around the circuit. The strength of the flux density is dependent on the size of the MMF and the reluctance of the material properties of the material in the equivalent circuit. MMF is measured in Amperes (shortened to Amp) turns (AT) and is defined as the force that occurs when 1 amp of DC current flows around a single turn of wire.

2.1.2.10 Anisotropy [15]

Isotropy means equal in all directions. If a ferromagnetic material is isotropic than it will produce the same flux density independent of the direction of the applied magnetic field. Anisotropy is the opposite of this, a ferromagnetic material will produce different flux densities depending upon the direction of the applied magnetic field. The determining factor for whether a material is isotropic or anisotropic is the orientation of the domains in the ferromagnetic materials crystal structure. If the domains are arranged randomly than the material will be isotropic, if the domains are aligned on the same axis then the material will be anisotropic.

2.1.2.11 Skin effect [16]

When a wire has a direct current fed into it the current is equally distributed through the cross sectional area (CSA) of the conductor. When a low frequency alternating current is fed into a wire the current is not spread evenly across the CSA but is nearer the edge of the conductor. As the frequency increases the charge carriers, which make up the current, move further from the centre of the CSA and towards the outer edge. At very high frequencies the charge carriers are found only on the skin of the wire with no charge carriers in the main bulk of the CSA of the wire. This is known as the skin effect.

2.1.2.12 Power factor

Power factor is a term that relates to how voltage and current waveforms relate to each other. A purely resistive load has a power factor of 1, termed unity. When a load has a unity power factor the voltage and current waveforms are matched so that peaks and troughs of the separate waveforms match.

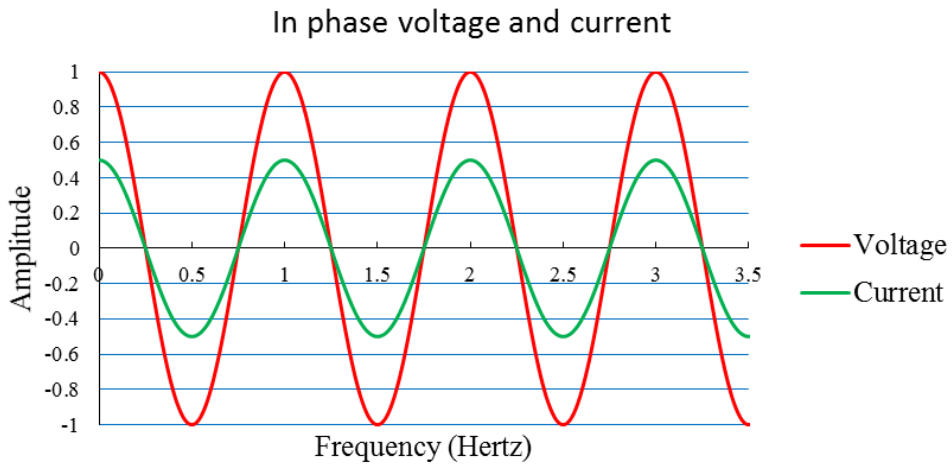


Figure 2-4. Graph of voltage and current waveforms with a unity power factor, resistive load.

Figure 2-4 shows the sinusoidal waveforms for both the voltage and current at a unity power factor. As the current and voltage change over time the rated output of an generator is taken from the maximum voltage multiplied by the maximum current.

In Figure 2-4 the maximum power is:

$$Power\ (watts) = Maximum\ Current * Maximum\ Voltage$$

$$Power\ (watts) = 0.5 * 1$$

$$Power\ (watts) = 0.5\ \ watts$$

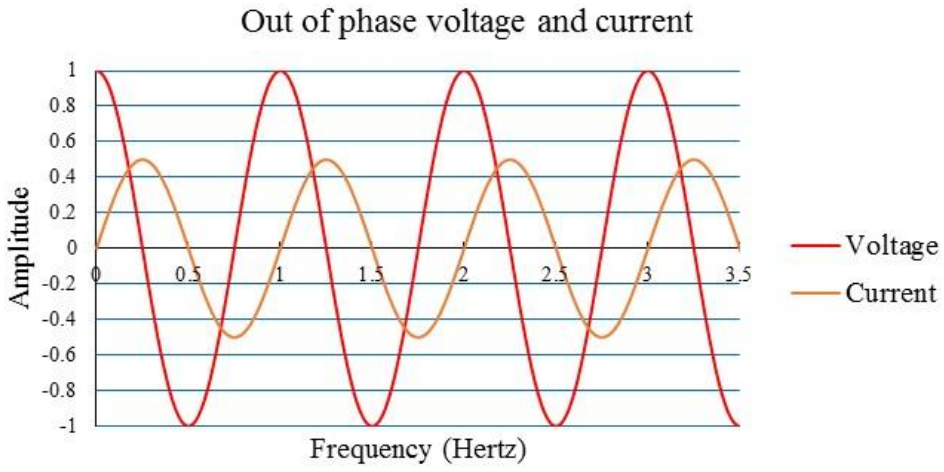


Figure 2-5. Graph of voltage and current waveforms with the current lagging the voltage by 90º.

In Figure 2-5 the waveforms of current and voltage are shown with the current lagging the voltage by 90°, indicating the load the generator is supplying is

inductive in nature. The power calculation takes the maximum voltage, but as the voltage and current are no longer in phase, the value of the current is no longer at its maximum so the calculated power is lower than the power calculated when the voltage and current were in phase.

The calculated power from when the voltage and current were in phase is called the apparent power whereas the calculate power from when the voltage and current were out of phase is called the true power.

For example:

$Power\ (watts) = 0.0314 * 1$

$Power(watts) = 0.0314watts$

The power factor is:

$$\frac{True\ power}{Apparent\ power} = Power\ factor$$

$$\frac{0.0314}{0.5} = 0.06$$

Power factor has no units and is given the notation PF. During testing the load applied to the generator is set at three different power factors, unity, 0.9, and 0.8.

As the loading of the generator, by the end user, may not be at unity power factor it is important that the generator is capable of suppling non-unity power factors without overheating. The generators are supplied to the end users with their output rating incorporating a 0.8 power factor.

2.2 Design and manufacture of generators

A generator converts a shaft's mechanical rotation energy into an alternating current. A generator can obtain its rotational energy from: a diesel engine, a wind turbine, a gas turbine, a steam turbine, or a water turbine. The mechanism that drives the rotating shaft of a generator is a prime mover. If a generator is coupled to a prime mover the combined machine is called a generator set. The type of generator used to produce a mains voltage is a synchronous machine, it maintains the frequency and voltage of its output independent of the load it is supplying. A generator has two magnetically active components: the rotor, and the stator.

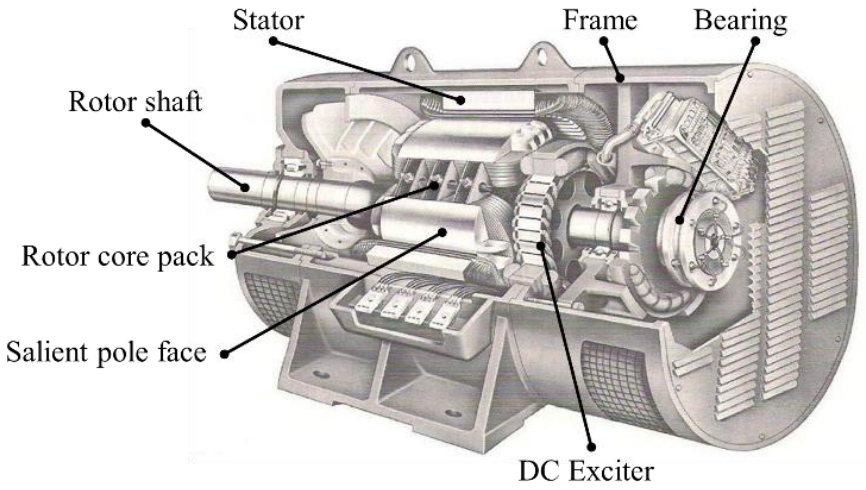


Figure 2-6. Section of a salient pole type generator [1]. As the rotor is spun by a prime mover (not shown) the DC exciter provides power to the windings on the rotor core pack. The magnetic field in the rotor core pack induces a AC current in the stators windings that produces the output of the generator.

In Figure 2-6 a cut away drawing of a generator shows the main components of the generator. As the rotor is spun by the prime mover (not shown) the DC exciter provides the power to the rotors field windings, the DC electromagnetic field than cuts across the windings of the stator to induce the AC output of the generator. The rotor pole faces experience induced eddy currents, from the harmonics and transients in the stator, and heat up during operation. The frame is not a magnetic component and is generally made from cast iron as it helps dampen the mechanical vibrations of the generator.

The rotor is a rotating component that produces a static magnetic field that induces a current in the stator, the rotor is discussed further in Section 2.2.1. The stator is a cylinder of electrical steel that surrounds the rotor, the stator does not rotate but the rotation of the rotors magnetic field results in an induced AC current flow in the stator. The induced AC current is the output of the generator further discussion of the stator is carried out in Section 2.2.4.

2.2.1 Rotor

The rotor of a synchronous generator produces a static magnetic field which, as it rotates, induces a current to flow in the stator which surrounds the rotor. There are two types of rotor; a non-salient pole rotor (Figure 2-7a) and the salient pole rotor (Figure 2-7b).

a)  b) 

Figure 2-7. (a) Non-salient pole rotor otherwise known as a cylindrical rotor due to the distributed windings the rotor cannot achieve the same power density, for the same length, as the salient pole rotor. (b) Salient pole rotors have concentrated windings that give a higher power density, for its length, than non-salient pole rotors.

Figure 2-7. (a) shows a non-salient pole rotor. The rotor is a cylinder of, generally forged, steel that has grooves machined into its surface to accommodate either Cu wire coils, for wound rotors; or permanent magnets. A non-salient pole rotor produces a smooth AC current output from the generator. Due to its cylindrical nature, the strength of magnetic field a non-salient pole rotor can produce is limited as deeper grooves weaken the mechanical properties of the rotor. To produce the same magnetic field as a salient pole rotor, non-salient pole rotors are longer making them less suited to applications that require portability. One key advantage of non-salient pole rotors is that they operate at far higher rotational speeds than salient pole rotors removing the need for gearboxes to reduce the output of the prime mover, and incurring the mechanical losses associated with gearboxes.

Figure 2-7. (b) shows a salient pole rotor. The protruding poles enable the use of concentrated field windings which increase the power density of the rotor for the unit length when compared to a non-salient pole rotor. The salient pole rotor is suited to low speed high torque prime movers such as hydroelectric and diesel engines.

The use of permanent magnets in generators is limited by the strength of magnetic field a permanent magnet can produce [17]. The use of REE magnets increases the strength of the magnetic field to a point where permanent magnet generators can produce 500kW. The use of REEs is also limited by the high costs of producing the magnets [18], only applications that can support a high unit cost can use large permanent magnet generators. Applications such as generators on aircraft [19], and wind turbines [20], are suited to permanent magnet salient pole rotors as the rotor is lighter than the equivalent electromagnetic based salient pole rotor. This thesis is based upon the salient pole rotor as it is the type produce by the sponsor of this work.

2.2.2 Salient pole rotor

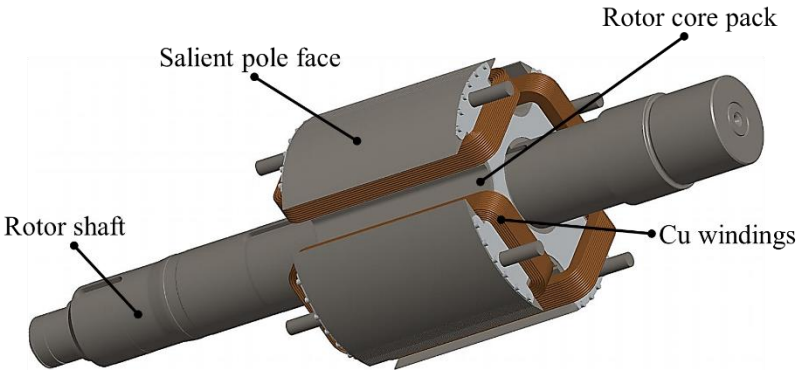


Figure 2-8. A 3D CAD rendering of a salient pole rotor. The core pack consist of hundreds of laminations hydrologically pressed together. The core pack is then pressed onto the shaft and the Cu windings are wound onto the salient poles

In Figure 2-8 a salient pole rotor has projections coming off the cylindrical shaft that allow more concentrated Cu windings, which produce a stronger magnetic field than the distributed windings of a non-salient pole rotor. A salient pole rotor induces a less smooth current in the stator, than in a non-salient poll rotor, resulting in the output of the salient rotor generator requiring power electronics to improve its AC output waveform.

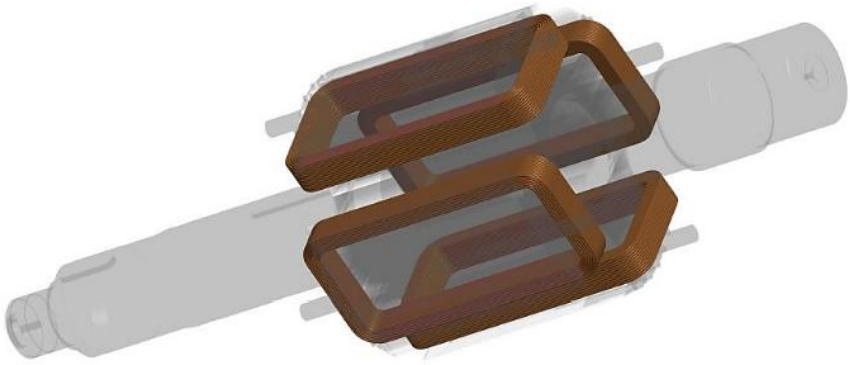


Figure 2-9. An assembled salient pole rotor with the Cu windings highlighted in-situ on the salient poles.

In Figure 2-9 a non-permanent magnet based salient pole rotor is shown with the Cu windings highlighted. The windings provide the electromagnetic field that induces an AC output in the stator. The windings are produced out of a Cu wire that has an insulating coating on it. The wire is wound directly onto the core pack.

The tensioning of the wire, as it is wound, is important as air pockets in the winding creates hot spots, when in operation, that can damage the windings. Once the windings are completed the core pack has a resin dripped onto the windings. The resin is set through ohmic heating by passing a current through the windings. The heated resin has a reduced viscosity that allows it to completely encase the windings. Once cooled the coating acts to prevent mechanical damage to the windings and stop them coming apart during generator operation. There are two forms of a salient pole rotor: the first is assembled from four principle components; the core pack, the damper windings, the support bars, and the shaft (Section 2.2.3), the second is machined from a single billet of steel (Section 2.2.3.5).

2.2.3 Assembled rotor

The following sections describe the four main components that together form an assembled salient pole rotor.

2.2.3.1 Core pack

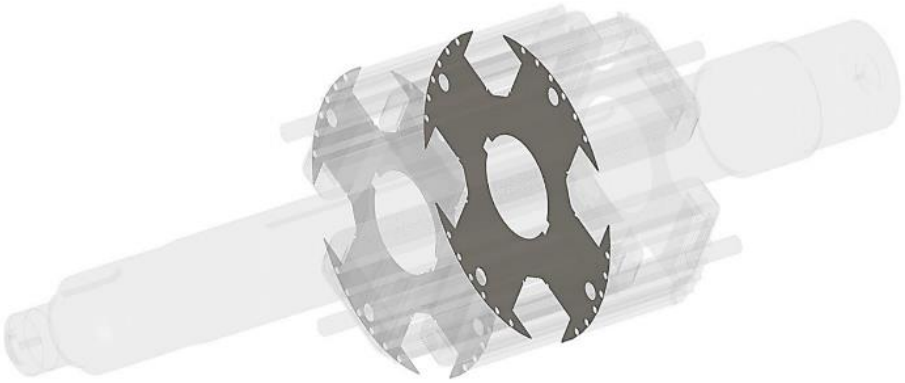


Figure 2-10. The core pack of a salient pole rotor with a single lamination highlighted. The rotor laminations are produced at the same time as the laminations that form the stator to reduce material waste.

In Figure 2-10 the core pack of a salient pole rotor is shown to be assembled out of a stack of electrical sheet steel that has been cut to the desired rotor typology. The layers, or laminations, are stacked to the required core length. The core pack has two functions, one mechanical and the other magnetic.

Mechanically the core pack supports the Cu windings and allows the mounting of dampener windings and support bars. Magnetically the core pack's role is to provide a high permeability material with a high saturation magnetisation. High permeability material reduces the current required to produce a magnetic field of a given strength. The core pack is produced by stacking laminations to the desired core length, hydraulically pressing the stack and then permanently fixing the shape of the core pack. The support bars and dampener windings are then hydraulically pressed into place. The part of the core pack that directly faces the inner surface of the stator is called the pole face, the pole face undergoes magnetic effects that the main body of the core pack does not [21]. Altering the thickness of the laminations that are stacked to produce the core pack, and changing the typology of the pole face can improve the efficiency of the generator [22].

2.2.3.2 Damper windings

A damper winding (or amortisseur winding) is a set of solid bars that run the length of the core pack, close to the pole face, the bars create a path for current flow [23]. Bars of Cu or Al are pressed into the pole faces of the core pack. The Cu or Al bars are then electrically shorted together. If all the bars in a pole face are shorted together but not connected to other poles faces then the damper windings are termed as: non-connected, incomplete, or open. If all the bars from each of the pole faces are connected together than the damper winding is termed complete, or connected.

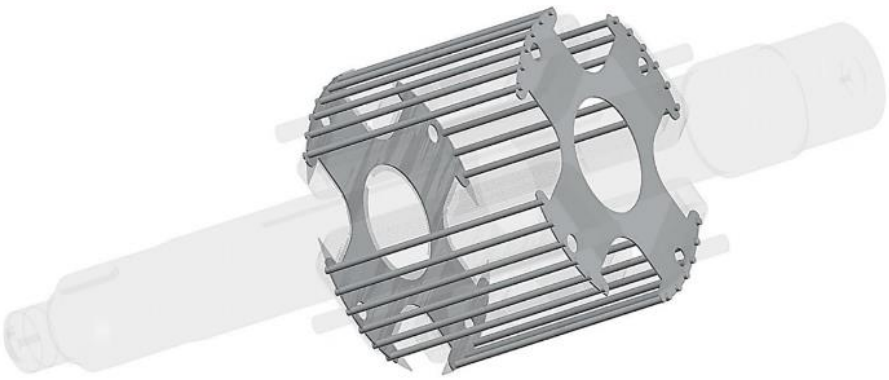


Figure 2-11. Damper windings shorted at both ends of a complete damper winding. In salient pole rotors the damper windings are used as a crude squirrel cage rotor to spin the rotor to near synchronous speed before the field windings lock the rotor to synchronous speed.

In Figure 2-11 a complete damper winding is shown with the core pack removed to show how the damper winding fits together. The damper winding can act as a squirrel cage rotor. A squirrel cage rotor is a steel rotor with Cu or Al bars embedded in the surface and electrically short together it is used in induction motors. By creating a squirrel cage rotor within its salient pole rotor the motor can be started as a simple induction motor until approximately 95% synchronous speed has been reached and the field winding is use to lock in the synchronicity. In synchronous generators the damper winding performs two functions [24]; the first is to reduce the under or over speed of the rotor when a load is added or removed; the second is to dampen oscillations in the output waveform caused by the induced currents coming from the stator [25].

2.2.3.3 Support bars

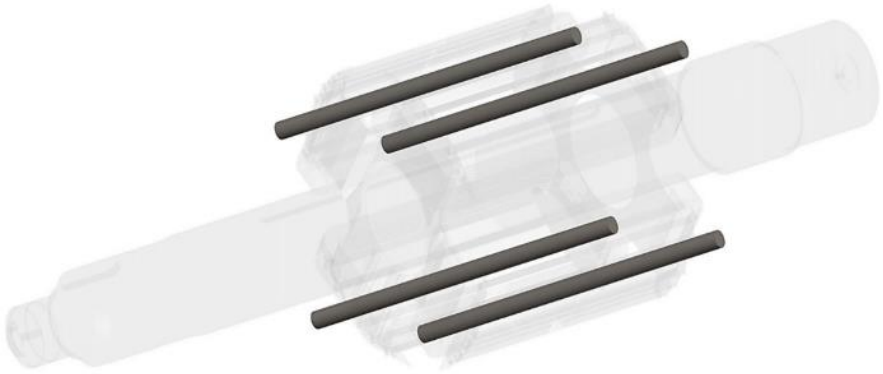


Figure 2-12. The support bars are produced out of steel and are hydraulically pressed into the core pack to improve the rigidity of the core pack and support the Cu windings to stop centrifugal forces bending the windings into the stator during operation

In Figure 2-12 the support bars are shown to be cylindrical bars of steel that have been hydraulically pressed into the core pack. The support bars perform two functions for the salient pole rotor. The first function is to stop the stack of laminations from twisting in the axial dimension as the rotor spins. The second function is to stop the ends of the Cu windings bending into the stator through the centrifugal force of the spinning rotor, causing extensive damage.

2.2.3.4 The shaft

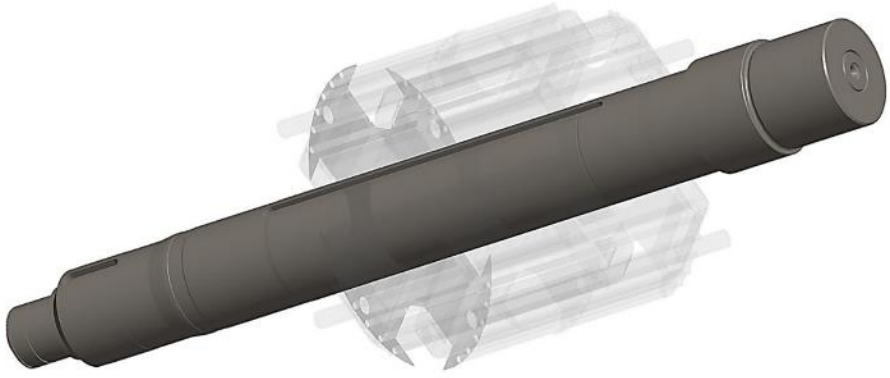


Figure 2-13. The shaft of the rotor is produced from steel billet and depending on the output power of generator can be heat treated to reduce the impact of cyclical fatigue during operation.

In Figure 2-13 the shaft of the rotor is machined from a cast steel billet. Once the shaft has been turned on a lathe to the dimensional and geometric tolerances required, a rectangular slot is milled into the shaft at the location the core pack will fit on to the shaft.

The rectangular slot forms the keyway/keyseat of an axial keyjoint that connects the core park to the shaft. Other keyways are cut into the shaft which allow the exciter (supplies current to the rotor) to be fitted directly to the shaft.

2.2.3.5 Solid salient pole rotors

Solid salient pole rotors are used in very large generators and motors that operate in harsh environments [26]. In very large generators the laminations required to produce the stator and rotor have a diameter that is larger than the width the rolls of electrical steel are supplied in. The stator laminations are produced in segments that are joined together to form the complete disk of the stator [27].

Some large rotor core packs are produced out of segments, however the rotational speed of the rotor causes difficulties with segmented rotors that make their use rare [26]. A solid rotor machined out of a billet of steel allows rotors of any size and typology to be produced. Solid rotors do not perform as well as the assembled rotor due to excessive heating cause by eddy currents [28] and the reduced permeability of steel billets when compared to electrical steels.

Solid rotors are used in applications where the extra losses incurred by having a solid rotor can be offset by the energy source for the prime mover. The production of solid rotors for applications where the prime mover has a limited fuel supply that must be carried with the generator, such as a diesel engine, has been set aside in favour of producing rotors out of laminations and using damper windings.

2.2.3.6 Air gap

Air has a relative permeability of 1 compared to a ferromagnetic material such as M700-65A electrical steel which has a relative permeability of 1730. This means that the electrical steel concentrates the magnetic flux, generated by current flowing through a conductor, 1730 times more than air.

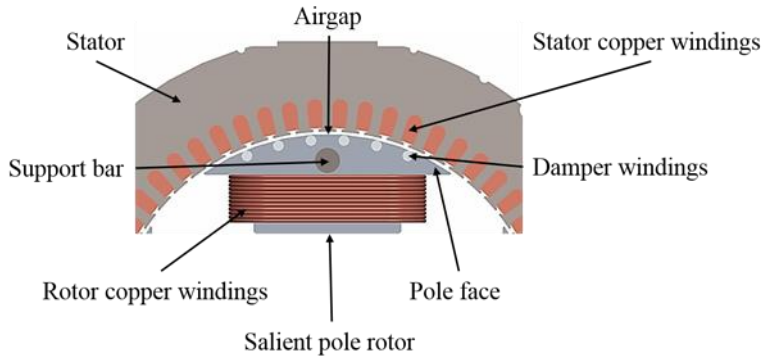


Figure 2-14. Key electromagnetic components of the rotor and stator. The rotor core and the stator core are produced out of the same electrical steel to reduce waste in the stamping process.

In Figure 2-14 the main electromagnetically active components of the rotor and stator are identified alongside the airgap that separates the rotor from the stator. In this example the air gap is 2mm.

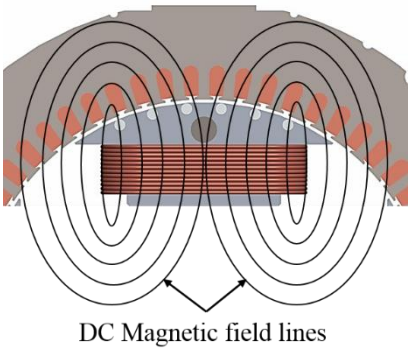


Figure 2-15. The main function of the rotor is to produce the DC magnetic field that cuts across the conductors in the stators windings to produce an induced current flow. As the rotor is rotating the amount of induce current in the stators varies over time resulting in an AC current flow.

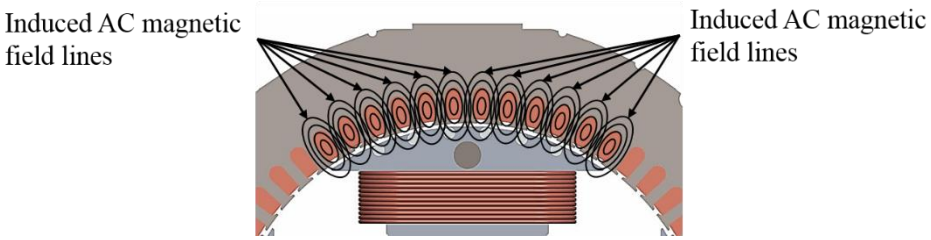


Figure 2-16. The induced AC current in the stator windings generate their own AC magnetic field which is strong enough to induce currents to flow in the surface of the pole shoe.

To stop the AC electromagnetic flux from inducing eddy currents in the pole shoes the outer diameter of the pole shoe could be reduced. This would increase the air gap and therefore reduce induced eddy currents.

The drawback to this method is that the DC electromagnetic field will need to be dramatically increased to cross the expanded air gap. Increasing the DC electromagnetic field results in an increase in the DC current in the coils of the rotor, which in turn produces more heat. The reduction of eddy currents is desirable because it allows an increase in the DC electromagnetic field increasing the output of the generator. The only limitations on the strength of the DC electromagnetic field are, the saturation magnetisation of the material that makes up the rotor, and the ability to cool the rotor. A reduction in heating caused by induced eddy currents allows extra heat to be added by the coils of the rotors electromagnet thus allowing an increase in the DC electromagnetic field increasing the power output of the generator.

2.2.3.7 Apparent air gap

The ideal method to reduce eddy currents and limit any required increase in DC current flow in the rotor is to use a material that filters electromagnetic fields based upon whether they are AC or DC in origin. The saturation magnetisation of a material may provide a method to achieve filtering of AC and DC magnetic fields.

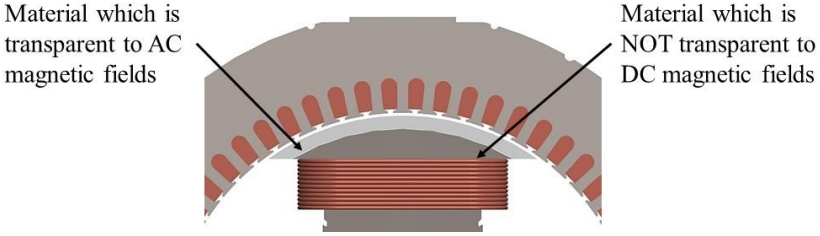


Figure 2-17. A salient pole rotor with the pole shoes made of a material that is driven to saturation by the DC electromagnetic field. The induced AC magnetic field sees the saturated pole shoe as an airgap.

If the material of the pole shoes, Figure 2-17, is at magnetic saturation then the AC electromagnetic field from the stator cannot induce eddy currents in it, and the saturated material acts as if it were air. If the saturated material of the pole face is 10mm thick the apparent air gap between the rotor and stator will be the actual air gap, in this example 2mm, and the thickness of the saturated material of the pole shoes (10mm). In this case the AC magnetic field would have an air gap of 12mm. This large air gap will result in the main rotor body not being subjected to induced eddy currents.

2.2.4 Stator

In Section 2.2 the stator was defined as a cylinder in which the rotor spins. The stator is the part of the generator that has a more complex electromagnetic function to perform than the rotor. The stator contains Cu windings that, when the rotors DC electromagnetic field passes through them, causes an AC current to be induced. The stator has three main components; Cu windings, the stator core, and the frame.

2.2.4.1 Cu windings (stator)

Insulated Cu wire can be inserted into the slots of the stator core either a singular wire at a time using needle winding or as complete coils formed on a jig using tumble winding. The amount of Cu in the slot is called the fill factor. The higher the fill factor the better the performance of the finished stator. Needle winding allows for the greatest amount of Cu fill as the tensioning on the coils and placement of each wire is carefully controlled. Tumble wound coils are much quicker to produce as the positioning of the wire is less critical. Once removed from the jig the wire coils lack any tensioning. It is possible to improve the fill factor, of tumble wound coils by compressing the windings once they have been inserted into the stator [29]. The use of round wire limits the total possible fill factor. On machines with a higher unit cost rectangular Cu bars are used, as they allow a much higher fill factor. How the Cu coils are connected together depends on the desired output of the generator but considerable variation exists in the laying out of the coils in the stator core.

2.2.5 The stator core

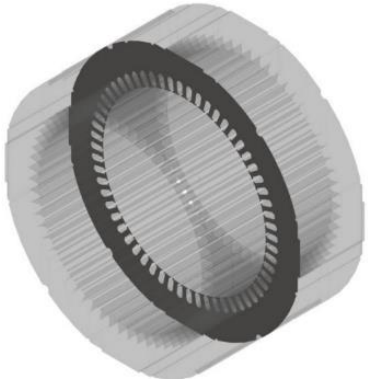


Figure 2-18. Image of a stator core with one of the laminations highlighted. The stator is produced on a fixture and then pressed to remove any oil left on the laminations from the stamping process.

In Figure 2-18 the stator core is made from pre-coated, with an insulative coating, high-quality electrical steel. The stack of laminations is hydraulically pressed to remove any air gaps or deformations caused by the cutting out process. Once the stator core is pressed it is welded on its outer diameter to fix its shape. The welded stator core has Cu wire inserted into the slots on its interior surface. The wound stator core is then coated in a layer of resin that fixes the Cu windings in place and stops the ends of the Cu coils from moving due to vibration when the generator is in operation.

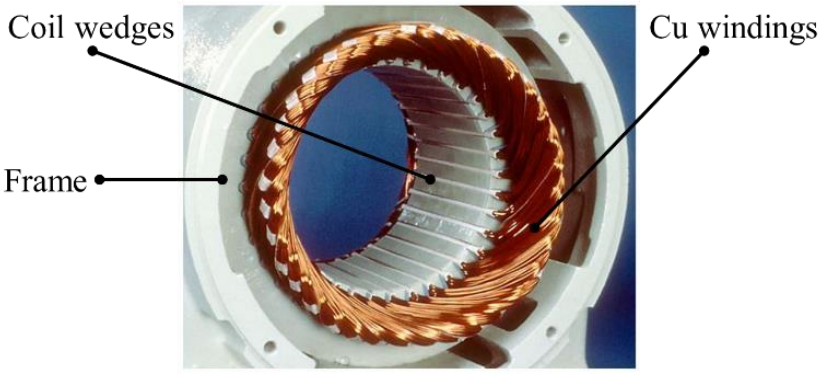


Figure 2-19. Stator core with Cu windings and wedges used to hold the windings in their slots. The frame dampens mechanical vibrations during operation.

In Figure 2-19 wedges of non-conductive material are inserted into the tops of the slots, containing the Cu windings, these wedges prevent the windings from coming loose during operation. The stator can be produced so that there is a skew angle parallel to its length, the skew angle reduces the clogging torque of the finished generator [30].

2.2.5.1 Segmented stator core

In large generator production the laminations for the stator have a very large diameter that cannot be produced as a single piece without the use of expensive machine tools. The production of large diameter laminations can waste a large amount of material and make handling the laminations very difficult. Large generator manufacturers design their stator and rotor laminations to be produced from smaller segments that fit together to form the final typology. The use of a segmented stator allows the use of smaller machine tools and eases the manual handing problems associated with large diameter laminations.

The segments are either connected together to form complete laminations or are connected via dovetail joints on the back of the segments to the stator core housing. Manufacturers of smaller scale generators have begun to use segmented stators due the reduction in material waste. The increased labour required to assemble the stator has been offset by the introduction of automated assembly systems [31]. The majority of automated assembly systems for segmented stator cores are based on high volume motor production [32][33][34] for production of smaller volume large motors or generators automation is not yet financially viable.

2.2.5.2 Frame

The frame is a cylindrical tube that the wound and resin coated stator core is hydraulically pressed into. The frame has no magnetic function, it is there to provide mechanical support for the stator core and to allow an air gap, between the outer diameter of the stator core and the frame, in which forced air cooling can be used to cool the generator during operation.

The frame is also there to allow the generator to be handled without fear of damaging the more delicate stator core. The frame carries all the electrical connections for the stator and mounting points to allow the generator to be mounted onto the desired prime mover.

2.3 Introduction to synchronous generators

A generator converts a shafts rotational mechanical energy into electrical energy. An example of this principle is a coil of wire rotating in the field of a permanent magnet, as the magnetic field cuts across the copper coil it induces a current to flow in the coil of wire. The stronger the magnetic field of the magnet the larger the induced current will be.

2.3.1 Synchronous Generator

The electrical supply in the United Kingdom (UK) provides a voltage of 230v -6% +10% supplied at a frequency 50 Hz [35]. The supply frequency is important as it defines the speed the rotor needs to spin at to produce the frequency required by the electrical appliances.

$$f = \frac{n}{60} * \frac{p}{2}$$

$f = the\ required\ supply\ frequency$

$n = the\ rotational\ \ speed\ of\ the\ rotor\ in\ rotations\ per\ minute\ (RPM)^{*}$

$p = the\ number\ of\ poles\ on\ the\ rotor^{**}$

*The rotational speed of the rotor is in revolutions per minute so needs to be changed to number of rotations per second by dividing by 60.

**As a magnetic field always has two poles (north and south) the number of poles is divided by two to get the number of pole pairs.

Table 2-1. Rotational speed and pole numbers required to produce 50 Hz.

Supply frequency (Hz)	Number of poles	Rotational speed (RPM)
50	2	3000
50	4	1500
50	6	1000
50	8	750
50	10	600
50	12	500

Table 2-1 shows how an increase in the number of poles reduces the rotational speed of the shaft. The supply frequency used for Table 2-1 is 50Hz which is common outside of the United States of America (USA). In the USA the supply frequency is 60Hz. Table 2-2 shows how the increase in supply frequency affects the rotational speed the generator needs to operate at.

Table 2-2. Rotational speed and pole numbers required to produce 60Hz.

Supply frequency (Hz)	Number of poles	Rotational speed (RPM)
60	2	3600
60	4	1800
60	6	1200
60	8	900
60	10	720
60	12	600

A synchronous generator operates at a pre-selected frequency, hence rotational speed. When no-load is connected to the generator the rotor spins at the correct speed to output the pre-set frequency. As a load is applied to the generator the increased current drawn from the stator causes the rotor to slow and the prime mover has to increase the torque on the rotor to maintain the output frequency of the generated current [36].

2.3.2 Losses

Losses in a generator affect the efficiency of the conversion of rotational energy to electrical energy. This is particularly important in portable generators where the fuel for the prime mover has to be carried with the generator. The higher the losses the greater the inefficiency of the generator.

Losses in a generator are divided into four main areas [12]:

- Resistive losses in the rotor and stator conductors (Section 2.3.2.1)
- Iron losses in the magnetic circuit (Section 2.3.2.2)
- Mechanical losses (Section 2.3.2.3)
- Additional losses (Section 2.3.2.4)

The rotor and stator each have these four losses but the relative size of these losses is different so a brief explanation of the losses for the rotor (Section 2.3.3) and the stator (Section 2.3.4) are given after the four loss types are explained.

2.3.2.1 Resistive losses in the rotor and stator conductors

The losses in the conductors are often termed copper losses due to the principle conductors in generators being made out of copper (Cu); although aluminium Al is sometimes used.

When a current flows through a conductor the conductor will resist the current flow, converting some of the current flow into thermal energy. The heat generated by copper losses are a large factor in machine design as the resistance of the conductor is proportional to its temperature. If inadequate cooling is provided in a generator the temperature rise will cause increased resistance in the conductors producing an increase in temperature. This feedback mechanism will lead to permanent damage to the generator (worst case) or a significant impact on the efficiency of the generator (best case) so care should be taken to provide adequate cooling. The ideal generator would have conductors with no resistance but in practice this is not currently possible.

2.3.2.2 Iron losses in magnetic circuit

The Iron losses [37] come in the form of hysteresis losses and eddy current losses [38]. The use of magnetic materials that have low coercivity reduces the losses from hysteresis. To reduce the eddy current losses the use of thin laminations to produce the magnetically active components reduces the size of the eddy currents. Iron losses are the result of the induce AC output of the generator. The DC components of the generator do not produce these losses but can have them induce onto them by the AC components.

2.3.2.3 Mechanical losses

Mechanical losses are caused by the friction of the bearings that the shaft rotates on, and the energy require to provide cooling (windage losses) [39]. If a gearbox is used to reduce the speed of the prime mover to provide a synchronous output, the mechanical losses will be greater as gearboxes are not 100% efficient.

2.3.2.4 Additional losses

The additional losses are the difference between the total losses and the sum of the conductor losses, the iron losses, and the mechanical losses. Additional losses are often referred to by the term stray load losses and are not static losses, they will vary depending on the loading of the generator. The use of modelling can help to show where the additional losses are produced in order to facilitate reducing them [40].

2.3.3 The rotor losses

The rotor produces a dynamic DC electromagnetic field that, if taken in isolation, would have losses from the resistance of the conductor only. However the induced AC electromagnetic field of the stator results in currents being induced back into the rotor from the stator. These currents are produced by the gaps between poles of the rotor producing non-sinusoidal induced currents in the stator. The best method to reduce them is to use conductors that run the length of the pole faces termed damper windings, Section 2.2.3.2.

As a load is applied the rotor slows, if allowed to slow too much the rotor would not produce the required supply frequency. As the rotor is slowed further currents are induced in the pole faces. The additional current flows through the damper windings on the pole faces, causing an electromagnetic field to form. This induced electromagnetic field opposes the force trying to slow the rotor down, this helps maintain the synchronicity of the generator.

2.3.4 The stator losses

The stator's losses are produced by hysteresis, iron losses, and copper losses. The standard method of reducing the stators losses are to use thinner laminations [41] to produce the stator core; and use grades of electrical steel that have undergone more extensive heat treatments, therefore are more expensive, to reduce their coercivity which reduce hysteresis [42].

Both of these methods result in an increase in production costs so the cost benefit ratio of using the more expensive material, or thinner laminations verses the improvement in performance must be carefully gauged.

2.4 Effects of material selection on performance

In ferromagnetic materials, particularly steel, the two fundamental requirements for high permeability and high saturation are impurities such as C and sulphur (S) content and microstructure. The manufacturing processes involved in generator production can have a detrimental effect on the magnetic performance of the finished generator [43].

2.4.1 Hard magnetic materials [44]

A material with a high remanence (Section 2.1.2.3) retains a magnetic field when an applied magnetic field has driven the material to saturation and is then removed. This creates a magnetised material which is termed a permanent magnet. Permanent magnets are used in applications where supplying an electrical current to produce an applied magnetic field is not practical. Although all ferromagnetic materials are able to act as permanent magnetics the addition of alloying elements can increase the strength of the retained magnetic field substantially.

2.4.1.1 Magnetic steel [44]

Before 1914 the primary material used to make permanent magnets was steel that had around 5%wt tungsten (W). During the First World War the expensive W was replaced with the less expensive chromium (Cr). During 1917 scientists in Japan developed a magnetic steel that was 30-40%wt Co with additional amounts of W and Cr. Researchers found that quenching steels to physically harden them also made the steel more magnetically hard. The increased magnetic hardness is derived from the quenched steels metastable martensite microstructure. Martensite has a high coercivity which makes it good at retaining a magnetic field once it has been driven to its saturation point [44]. Continued development of new hard magnetic materials has seen the use of magnetic steels reduce. One of the main reasons for this reduction is the high cost of the Co that makes up 30-40%wt of the finished magnet.

2.4.1.2 ALNICO

ALNICO takes its name from the chemical elements that form it: aluminium (Al), Ni, and Co. Although not mentioned in the name, a large constituent part of the alloy was also Fe. Originally a trade name the term ALNICO went on to encompass a range of alloys that included addition alloying elements of copper (Cu) and Cr.

Development has continued on ALNICO derivatives [45], but the field has largely been overshadowed by the use of REEs which exhibit much higher remanence.

2.4.1.3 Rare earth magnets

Many REEs are ferromagnetic although their use in their pure form is not possible, as their Curie temperatures are below room temperature (21˚C). This means that above room temperature the metals are paramagnetic. To use REEs in magnets that operate at temperatures above their Curie temperature the elements are alloyed with the more common transition ferromagnetic materials Fe, Ni, and Co. Rare earth magnetics can be 10 times stronger (magnetically) than ALNICO alloys. Although termed REE the elements are not rare in the sense of the volume available in nature [46]. The difficulty with rare earth extraction is that the REEs do not form easily extractible ores in the same way as elements like Fe and Al. The ores that are refined for REE production contain elements such as thorium (Th) which is toxic, so the production of REEs produces large amounts of toxic waste making them very expensive to produce and therefore use [18] in REM production.

2.4.2 Soft magnetic materials

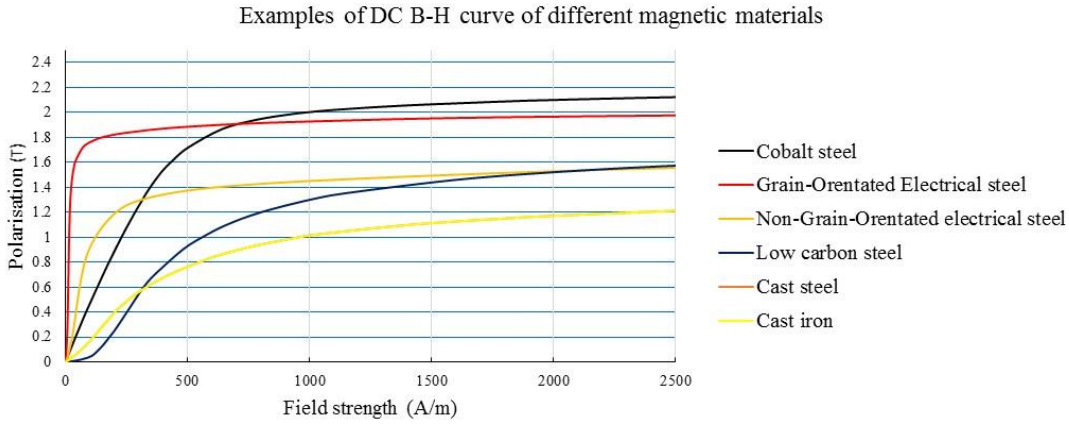


Figure 2-20. The B-H curves of multiple materials that are termed as soft magnetic materials

In Figure 2-20 the DC magnetisation curve of commonly used soft magnetic materials is shown. The samples are from multiple manufacturers and the data is not directly linked to a single grade of each material since each grade has multiple sub-grades available [47]. The shown B-H curves are useful for demonstrating the differences in the magnetisation curves of materials with different compositions.

The determining factor for classifying a material as magnetically soft or hard is its coercivity. An ideal soft magnetic material has zero coercivity, zero remanence, high permeability, and high magnetic saturation. There are three main groups of soft magnetic materials [48] based upon the function the materials are used for, they are:

1. Heavy duty flux multipliers - This group consists of transformers, generators, and motors. The machines tend to be large and heavy. For these applications the material needs to operate with a high flux density so a high saturation and high permeability are ideal. The principle operation of these machines are at low frequencies. Due to the size of the machines the main component of the material is Fe, as this has high saturation and is relatively cheap when compared to other ferromagnetic elements. The principle form of the Fe is in thin steel sheets with very low carbon content and with a non-conductive coating on both sides. This is classed as electrical steel (Section 2.4.2.1)
2. Light duty flux multipliers - The applications for this group are for smaller motors, high frequency transformers, and inductors. As the applications for this group are more specialised the cost of the material is less important than its magnetic properties, (Section 2.4.2.2)
3. High frequency components - These are generally made from ceramics such as Fe oxide. These ceramics have low magnetic saturation and poor permeability but very low coercivity. Ceramic components are non-conductive so do not have eddy currents associated with them, ceramic components are termed ferrites due the high Fe content (Section 2.4.2.3)

2.4.2.1 Heavy duty flux multipliers

Electrical steel

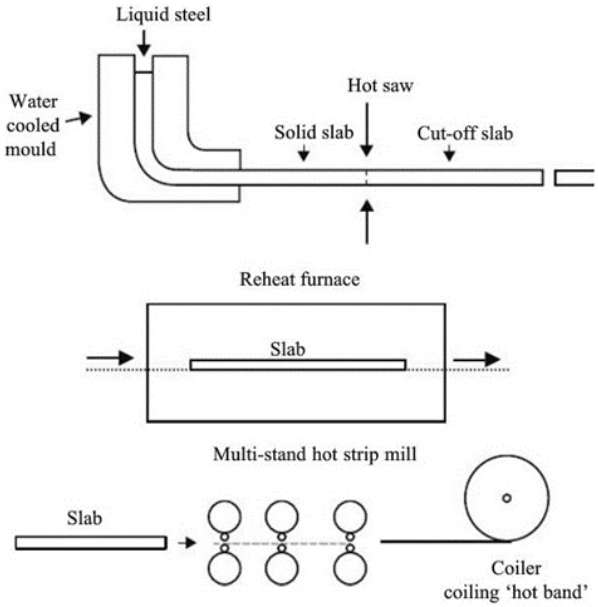


Figure 2-21. A continuous casting method for the production of electrical steel [49].

In Figure 2-21 the first step in the production of an electrical steel is shown. The high purity molten steel is poured into a mould that forms the cooling steel into a continuous sheet, which is then cut into 20 ton slabs. The slabs are then reheated in a furnace and passed through a series of rollers until the sheet is between 2-4 mm thick the sheet is termed "hot band" and is collected onto a roll.

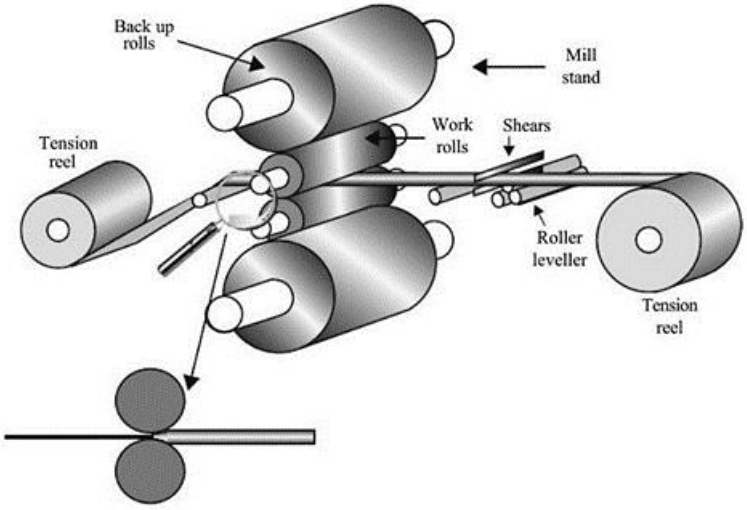


Figure 2-22. Reducing the thickness of "hot band" steel to the finish thickness requirement [49].

In Figure 2-22 the “hot band” steel is then passed through a series of rollers that cold roll the sheet to the required thickness [50]. During the cold rolling process the steel develops a Goss texture [51] that further improves its magnetic performance. Once the steel has been cold rolled it is annealed. Annealing is the process of heating a material and allowing it to cool slowly to remove stress built up during rolling. Additional processes are normally carried out such as decarbonisation and desulphurisation to further improve the steel’s magnetic properties, by reducing coercivity. The production of electrical steels is very complex and the magnetic effects of cold rolling can be improved upon by the use of special annealing heat treatments [52] and by altering the atmospheric content the heat treatments are carried out in [53]. There are two categories for the finished steel; one is fully processed, this has had all of the heat treatments applied, and an electrically insulative coating applied to both sides of the steel; the other is semi-processed which has not had the final annealing heat treatment applied nor the insulative coating. The semi-processed steel allows the annealing process to be carried out after a machining process has been carried out on the sheet steel to produce the final part. Machining of the sheet steel affects the magnetic properties of the part, so by carrying out the final annealing after the part has been cut out of the steel the magnetic properties can be maximised.

There are three types of steel that can be classed as electrical steel: low-carbon, non-grain orientated, and grain-orientated.

Low carbon steel

Low carbon steel was the first type of steel to be used to produce motors, generators, and transformers [54]. Low carbon steels are produced in large quantities and are relatively cheap to produce and machine. In an alternating magnetic field application low carbon steels have losses that can be 10 times that of a silicon (Si) steel [54]. This is due to the low resistivity of the steel allowing large eddy currents to form. However, in static magnetic field applications no eddy currents are formed allowing the use of low carbon steels.

Non-orientated grain steel

Non-orientated grain steel has a quantity of Si (1-6.5%) added to increase the steel's resistivity and helps to tailor the finished steel's microstructure [55]. The addition of Si as an alloying element causes steel to become brittle, resulting in a material that is more expensive to machine than low carbon steel. As the understanding of the magnetic effects of crystal size [56] and levels of impurities [52] has increased, the processes used to produce non-grain orientated steels have been refined [57]. Non-orientated grain steel magnetises equally well in all directions, this is important in generator production and is termed isotropic.

Grain orientated steel

Grain orientated steels are a special group of electrical steels that have been produced with a crystal structure that causes the steel to magnetise more strongly in one direction, this results in the steel being anisotropic in nature. As it is more strongly magnetised in one direction the use of grain orientated steel in generators requires careful design of the machine.

Grain orientated steel is used in transformers as its anisotropic nature can be used to improve the transformers efficiency.

2.4.2.2 Light flux materials

Electrical steels make up the bulk of the material used to produce large generators and transformers. For smaller applications materials that have less coercivity and remanence are required to increase efficiency. For these smaller applications where an increase in efficiency, but not power density, is required the use of Si steel laminations is replaced with iron-nickel (Fe-Ni) alloy laminations, or iron-cobalt (Fe-Co) alloys.

Ni-Fe alloys

Fe-Ni alloys for magnetic applications come in two main varieties, those with less than 50% by weight, (wt%), Ni content and those with 50-80wt% Ni content. The magnetic saturation of pure Ni is less than that for Fe or Co. The lower saturation of Ni results in any alloy that contains Ni having a lower saturation magnetisation than either Fe or Co.

The higher Ni content reduces the saturation magnetisation of the alloy but the permeability of the material increases significantly.

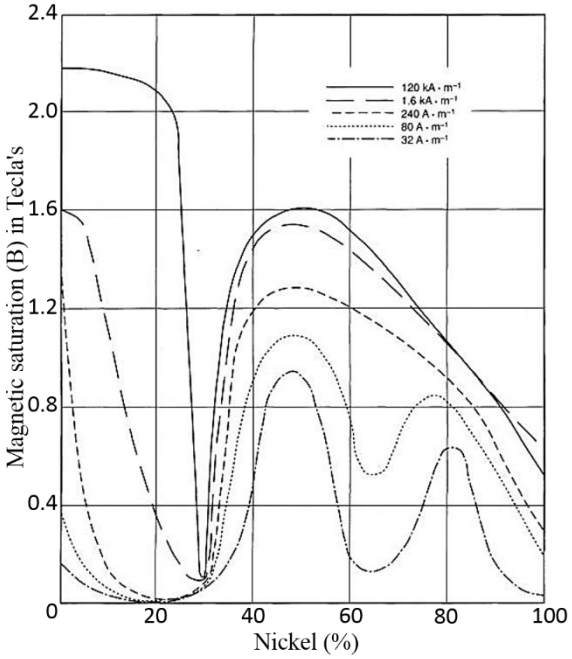


Figure 2-23. Changes in the Ni content of a NI-Fe alloy result in changes in magnetic performance [58].

In Figure 2-23 the initial alloy is 100% Fe and has a high magnetic saturation but as the Ni content increases past 20% the saturation decreases sharply. The body centric cubic (BCC) structure of the Fe alloy starts to change at around 30% Ni content into a face centric cubic structure (FCC). As the Ni content increases to 35% Ni content the structure of the alloy becomes uniformly FCC which in a steel alloy is termed austenitic. At this point the magnetisation saturation is lower than for pure Fe after this point the saturation of the alloy increase sharply as the %wt of nickel content is increased.

Fe-Co alloys

Fe-Co alloys that have 50wt% of each metal have a magnetic saturation that is 17% higher than pure Fe. The addition of Co increase the saturation magnetisation of the resultant alloy as well as increasing its permeability. A Fe-Co alloy with a Co content of 35wt% has the highest magnetic saturation of any binary alloy. As the Co content increases the permeability of the alloy increases.

The most efficient generators and transformers use Fe-Co laminations, with its higher magnetic saturation and higher permeability the alloy can outperform both Fe-Si and Fe-Ni alloys [59].

The use of an Fe-Co alloy allows for smaller generators, however the main difficulty with the use of Co is its high cost which is 31x the price of a ton of electrical steel for comparison Ni is 12x the price of electrical steel [60].

2.4.2.3 Ferrites

In high frequency applications the use of an electrically conductive material such as Fe, Co, or Ni causes a reduction in the generators operating efficiency due to circulating eddy currents. Non-conductive oxides of Fe, Co, and Ni are mixed with ceramics to produce ferrites.

Ferrites do not have high magnetic saturation or permeability when compared to the previously discussed soft magnetic materials but they have very high resistivity which in high frequency applications is more important than saturation or permeability.

2.4.3 Microstructure

The requirements for a magnetic material are based on what type of magnetic field they are used to produce. For low frequency AC applications the need for high permeability and high saturation are of prime importance, but the need to switch polarisation also adds the need for low coercivity and low remanence. As the AC frequency is increased the importance of coercivity and remanence increases with respect to permeability and saturation. DC magnetic materials can be concerned with the permeability and saturation alone.

A harder magnetic material is better suited to DC applications as once the magnetic field is setup the magnetisation of the material will become permanent reducing the energy required needed to maintain the DC magnetic field [61].

There is a considerable selection of alloys that make up soft magnetic materials, each has its own preferential crystal structure to obtain the best magnetic performance.

The non-grain orientated electrical steels are by far the most common material used in generators production. The crystal structure of the steel is affected by the addition of Si (between 1 and 6.5wt% [62]). The Si is added to increase the steel's resistivity which reduces eddy currents [63], the addition of Si reduces the Fe content, reducing the steels saturation magnetisation. The addition of Si also results in an improvement in microstructure during annealing [64]. Steel can have three stable crystal phases: austenite, ferrite, and carbonite (cementite). These three phases can combine in different ways producing differing microstructures which have different magnetic properties. Heat treatments can alter the microstructure of the steel into metastable structures such as martensite, and bainite.

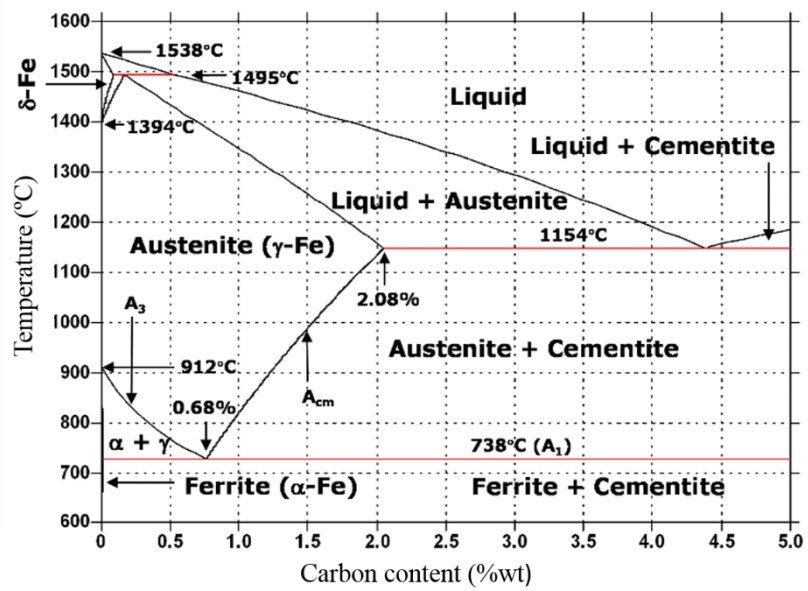


Figure 2-24. Phase diagram for steel [65]. The C content of electrical steels is typically below 0.03%wt resulting in a pure ferrite crystal structure.

In Figure 2-24 the phase diagram for steel shows how the C content of a steel will have a large impact upon the microstructure.

2.4.3.1 Austenite (γ-Fe)

To produce austenitic steels around 17wt% of Cr is added to the steel, there are limited uses of austenite steel in magnetic applications [66]. Austenite has a FCC structure that is not ferromagnetic, and so cannot produce a strong magnetic field.

From the phase diagram (Figure 2-24) it can be seen that in low carbon steels, generally considered to have between 0.05wt% and 0.15wt% C, austenite can only exist at temperatures above 850°C, as the steel cools the austenite transforms to pearlite and ferrite.

2.4.3.2 Ferrite (δ-Fe, β-Fe, α-Fe)

There are three types of ferrite crystal structure the first, δ-Fe, is formed as the molten steel cools to a solid and remains until the steel cools below approx. 1500°C, for steels with a C content of below 0.2wt%. Below this temperature the δ-Fe transforms into austenite (γ-Fe). δ -Fe is paramagnetic, as the temperature it is formed at is above the Curie temperature for Fe which is 727°C (depending on levels of impurities). As the steel cools further the austenite phase transforms into two phases this is termed a eutectoid transformation. The austenitic phase transforms to ferrite (β-Fe) and cementite (Fe_3C). The β-Fe then cools below the Curie temperature and becomes α-Fe and has a BCC crystal structure that is ferromagnetic [67].

2.4.3.3 Cementite

β-Fe, and α-Fe ferrites can only contain 0.02wt% C. If the steel has more than 0.02wt% C content the C not in solution will need to be incorporated into the microstructure. It is this process that can control the formation of different phase structures in steel and affects both its magnetic and mechanical properties.

If steel with 0.5% C content cools gradually it undergoes a eutectoid transformation into ferrite containing 0.02wt% C. The remaining 0.48wt% C content will form cementite. Cementite is a Fe-C carbide (Fe_3C) which contains 6.67wt% C with the remainder being α-Fe. How the cementite is incorporated into the microstructure is fundamental to the use of heat treatments to obtain the desired material characteristics [68]. Cementite is a ferromagnetic material whose magnetic properties vary depending on how it is formed. If the cementite is formed into spheres the coercivity is lower and permeability higher than if the cementite is formed as laminar sheets with ferrite separating them [69]. The principle effect that determines the magnetic properties of steel is the size of the ferrite crystals that are the principle magnetically active constituent of the steel.

Cementite spheres have the lowest possible surface area for the volume they contain, if the cementite is in a laminar form its surface area is greater, increasing the number of pinning sites between magnetic domains the cementite forms with ferrite crystals. It is the pinning of domains to defects in the crystal lattice structure that directly affects the magnetic properties of the steel [70].

2.4.3.4 Pearlite

Pearlite is formed of layers of ferrite (88%) and cementite (12%), both of these materials are ferromagnetic although the cementite has significantly lower magnetic performance when compared to ferrite [71].

If the pearlite is formed during slow cooling of a steel it forms fine pearlite if it is cooled quicker (in air) the pearlite will be coarser. The slower cooling rate used to produce fine pearlite allows more time for C inclusions in the ferrite crystal structure to migrate out of the ferrite crystal into adjacent pearlite formations [72] this reduces the number of defects in the crystal lattice structure reducing the pinning of magnetic domains to these defects reducing the coercivity of the steel. Where finer pearlite is present in a steel there is less cementite present as inclusions and less C at the grain boundaries of the ferrite crystals. The reduction of C at grain boundaries improves the permeability and magnetic saturation of steel in magnetic applications [73].

2.4.3.5 Martensite

If a steel is heated until its structure is purely austenitic and then cooled very rapidly the C that is in solution in the austenite does not have time to precipitate out of the austenite to form cementite. The BCC crystal structure of ferrite is changed into body centric tetragonal (BCT) of martensite by the C that is unable to precipitate out of the crystal's structure [74]. The primary method of cooling the austenite quickly so it forms martensite is by removing the steel from the furnace and quickly placing it in oil or water. This process in known as quenching. Martensite is a metastable crystal formation, meaning that if exposed to thermal energy over time it will break down into its more stable daughter products of cementite and ferrite [75], the transition from martensite to ferrite and cementite is well known to metallurgists as ageing.

Martensite is still a ferromagnetic material but due to the crystal structure being in a constantly stressed state the magnetic properties are worse than those for pearlite or ferrite [76]. In practical applications a quenched steel's martensitic structure results in high hardness making machining of the martensitic steel difficult. To reduce the steel's brittle nature the steel is reheated to around 600°C to allow some C to defuse out of the martensite and form cementite [77].

2.4.3.6 Bainite

When steel is quenched the austenite transforms into martensite, however if the cooling is halted at a temperature above which martensite forms but below the point fine pearlite forms, then a new form of crystal structure is produced known as Bainite. Bainite is "tougher for the same hardness as tempered martensite" [78]. Magnetically bainite has the same performance as martensite as it is also a metastable structure in a constantly stressed state.

2.4.3.7 Ideal microstructure for magnetic applications

The ideal microstructure for magnetic applications is pure ferrite as it has the strongest ferromagnetic crystal structure of all the microstructures that steel forms. Ferrite can only contain 0.02wt% C before it becomes saturated. Excess C is force out of the ferrite and forms either at the grain boundaries or forms cementite that goes into forming pearlite. If a steel has more than 0.02wt% C the magnetic properties will be poorer than when compared to a steel with sub-0.02wt% C content. To improve the magnetic properties of a steel with greater than 0.02wt% C the steel can be decarbonised but the process has a limited effect on thick steel as the C cannot diffuse out of the steel easily. The main method to improve the magnetic properties of thick steel is to anneal the steel to allow the C trapped at grain boundaries to form cementite. The reduction of C at the grain boundaries has the greatest effect on magnetic properties. Annealing also changes pearlite type from coarse to fine which reduces the number of grain boundaries further improving magnetic properties. An ideal steel for DC applications consists of a single crystal. A single crystal has only one grain boundary, and it is the boundaries between crystals that reduce the permeability of the bulk material.

Whilst pearlite is ferromagnetic, due to its composition of 88wt% ferrite and 12wt% cementite, it has a laminar structure consisting of layers of cementite separated by layers of ferrite. This results in a large number of grain boundaries between the cementite and ferrite that reduce the permeability of the bulk steel. In optical images ferrite can appear pure white or white with grey inclusions. The inclusions are small cementite layers that have formed within the ferrite crystal as the steel has cooled too rapidly for the C to defuse out of the ferrite crystal and instead joins together within the ferrite crystal to produce a cementite inclusion. Ferrite with no inclusions indicate a slower cooling rate as C held within the austenite microstructure, when the samples were heated to 950ºC it had a pure austenite structure, has had time during cooling to defuse out of the austenite to the forming grain boundary as the austenite transforms into ferrite and pearlite and forms large pearlite crystals. The grey ferrite's cementite inclusions increase the number of grain boundaries within the ferrite crystals reducing its permeability. Martensite is ferromagnetic but has a lower permeability than ferrite but a higher permeability than pearlite. The changes caused by quenching result in a material that takes a stronger applied magnetic field to magnetise than the normalised or annealed samples. Once the initial resistance to magnetisation is overcome.

2.4.3.8 Crystal size

The crystal size of a steel does not have as large an effect on magnetic properties when compared to C content and impurity levels, but by selecting the correct heat treatments it is possible to reduce C content at the grain boundaries as well as allow large crystal growth both of which increase the magnetic properties of the treated steel [79]. Depending on the composition of the steel different grain sizes will be optimal for magnetic performance however a general rule is that larger crystal growth gives better magnetic performances, due to the reduction in grain boundaries between magnetic domains. Conversely the larger the crystal size the higher the coercivity as the magnetic domains are more strongly coupled. There is a point (which varies depending upon application) at which the improvement due to crystal size is counteracted by the increase in hysteresis losses due to increase coercivity.

2.4.4 Casting

There is no literature on the use of casting to produce steel components with good magnetic performance so this section focuses on the impact of the casting process and heat treatments of a cast part on the performance of a magnetic component.

2.4.4.1 Melting

The presence of impurities in magnetic materials has a large impact on the material's magnetic performance [80]. To reduce the impurities and the amount of C, S, and N taken into solution in the melt during melting of the metal pre-casting, the melting process should be carried out in either an inert atmosphere of Ar [81][82] or under vacuum however this adds significant cost to the casting processes..

2.4.4.2 Casting method

The various types of casting process are primarily concerned with the mechanical properties of the cast part and the cost (depending on production volume). For the casting of magnetic materials the use of expendable casting patterns can result in the inclusion of particulates of the mould material being incorporated into the cast material reducing the magnetic properties of the part [83]. The use of investment casting (sometimes referred to as lost wax casting) reduces the amount of inclusions in the cast part [84] however investment casting is only capable of producing parts in a limited size range. The use of metal moulds for the casting of ferrous metals is complicated by the high temperatures required to get the flowability of the molten metal high enough to fill in all the mould cavities.

The preferred casting method for magnetic materials is investment casting due to its low levels of inclusions. The relatively high cost of this form of casting, when compared to sand casting, makes its use only suitable for high cost parts or high volume production.

2.4.5 Heat treatments

Carbon (C), Sulphur (S), Nitrogen (N), and Oxygen (O) are the principle impurities that affect the magnetic performance of soft magnetic alloys (SMA). They enter the lattice structure of the material interstitially during melting and annealing [85]. The use of vacuum induction melting can significantly reduce the volume of impurities within an intermetallic alloy [86]. Further reduction of impurities can be accomplished with the use of different compositions of atmospheres during annealing processes [87]. Annealing in an air or nitrogen atmosphere will cause impurities to diffuse into the alloy increasing the level of interstitial impurities so air and nitrogen atmospheres are not used for SMA. The use of dry hydrogen and wet hydrogen atmospheres, during annealing, reduce the levels of impurities within SMA [88]. This is the result of impurities diffusing through the solid during heating. Once the impurities reach the surface of the alloy they react with the annealing atmosphere and either form precipitates on the surface during cooling or form gases [89] that then outgas off the component being annealed, surface diffusion. The use of wet hydrogen (9-15% H_2O) results in a greater reduction in the levels of impurities, particularly C and a greater increase in magnetic performance. The use of wet hydrogen can also lead to subsurface oxidation [89]. The use of Ar annealing will not result in the removal of impurities from the SMA. This is due to the lack of anything for the impurities to react with once they reach the surface of the alloy, stopping them precipitating out of the alloy. In Ar annealing as the temperature starts to decline the impurities will diffuse back into the alloy to reach a state of equilibrium. The high cost and size limitations for the use of vacuum annealing make its use in annealing soft magnetic materials impractical.

Removal of impurities is one of two benefits of annealing a SMA, the second is recrystallization of the microstructure [90]. This mechanism has a profound effect on the magnetic properties of the annealed SMA altering the crystal size [56] and the surface texture [51] this process occurs at the same time as the removal of impurities in H annealing [91] but in Ar annealing it happens without a reduction in the impurity levels, so for Ar the alteration of microstructure is the only way it affects the performance of the SMA.

The previous discussion of annealing has been in the context of thin sheets of SMA (<1mm) for materials thicker than 1mm the effects of annealing atmosphere changes due to the greater distance the impurities must diffuse through to reach the surface. In thick material only the material near the surface can have its impurities removed by diffusion. The use of H, as an annealing atmosphere may become a negative factor to the production of good magnetic performance as the atomic hydrogen is able to use grain boundaries, that form during the cooling phase of annealing, to penetrate into the SMA [92]. The effect of H on steel, hydrogen embrittlement [93], occurs through mechanisms such as hydride formation [94], hydrogen assisted cracking [95] and hydrogen enhanced local plasticity [96]. The use of H annealing at 1150°C will remove impurities from the near-surface of the thick SMA and through the same mechanism allow atomic H to diffuse into the SMA. The affect H absorption has on the magnetic properties of a thick SMA is unknown.

2.4.6 Additive manufacturing

Additive manufacturing (AM) is defined as "process of joining materials to make parts from 3D model data, usually layer upon layer, as opposed to subtractive manufacturing and formative manufacturing methodologies" [97]. The American standard ASTM52900 [97] gives terms and definitions to the different processes that can be used to build parts layer by layer.

2.4.6.1 Powder bed fusion

Powder bed fusion is the most common AM method [98]. In its selective laser melting (SLM) configuration powder bed fusion has been used to produce components for magnetic testing using mixed Ni-Fe powders [99]. Fe-Ni (30wt% Ni content) intermetallic alloy [100], and Ni-Fe (80wt% Ni content) intermetallic alloy [101]. These studies have shown the microstructure and coercivity of SLM produced magnetic components but the effect on permeability or resistivity have not been tested. Metal parts produced by powder bed fusion are limited to a single composition.

Binder jetting or material jetting are not suited to produce dense ferrous parts.

2.4.6.2 Ultrasonic consolidation

In ultrasonic consolidation (UL) a high frequency low amplitude ultrasonic vibration is applied to thin sheets of material to form a solid object. The ultrasonic vibration causes normal and oscillation shear forces that cause any surface oxides to be displaced resulting in the atomically pure material making direct contact [102]. The atomically pure foils are then subjected to heating (<50% of melting temperature) from the ultrasonic vibrations and pressure from the sonotrode (ultrasonic vibration emitter). The bonding mechanism between sheets is metallurgical in nature, the process does not result in a heat affected zone. Once all the layers are deposited a CNC contour cutter is used to produce the final part to net shape. The process allows the welding of dissimilar metal sheets [103]. The initial process of UC has the drawback of not being net shape, it is both additive and subtractive manufacturing. The range of materials available in thin sheet form is limited so the use of bespoke compositions results in high consumable costs. The use of contour cutting of the welded layers makes the separation of waste material for scraping impossible resulting in a decrease in the recoverable material (scrap) to help mitigate high consumable costs.

2.4.7 Laser cladding

Parts produced by laser cladding can produce dense metal components [104][105] and can vary their composition as desired. There is a gap in the literature centred on the production of soft magnetic alloy coatings using laser cladding. The use of powder enables the magnetic properties of the resultant coating to be customised for each application [106][107]. The use of laser cladding to produce complete stators or rotors is limited by its high cost [108]. Possible applications are for smaller generators and motors and for use as a form of coating to improve the magnetic performance of the magnetically active surfaces of a component, produced conventionally out of a lower quality material. Laser cladding can be based on the use of a laser or electron beam. The use of an electron beam adds significantly to the overall production costs as the part for coating must be placed into a vacuum chamber to allow the electron beam to function.

2.4.7.1 Laser cladding bond strength

Like ultrasonic consolidation the bond between coating and substrate is metallurgical in nature [109]. The bond strength is heavily dependent on the coating composition and the process parameters such as powder feed rates, process speeds and gas supply. Laser cladding does result in a heat affected zone (HAZ) as both the substrate and feed powder is melted during deposition. Laser cladding also results in the growth of columnar crystals in the microstructure [110] although this can be controlled by the refinement of cladding parameters.

2.4.8 Powder production

Metal powders for PM can be produced from any pre-alloyed bulk material using three procedures to atomise them to a powdered state. To turn a solid piece of metal into a powder it is melted, then atomised in its molten state, and then solidified (by cooling). The atomisation is carried out by the use of water, an inert gas, or a plasma atomisation processes [104]. Each method of atomisation results in different powder characteristics that will impact the finished part's mechanical and magnetic performance. The use of water atomised powders is limited by the powders irregular morphology and high oxide content [104]. Water atomisation is the cheapest method of atomising a metal so is used if cost and not mechanical or magnetic properties are the main concern. The use of inert gas atomisation allows for low impurity levels and a spherical morphology that is better suited to reactive metals. The inert gas used in the process directly influences the formation of crystal structures in parts produced from the powders. If Nitrogen (N) is used as the inert gas nitrides can be formed in the powders, affecting the mechanical and magnetic properties of the powder [111]. Nitrides are either anti-ferromagnetic or paramagnetic (depending on their exact composition), which shows that the use of Ar is preferable to atomise metals that are going to be used to produce magnetically active components [81]. Inert gas atomisation has a drawback that it can entraps gases as it rapidly solidifies [112].

Plasma atomisation produces a powder that has a better spherical morphology than gas atomised powder and has no entrapped gas [113]. Plasma atomisation however is a very expensive and recent development so its applications have not been fully explored

Once the metal has been atomised it is sieved to separate the specified particle fractions. Work on metal powders for magnetic applications has previously been carried out for use in magnetic tapes [114], such as cassettes, however the death of the magnetic tape medium has reduced the applications for magnetic powder research in this area. Magnetic powder research is now focused on magnetic powders to produce either composite ferrites for high frequency applications [115][108] or hard magnetic materials to produce permanent magnetics that can match REE magnetics without the high material costs [116][117].

2.5 Knowledge gaps

The use of casting to produce DC components for salient pole generators is an area where little research has been carried out, in particular the testing of the DC magnetic properties of commonly cast steels to ensure that the material with the best magnetic properties is used to reduce the impact of switching between an electrical steel and a cast steel. The use of heat treatments to alter the magnetic properties of cast steel is also of interest to improve the magnetic performance of a cast rotor.

Testing of a cast rotor prototype and comparison with a standard rotor has not be carried out previously. By testing the performance of a solid cast rotor the differences in performance can be quantified as the first stage in an iterative process to produce a solid rotor that can match the performance of a laminated rotor.

The idea of using a materials magnetic properties to block the effects of harmonics and transients from the stator to the rotor has not appeared in the literature. This is primary due to the difficulty of selecting a single point to have the lower saturation material saturate, thus blocking transients and harmonics, as generators feed varying loads. Additive manufacturing is not suited to the production of a complete rotor, due to the high cost of both the feedstock and the manufacturing process. The ability of DED to mix elemental feedstocks to produce an SMA with the exact magnetic performance required to fulfil a specific role [118] would enable coatings with differing magnetic properties.

The use of DED to produce thick (>10mm) coatings of soft magnetic material is not shown in the literature and if proven could be used in the production of coatings with graduated magnetic properties

3 Experimental methods

There are two fundamental properties that a solid rotor needs to address if its magnetic performance is to match that of a salient pole rotor produced out of laminations. The first is to have a similar initial permeability and saturation magnetisation as a conventionally produced lamination based rotor. The initial permeability of the cast steel, used to produce the rotor core, will directly affect the strength of the magnetic field produced by the current and voltage in the field windings. The second is the large circulating eddy currents that occur in all salient pole rotors. Rotors produced out of laminations have these eddy currents reduced by the use of thin laminations and the damper winding. The use of thin laminations and damper windings is not possible in a solid rotor so another method needed be found to reduce eddy current losses in the rotors pole faces.

This thesis consists of three areas of research to answer the research questions posed in Chapter 1. The first results chapter focuses on the DC magnetic properties of cast steels before heat treatments are applied and again afterwards. In total 36 samples had their characteristics measured 288 times to provide a dataset that allowed the best performing cast steel to be identified. The second results chapter shows how the material selection from the first chapter was used to produce a prototype solid rotor that had its performance compared to a standard CGT rotor, upon which it was based, and to prove the concept of blocking transients and harmonics from inducing eddy currents on the rotor. The third results chapter shows how laser cladding can be used to produce a Ni-Fe soft magnetic alloy onto a substrate to produce a solid coating which matches the magnetic characteristics of a commercially available alloy. The use of laser cladding enables different ratios of elemental ferromagnetic metals to be combined to produce layers with differing composition that magnetically saturate at different points to allow a graduated magnetic shield that increases the apparent air gap between the rotor and the stator as the power output of the generator increases.

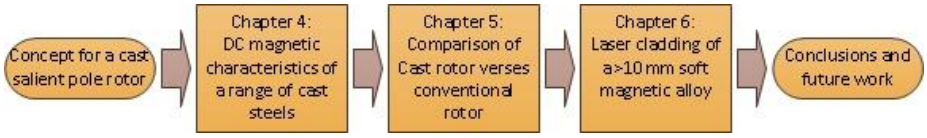


Figure 3-1. A flow chart showing how the three results chapters are linked together to produce a methodology for producing a solid salient pole rotor

In Figure 3-1 a flow chart showing how the three results chapters of this thesis come together to provide a methodology to produce a solid salient pole rotor.

The following sections highlight an overview of the work carried out for each chapter.

3.1 Material characterisation for cast salient pole rotor

There are hundreds of different grades of cast steel and testing all of them for their magnetic properties would take longer than the timeframe of this project. To reduce the number of materials to test a number of UK based foundries were approached to determine whether they could produce a one-off cast rotor. Of all the foundries approached only one had the capability to produce rotors for both the largest and smallest rotors used in CGT generators. This foundry was asked to supply a representative range of steels they were able to cast. The foundry provided twelve steel samples produced to BS3100:1991[119]. The samples had their DC B-H curves tested to determine which of the supplied grades of steel was most suited to cast the rotor.

The samples were also subjected to various heat treatments, commonly applied to cast steels, to determine if the application of heat treatments would improve their magnetic performance. The composition of each billet is shown in Table 3-1. Three 10mm thick specimens were extracted from these for additional heat treatment and B-H curve measurements.

Table 3-1. Composition of the twelve samples for testing. The composition of the steels was provided by the foundry that provided the steel billets for testing. The grades of steel are produced to meet thee specifications laid out in BS3100:1991[119]

UoN Sample No	Grade (BS3100:1991)	Percentage by weight (wt%) of impurities and additives										
		C	Si	Mn	S	P	Ni	Cr	Mo	Cu	Al	N
AS1	A4	0.2119	0.3147	1.376	0.0095	0.0207	0.0871	0.1098	0.026	0.0878	0.0411	0.012
AS2	BT3	0.3185	0.2663	0.992	0.01	0.0186	0.0883	0.988	0.2438	0.0472	0.0313	0.003
AS3	BT1	0.2934	0.3096	1.033	0.0088	0.02	0.118	1.003	0.2683	0.0653	0.0378	
AS4	A1	0.1994	0.2956	0.797	0.0055	0.0184	0.1247	0.1174	0.0695	0.0538	0.0349	0.003
AS5	P310	0.2898	0.3961	0.92	0.0088	0.0184	1.243	1.256	0.3347	0.0468	0.0329	0.0128
AS6	A2	0.2764	0.2735	0.902	0.01404	0.0184	0.01493	0.086	0.0159	0.0313	0.0322	0.005
AS7	MSS013	0.2782	0.2797	1.455	0.0091	0.0212	0.0693	0.078	0.3196	0.0388	0.0309	0.01
AS8	P310	0.3203	0.506	0.906	0.0096	0.0206	1.228	1.213	0.329	0.0721	0.0283	-
AS9	P330	0.2806	0.2622	1.536	0.0076	0.0211	0.09	0.1363	0.304	0.0524	0.033	0.004
AS10	A2	0.28	0.283	0.908	0.0098	0.0173	0.0458	0.0331	0.0203	0.0331	0.0359	0.006
AS11	Mac 1	0.109	0.55	0.63	0.0081	0.0153	0.0424	2.79	0.956	0.0254	0.0255	0.013
AS12	BT2	0.1958	0.3714	1.301	0.0063	0.0162	0.0812	0.0751	0.037	0.0373	0.0413	0.007

Table 3-2 The heat treatments the steel samples chemical composition have been optimised for. the supplied billets of the steels from the foundry had these heat treatments applied before they were normalised to remove machining stress and reset their microstructure for baseline property testing.

Sample ID	Steel grade	Chemistry optimized heat treatment
AS1	A4	Normalised
AS2	BT3	Normalised then Quenched and tempered
AS3	BT1	Normalised then Quenched and tempered
AS4	A1	Normalised
AS5	P310	Normalised
AS6	A2	Normalised
AS7	MSS013	Normalised
AS8	P310	Normalised
AS9	P330	Normalised
AS10	A2	Normalised
AS11	Mac 1	Annealed
AS12	BT2	Normalised then Quenched and tempered

Samples for B-H curve analysis

To evaluate the B-H curves of the cast steels; a toroid 28mm outer diameter x 20mm inner diameter was machined from each of the three 10mm thick billet slices. The samples complied with the requirements laid out in BS EN 60404-4:1997 [2]. The samples provided by the foundry were supplied with various heat treatments already applied however as the heat treatments were applied by the foundry their exact cooling rates and how the heat treatments were applied was unknown. As the samples have been stored at the foundry it is not possible to know what effect storage would have on the metastable microstructure of quenched and tempered samples. In order to be able to provide a baseline DC B-H curve all the samples will be subjected to a normalising heat treatment. The normalising heat treatment was above the AC3 temperature to ensure that any ferrite, pearlite, martensite, bainite is converted into a pure austenite microstructure before cooling in air into ferrite and pearlite. The normalising process also removes any stresses imparted into the samples during machining [52], By normalising the sample before testing it is noted that some of the samples will not have the microstructure that their chemical composition has been optimised for.

The need to start all the samples in the same condition and apply heat treatments in a controlled environment makes normalising the supplied samples critical to be able to produce a comparison of their DC B-H curves. The samples were normalised in a furnace at 950°C for 20 minutes. The samples were removed from the furnace and allowed to cool in air. The samples then had 30 turns of 0.1mm^2 wire wrapped around the circumference of the toroid, this formed the sensor coil. Another 30 turns of 1.0mm^2 wire were wrapped on top of the sensor wire; this provided the source for the applied electromagnetic field. The coils were then connected to a Brockhaus Measurements electrical steel tester and a DC current was applied to the source coil. The effect of the applied magnetic field was detected by the sensor coil and the baseline B-H curve of the cast steel samples was calculated [120] to standard BS EN 60404-4:1997 [2].

3.1.1 Applying heat treatments

To carry out annealing and quenching heat treatments the toroid's needed to be heated above their upper critical temperature (Ac3), the point at which all ferrite has undergone a complete eutectoid transformation to austenite. The Ac3 temperature varies depending on C content and the quantities of impurities and alloying elements present, but can be taken as 900°C for steels with <0.1wt% C decreasing to less than 800°C for steels with <0.4wt% C. The materials used here were between 0.1 - 0.4wt% C content therefore the use of 950°C as the temperature for the annealing and quenching process was deemed to be suitable.

3.1.2 Baseline B-H curve

Each billet produced three toroids that each had their B-H curves experimentally determined. The three sets of results were then averaged to give the B-H curve for the billet that they were produced from.

Once the initial testing was completed, one of the toroidal samples from each billet was set aside to act as a control. The set aside toroid was labelled as sample 1. Sample 1 remained in the normalised state.

The two remaining samples from each billet were separated and labelled as sample 2 and sample 3. Sample 2 was used to determine the effect of annealing at various cooling rates on permeability. Sample 3 was quenched then tempered to determine what effects quenching has on permeability.

3.1.3 Annealing

Sample 2 from each billet was annealed by placing in a furnace at 950°C for 20 minutes. When the heating cycle was completed the furnace was switched off and the cooling rate of the furnace was recorded using a thermocouple attached to a data logger.

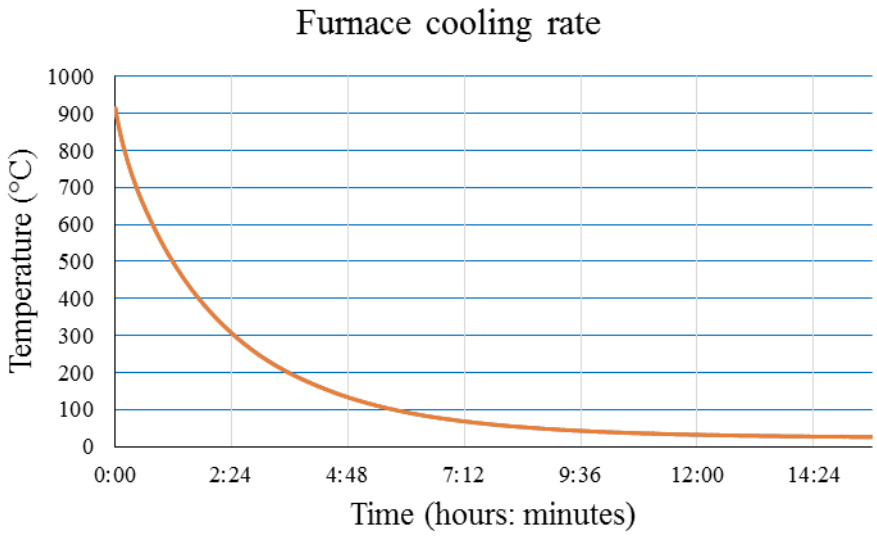


Figure 3-2. The data logger data describing the cooling rate of the furnace when it is heated to 950°C held for 20 minutes and then switched off and its cooling rate determined.

The experimental derived cooling rate for the furnace is shown in Figure 3-2, when the furnace is switched off the resultant cooling rate determines the fastest possible cooling rate as the furnace does not have a forced air cooling system.

Newton's law of cooling formula:

$$T(t) = Ts + (T0 - Ts)e^{(-kt)}$$

Where:

$T(t) = \ temperature\ of\ an\ object\ at\ a\ certain\ time$

$t = \ time\ (s)$

$Ts = temperature\ of\ the\ surroundings$

$T0 = starting\ temperature\ of\ the\ object$

$k = a\ cooling\ constant, specific\ to\ the\ object\ (1/s)$

$\therefore$

$t = 60\ minutes$

$T(t) = 544°C$

$Ts = 25°C$

$T0 = 926°C$

Solving for k

$T(544) = 25 + (926 - 25)e^{-kt}$

$T(544) = 25 + 901e^{-k60}$

$544 - 25 = 901e^{-k60}$

$\frac{519}{901} = e^{-k60}$

$\frac{901}{519} = e^{60k}$

$li(1.736030829) = \ln(e^{60k})$

$li(1.736) = 60k$

$\frac{li(1.736)}{60}$ = k

K=0.009193356

K cross check

$T(544) = 25 + (926 - 25)e^{-kt}$

$T(544) = 25 + (901)e^{-kt}$

$T(544) = 536$ Calculated results are within 8°C of measured results

These samples had been annealed using the cooling rate of the furnace; providing the fastest annealing cooling rate (FACR) which will be termed the FACR. Once the samples were cooled to room temperature the samples had their B-H curve determined, and compared with the normalised state B-H curves.

Once tested the samples were returned to the furnace at 950°C for 20 minutes to return the microstructure to a pure austenitic state. The annealing process was then carried out at set cooling rates of 3°C/min, 4.5°C/min, and 6.0°C/min and the B-H curves were determined after each applied heat treatment.

3.1.4 Quenching and Tempering

Sample 3 from each billet was placed into the furnace and heated to 950°C for 20 minutes. These were immediately removed from the furnace and quenched in oil at room temperature (approx. 21°C). The furnace was cooled to 600°C, and the samples returned to the furnace for 20 minutes to temper the steel. After tempering the samples were removed from the furnace and cooled in open air. These samples than had their B-H curves measured and the results were plotted against the results from before they were quenched. Figure 3-3 is a schematic diagram of the complete testing procedure. From this point onwards quenching then tempering will be referred to as quenching.

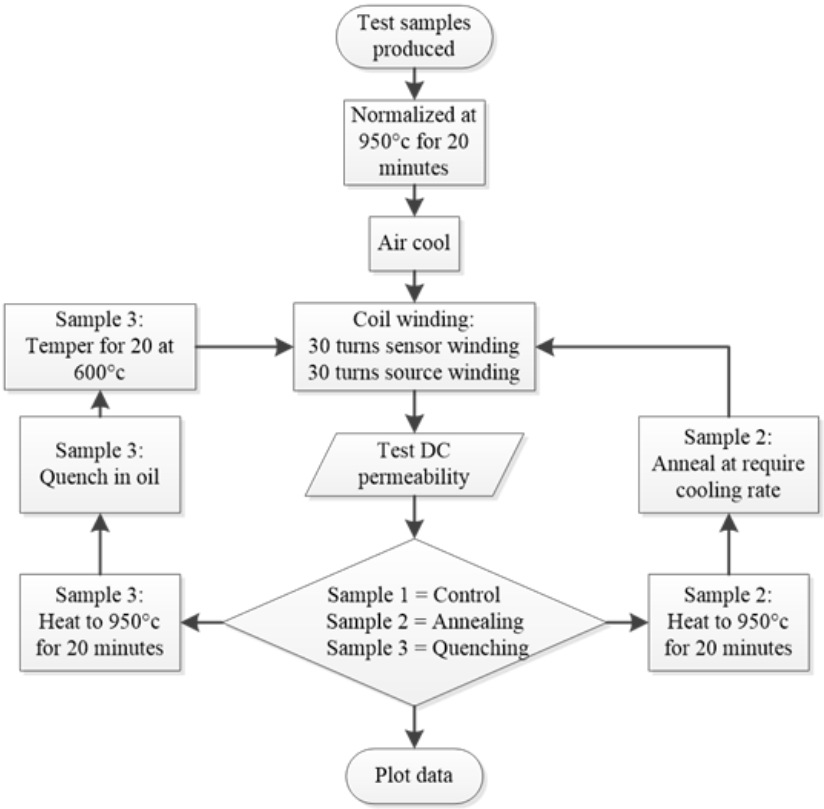


Figure 3-3. A summary of the permeability testing process.

3.1.5 Optical microscopy

Optical imaging of the specimen's microstructures was required in order to identify microstructure changes before and after the application of heat treatments. Three cylinders 10mm in diameter were machined from the billet slices. These cylinders were normalised alongside the toroidal samples

After normalisation one of the cylinders from each billet was labelled as sample 1 and was set aside as a control, so an image of the microstructure after normalisation could be obtained.

The remaining two samples, from each billet, were given heat treatments at the same time as the toroids, and were used to compare the effects of heat treatments on microstructure with that of the set aside normalised cylinder. One of the two remain cylinders from each billet was labelled sample 2 and was annealed at the cooling rate of the furnace (FACR) and the final cylinder from each billet was labelled as sample 3 and was quenched at the same time as the toroidal samples.

Sample preparation for the samples for optical imaging was carried out using the suggested methodology in the ASM Handbook, Volume 10: Materials Characterizations, p 299-308 [121]. As described in Sections 3.1.5.1 to Section 3.1.5.5.

3.1.5.1 Mounting samples

To allow the samples to be easily ground and polished the optical samples were mounted in a conductive thermosetting plastic block. The sample for mounting was placed in a mould and powdered plastic added until the sample was completely covered by the powder. The mould was then placed under pressure and heated to cause the powered plastic to liquefy around the sample. A conductive plastic was used to allow the samples to be viewed with an optical microscope and a scanning electron microscope (SEM).

3.1.5.2 Grinding and polishing

The surface of the mounted sample was prepared for imaging by the use of water lubricated grinding wheels. The use of progressively finer grits, 240, 320, 480, and 800 resulted in a surface that was suitable for polishing.

After grinding for 60 seconds the samples were cleaned with liquid soap and cotton wool to remove detritus, and then with acetone to prevent watermarks on the surface. During this process it was found that the hot air blower used to dry the samples after cleaning was causing blueing of the steels surface. Blueing is the formation of a particular Fe oxide that resists chemical etching. To stop the blueing the hot air blower was switched to cold air, this increase drying time for the samples but eliminated Fe oxide formation. Once the finest grit had been used the samples were first polished, lubricated with white spirt, using a 10μm diamond paste and then a 1μm paste. The polishing stage was also found to cause blueing of the steel's surface.

The resistance of the Fe oxide to etchant resulted in the polished samples being unstable for chemical etching. To eliminate the blueing, caused by the polishing wheels, two finer grade grits were used (1200 and 1400) in place of the polishing wheels.

3.1.5.3 Etching

The choice of etchant was determined by the expected microstructure of the heat treated samples [122]. As all the samples are low–medium carbon steels the dominant microstructures expected were pearlite, ferrite, and martensite. The best etchant for imagining these microstructures was found to be 2% Nital [123]. The etchant was applied by swabbing the surface with etchant saturated cotton wool for 30 seconds then rinsing in water and checking under an optical microscope to judge the effect of the etchant.

3.1.5.4 Imaging

After the etching stage images of the samples were taken using an optical microscope at 20x, 50x and 100x magnification. Due to the wide variation in crystal sizes found during optical imagining and the risk of confusion when comparing images taken at different magnifications, it was decided to mitigate this risk of confusion by only using the 50x magnification images for all the microstructure images.

3.1.5.5 Grain sizing

After heat treatments had been applied one of the most obvious changes in the steel sample's microstructure, was the size of the individual crystals. To easily quantify the change in crystal size an open source software package called "ImageJ" was used to automatically obtain average crystal sizes for each sample. The software works by changing the image to a greyscale image and it then uses an algorithm to change the greyscale image into a black and white image of the two main types of crystal in the microstructure. The pearlite shows up as black crystals while the ferrite is represented by white crystals.

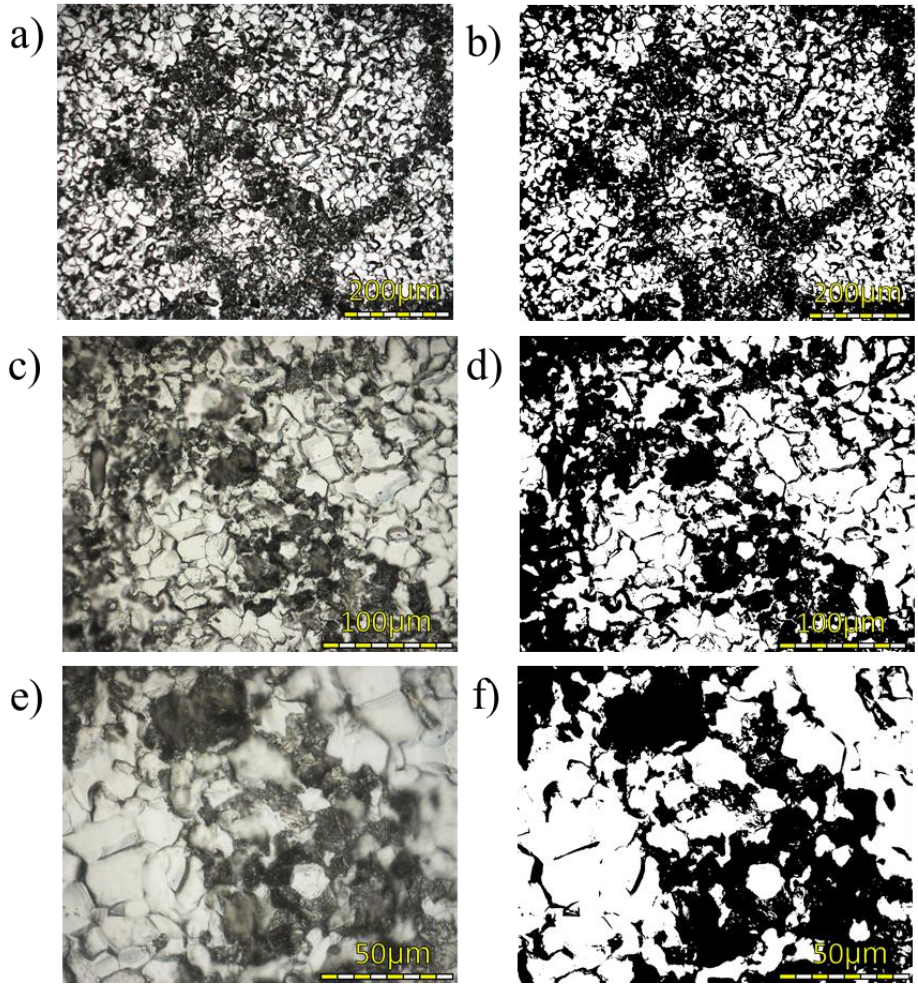


Figure 3-4. Unaltered image (a,c,e) and altered image (b,d,f) for multiple magnifications (a) 20x magnification unaltered image, (b) 20x magnification analysed for crystal size, (c) 50x magnification unaltered image, (d) 50x magnification analysed for crystal size, (e) 100x magnification unaltered image, (f) 100x magnification analysed for crystal size.

Figure 3-4 shows the images of the annealed sample AS4 taken at three different magnifications, but of the same location on the sample (Figure 3-4 (a), (c), and (e)) alongside the black and white image, produced by ImageJ using an algorithm to separate crystal types (Figure 3-4 (b), (d), and (f)).

The three different magnifications were used to test the capability of the software to correctly calculate crystal sizes by comparing the software derived crystal sizes for the same location on a sample but under different magnification. The scale for each of the images has been entered into the software so if the software could correctly differentiate between pearlite and ferrite the average crystal sizes should be the same for the three analysis.

Table 3-3. Results of ImageJ analysis of annealed sample AS4 at different magnifications. The software showed different crystal sizes for the same under different magnifications.

Magnification	Area of pearlite (%)	Area of ferrite (%)	Crystal size (microns)
x20	57	43	234
x50	51	49	37
x100	47	53	154

As can be seen in

Table 3-3 the software produces different crystal sizes for the same sample at different magnifications. The different areas of both pearlite and ferrite are expected to change due to the area of the sample each image focuses on being slight different. Research into a reliable method to size mixed pearlite and ferrite steels is ongoing [124].

Scanning electron microscope (SEM)

Optical microscope images are therefore not currently suited to finding the crystal size in the samples under consideration in this thesis. It was decided to try sizing the crystals using SEM images to see if the results were more reliable than optical imaging and software analysis.

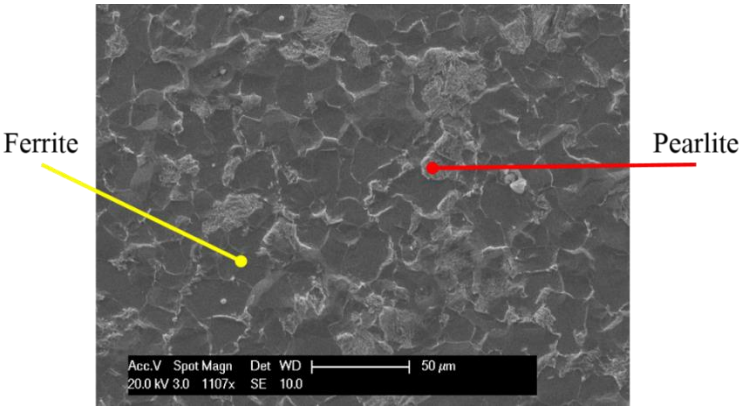


Figure 3-5. SEM image of annealed sample AS4.

Figure 3-5 shows an SEM image of the sample that was optically imaged in Figure 3-4 (AS4). The ferrite appears as single blocks of grey whilst the pearlite is shown as differing shades of grey. This image shows that the ferrite contained in the pearlite is very difficult to separate from standalone ferrite crystals using an SEM image.

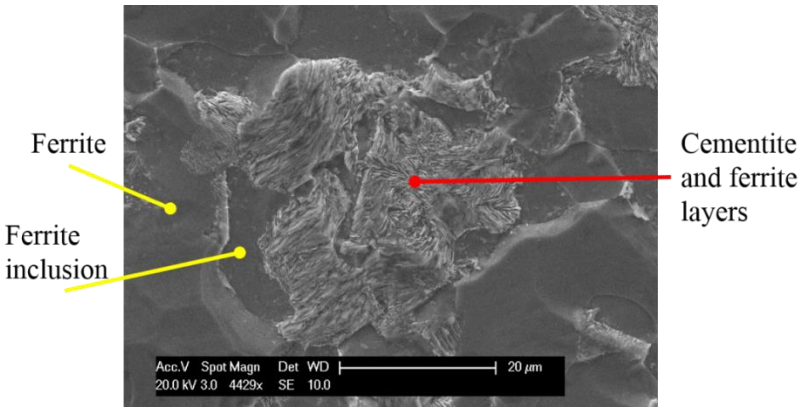


Figure 3-6. A SEM image of a single pearlite grain in the annealed sample AS4.

Figure 3-6 shows a magnified image of a fine pearlite grain in the annealed AS4 sample. Large ferrite inclusions are clearly visible, as is the ferrite in-between the layers of cementite however the imaging software cannot view a pearlite crystal as a single crystal. Instead it separates the ferrite inclusions and ferrite and cementite layers into separate crystals. The software averages the small ferrite crystal inclusions along with the pure ferrite crystals resulting in a net reduction in overall ferrite crystal size. This makes the sizing of crystal grains for all the samples under test not possible using SEM.

The difficulty of accurately measuring grain sizes of hypoeutectoid steels (C content of below 0.8wt%) is well known but as yet no method has been developed that can differentiate between ferrite as a standalone crystal and ferrite that is incorporated into pearlite either as an inclusion or in the laminated structure of the pearlite itself [124].

Because of this the exact crystal sizes for the samples will not be taken, instead the change in DC permeability will be explained by comparing the optical images for different heat treated states and showing how the changes in the microstructure effect the permeability of the samples.

3.2 Prototype rotor design and testing

Solid salient pole rotors are currently used in applications where the physical size of the generator is less important, for example where the generator is in a static location such as hydro-electric power stations. CGT produce generators are portable so the physical size and weight of the generator is a critical aspect of their design. The size of a generator is based on its energy density, which is the amount of output power it can produce verses is physical size. The key to producing a solid rotor generator, that has the same energy density as a standard laminated rotor generator, is to control the amount of heat the generator produces during operation. The static component of the generator is the stator, it is relatively easy to cool the stator as it is mounted into a housing where air flow can be directed around the housing, and through vents built into the stator, to increase cooling. The rotor is more difficult to cool as air can only be directed into the gaps between the salient poles. The air gap between the pole faces and the stator has to be kept to a minimum to reduce electrical losses this restricts the cooling airflow. The difficultly of increasing cooling of the rotors pole faces limits the power density of the completed generator. Solid rotors currently heat up more during operation due to the harmonics and transients produced in the stator inducing eddy current in the pole faces and the lower permeability of the material used in its production which results in an increase in current and voltage in the field windings.

To increase the power density of the rotor the reduction of heating of the pole faces is critical to allow a stronger DC electromagnetic field to be used. Currently the reduction in pole face heating is achieved using damper windings and laminated construction. This thesis aims to produce a design for a new solid rotor with reduced complexity and a power density that has the potential to match the current rotor design.

3.2.1 Material selection for pole shoes

The main rotor body is subjected to only a DC electromagnetic field whilst the pole faces experience an induced AC electromagnetic field. In this thesis the pole faces are separated from the main body of the rotor and are termed pole shoes, the best way to stop an AC electromagnetic field causing eddy currents in the rotor is to consider increasing the air gap between the rotor and the stator in order to isolate them from each other.

3.2.1.1 Pole shoe composition

The magnetisation of a rotor in an alternator varies depending upon the amount of current being drawn from the stator windings. Since it is not currently possible to produce a material that varies its saturation (with a DC applied magnetic field) the material that forms the pole shoes will need to saturate at the normal operating polarisation of the rotor. If the electrical load of the alternator increases beyond the normal operating polarisation the DC current in the rotor will need to increase exponentially as the pole shoe material will be at saturation. The extra DC current will be required to use the permeability of free space to increase the rotors magnetic field. If the electrical loading is less than the normal operating polarisation than the material will experience some induce eddy currents. To reduce the eddy currents the material should also have a high resistivity for when the pole shoe is below saturation.

Fe-Ni based alloys, unlike Fe-Co alloys, have a saturation that is lower than steel and a higher resistivity, so the best material to produce the pole shoes is a Fe-Ni based alloy. Alloys with a Ni content of 36% have a higher saturation than those with a Ni content of 80% [125].

To show the different magnetisation characteristics of a Fe-Ni36 alloy verses cast steel, a toroid of the material was produced and its B-H curve measured.

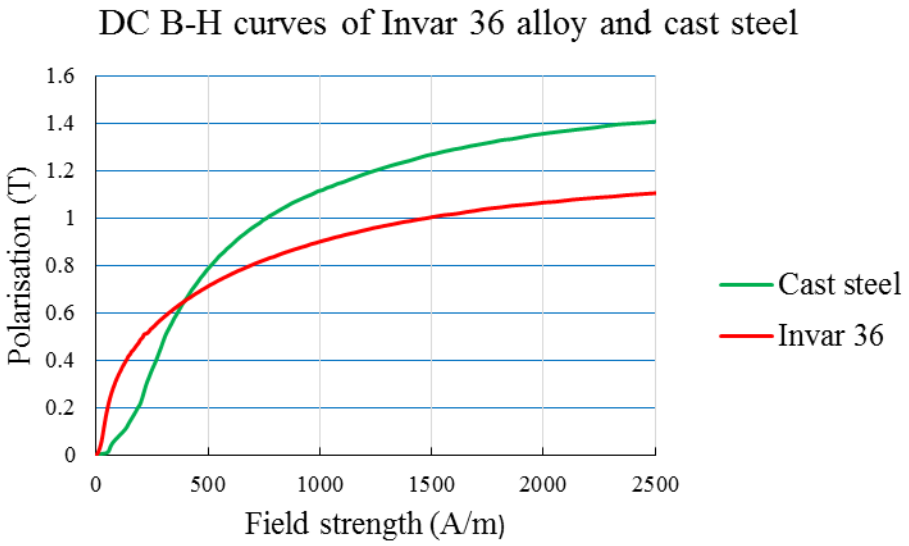


Figure 3-7. Comparison of the B-H curves of A1 cast steel in its normalised state and a Fe-Ni36 alloy

Figure 3-7 shows that a Fe-Ni36 alloy has a stronger initial response to an applied magnetic field when compared to the A1 cast steel. Also of note is the lower overall polarisation of the Fe-Ni36 alloy. When the Fe-Ni36 alloy reaches saturation the DC current needs to dramatically increase to reach the same polarisation as a steel pole shoe.

Fe-Ni alloys are most suited to the production of poles shoes due to their saturation which is controlled via Ni content. Fe-Ni alloys also have a high electrical resistivity when compared to steel so when the polarisation of the rotor is below the saturation of the Fe-Ni alloy and eddy currents are induced in the pole shoes the high resistivity of the alloy helps reduce the eddy current size. Increasing the resistivity of the pole shoe material is carried out in electrical steels by the addition of Si to the steel. In the prototype rotor the use of a 36wt% Ni alloy is preferred as its saturation value is not so low that the operating polarisation will drive it to saturation well before reaching operating polarisation, requiring an increase in DC current flow in the rotor coils (producing excess heating).

Once the operating polarisation of the prototype is measured the ability to produce a Fe-Ni with the exact saturation required can be obtained by increasing or decreasing the Ni content.

This is an expensive process as it requires the production of a special alloy custom made for the operating saturation of the rotor. It is possible to reduce the cost of making a bespoke alloy by using elemental powders of Fe and Ni and mixing them to produce a powder blend with the required saturation. The difficulty of using powders is how to produce a coating of the powders that is sufficiently thick to act as an air gap, but also dense enough to not inhibit the overall saturation of the coating.

3.2.2 Prototype design

The first stage of this process was to identify the critical design elements of the current rotor core pack and shaft so that these could be incorporated into the prototype rotor. Once design concepts had been generated the concept that produces the most flexible prototype for testing and iterative development was selected to be manufactured. A standard HCI444C generator was tested to determine the baseline performance of the current state of the art generator CGT produce. Once testing of the standard HCI444C was complete the standard rotor was removed and the prototype rotor fitted. The generator was then retested and its performance compared with the baseline. Using the same stator, housing, etc. with the new rotor the changes in performance are directly linked to the prototype rotor. Once the differences in performance were identified design modifications were developed to show how to reduce/remove the differences in performance.

A prototype rotor with the same dimensions as that used in the current HCI444C was funded by CGT on the condition that the core pack and the rotor shaft were produced as a single piece. From a manufacturing point of view the production of a solid rotor core pack and separate shaft is more desirable than producing both the core pack and shaft as one piece. This is due to the difference in circumference between the core pack and rotor shaft resulting in excessive machining requirement if the rotor is produced out of a single billet.

The amount of material that would need to be removed from a billet of material (that matches the critical dimensions of the end part) to produce the typology for the shaft and core pack is shown in Table 3-4.

Table 3-4. Comparison of the amount of material machined from a billet of material to produce the core pack and to produce both the core pack and the shaft.

Part	Volume of component (mm^3)	Volume of billet (mm^3)	Waste (%)
Core pack	15900569	32731875	51
Complete rotor	26959144	131827329	80

In order to reduce the amount of machining used to produce the prototype rotor it was decided to cast the complete rotor and then machine the cast part to the final dimensions. The use of casting to manufacture a rotor for a high power density generator has not previously been undertaken as the magnetic properties of cast steel had not been investigated previously.

Without knowing the magnetic properties of the steel to be used it would be impossible to optimise the type of steel used in the casting. The previous Section 3.1 investigated the methodology for determining the magnetic properties of different cast steels to allow the best performing cast steel to be used to cast the rotor whose design is the focus of this chapter.

3.2.2.1 Original rotor design

The current rotor is made from two main components the shaft and the rotor core pack. The core is made up of 424 laminations of M700-65A electrical steel that are 0.65mm thick, 3% of the thickness of the lamination is the insulating coating applied to each side of the lamination. The laminations are stacked one upon the other and welded into the final core pack. The pressing of the core pack onto the shaft requires an interference press fit between the two components, this requires the careful selection of a shaft that will fit the core pack. Due to the dimensional variations in the shafts GCT purchases not every shaft fits every core pack.

The design brief from the sponsor was to remove this problem by combining the two components into a single piece for casting, each component required changes to be made in their design to allow their construction from a single casting. A commentary upon the preliminary redesign of these is presented below.

The shaft

The shaft for this rotor has multiple key bearing surfaces that require surface finishes that are superior to the surface finish of a sand cast part. The surface finishes on the shaft are to ISO standard (ISO 1302:1992) [126] shown in Table 3-5.

Table 3-5. ISO roughness grade with roughness value equivalent

Roughness grade (ISO 1302:1992)	Roughness value (Ra) in µm
N12	50
N11	25
N10	12.5
N9	6.3
N8	3.2
N7	1.3
N6	0.8
N5	0.4
N4	0.2
N3	0.1
N2	0.05
N1	0.025

The key surfaces are used to mount large sub-components of the rotor. The finish selected is determined by the fit required of the sub-components.

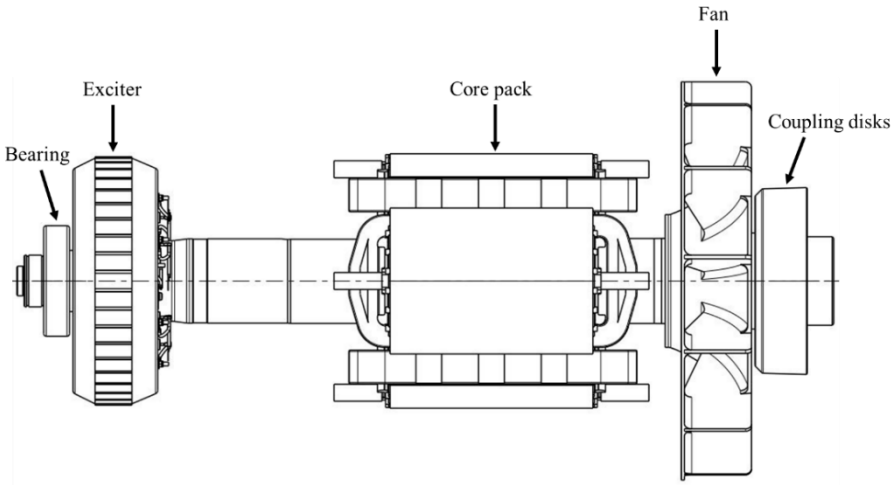


Figure 3-8. Main sub-components as fitted onto the shaft, the non-drive end is on the left side of the drawing with the drive end next to the cooling fan. This shaft is termed a single bearing as it only has a single bearing at the non-drive end.

In Figure 3-8 the sub-components are shown as they are fitted to the shaft. The bearing, exciter, fan, and coupling disk are not produced by CGT they are bought in components and so are outside the scope of this thesis, however the prototype needs to accommodate these, so the surface finishes on the original shaft needed to be reproduced on the prototype. This type of shaft is termed a single bearing by CGT as it has one bearing at the exciter end and a mounting hub at the drive end next to the fan. Having a single bearing on the non-drive end of the shaft and a disk coupling on the drive end that is coupled to the prime mover makes the coupling of the generator to the prime mover critical, as the single bearing cannot dampen vibration to the same extent as a two bearing shaft.

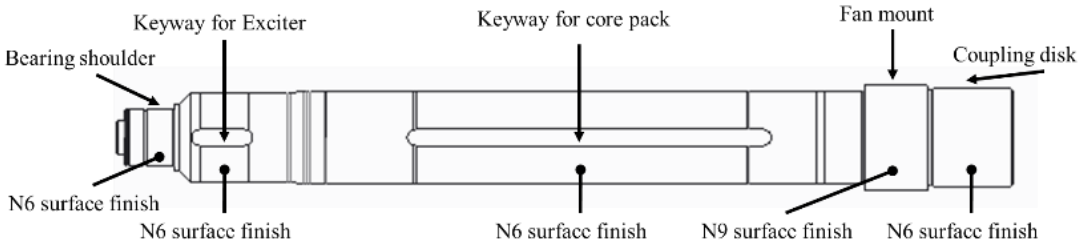


Figure 3-9. The critical surface finishes of the single bearing shaft. The best surface finishes are for the bearing mount, exciter mount, and coupling disk mount..

In Figure 3-9 the shaft for the standard HC4 series is shown with the areas that the sub-components are mounted onto labelled to identify their surface finish.

The fan mount has a comparatively rough surface texture as the fan is welded into place so the fit is less critical than for the bearings. Areas not marked in the diagram are not critical and have a surface finish of N8. As the shaft and core pack were combined in the prototype, the keyway for the core pack and surface finish for the core pack mounting area can be discounted.

The remaining surface finishes and dimensions were retained and form the basis of the prototype design.

The core pack

The core pack is constructed from 424 identical laminations. The lamnations for the rotor are produced using a progressive press. The dies in the press cannot be altered after each lamination is produced so there is no flexibility in the design of the typology of the overall core pack. This prototype does not need to keep to the original design and can have a completely different geometry. The drawback to a new geometry is that there would be no way to determine if changes in the performance of the solid rotor are due to its new production method or to its new geometry. In order to gain a comparison between the current core pack and a solid cast core pack the basic geometry of the core pack was kept the same. However the pole faces needed to be removable to allow different materials, with different soft magnetic properties, to be put onto the rotor to test their ability to reduce cirulating eddy currents.

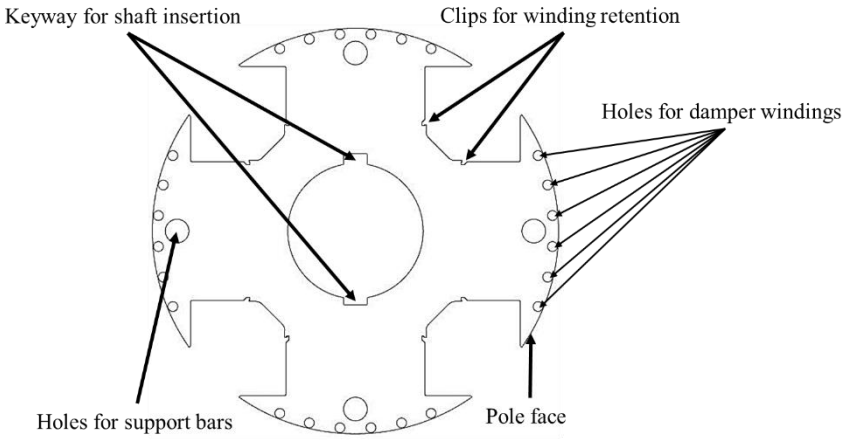


Figure 3-10. A single rotor lamination with keys features labelled.

In Figure 3-10 the design for a single rotor lamination is shown with the key features labelled. As the design for the rotor core, was kept for the prototype rotor the typology of the lamination was retained. The damper winding predominantly works in laminated rotor cores by shorting the electrically isolated laminations together allowing the eddy currents built up at the pole faces during operation to flow out of the core pack. In a solid rotor the eddy currents can circulate freely. The primary purpose of the damper windings is thus negated by using a solid rotor and they can be removed from the rotor design. The holes for the support bars can also be removed as the primary function of the support bars is to make the laminated core pack more ridged. A cast core pack does not require support bars to improve its rigidity. The clip cut-outs on the lamination are to allow plastic supports to help retain the coil structure of the rotor windings during operation.

The clips can be attached to a solid rotor with an adhesive so the clip cut-out is not required. The rotor core and shaft will be cast as one piece so the cut-out for the shaft and keyways can be removed.

The surface finishes for the rotor core differ from those of the shaft as the rotor core is constructed from laminations. The core pack has ridged edges parallel to the shaft due to the burr on the edge of the laminations.

The surface of each lamination has a finish that is determined by the insulating materials applied to the surface during the production process but can be assumed to be self-levelling and therefore given a roughness of N1. A sand cast part can have a surface finish of N11 which would be suitable for the surface finish of the rotor core, excluding the pole faces. Sand cast parts are not net shape so some machining of the cast rotor will be required to obtain the final dimensions. The final surface finish for the core pack will be N11 which is the same finish as a sand cast part but with the dimensional accuracy the sand cast part lacks. If the pole faces are made from sheet material bent to the radius of the cast rotor, the surface finish would be that of the sheet material used. If the pole shoes are machined out of billet then the machined surface would require grinding to N5.

3.2.3 Prototype fabrication

The following sections details the production of the pole shoes and the rotor core that together form the completed prototype rotor.

3.2.3.1 Pole shoes

The material selected to produce the pole shoes was Invar 36, a nickel alloy. Invar 36 was purchased from William Gregor Ltd as four pieces of plate (35mm x 204mm x 290mm). The plate was delivered directly to the machining company: G.S. Precision Ltd. The plate was conventionally machined to the drawings provide by the author. Once completed the pole shoes were shipped to Summerfield Ltd who had been selected to machine the main rotor body to ensure the fit of the pole shoes onto the rotor body.

3.2.3.2 Rotor body

From the material selection chapter the steel chosen to cast the rotor was A1 grade to BS3100:1991 [119]. The casting was carried out by the foundry, H.I Quality Steel Casting Ltd, which provide samples for the material testing. Once a formal quotation had been accepted by CGT and the order placed the foundry produced a pattern to be used to form the sand mould for casting the rotor.

During the material selection phase the ideal heat treatment in terms of magnetic properties was found to be annealing with a cooling rate of 4.5°C/min, for this prototype the casting was normalised in air. The lack of the annealing of the cast rotor will increase the current and voltage required by the field windings to produce the required field strength, however the dataset produced during testing, will in future, allow computer modelling to assess the impact of new DC characteristics from the further testing of cast steel grades made the additional cost of the annealing process unnecessary.

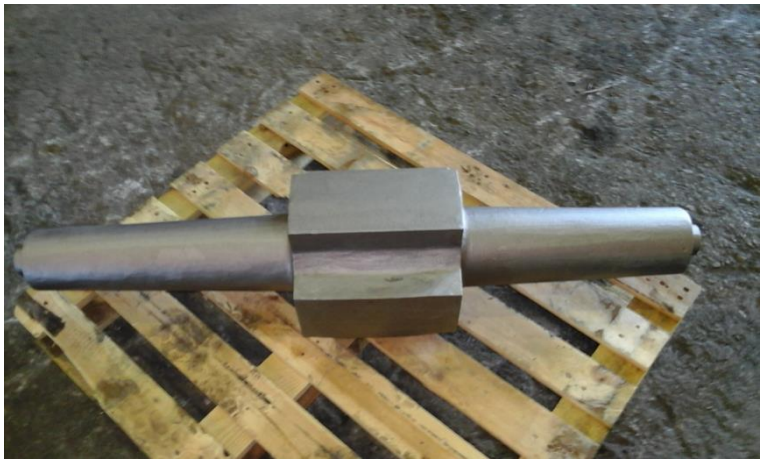


Figure 3-11. The cast and normalised rotor ready for shipping to the machining company to be machine to its finished typology. If the rotor was going for annealing this is the stage at which it would be carried out.

In Figure 3-11 the cast rotor is shown after it has been normalised in air and is ready for dispatch to the machining company, Summerfield Ltd.

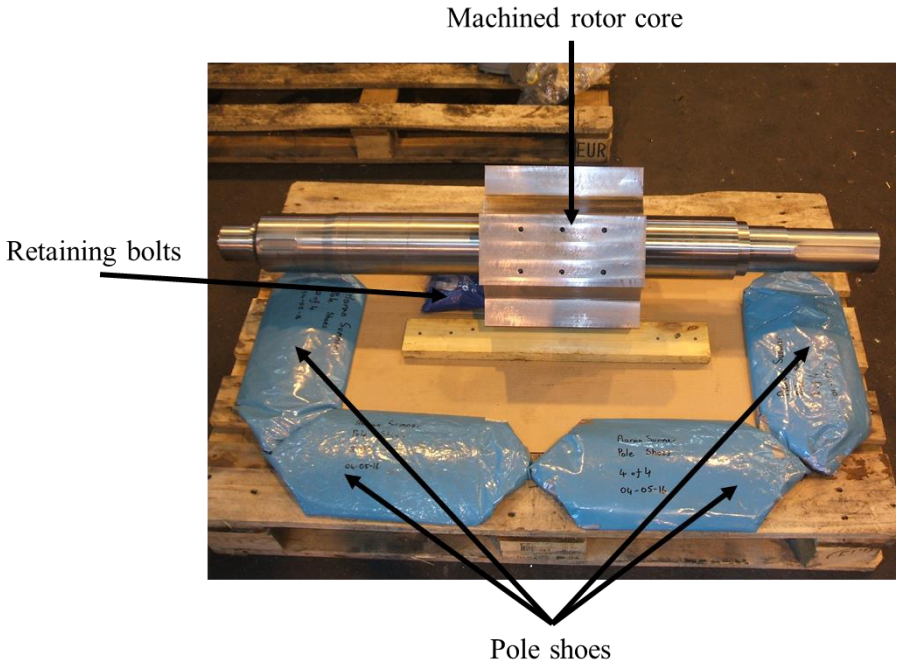


Figure 3-12. The machined rotor is shown ready for dispatch to AlTech Ltd to have its field windings tumble wound into place. Also shown are the pole shoes that were machined by G.S. Precision Ltd and sent to Summerfield Ltd to confirm the pole shoes fitted correctly.

In Figure 3-12 the machined rotor is shown loaded onto a pallet for shipping to a specialist winding company, AltTech Ltd. The four packages surrounding the rotor are the Invar 36 pole shoes and the 24 pole shoe retaining bolts.

AltTech fitted the poles shoes to the rotor body and then tumble wound the field windings on the rotor body.

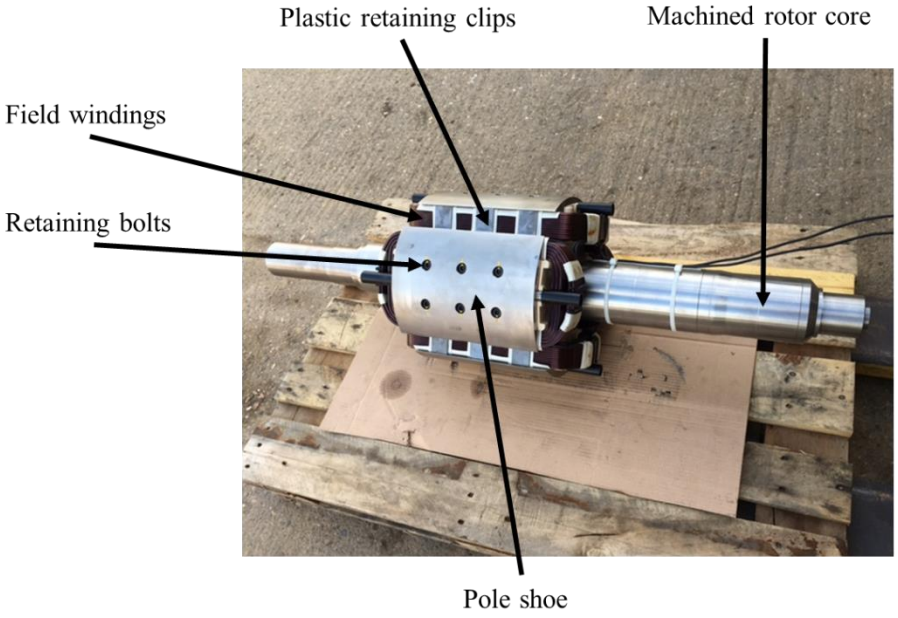


Figure 3-13. The rotor fitted with pole shoes and windings fitted, also visible are the plastic clips that were glued onto the main rotor body.

In Figure 3-13 the machined rotor body is shown with the poles shoes bolted into place and the windings fitted. The plastic clips help retain the shape of the windings under the centrifugal loading during operation. At this stage the wound rotor was shipped to CGT's facility in Stamford for final assembly and insertion into a stator to produce a compete generator for testing. In Figure 3-14 the rotor, after final assembly has been carried out, at CGT's factory in Stamford is shown before fitting into a stator for testing.

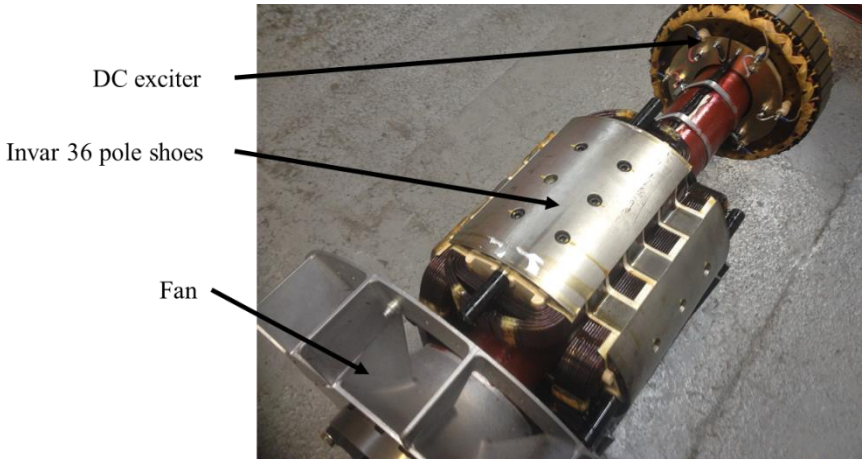


Figure 3-14. The completed rotor ready for insertion into a stator for testing. The aluminium fan can be seen at the bottom left of the image with the DC exciter at the top right.

3.2.4 Testing

To provide a baseline, to compare the prototype rotor against, a standard rotor was fitted into a stator and its performance characteristics recorded. The standard rotor was removed and the prototype rotor was inserted into the same stator, and the performance of the prototype analysed.

The results from the magnetic testing of the A1 grade steel, that makes up the main rotor body, and the Invar 36, that make up the pole shoes, will be used to explain the performance of the prototype verses the performance of the standard rotor.

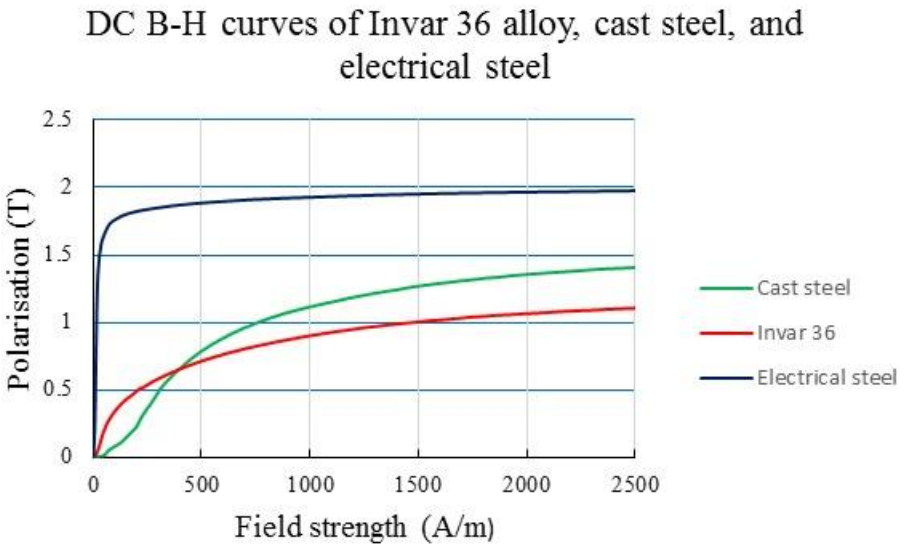


Figure 3-15 . The DC B-H curves of the A1 grade steel that forms the main rotor body (in green) and the Invar 36 that forms the pole shoes (in red). Also shown (in black) is the B-H curve of the steel that forms the steel laminations in the standard rotor.

In Figure 3-15 the DC B-H curves of the two main materials that form the prototype rotor and the material that forms the rotor core pack of the standard rotor are shown. At a field strength of 1500A/m the Invar 36 reaches magnetic saturation, whilst the steel continues to magnetise. The point at which the pole shoe saturates and the magnetisation of the steel continues will be visible in the performance data of the prototype.

3.2.4.1 Prototype testing

The prototype was tested at the CGT test centre in Stamford (UK). This test facility carries out the testing of the all generators produced at the Stamford plant. The test centre and its test methodologies are considered commercially sensitive so the results from testing were presented to the author as fact with all calculations and error calculations already taken into account.

The HCI444C is rated to output 260kVA at 400V with a frequency of 50Hz supplying a load with a power factor of 0.8.

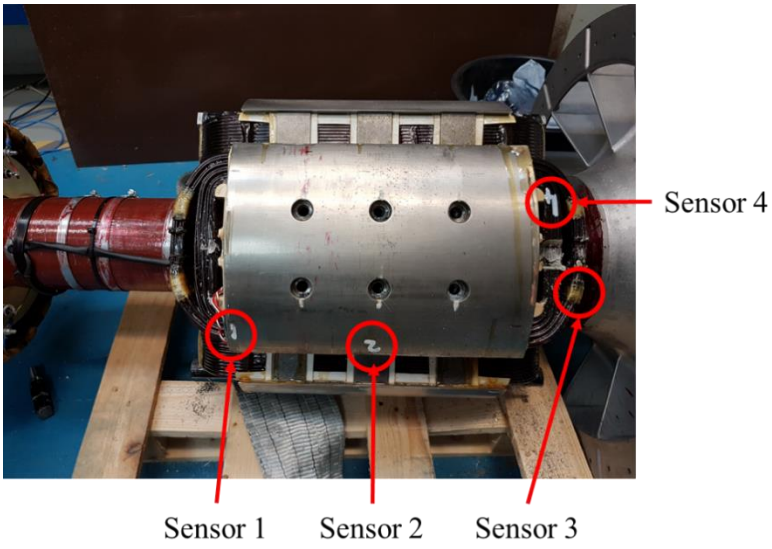


Figure 3-16. The position of the four resistance temperature detectors (RTD) on one of the poles shoes is shown. Sensor 1 is positioned on the side of the poles shoe. Sensor 2 is midway along the edge, on the underside of the shoe. Sensor 3 is on the outer set of windings. Sensor 4 is on the inner set of windings.

When testing a generator to determine its performance characteristics there are two main testing methodologies. The first is with a load attached to the output terminals drawing current called 'on-load' testing and the second is with the generator operating with no load attached and therefore no current flow called 'no-load' testing.

On-load testing

On-load testing is required to determine at what output power, the prototype should have its no-load testing carried out at. As the term suggests on-load testing involves testing the performance of the generator as it has an increased percentage of its rated load applied to it.

As the generator will be producing up to 260kVA of power the generator is connected to the national grid in order to have a load large enough to run at its rated output. Between the generator under test and the national grid is a synchroniser. The synchroniser is an electronic system that ensures that the frequency of the generator matches that of the nation grid. Failure to ensure the frequencies match will result in the national grid "driving" the generator's stator to rotate in the opposite direction to the spinning rotor, this results in catastrophic damage to the generator.

The synchroniser can be used to change the amount of load applied to the generator and also change the power factor the generator operates at.

No-load testing

No-load testing involves attaching a motor to the generator to act as its prime mover. The generator itself is not connected to an electrical load. As the generator is not supplying electrical power to a load any performance metrics of the generator have not been altered by the type of electrical load it is supplying. No-load testing is carried out using two different methodologies to completely characterise the magnetic characteristics of the generator's performance. The first methodology is open-circuit magnetic characterisation (OCC) and the second is short-circuit magnetic characterisation (SCC).

Open circuit magnetic characterisation

The OCC determines the magnetic saturation capabilities of a generator. The OCC test drives the generator until the soft magnetic materials reach saturation. The saturation characteristics of the rotor can be determined from the data taken during the OCC testing.

The OCC of a generator are measured by using the following methodology:

- The output terminals of the generator are not connected to anything, it is open-circuit
- A voltmeter is connected across each phase of the output terminals
- The motor, acting as a prime mover, spins the rotor up to the synchronous speed of the generator.
- The current to the field windings is increased in stages to produce stepped increases in the output voltages

Short-circuit magnetic characterisation

The SCC determines how much current the generator can supply during operation. The SCC test involves running the generator at its operating speed using a stepped increasing current supplied to the field windings.

At each step of current increase the output terminals of the generator are shorted together and the current that flows during the short circuit is measured. The results from this test show the current generated by the generator depends upon the amount of current suppled to the field windings.

The short-circuit characteristics (SCC) of a generator are measured by using the following methodology:

- The rotor current is set to zero
- The output terminals of the generator are shorted together
- The motor, acting as a prime mover, spins the rotor up to the synchronous speed of the generator.
- The field winding current is steadily increased until the short circuit armature current reaches the rated design value

Losses

The efficiency of the generator is determined by the following equation:

$$Efficiency\ of\ generator = \frac{a * b}{(c + d + e + f) + (a * b)} * 100$$

Where:

$a = Rating\ of\ alternator$

$b = Power\ factor$)

$c = Windage\ and\ friction\ losses$ (kW)

$d = Iron\ losses\ (kW)$

$e = Stator\ core\ losses\ (kW)$

$f = Rotor\ losses\ (kW)$

3.2.4.2 Further testing

Testing until this point was carried out at the CGT factory in Stamford. Once the initial testing was completed the generator (fitted with the prototype rotor) was sent to the UoN high power test facility.

Cross-platform calibration

Before testing of the rotor could begin at the UoN the test apparatus at the University needed to be cross calibrated with that of the CGT test facility in Stanford. To do this both the OCC and SCC testing was repeated at the UoN and the results compared.

The UoN test facility lacks the capability to measure the current and voltage of the rotor during operation so the current and voltage of the exciter stator, which feeds power to the rotor, was used as a proxy. The exciter stator currents and voltages are part of the test data from Stamford so a direct comparison of the test apparatus is possible.

Characterisation of the pole shoes saturation (Thermal)

During initial testing the poles shoes saturated at around 72kVA. To prove the concept of using a material with a lower saturation point than the material that makes up the main rotor body the rotor needs to be subjected to transients and harmonics before and after the pole shoes reach saturation. The generator was connected to a load bank that allowed switching of a variable load while the generator was under test.

- RTDs mounted on the rotor were connected to data loggers mounted to the rotor shaft and set to record its temperature every 10 seconds.
- The generator was started with a load of 60kW and left to heat for an hour
- Transients of 30kW were put onto the pole shoes for one minute with one minute in-between transients.
- The load was increased by 5kW, to 65kW, and left to heat for 15 minutes
- Transients of 40kW were put onto the pole shoes for one minute with one minute in-between transients.
- The load was increased by 5kW, to 70kW, and left to heat for 15 minutes
- Transients of 50kW were put onto the pole shoes for one minute with one minute in-between transients.
- The load was increased by 5kW, to 75kW, and left to heat for 15 minutes

- Transients of 40kW were put onto the pole shoes for one minute with one minute in-between transients.
- The load was increased by 5kW, to 80kW, and left to heat for 15 minutes
- Transients of 30kW were put onto the pole shoes for one minute with a one minute in-between transients.
- The generator was then spun down and the RTD temperature readings were downloaded for study

3.3 Laser cladding of Ni-Fe soft magnetic alloy

The concept of using a Ni-Fe alloy with a lower magnetic saturation than the bulk cast steel of the rotor has been proposed as a method to reduce heating on the rotor pole faces by harmonics and transients from the stator. In the prototype, the Invar 36 saturated when the output of the generator was only 72kW, this is 28% of the rated 260kW output of the HC1444C. To make the concept of a shielded rotor practical the saturation of the material on the pole faces would need to occur at the normal operating output of the generator not its maximum rated output of 260kW. During operation a generator will not operate at its maximum rated output as this would not allow for the normal fluctuations in load that can be expected during operation. If a material is used that saturates before the 260kW maximum rated output is reached, extra heating will occur in the rotor. The current in the field windings will need to increase to produce a stronger magnetic field capable of bridging the increased air gap caused by the saturated material. A solid sheet of lower saturation material affixed on the pole faces will result in a uniform magnetic saturation that would need to be calculated to match the normal operating output of the generator. The many different applications for a generator make the specification of a “sweet spot” for normal operating output impossible. What is needed is a methodology to allow the protection of the rotor from harmonics and transients at different outputs. This could be obtained by the use of thin sheets of material, each with a different saturation point, affixed to the rotor with the sheet with the highest saturation point closest to the rotor body.

This would result in the apparent air gap between the stator and rotor increasing as the output of the generator increases, thus reducing the effect of harmonics and transients on the heating of the pole faces.

Previous work on shielding solid rotors from transients and harmonics has focused on the use of thin copper sheets, mounted on the pole faces [28]. The use of copper screens on the pole faces has a two-fold effect on reduction of eddy currents: firstly the highly conductive copper allows the induced eddy currents to flow from the rotor without inducing heating, secondly the copper increases the air gap between the rotor and the stator [127].

The problem with using multiple thin sheets applied to the pole faces is that the method to affix the sheets would need to be robust enough to prevent centrifugal forces from distorting or ripping off the sheets. A secondary problem with the use of thin sheets is that the range of thin sheets of soft magnetic material is limited, and getting a graduated decrease in material saturation points from commercially available soft magnetic materials is not currently possible. Laser cladding sidesteps the difficulty of having to use thin sheets by using multiple powders or wires that are composed of elemental ferromagnetic metals which can have their feed rate individually controlled during application to the pole faces. This level of control allows layering of alloys with different compositions and hence magnetic saturation. The thickness of the layers can be controlled using the standard methodologies employed in laser cladding.

To produce a >10mm coating of a soft magnetic material onto a pole shoe an additive manufacturing process will need to be selected that allows a number of critical characteristics to be met, they are:

- As close to 100% density as possible,
- Able to apply a coating onto a substrate (to act as a proxy for a pole shoe),
- Able to vary the composition of the coating between layers.

Laser cladding, using a laser to provide thermal energy, is a manufacturing process that allows a layer of material to be applied to a substrate.

Typical coatings maybe 1-15mm in thickness and serve to enhance tribological [128], corrosion [129] and thermal properties [130] of the substrate component. The cladding media may be delivered in wire, strip or powder form and a laser beam provides sufficient thermal energy to create a weld. Laser clad parts are near net shape but do require further machining to obtain the desired finish. The use of laser cladding on the magnetic performance of thin films of permalloy, produced from elemental powders, have been investigated [131] and shown that the deposited permalloy has a single gamma phase (Fe-Ni_3) with the elemental powder mixing in the melt pool to produce a near homogeneous intermetallic clad film.

The use of laser cladding to deposit material selectively can reduce the amount of alloy used and reduce the cost of the resultant parts. The use of laser cladding of soft magnetic alloys is predominantly based on work for the electronics industry [132] the current work focusses on the production of <1mm thick coatings (thin films) for sensors.

To produce coatings that can be >10mm thick the non-uniform microstructure of the deposited material will need to be addressed through post production annealing of the substrate and coating.

3.3.1 Material selection

The effect of laser cladding on the magnetic properties of a Ni-Fe alloy needed to be evaluated in order to be able to use laser cladding to produce Ni-Fe alloys with the desired magnetic properties to block induce eddy currents from the pole faces.. To do this a Ni-Fe alloy that has a characteristic B-H curve was selected, this allowed a direct comparison of a commercially available soft magnetic alloy verses a deposited coating. The powder feedstock was based upon the commercial alloys composition. The alloy selected was permalloy. Permalloy is a term given to a range of soft magnetic nickel-iron (Ni-Fe) alloys that have very high initial permeability, low coercivity, and low magnetostriction [133].

If a laser clad permalloy coating could be produced that matched or exceeded the performance of a commercially available permalloy, with an identical composition (as identical as practically possible) the use of laser cladding to produce Ni-Fe soft magnetic coatings would be proven. The addition of 5 weight percentage (wt%) molybdenum (Mo) to permalloy can increase permeability tenfold but reduce its maximum saturation magnetisation.

The addition of Mo also results in a threefold increase in the resistivity of the alloy which serves to reduce losses due to eddy currents in electrical machines [134] which will be vital to reducing eddy currents before the coating reaches saturation on the pole shoes. The highest permeabilities are obtained in these alloys, when in >1mm sheet form, using a hydrogen annealing heat treatment to remove interstitial impurities [58] such as O, S, C, N, from the bulk material, The removal of the interstitial impurities removes dislocations in the microstructure causing an increase in magnetic performance.

3.3.2 Powder production

To provide a comparison of the effects of laser cladding on the magnetic properties of a permalloy coating verses a conventionally produced permalloy, a commercial alloy was selected on which to base a powder for laser cladding.

The alloy selected was Vacoperm 80® produced by Vacuumschmelze GmbH & Co and supplied under the name Alloy 79 by Ed Fagan Ltd.

A powdered version of Alloy 79 was produced by Phoenix Scientific Industries (PSI) Limited using a Hermiga 100/10 vacuum induction gas atomizer. The powder was sieved to yield a size range of 53µm-150µm as commonly used by laser cladding apparatus. A sample of the powder was sent to an accredited laboratory (to ISO17021:2011), AMG Superalloys Ltd, for metallurgical analysis to confirm composition. This is shown in

Table 3-6 along with the nominal composition of the Alloy 79 according to ASTM A753 - 08(2013) [135].

Table 3-6. Composition of permalloy powder, Alloy 79, used in this study.

Element	Permalloy powder	Nominal Alloy 79
	Percentage by weight (wt%)	
Ni	79.90%	80.35%
Fe	Bal	Bal
Mo	4.82%	4.59%
Mn	0.32%	0.50%
Co	0.16%	<0.3%
Si	0.15%	0.28%
P	<0.01%	0.02%
C	<0.003%	<0.003%
S	<0.005%	<0.007%

3.3.3 Laser cladding

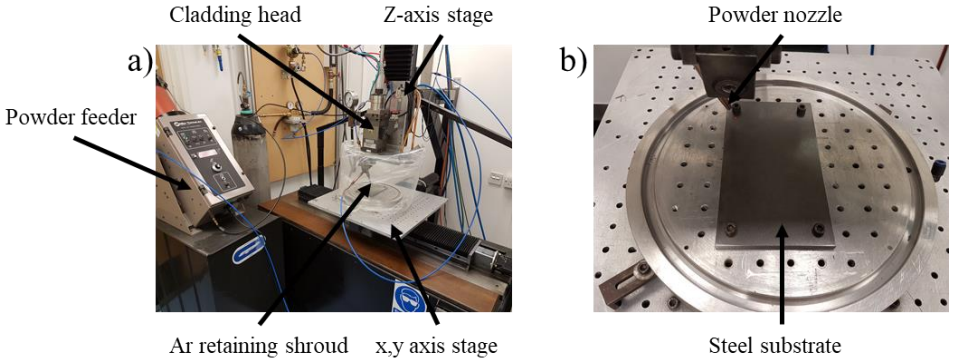


Figure 3-17. Images of the experimental setup. (a) shows the powder feeder, cladding head, shroud used to create a glove box arrangement to retain a Ar atmosphere, and (b) the x,y stage that moves the substrate during cladding.

In Figure 3-17 the experiment setup is shown with main components labelled. Laser cladding was carried out using a 2kW GSI Group Ltd JK400FL continuous wave (CW) fibre laser. The cladding head was mounted onto a z-axis stage that was controlled by an ECS CNC1400D controller. The substrate (to be clad) is mounted to an x,y-axis stage also controlled by the CNC1400D controller. The powder is fed into the melt pool, created by the laser, by a Millar Thermal Inc model 1264 powder feeder. The powder is fed into a continuous stream of Ar flowing at a rate of 10 litres per minute. The area in which the laser

cladding took place was shrouded by an Ar atmosphere contained by a plastic bag.

3.3.3.1 Development of cladding parameters

The substrate plate for cladding was an EN3b plate that was 6mm thick and bolted onto the x,y-axis stage. The laser power was set to 1.2kW and stage traverse speed to 400mm per minute this results in a power density of 180W/mm^{-1} for an initial trial. Previous experiment with this apparatus indicated that this power density would produce a high density bead [136] the previous study on the use of laser cladding on permalloy were used to further refine the initial cladding parameters [131].

For this study a coating of >10mm was required and so beads were built-up, one upon the other to increase the coating thickness.

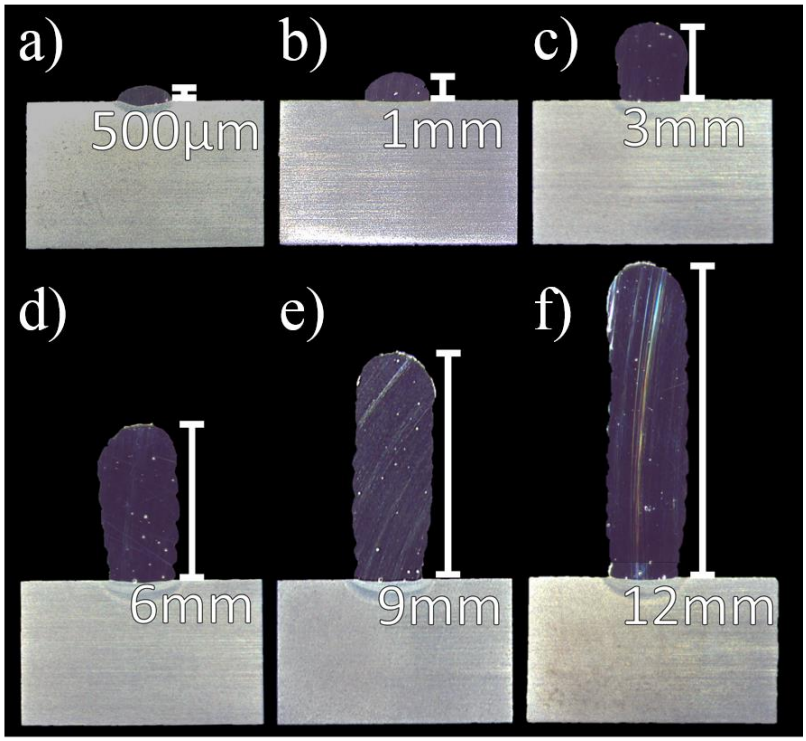


Figure 3-18. EN3b substrate with six laser clad beads; (a) was obtained with a power density of 180W/mm^{-1} (b) was obtained with a power density of 360W/mm^{-1} beads c-f are all produced with a power density of 360W/mm^{-1} (c) is constructed from three beads one upon the other, (d) is six beads one upon the other, (e) is nine beads one upon the other and (f) is twelve beads one upon the other.

In Figure 3-18 the first six laser clad beads are shown. The initial power density of 180W/mm^{-1} produced a bead that was 0.5mm thick (a). The power density

was increased to 380W/mm^{-1} to increase the thickness of the deposited bead to approximately 1mm (b).

Once a ~1mm bead thickness was achieved the next step was to build three beads one on top of the other (c). Increasing the distance between the substrate and the laser emitter (z-axis) by 1mm increments allowed a bead six layers high to be produced (d). This was subsequently exceed by a bead with 9 layers (e) and again with 12 layers (f). All beads created were no less than 2.5mm wide.

3.3.4 Production of samples for magnetic testing

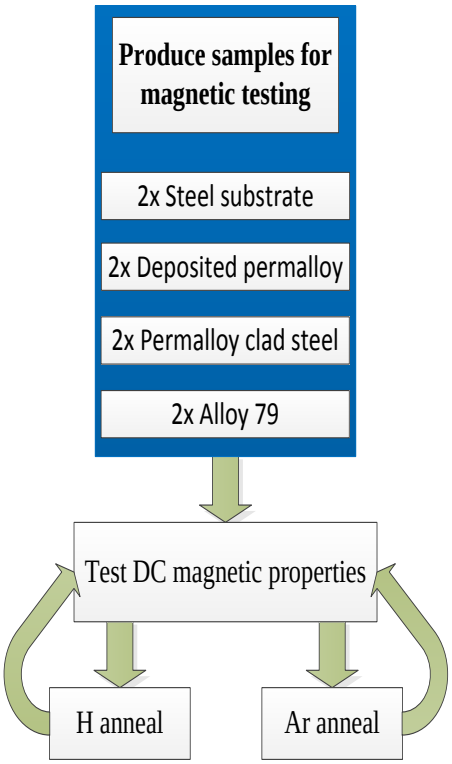


Figure 3-19. Flow chart of the procedure for testing the magnetic properties of permalloy before and after annealing heat treatments are applied.

In Figure 3-19 the layout of the methodology for testing the magnetic performance of laser clad permalloy and allowing a comparison between conventionally produced Alloy79 is shown. The magnetic performance of permalloy clad steel and the steel substrate samples was also tested. Two of each of the samples were produced to allow each type of sample to be annealed in both H and Ar and the difference between the effects of the annealing atmosphere on the DC magnetic performance of the samples was found.

The deposited permalloy samples, steel substrate samples, and Alloy 79 samples for magnetic testing were toroids with an inner diameter of 20mm x outer diameter of 28mm x and a height of 10mm. In order to compile with the sample specifications laid out in IEC 60404-4:1997 [2] a 10mm thick coating could not be used for the permalloy clad steel samples instead a 5mm thick coating was used. The permalloy clad steel samples had an inner diameter of 20mm x outer diameter of 38mm x and a height of 10mm. All sample dimensions comply with standard IEC 60404-4:1997 [2] for testing of DC magnetic properties.

In Table 3-7 a list of all the samples for magnetic testing is shown with the method used to produce them.

Table 3-7. Table of samples produced for magnetic testing with sample identifiers and summary of methodology

Sample name -sample number:	Material	Production method
Steel substrate -1	EN3b steel	Cold drawn
Steel substrate -2	EN3b steel	Cold drawn
Deposited permalloy -3	Permalloy 80	Laser clad (block)
Deposited permalloy -4	Permalloy 80	Laser clad (block)
Permalloy clad steel -5	EN3b/P80	Laser clad substrate
Permalloy clad steel -6	EN3b/P80	Laser clad substrate
Ed Fagan -7	Alloy 79	Hot rolled
Ed Fagan -8	Alloy 79	Hot rolled

3.3.4.1 Samples for magnetic testing of steel substrate

A baseline B-H curve of the EN3b substrate was required. Two toroids were prepared from a 30mm diameter rod of cold drawn EN3b steel. In Table 3-7 these are samples 1, and 2.

3.3.4.2 Samples for magnetic testing of laser clad permalloy

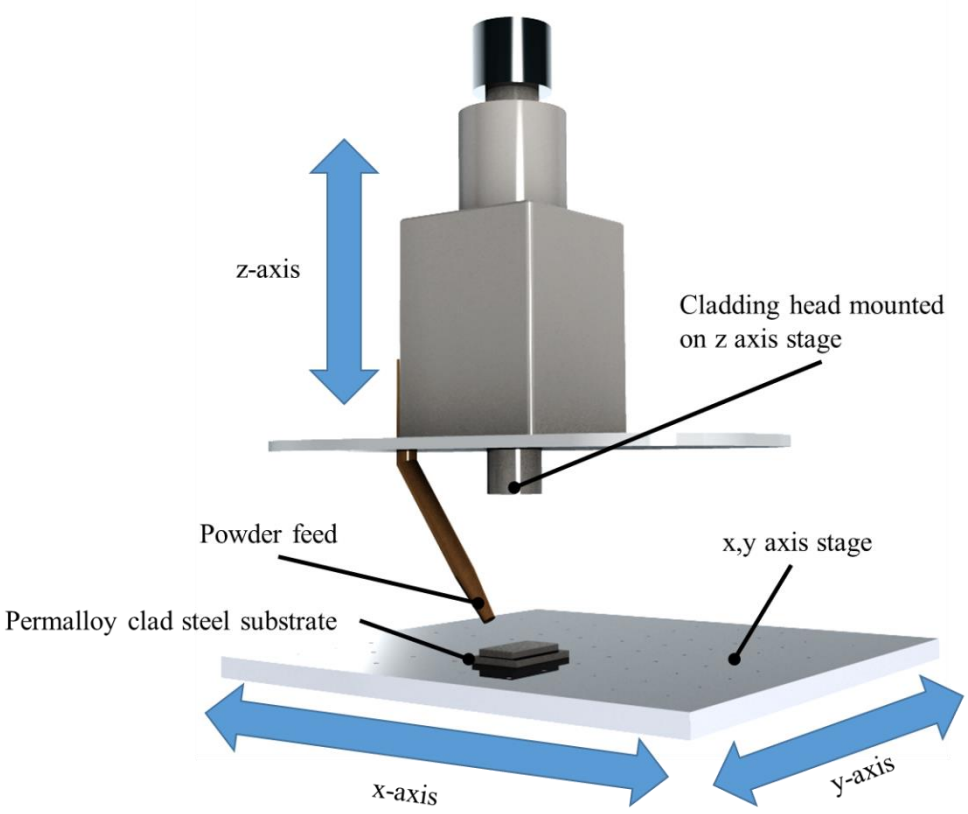


Figure 3-20. Schematic of the laser cladding of an EN3b substrate. The cladding head deposits an approximately 1mm thick layer of material in a raster pattern. Once the raster is completed the cladding head raises by 1mm in the z-axis and the next raster is laid down on top of the previous raster.

In Figure 3-20 the experimental setup for the deposition of a permalloy block is shown. The laser clads a bead of permalloy in a raster pattern onto an EN3b substrate.

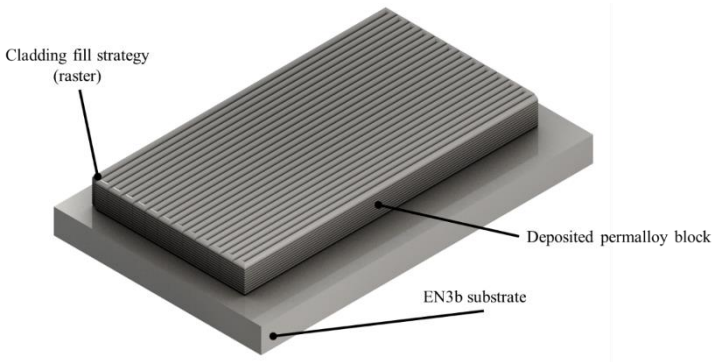


Figure 3-21. Schematic of the raster pattern used to produce a solid block of laser clad material. The waviness on the top surface is characteristic of a laser clad coating.

In Figure 3-21 a schematic of the cladding fill strategy to produce a solid block of deposited permalloy is shown. Each raster produced a ~1mm thick layer of deposited material. When the raster was completed the cladding head was raised 1mm in the z-axis and the next raster began from the end of the previous layer's raster. The beads of clad material overlapped each other by 30% to ensure that there were no voids in the solid block. The block was sectioned to produce specimens for optical imaging of the microstructure of the coating. The remaining block of deposited material had the substrate milled away and the resultant block of purely deposited permalloy was then machined and turned to produce two toroid sample for testing, in Table 3-7 these are referred to as samples 3 and 4.

3.3.4.3 Samples for magnetic testing of permalloy clad steel

To understand the effect of laser cladding on the properties of a steel substrate the parameters defined in Section 3.3.4 were reused, but the substrate was changed from a flat 6mm thick plate of EN3b steel to a 50mm long cylinder of EN3b.The cylinder was fitted to a CNC controlled 4 jaw chuck that rotated the cylinders at a rate that equalled the feed rate used previously in Section 3.3.4.

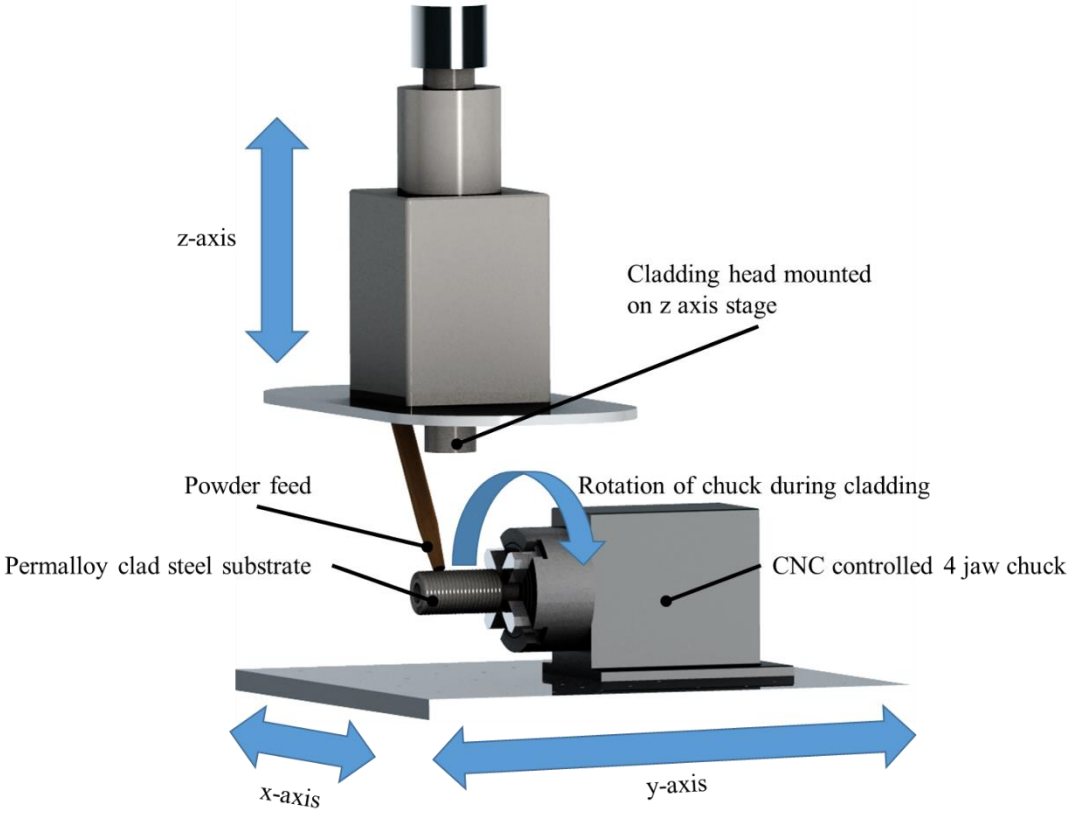


Figure 3-22. A diagram of the laser cladding of an EN3b cylinder. The cladding head deposits a 1mm thick layer of material on the circumference of the cylinder. Once the circumference has been coated the x,y stage moves 1mm and the next track is laid down. When the whole surface area has been coated the cladding head raises by 1mm in the z-axis to deposit a new layer onto of the recently deposited coating.

In Figure 3-22 a diagram of the coating of a EN3b cylinder is shown. The laser cladding was preformed perpendicularly to the axis of the cylinder and the overlap between beads of 30% was used to produce a solid coating.

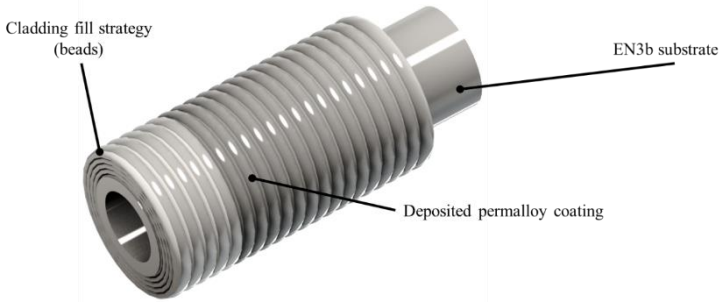


Figure 3-23. Image of the raster pattern used to produce a coating of permalloy onto a steel cylinder. The laser claddings characteristic waviness of the coating runs perpendicular to the axis of the cylinder.

In Figure 3-23 the finished coating comprising of six layers of laser clad material is shown.

The coating was 6mm thick overall, as the coating was applied evenly over the diameter of the substrate the outer diameter of the coated substrate changed from 28mm to 40mm. The coated cylinder was machine to produce two toroids with an outer diameter of 38mm x inner diameter of 20mm x and a height of 10mm for magnetic testing. As the coating was 5mm thick the overall diameter of coated substrate was increased by 10mm. In Table 3-7 these are referred to as samples 5, and 6.

3.3.4.4 Samples for magnetic testing of Alloy 79

To quantify the difference between laser clad permalloy and 'bulk' or as rolled. A 31mm diameter rod, produced via hot rolling, of Alloy 79 was machined into toroids, In Table 3-7 these are referred to as samples 7, and 8.

3.3.5 Magnetic testing

The machining of all the toroids for magnetic testing was carried out using similar processing speeds and techniques to minimise differences in magnetic performance due to differing machining parameters.

The samples for magnetic testing complied with the standard IEC-60404-4:1997 [2]. The samples had 30 turns of 0.1mm^2 wire wrapped around the circumference of the toroid; this formed the sensor coil. Another 30 turns of 1.0mm^2 wire were wrapped on top of the sensor wire; this provided the source for the applied electromagnetic field. The coils were connected to a Brockhaus Measurements electrical steel tester and an increasing DC current was applied to the source coil.

The effect of the increasing DC current on the strength of the produced magnetic field was detected by the sensor coil and the DC B-H curves of the samples was determined automatically using a standard method of calculation set out in standard IEC 60404-4:1997 [2].

3.3.6 Optical microscopy

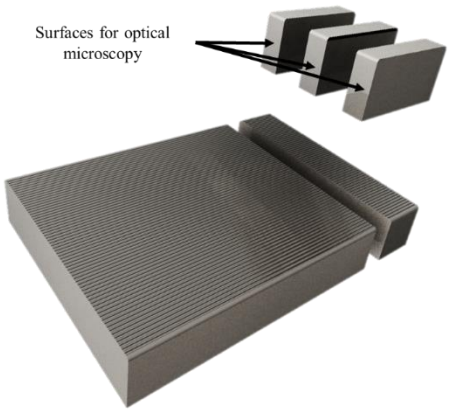


Figure 3-24. Image of the solid block of laser clad material a 5mm thick section removed to provide specimens of the laser clad blocks interior for optical microscopy.

In Figure 3-24 an image of the deposited permalloy block (described in Section 3.3.4.2) is shown with a 5mm thick section removed and sub-divided into three blocks. The surface of the blocks for imaging shows the interior microstructure of the deposited block.

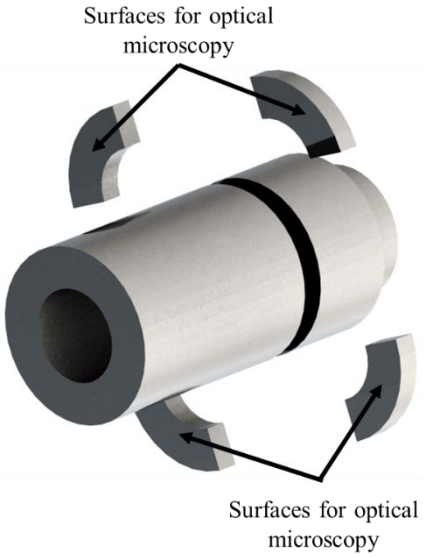


Figure 3-25. Image of the cylinder of substrate with a 5mm coating of laser clad Ni-Fe. The cylinder was sectioned to provide a 5mm thick disk that was quarter to provide four specimens for optical microscopy.

In Figure 3-25 an image of the EN3b cylinder with the deposited permalloy coating is shown with a 5mm disk cut-out and further divided into four specimens for optical microscopy.

All the samples were prepared for optical imaging following the guidelines defined in the ASM Handbook, Materials Characterizations, pp. 299–308 [121]. To etch the permalloy a Marbles etchant (10 g $CuSO_4$ + 50ml HCl + 50ml H_2O) was used.

3.3.6.1 Grain sizing

To determine the effects of annealing on the microstructure of the samples optical images taken of the samples were processed by ImageJ software using the same methodology as in Section 3.1.5.5. In that section ImageJ was found to be unable to accurately determine the crystal sizes of the samples. For the laser clad samples there are only one crystal type to analyses ($FeNi_3$). The changes in colouration of the samples is due to crystal orientation not crystal type.

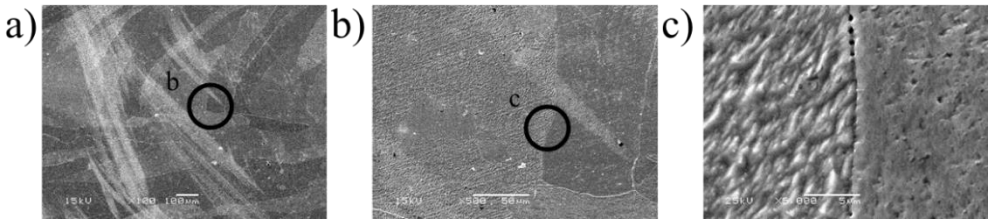


Figure 3-26. SEM images of the non-annealed deposited permalloy which shows how the differences iin microstructure colourisation is based on the orientation of the individual crystals when sectioned. (a) shows the boundaries between visibly different crystal at 100µm, (b) shows the circled area in (a) at 50µm the change in texture between the two crystals is more evident, (c) shows the circled area in image (b) at 5µm the different surface texture between the two $FeNi_3$ crystals is apparent. The finer the surface texture the less electron scattering takes place therefore the darker the surface appears.

In Figure 3-26 a progression of SEM images is shown highlighting the boundary between light and dark crystals within the non-annealed sample's microstructure. In the EN3b steel the material consisted of two phases ferrite and pearlite, permalloys are single phase polycrystalline FCC alloy [137] [138] the apparent differences in colouration is due to the orientation of the crystals when sectioned to provide specimens for optical analysis as opposed to two different phases within the alloy, Ni-Fe alloys containing >35%wt Ni are single phase. The use of software to determine the crystal size of the laser clad coating was found to be inaccurate as sections of the non-annealed clad material had different crystal sizes depending on the depth they were located at in the clad coating. The growth of a crystal within the coating would be influenced by the amount of residual heat in the sample during deposition.

The use of software to determine the crystal grains sizes of the annealed samples was inaccurate due to large blocks of crystal growth in the same orientation, this gave the appearance of the block as being one very large crystal as opposed to many crystals in the same orientation.

The author has not found a method to determine the crystal size of a single phase microstructure of a thick laser clad sample so crystal comparisons will be made by visual comparisons.

3.3.7 Annealing

The eight samples were divided into two groups, each group containing one of each different type of sample. One of the groups of samples was annealing in Ar while the second group was annealed in an H atmosphere. The heating rates used for annealing the samples is laid out in Table 3-8, the heating rate, cooling rate, and hold time are matched to that defined in another study of the effect of annealing on Ni-Fe alloys [139].

Table 3-8. The heating rate for the H and Ar annealing cycles of the laser clad samples is shown.

Heating rate	Annealing temp	Holding time	Cooling rate
4.0°C/min	1150°C	130 mins	1.0°C/min

4 Material characterisation for cast salient pole rotor

4.1 Introduction

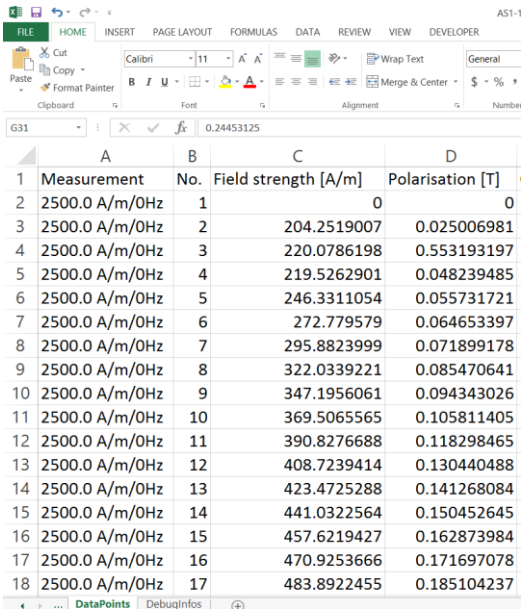
In the literature review the use of a cast rotor body was identified as a gap in the current knowledge for the production of generators. The use of a different ferromagnetic material in the areas that are exposed to AC electromagnetic fields can shield the main body of the rotor from circulating eddy currents. Shielding the main body of the rotor from AC fields makes the use of cast steel possible by removing the some of the losses associated with solid steel rotors.

The use of cast steel in applications where the steel will be exposed to only a DC electromagnetic field has not been explored in the literature and so there is limited knowledge on the magnetic performance of cast steels.

4.2 Effects of heat treatments on electromagnetic properties

4.2.1 Data quality

The datasets outputted by the test apparatus did not have any processing carried out on it verify its accuracy or reproducibility. The datasets consist of two columns the first with field strength and the second with polarisation, each with 100 data points.



	A	B	C	D
1	Measurement	No.	Field strength [A/m]	Polarisation [T]
2	2500.0 A/m/0Hz	1	0	0
3	2500.0 A/m/0Hz	2	204.2519007	0.025006981
4	2500.0 A/m/0Hz	3	220.0786198	0.553193197
5	2500.0 A/m/0Hz	4	219.5262901	0.048239485
6	2500.0 A/m/0Hz	5	246.3311054	0.055731721
7	2500.0 A/m/0Hz	6	272.779579	0.064653397
8	2500.0 A/m/0Hz	7	295.8823999	0.071899178
9	2500.0 A/m/0Hz	8	322.0339221	0.085470641
10	2500.0 A/m/0Hz	9	347.1956061	0.094343026
11	2500.0 A/m/0Hz	10	369.5065565	0.105811405
12	2500.0 A/m/0Hz	11	390.8276688	0.118298465
13	2500.0 A/m/0Hz	12	408.7239414	0.130440488
14	2500.0 A/m/0Hz	13	423.4725288	0.141268084
15	2500.0 A/m/0Hz	14	441.0322564	0.150452645
16	2500.0 A/m/0Hz	15	457.6219427	0.162873984
17	2500.0 A/m/0Hz	16	470.9253666	0.171697078
18	2500.0 A/m/0Hz	17	483.8922455	0.185104237

Figure 4-1 Output of B-H curve testing machine

In Figure 4-1 a screen grab of the excel file outputted by the Brockhaus Measurements electrical steel tester is shown. In this work each toroid was tested three times, with three toroids for each cast steel sample the baseline B-H curve testing resulted in 96 datasets like that shown in Figure 4-1.

AS1-1	No.	Field strength [A/m]	Polarisation [T]	AS1-1	Field strength [A/m]	Polarisation [T]
A	1	0	0	B	0	0
	2	204.2519007	0.025006981		190.5794652	0.529254188
	3	220.0786198	0.553193197		219.1897452	0.046497869
	4	219.5262901	0.048239485		247.8554561	0.056208201
	5	246.3311054	0.055731721		279.9064132	0.067282252
	6	272.779579	0.064653397		305.2264714	0.076072485
	7	295.8823999	0.071899178		327.7155927	0.084879149
	8	322.0339221	0.085470641		351.4717067	0.098220587
	9	347.1956061	0.094343026		374.0004214	0.109376789
	10	369.5065565	0.105811405		395.2621435	0.121354509
	11	390.8276688	0.118298465		412.8416678	0.13099912
	12	408.7239414	0.130440488		429.3323703	0.142648232
	13	423.4725288	0.141268084		444.6550638	0.154133042
	14	441.0322564	0.150452645		456.5331208	0.1631533
	15	457.6219427	0.162873984		471.6776435	0.175229601
	16	470.9253666	0.171697078		484.0506195	0.184677048
	17	483.8922455	0.185104237		497.0174984	0.195981124
	18	495.6911154	0.197213399		507.8661238	0.206562264
	19	507.3910016	0.207022314		517.5071468	0.215253915
	20	519.1106845	0.217784188		529.860326	0.22557217
	21	531.1471156	0.227888848		537.7394372	0.232440053

Figure 4-2, A screen grab of the combine test data from the same toroid measured twice. Showing the offset of the data due to the PID controller that controls the data acquisition of the steel test machine

In Figure 4-2 a screen grab of a combined dataset shows how the same sample can produce data that appears offset. The appearance of being offset is due to how the measurement machine determines where to take each one of the hundred data points it measures during each test cycle. The data acquisition is based on the tuning of a proportional–integral–derivative controller (PID), as the controller is constantly responding to feedback from the system no two datasets will appear identical.

To be able to carry out standard deviation calculations on the data all of the datasets were normalised to the field strength by using the LINEST function in excel to produce a 5^{th} order polynomial that produces a curve that matches the curve produced from the raw data.

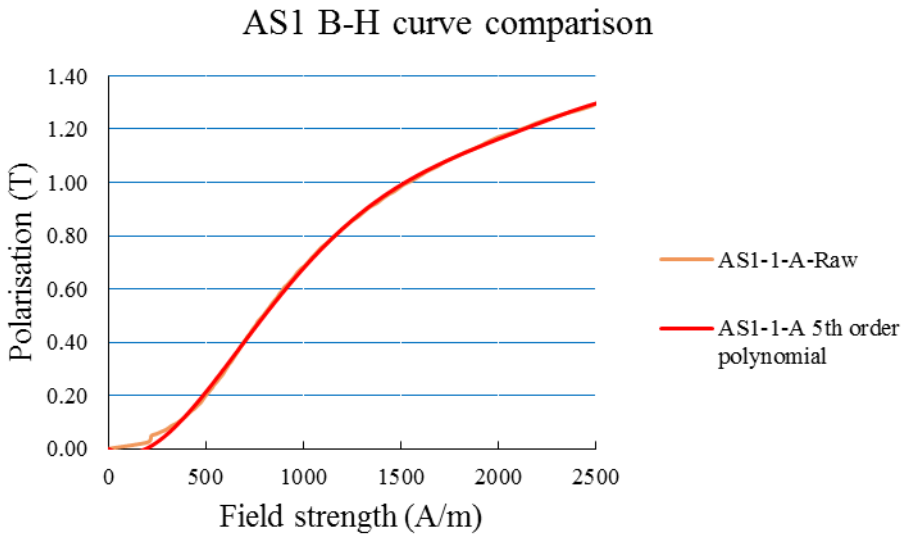


Figure 4-3, A comparison of the dataset outputted from the test equipment with the curve produced by a 5th order polynomial created by the LINEST excel function.

In Figure 4-3 a graph that shows a comparison of two B-H curves in shown, one is produced from the outputted dataset of the measurement system the other is the result of normalising the field strength using a 5th order polynomial of the raw dataset. By normalising the raw dataset to allow the normalisation of the field strength a comparison can be made for each of the outputted datasets.

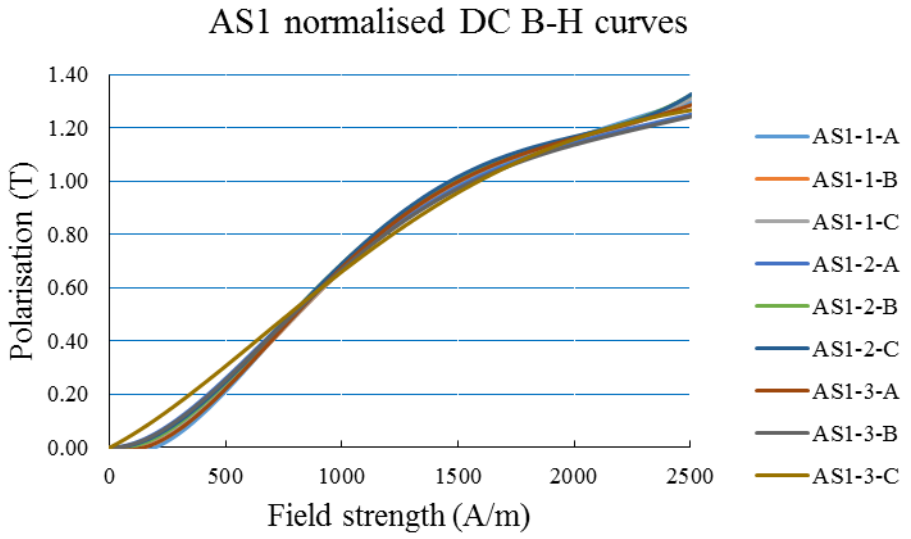


Figure 4-4, A graph of nine datasets, each toroid was tested three times (A,B,C). The raw data was then normalised by the LINEST excel function.

In Figure 4-4 nine normalised datasets are shown plotted on a graph. Once the datasets were normalised an average can be taken to represent the B-H curve of the cast steel sample and the standard deviation of the nine datasets was taken to quantify the quality of the data. The individual standard deviation for each row was taken across the nine samples. Each sample is graphed with the 5th order polynomial value for the tested samples and the standard deviation of the combine datasets is shown on a secondary vertical axis.

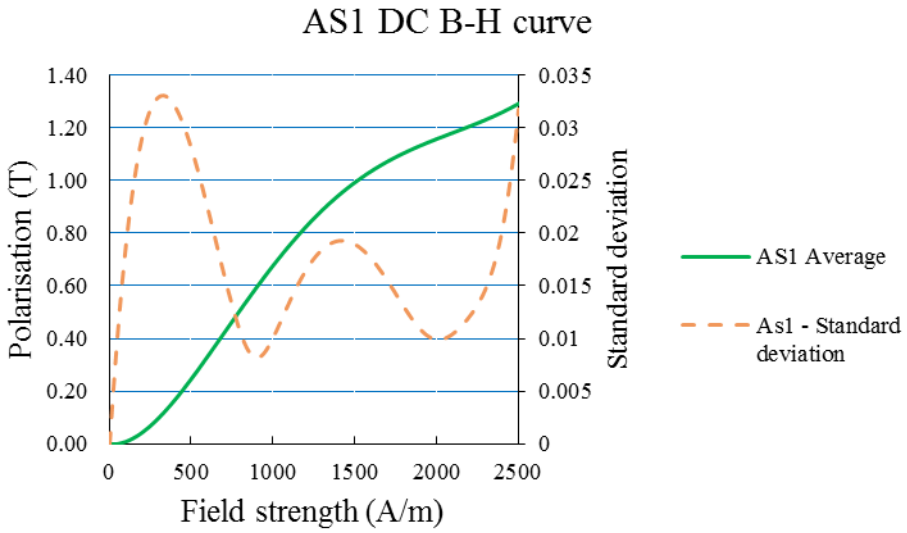


Figure 4-5, This graph is for the baseline B-H curve of sample AS1 with the standard deviation of the nine datasets plotted on the secondary axis.

In Figure 4-5 the average B-H curve for sample AS1 is shown with the standard deviation of the nine datasets also shown.

4.2.2 Permeability

In the following graphs the DC B-H curves of the steel samples are shown as a non-linear curve. In Section 2.1.2.1 the permeability over the whole of the B-H curve is defined as:

$$\mu' = \frac{dB}{dH}$$

For the graphs in in this thesis the permeability was taken at 100 points as the applied field strength was increased to a maximum value of 2000A/m.

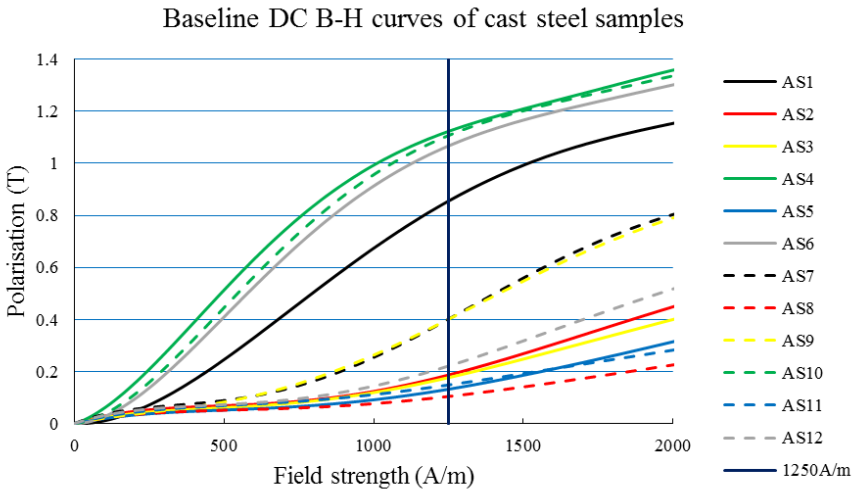


Figure 4-6. The DC B-H curves of the 12 normalised steel samples supplied from the foundry, the dotted line represents the field strength that the permeability will be taken from.

As stated in Section 2.1.2.1 it is common practice in industry and academia to calculate the permeability at a given polarisation or field strength values. The B-H curves of the tested cast steels, in Figure 4-6, show considerable variation in the level of polarisation reached for this reason the permeability will be calculated at a constant field strength of 1250A/m. The permeability of the samples was then converted into relative permeability using the equation shown in Section 2.1.2.1.

Table 4-1. Relative permeability of cast steel samples at a field strength of 1250A/m

Sample ID	Relative permeability
AS1	511
AS2	131
AS3	115
AS4	674
AS5	93
AS6	654
AS7	260
AS8	72
AS9	249
AS10	641
AS11	98
AS12	147

In Table 4-1 the relative permeability of the cast steel samples taken at 1250A/m is shown. The relative permeability values shows no apparent correlation between carbon content, alloying elements, or chemical optimisation. The samples optimised for normalising had some of the lowest permeabilities.

4.2.3 Effects of heat treatments on B-H curve

The data for each billet was plotted on a graph to allow easy comparison of the effect of each applied heat treatment. The normalised samples are shown as solid lines, the heat treated samples are shown with various dashed lines. The effects of heat treatments are shown for the three samples (AS4, AS8, AS11) that had the strongest change in magnetic performance due to the applied heat treatments. The results for the other nine samples can be found in Appendix A.

4.2.3.1 Effect of heat treatments on B-H curve of sample AS4

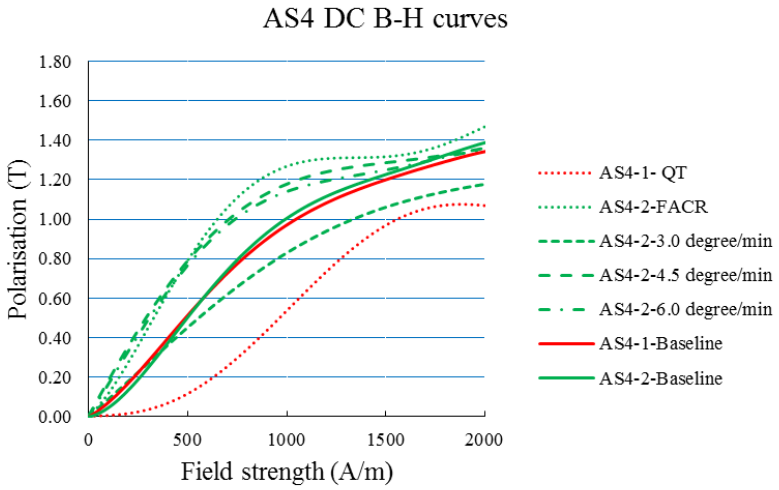


Figure 4-7. The range of B-H curves obtain in sample AS4 with the application of different heat treatments, The best performing sample was that annealed at the FACR with the other annealed sample reducing in performance the lower the cooling rate. The quenched sample had the worst performance of the samples.

In Figure 4-7 the effect of heat treatments on the permeability of sample AS4 is compared to the normalised sample. The highest B-H curve is obtained by annealing at the FACR rate. The B-H is reduced by the application of quenching, and annealing with a cooling rate of 3.0°C/min. Figure 4-7 also shows that annealing at 4.5°C/min gives a higher B-H curve than annealing at 6.0°C/min but a lower B-H curve than annealing at FACR.

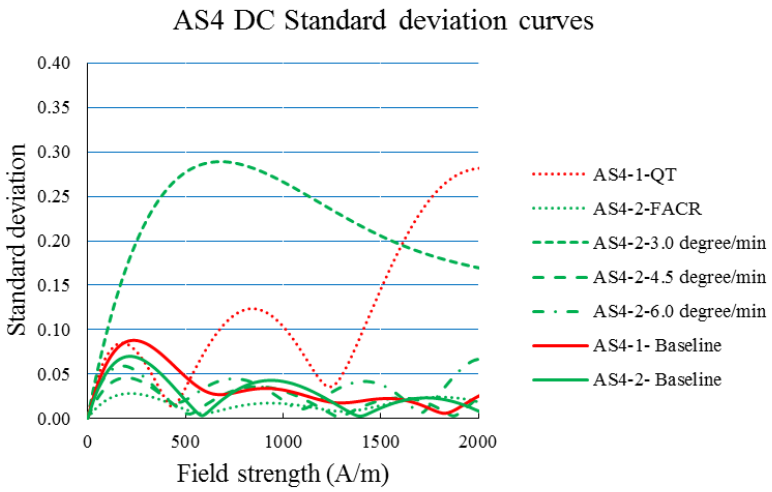


Figure 4-8. The standard deviation of the datasets plotted in Figure 4-7. The smallest deviation occurs at the initial magnetisation and at the knee point that follows the linear section of the magnetisation curve.

In Figure 4-8 the standard deviation of the datasets for sample AS4 is shown the lowest values of deviation occur at the knee points at the start of the magnetisation curve and at the end of the linear section of the magnetisation curve.

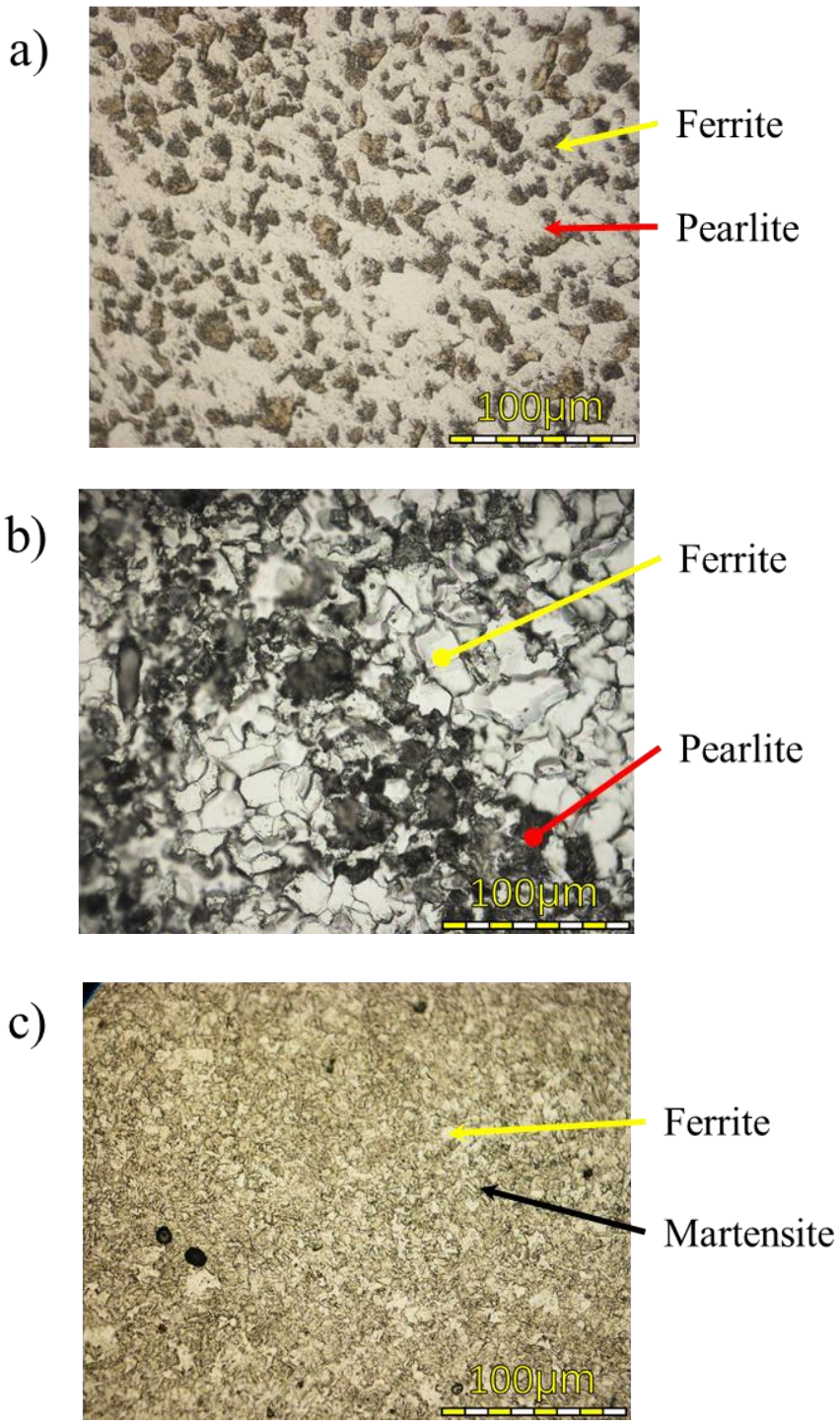


Figure 4-9. (a) image of the ferrite/pearlite microstructure of the normalised A1 grade steel, (b) image of ferrite/pearlite microstructure of the annealed A1 grade steel, (c) image of the ferrite/martensite microstructure of the quenched A1 grade steel.

In Figure 4-9.(a) the microstructure of the normalised structure shows a mixture of fine pearlite and ferrite crystals.

AS4 had the highest B-H curve of all the normalised samples and the presence of fine pearlite not coarse pearlite is the reason for its good performance. Fine pearlite has fewer grain boundaries than coarse pearlite and so results in fewer pinning sites that disrupt magnetic domains. The normalised sample has large distinct crystals that also result in an increase in B-H curve. The presents of cementite inclusions in the ferrite is visible as grey flecks in the ferrite matrix this increases pinning sites so will cause a reduction in magnetic performance.

The annealed sample (Figure 4-9.b) has larger crystals than the normalised sample which produces a higher B-H curve but also has very few cementite flecks in the ferrite further reducing the number of pinning sites and increasing the samples B-H curve. Figure 4-9.(c) has a metastable martensitic structure with small ferrite crystals caused by the tempering process. Martensite is ferromagnetic but due to its stressed condition has a lower B-H curve and saturation magnetisation than ferrite or fine pearlite. The poorer magnetic properties of martensite results in the samples lower B-H curve.

4.2.3.2 Effect of heat treatments on B-H curve of sample AS8

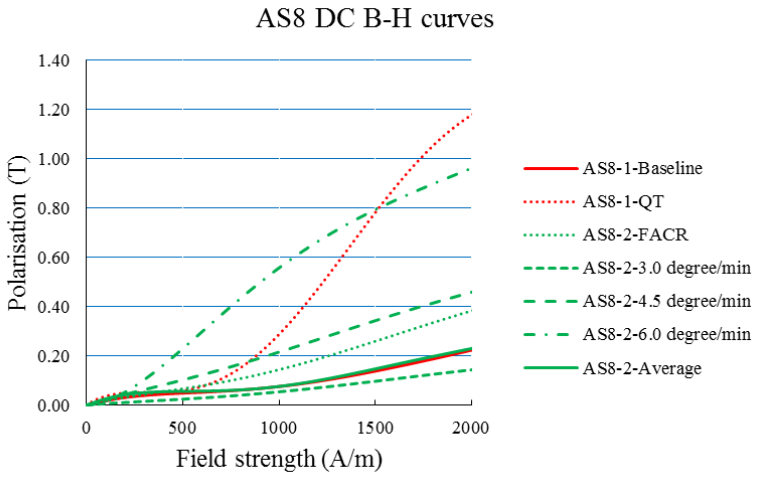


Figure 4-10. The effect of heat treatments on the B-H curve of a sample of P310 grade steel. Up until 1500A/m the annealed at a cooling rate of 6.0°C/min has the highest B-H curve after this point the initial resistance of the quenched samples martensitic structure is overcome and its B-H curve increases sharply. Aside from the 6.0°C/min cooling rate the rest of the annealed samples have very little improvement in there B-H curve.

In Figure 4-10 the effect of heat treatments on the B-H curve of sample AS8 is compared to the normalised sample.

The highest B-H curve is obtained by annealing at a cooling rate of 6.0°C/min until 1500A/m when the quenched samples B-H curve overtakes that of all the annealed samples. Annealing with a cooling rate of 3.0°C/min produces the lowest B-H curve with the remaining annealing cooling rates giving an improved B-H curve when compare to the normalised sample.

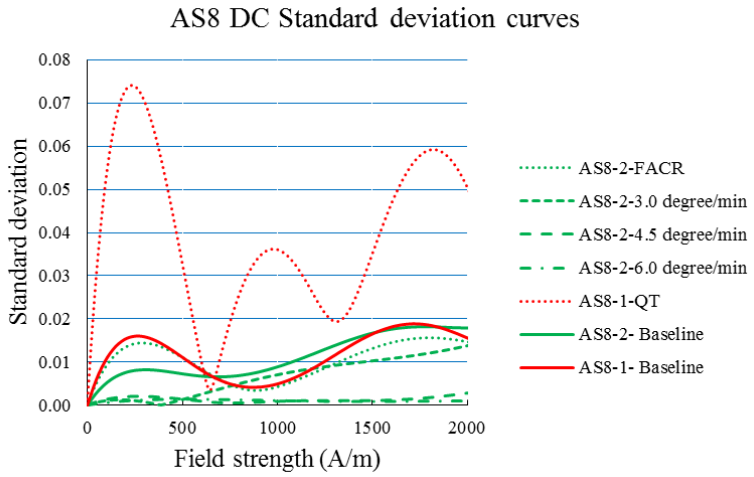


Figure 4-11. The standard deviation of the datasets plotted in Figure 4-10. The smallest deviation occurs at the initial magnetisation and at the knee point that follows the linear section of the magnetisation curve.

In Figure 4-11 the standard deviation of the datasets for sample AS8 is shown the lowest values of deviation occur at the knee points at the start of the magnetisation curve and at the end of the linear section of the magnetisation curve. The dataset with the largest deviation is the quenched sample.

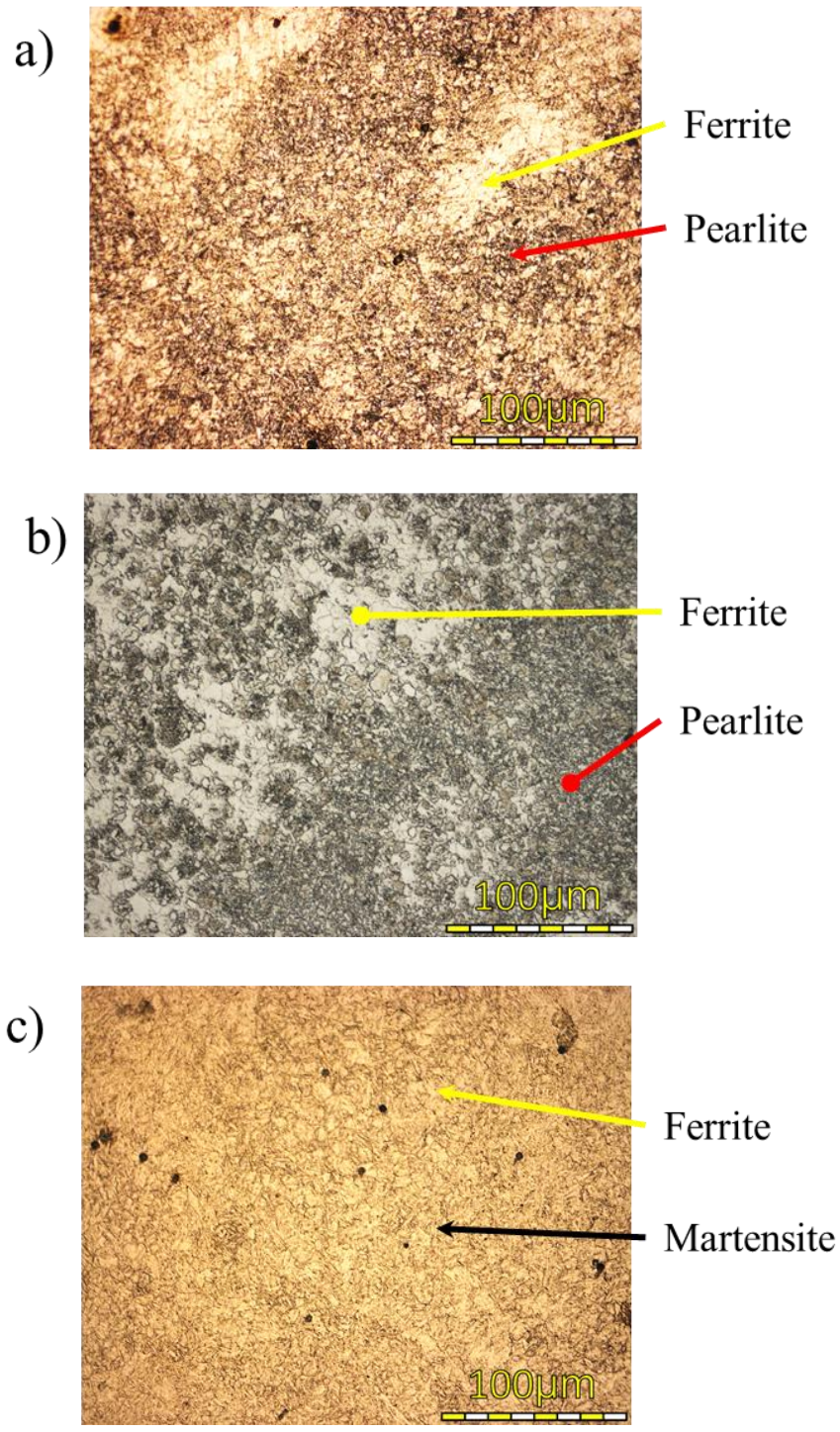


Figure 4-12. (a) Graph of the B-H curve of three heat-treated samples of P310 grade steel, (b) image of the ferrite/pearlite microstructure of the normalised P310 grade steel, (c) image of ferrite/pearlite microstructure of the annealed P310 grade steel, (d) image of the ferrite/martensite microstructure of the quenched P310 grade steel.

Figure 4-12.(a) shows the microstructure of the normalised sample, it predominantly consists of coarse pearlite with small crystals of ferrite. There are patches of light material that are under etched sections of the sample.

The coarse pearlite and small ferrite crystals result in a very low B-H curve and a low saturation magnetisation. Figure 4-12.(b) shows the annealed sample's microstructure. It consists of coarse pearlite with small ferrite crystals. The microstructure has changed very little from the normalised state and this explains why the B-H curve remains low. Annealing at 6.0°C/min had a greater impact on the B-H curve than annealing at FACR or 4.5°C/min. Figure 4-12.(c) shows the microstructure of the quenched sample. The structure is primarily martensite with small ferrite crystals. The removal of any coarse pearlite has left behind only martensite and ferrite crystals, as martensite has better magnetic properties than coarse pearlite, but not fine pearlite, the martensite structure has improved the magnetic properties more than annealing. The better performance of martensite is only visible after the reluctance of the martensite to magnetise is overcome at 1500A/m.

4.2.3.3 Effect of heat treatments on B-H curve of sample AS11

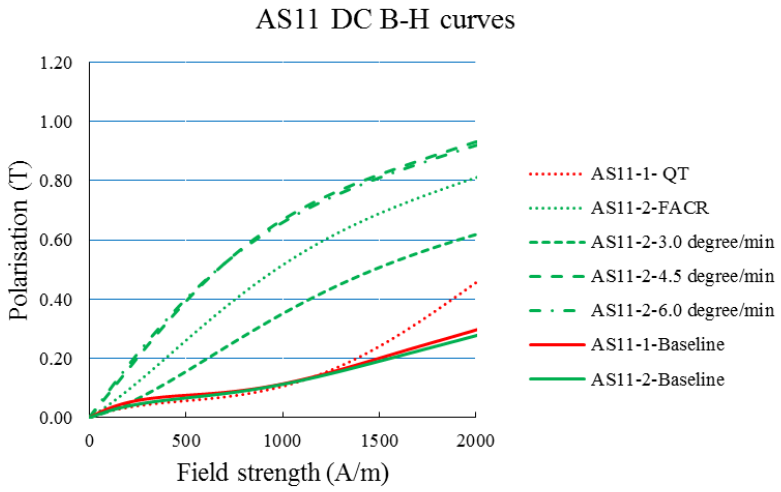


Figure 4-13. The effect of heat treatments on the B-H curve of a sample of Mac 1 grade steel. The best performing heat treatments are the annealing at cooling rates of 6.0°C/min and 4.5°C/min. The quenched sample produces the lowest B-H curve until 1000A/m where the martensitic structures initial resistance to magnetisation is overcome and the normalised sample becomes the lowest B-H curve sample.

In Figure 4-13 the effect of heat treatments on the B-H curve of sample AS11 is compared to the normalised sample. The highest B-H curve is obtained by two annealing heat treatments with a cooling rate of 4.5°C/min and 6.0°C/min. The remaining heat treatments all improved the B-H curve when compared with the normalised sample.

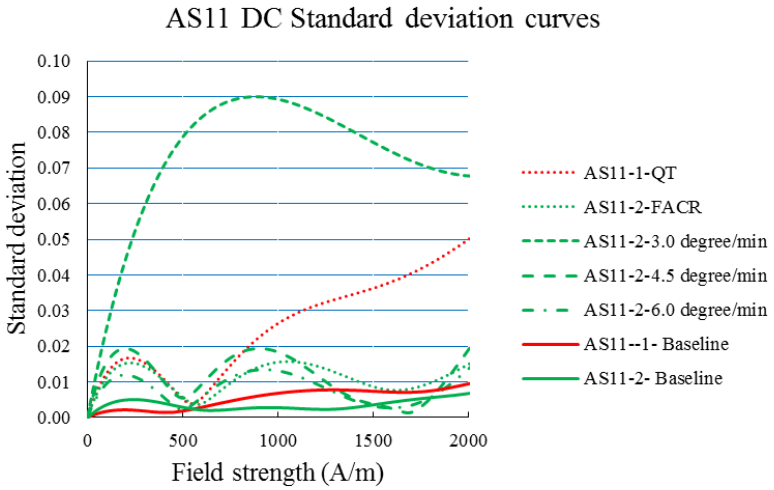


Figure 4-14. The standard deviation of the datasets plotted in Figure 4-13. The smallest deviation occurs at the initial magnetisation and at the knee point that follows the linear section of the magnetisation curve.

In Figure 4-14 the standard deviation of the datasets for sample AS11 is shown the lowest values of deviation occur at the knee points at the start of the magnetisation curve and at the end of the linear section of the magnetisation curve. The dataset with the largest deviation is the annealed at a cooling rate of 3.0 degrees/min.

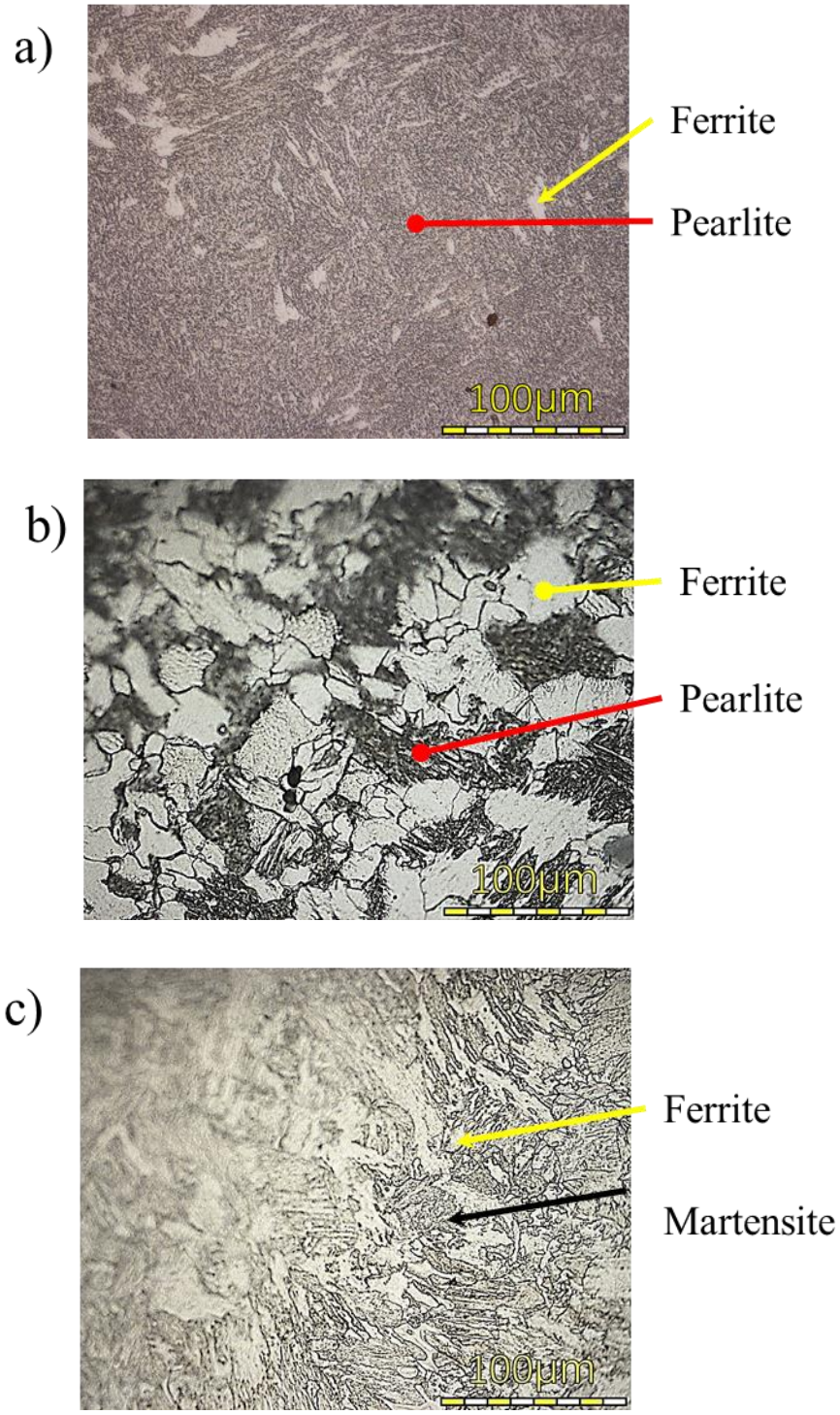


Figure 4-15. (a) image of the ferrite/pearlite microstructure of the normalised Mac1 grade steel, (b) image of ferrite/pearlite microstructure of the annealed Mac1 grade steel, (c) image of the ferrite/martensite microstructure of the quenched Mac1 grade steel.

Figure 4-15.(a) shows the normalised sample's microstructure is predominantly composed of a coarse pearlite with few small ferrite grains

The large amount of coarse pearlite means that there are lots of grain boundaries, and so pinning sites between magnetic domains reducing the B-H curve of the sample. In Figure 4-15.(b) the microstructure of the annealed sample is composed of equal amounts of fine pearlite and ferrite. The change from coarse pearlite in Figure 4-15.(a) to fine pearlite in Figure 4-15.(b) is the result of the slowing cooling annealing provides. The clear separation between ferrite and pearlite in the annealed sample when comparing the normalised sample's course pearlite results in an increased B-H curve. The larger crystal sizes of the pearlite and ferrite in the annealed sample also leads to an increase in B-H curve of the sample. Figure 4-15.(c) shows the microstructure of the quenched sample, it consists of martensite and ferrite with a greater proportion of martensite. The large crystal size and clear separation of the quenched steel phases result in a B-H curve that is higher than the normalised sample but lower than the annealed sample.

4.2.4 Comparison of B-H curve at 0.5 tesla

An electrical steel manufacturer gives the B-H curve of their product at a set polarisation (in tesla) and a given frequency (50 or 60Hz). As these steels are not going to be used for an AC components the frequency component is not relevant however the use of a standard polarisation would allow for an easier comparison of the steel's performance. As the majority of the steel samples do not have a B-H curve that goes below 0.5 tesla this will be used as the comparison point for the performance of the cast steel samples.

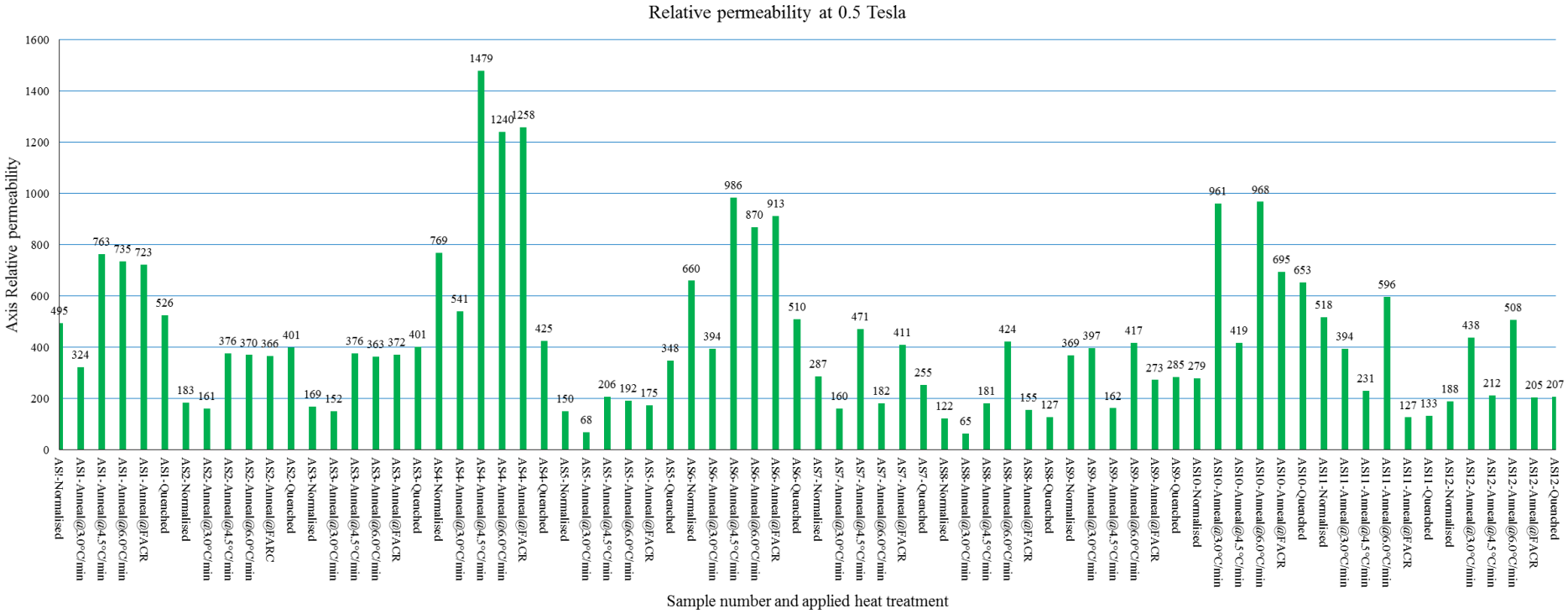


Figure 4-16. Chart showing the twelve cast steels permeabilities before heat treatments and with heat treatments.

In Figure 4-16 the μ_r values are shown for the twelve cast steel samples with the effect of heat treatments also shown. Sample AS4 had the highest μ_r in the normalised state and had the highest μ_r achieved by annealing at a cooling rate of 4.5°C/min. None of the other samples achieved a μ_r of over 1000. The best steel from which to cast the rotor was found to be AS4 which is grade A1 to BS3100:1991.

Table 4-2. Relative permeability of normalised (Norm) verses annealed cast steel (with different cooling rates) tested at 0.5 Tesla

Sample number	Normalized	3.0°c/min	% diff 3.0°c/min*	4.5°c/min	% diff 4.5°c/min*	6.0°c/min	% diff 6.0°c/min*	6.3°c/min	% diff 6.3°c/min*	Heat treatment with greatest effect
AS1	495	324	-35%	763	54%	735	48%	723	46%	4.5°c/min
AS2	184	161	-12%	376	104%	370	101%	366	99%	4.5°c/min
AS3	169	152	-10%	376	122%	363	115%	372	120%	4.5°c/min
AS4	776	541	-30%	1479	90%	1240	60%	1258	62%	4.5°c/min
AS5	151	68	-55%	206	36%	192	27%	175	16%	4.5°c/min
AS6	666	394	-41%	986	48%	870	31%	913	37%	4.5°c/min
AS7	284	160	-44%	471	66%	182	-36%	411	44%	4.5°c/min
AS8	121	65	-46%	181	50%	203	68%	155	28%	6.0°c/min
AS9	279	162	-42%	417	49%	419	50%	397	42%	6.0°c/min
AS10	688	419	-39%	968	41%	973	42%	961	40%	6.0°c/min
AS11	135	231	71%	596	343%	609	352%	394	192%	6.0°c/min
AS12	208	212	2%	508	144%	443	113%	438	110%	4.5°c/min

* % difference between heat treated relative permeability and baseline relative permeability

In

Table 4-2 the increase/decrease in relative permeability due to the different cooling rates is shown at 0.5T. Annealing at 4.5°C/min improves all of the samples relative permeability in the case of AS11 by 343%, however when the permeability in the normalised condition is so low the improvement in permeability is still very low. Samples AS8, AS9, AS10, and AS11 obtained large increases in permeability from the cooling rate of 6.0°C/min.

Table 4-3. B-H curve of normalised (Norm) verses quenched (then tempered) cast steel tested at 0.5 Tesla

Sample number	μ_r	Quenched	% diff*
AS1	494	526	6%
AS2	181	401	121%
AS3	171	401	134%
AS4	794	425	-46%
AS5	151	348	130%
AS6	643	510	-21%
AS7	290	255	-12%
AS8	127	325	155%
AS9	285	279	-2%
AS10	653	518	-21%
AS11	133	188	41%
AS12	207	407	96%

* % difference between heat treatment permeability and baseline permeability

In

Table 4-3 the increase/decrease in permeability due to quenching then tempering is shown at 0.5T. None of the quenched samples has a permeability that is close to the best performing annealed samples.

4.2.4.1 Discussion on cause and effect of heat treatments

From the previous graphs it is possible to see which material has the highest baseline (normalised) B-H curve and which has the best response to an applied heat treatment. The best ferromagnetic crystal type is ferrite followed by fine pearlite then martensite and the worse performing crystal type is coarse pearlite. The optical images of the samples shown in Section 4.2.3 and Appendix A show that the annealing heat treatments improve the magnetic properties of the steels in two ways, the first is to allow more time for larger crystal grains to grow (with fewer cementite inclusions), and the second is changing coarse pearlite into fine pearlite. The change in crystal size happens at the same time as the pearlite changes from coarse to fine, although the worst preforming annealing cooling rate was 3.0°C/min which allowed for the largest crystal grain growth. The fact that the 3.0°C/min annealing cooling rate made the magnetic performance of many of the samples worse indicates that it was the change of the coarse pearlite to fine that had the biggest effect on magnetic performance improvement. The larger crystal sizes promoted by the 3.0°C/min cooling rate made the crystal too large and resistant to magnetisation. This is a common phenomenon in the production of electrical steels [49] where the cooling rate for the steel must be

carefully controlled [140] to prevent large crystals which decrease the B-H curve of the finished steel. The fact that martensite has a better magnetic performance than coarse pearlite is the reason some of the steel samples had a better performance when quenched than annealed (samples AS2, AS3, AS5, and AS8). These steels are supplied in the quenched then tempered condition so the additives put into the steel optimise the performance of that heat treatment process. When quenched the austenitic delta iron microstructure transitioned directly into martensite so no coarse pearlite was formed this resulted in samples with a mix of martensite and ferrite (from the tempering process). Martensite resists magnetisation more than coarse pearlite but once this resistance is overcome it magnetise more rapidly resulting in a higher permeability.

The main factor in deciding how good the samples are magnetically is how the microstructure forms during cooling. The amount of C is important but for hypoeutectoid steel where the C is located has a greater impact on the magnetic performance. As many of the elements added to the steels effect the microstructure formation they alter where the C is located. Heat treatments allow further modification of the C location but as some of the steels are optimised for different heat treatments the heat treatments effect on each steels microstructure is not uniform so a heat treatment that improves one steels magnetic performance has a negative impact on another's. Steels that have been designed to be supplied quenched then tempered perform better magnetically in that condition but as the microstructure is martensitic they will not be able to perform as well as steels optimised for annealing which have a ferrite and fine pearlite composition.

Of all the samples tested AS4 has the highest values for permeability in both a normalised state and in an annealed state, at a cooling rate of 4.5°C/min. The AS4 sample is comprised of A1 grade steel and the casting of a salient pole rotor was carried out with this material.

4.3 Conclusions

In this chapter a range of cast steels was selected, based on their availability from the foundry that will produce the prototype cast steel rotor. The range of steels were tested for their magnetic properties and then subjected to commonly

applied treatments to determine to what extent heat treatments can be used to improve magnetic performance. The grade of steel selected for production of a prototype was A1 grade steel, this grade of steel can have its magnetic performance increased by the application of an annealing heat treatment with the cooling rate of 4.5°C/min. The prototype will not have this heat treatment applied as the cost for the heat treatment of a single part, with this degree of control on cooling rates adds too much additional cost to the production of the prototype. The application of this heat treatment would be more practical if the prototype goes into batch production.

There is no clear correlation between carbon content of composition of alloying elements that give a clear method to determine the best performing cast steel. Without finding a correlation it is not possible to predict what composition of cast steel will produce the largest B-H curve. The impurity content of a cast steel is known to have a strong impact on the magnetic performance of steel however the data collected in this chapter shows that the impurity content alone is not the determining factor on magnetic performance.

5 Prototype rotor design and testing

5.1 Introduction

The literature review identified a lack of meaningful contributions relating to solid rotors. Consequently there are no comparisons of the magnetic properties of a laminated rotor verses a solid rotor on which to base further development work. In the introduction a model was selected from the CGT portfolio to carry out the development work. This chapter focuses on the design, production, and testing of a solid rotor for the HC1444C generator.

5.1.1 Design concepts

The following section describes the iterative design process. After each design iteration a review of the design concept is undertaken to determine strengths and weaknesses of the design, which then fed into the succeeding design concept.

5.1.1.1 First design concept

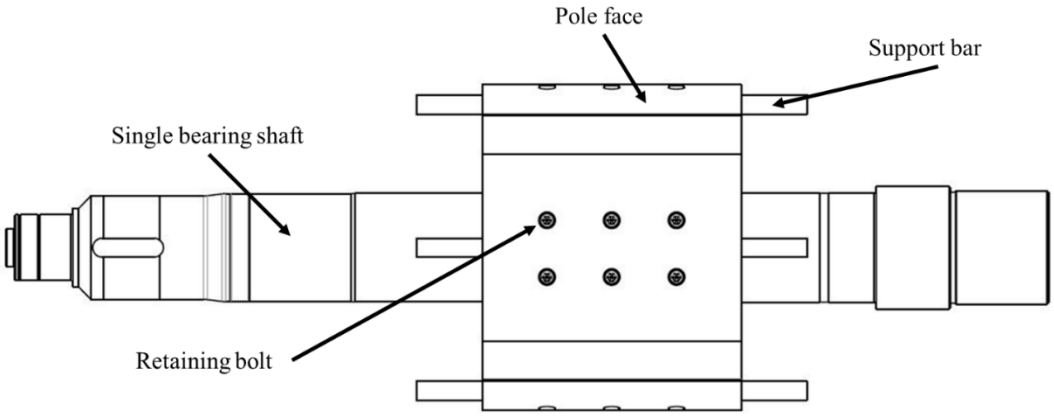


Figure 5-1. First concept design for a cast rotor with removable pole shoes.

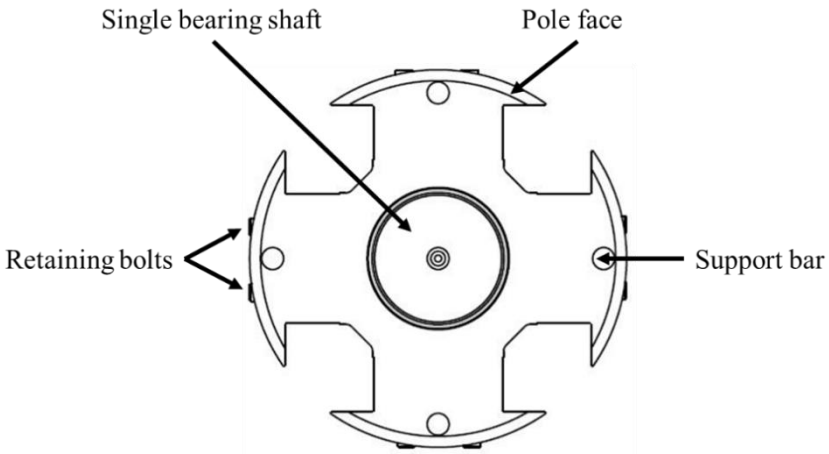


Figure 5-2. First concept view of the core pack with removable pole shoes bolted into place.

In Figure 5-1 the first concept design for casting as one piece with machining to the final dimensions is shown. The support bars which had previously been separate rods of steel pressed into the core pack to provide rigidity, are produced during the casting in this design. The pole faces have each had 10mm removed from their circumference, making a total of 20mmm reduction in the diameter of the core pack, shown in Figure 5-2. This enables soft magnetic materials to be placed over the cast pole faces to determine the effect on the performance of the prototype rotor of different soft magnetic materials.

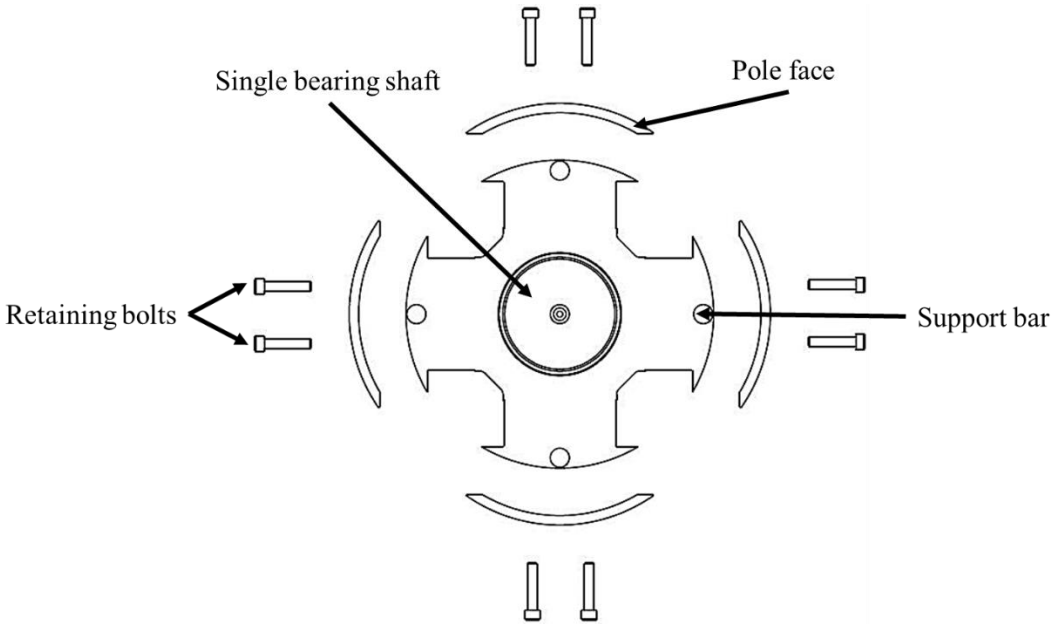


Figure 5-3. Exploded view of first design concept of the core pack. The separate pole faces allow the use of different magnetic materials to be used to block inducted eddy currents from the rotor.

The surface of each pole face has six M10 holes drilled and tapped to provide a method of securing the pole face pieces to the pole body. Figure 5-3 shows an exploded view of the rotor core, the removable pole faces, and pole face retention bolts.

The retaining bolts are M10-1.25Px50mm socket headed bolts, the heads have a thickness of 10mm so cannot be countersunk at the same angle as the radius of the removable pole shoe as the pole face is only 10mm thick.

A review of the strengths and weakness of this design concept was undertaken to determine the suitability of the concept for the production of a prototype.

Strengths:

- The 10mm thick removable pole faces allows the use of many different compositions of alloys that are readily available in sheet form
- The use of sheet material provides a surface finish that is superior to the current rotors pole faces
- Using retaining bolts to fix the pole faces in place allows easy assembly and disassembly of the prototype
- Producing the support bars during casting reduces the number of sub-components in the rotor

Weaknesses:

- Due to the thickness of the pole faces the retaining bolts are proud of the pole faces, risking the bolt catching the inner surface of the stator during operation
- The machining operation to finish the support bars to net shape is very difficult to carry out
- The overhang on the cast section of the pole shoe means that the windings can only be tumble wound directly onto the rotor.

5.1.1.2 Second design concept

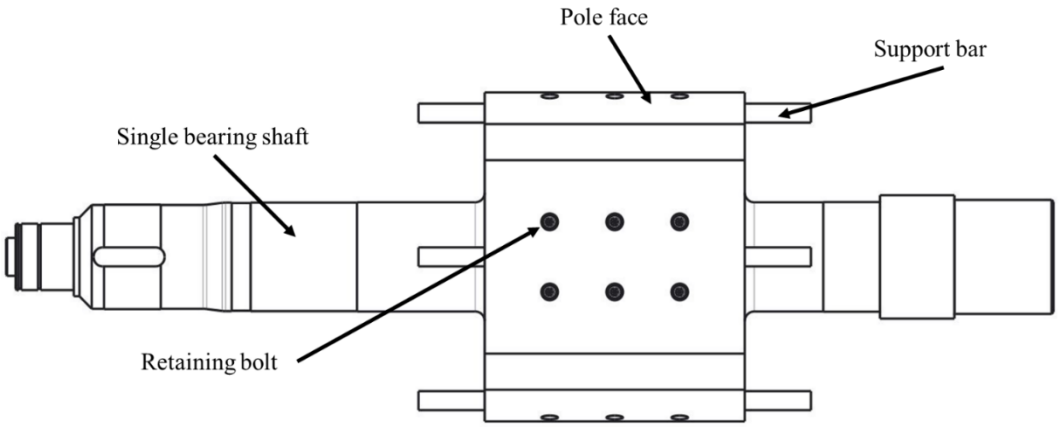


Figure 5-4. Second concept design for a cast rotor with removable pole shoes.

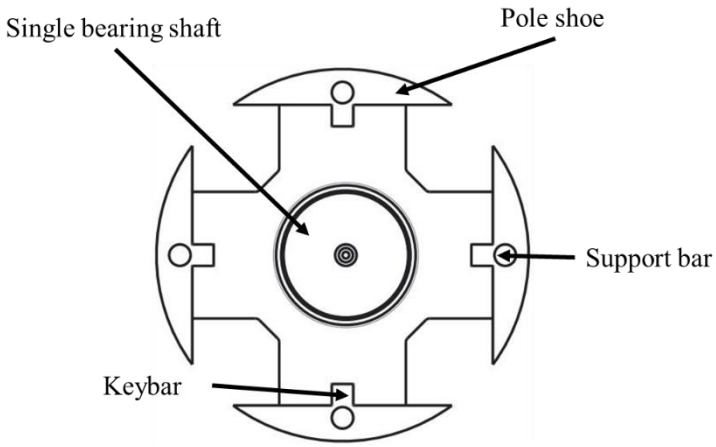


Figure 5-5. Second design concept of the core pack with removable pole shoes bolted into place.

In Figure 5-4 the second design concept is shown. Unlike the first design concept the second has poles that can be completely removed. The removed pole faces are now termed pole shoes as they are distinct from the main body of the rotor.

This allows the production of the rotor to be simplified as the radius of the cast pole faces has been removed. The surface finish of the interface between the pole shoes and the cast rotor can be reduced from a N5 finish to a N11. As in the first iteration (Figure 5-2) the pole shoes are bolted onto the main body of the rotor with M10 bolts. To facilitate a strong join and good positioning of the pole shoe a keyway has been added to the pole body of the main rotor, this was added to help reduce the shear loading experienced by the bolts by reducing the effects of centrifugal force on the pole shoe.

In Figure 5-5 the cross-section of the core pack is shown, the total removal of the pole faces is evident. To reduce the complex machining required for the cast support bars in the first design concept the support bars for the second concept are produced separately. The support bars are made from bright drawn mild steel (EN19 grade) that have a M10 thread machined into the bar. The pole shoes have M10 threaded holes machined into them allowing the support bars to be screwed directly into the pole shoes as shown, in Figure 5-6.

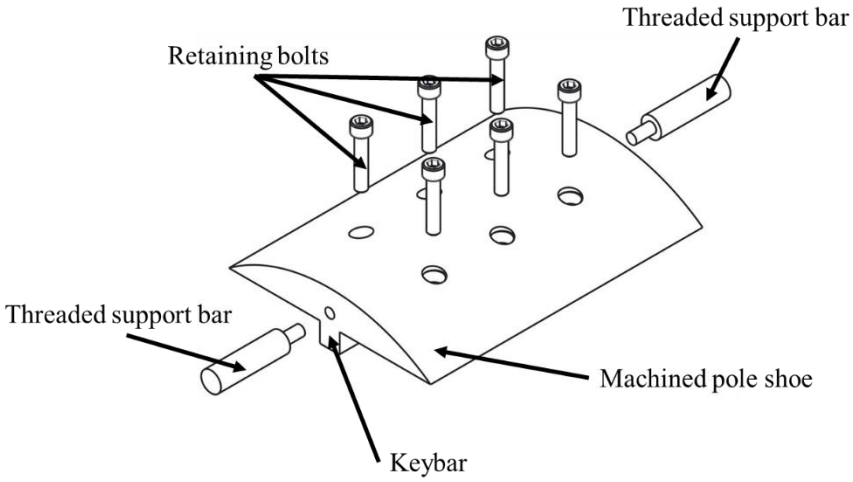


Figure 5-6. Second design concept for removable pole shoes with removable support bars.

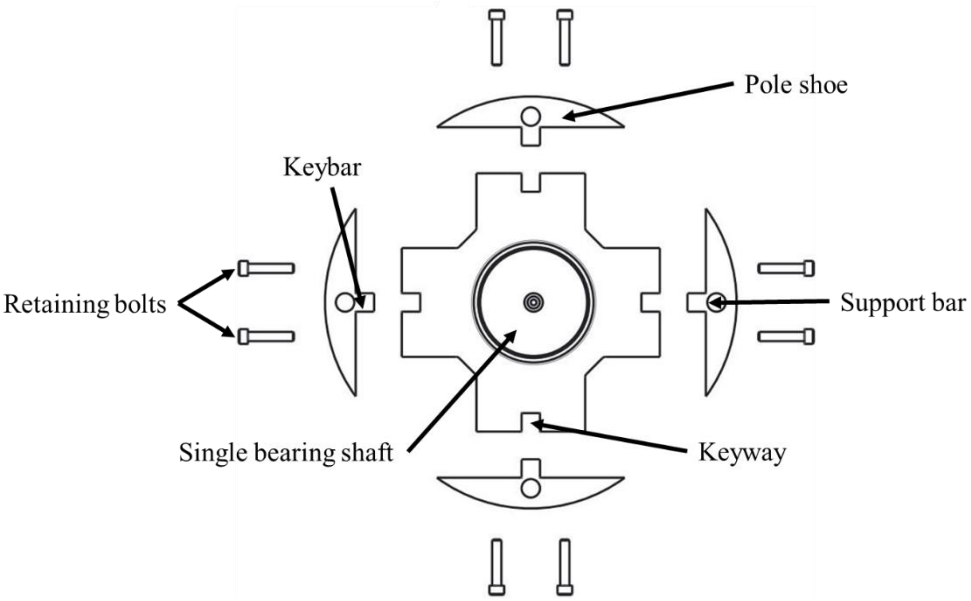


Figure 5-7. Exploded view of second design concept.

In Figure 5-7 an exploded view of the second design concept is shown, the removal of the radii of the cast section of the pole shoe simplifies the machining of the cast rotor but increases the complexity of machining the pole shoe itself.

The machining of the pole shoe out of billet material transfers the difficult radii onto a separate workpiece from the cast rotor. The machined radii requires grinding to a N5 finish.

A review of the strengths and weakness of this second design concept was undertaken to determine the suitability of the concept for the production of a prototype.

Strengths:

- Removable support bars reduce the machining complexity of the cast rotor
- The pole shoe keyways allow accurate location of the pole shoe onto the rotor
- Using retaining bolts to fix the pole faces in place allows easy assembly and disassembly of the prototype
- Field windings can be produced separately and fitted to the rotor.
- The surface finishes of joining surface of the cast rotor and the machine pole shoe can be reduced to N11

Weaknesses:

- The production of the pole shoes out of billet increases the amount of machining required for the pole shoes, when compared to the first design concept
- If a billet which matches the width, height, and depth of the pole shoe is machined into the pole shoes, 54% of the billet would be scrap.
- The centrifugal forces on the pole shoes act perpendicular to the rotation of the rotor, this means that the keyway bar will have little effect in reducing the stresses on the pole shoe retention bolts

5.1.1.3 Third design concept

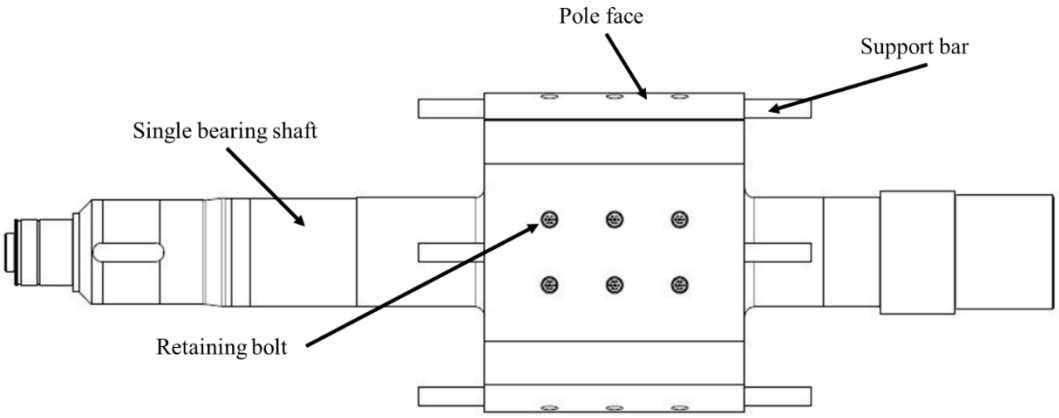


Figure 5-8. Third concept design for a cast rotor with removable pole shoes.

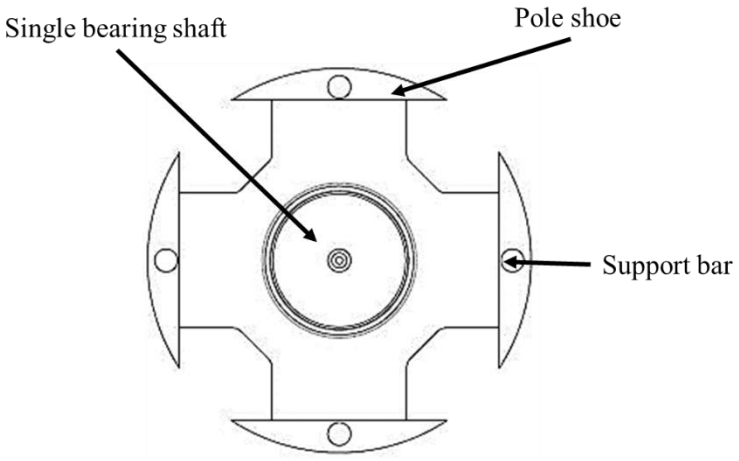


Figure 5-9. Third design concept of the core pack with removable pole shoes bolted into place.

In Figure 5-8 the third design concept is shown. In Figure 5-9 the keybar has been removed from the pole shoes. Figure 5-9 also shows the removal of the keyway in the cast rotor, which results in a reduction in the amount of machining required on the rotor body.

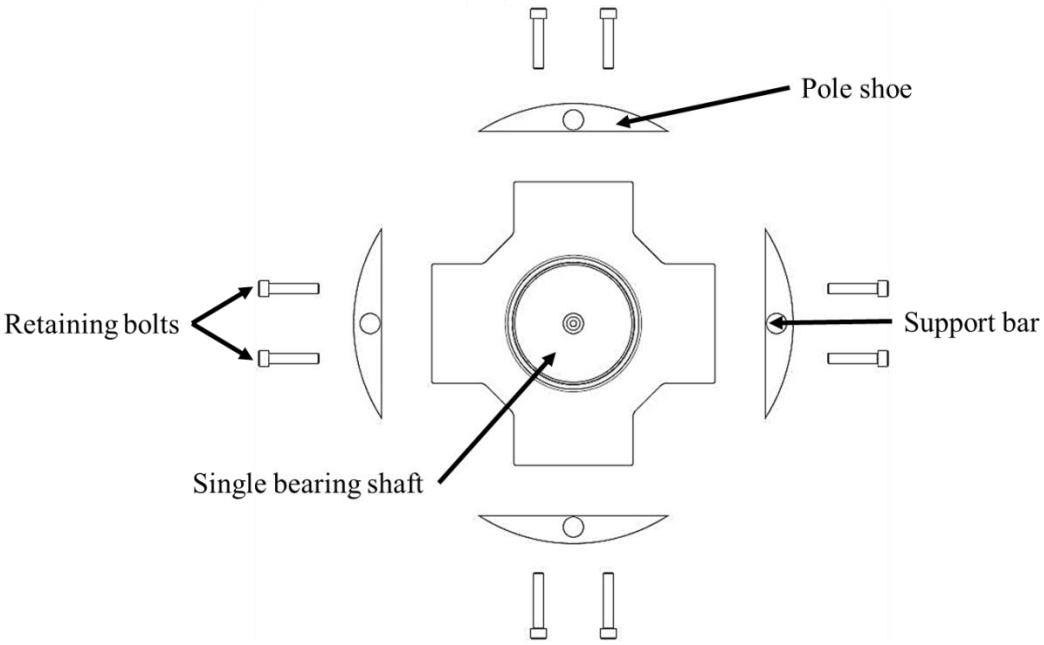


Figure 5-10. Exploded view of third design concept.

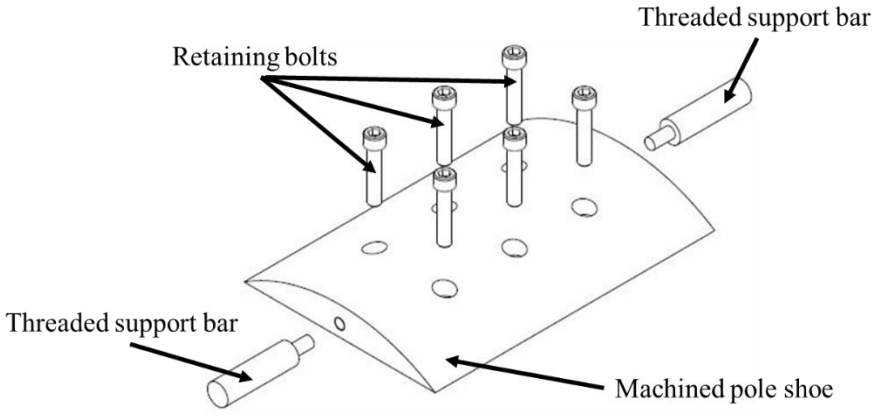


Figure 5-11. Third design concept for removable pole shoes with removable support bars.

Figure 5-10 shows an exploded view of the core pack showing how the removable pole shoes are bolted onto the cast rotor. The keybar, which was on the bottom of the removable pole shoes in the second design concept (Figure 5-7) has been removed. This results in a thinner billet of raw material being needed to produce the pole shoe.

A review of the strengths and weakness of this third design concept was undertaken to determine the suitability of the concept for the production of a prototype.

Strengths:

- No keyway or keybar is required in the cast rotor and pole shoe reducing machining required
- If a billet which matches the width, height, and depth of the pole shoe is machined into the pole shoes 34% of the billet would be scrap, compared to 54% for the second design concept
- Using retaining bolts to fix the pole faces in place allows easy assembly and disassembly of the prototype
- Field windings can be produced separately and fitted to the rotor.
- The surface finishes of joining surface of the cast rotor and the machine pole shoe can be reduced to N11

Weaknesses:

- The production of the pole shoes out of billet increases the amount of machining required for the pole shoes, when compared to the first design concept

5.1.1.4 Discussion of design concepts

By transferring the key dimensions from the original rotor to the design concepts for a prototype cast rotor any testing results for the cast rotor are comparable with the standard rotor. The dimensions of the standard rotor have been optimised over the previous 30 years to improve the performance of the rotor in parallel with optimising the production process. The aim of the cast rotor is to give a baseline performance that can be optimised through iterative development to match the performance of the standard rotor. Once a solid rotor that can match the current rotor in terms of performance has been proven the design of the solid rotor can be optimised to take advantage of the flexibility the new production method provides. By the third iteration most of the weaknesses in the prototype had been addressed so the third concept will be used as the design for the cast steel prototype.

5.1.2 Cast rotor production

The third design concept was sent to CGT for their approval. Cummins Generator Technologies approved the design with one condition. CGT wanted to change the shaft design from a single bearing shaft to a two bearing model, this would make testing of the prototype simpler for CGT to carry out.

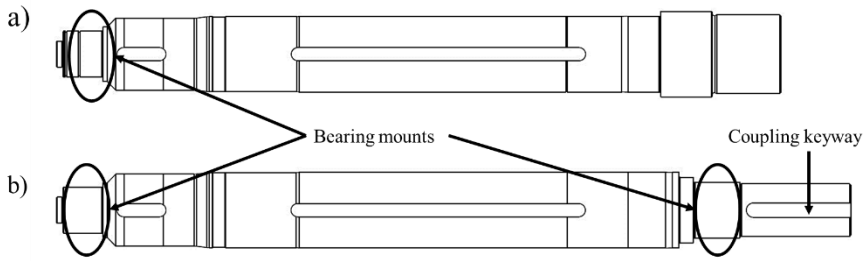


Figure 5-12. An image comparing a) the original single bearing shaft b) the new two bearing shaft.

In Figure 5-12 the original shaft is compared to the new shaft required by CGT. The new shaft is slightly longer than the original, and has an additional keyway to allow better coupling of the rotor shaft to the prime mover. At this stage the overall design had been approved by CGT so the stresses on the retaining bolts that hold the pole shoes in place and the stresses on the support bars were calculated to make sure the correct thread size and bolt type were selected. The calculations for the thread strengths can be found in Appendix B.

In Figure 3-16 the positions of the four RTDs is shown in position on one of the four poles shoes. The positioning of the RTD followed CGT standard positioning methodology to obtain a complete picture of the heating of the pole shoes and the windings. As the performance of the prototype was unknown the output power was increased in stages, at a power factor of 0.8. The temperature of the rotor was monitored to ensure that the rotor did not overheat and melt the insulation of the field windings. The standard rotor has a temperature rise of 100°C when at full load, so if at start up the generator had an ambient temperature of 21°C it would rise to 121°C during operation.

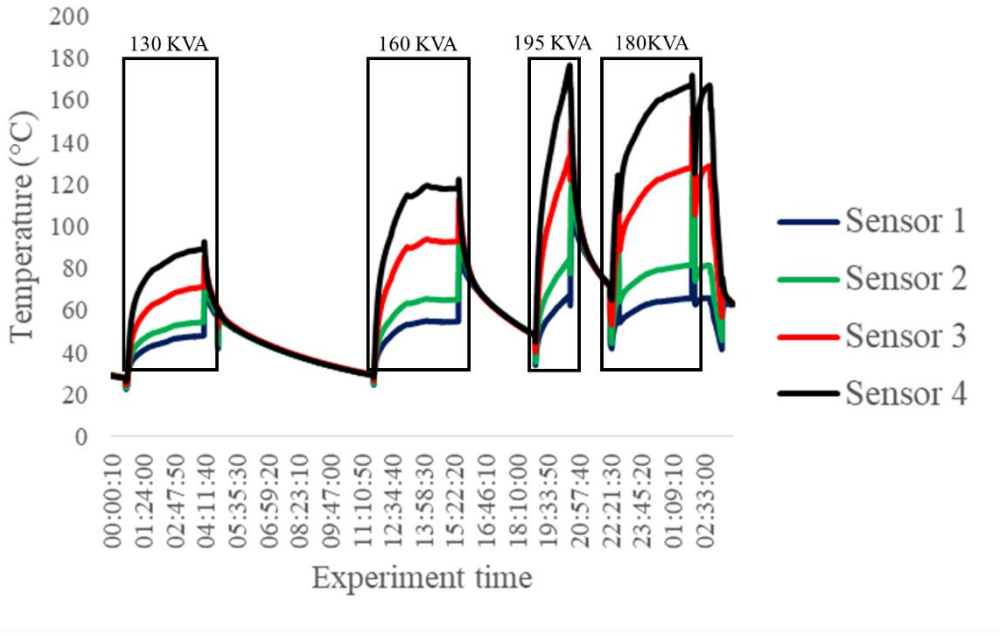


Figure 5-13. Outputs of resistance temperature detectors (RTD) attached to four locations on the prototype rotor. Sensor 4 is between the two sets of Cu windings so is the hottest place on the rotor. Sensor 3 is one the second first set of windings so is the second hottest. Sensor 2 is on the underside of the pole shoe midway along its length. Sensor 1 is on the edge of the pole shoe on its profile edge.

In Figure 5-13 the absolute temperature of the prototype rotor is shown as the output power of the generator is increased from 130kVA to 195kVA. At 195kVA the temperature on sensor 4 increased to levels where the insulation of the field windings is at risk of failure. As the temperature rise failed to stabilise the test was stopped due to the risks of damaging the prototype.

At this point in testing the output power was reduced to 180kVA and the testing of the prototype was restricted to 180kVA only.

5.2 Performance of standard and prototype rotor

As stated in Section 3.2.4.1 the results obtained from the Stamford test centre were supplied with all data processing carried out before the result were released to the author. The commercial sensitivity of the Stamford test centre means that the data should be regarded as a black box with error, and calibration methods already carried out.

5.2.1 On-load characteristics

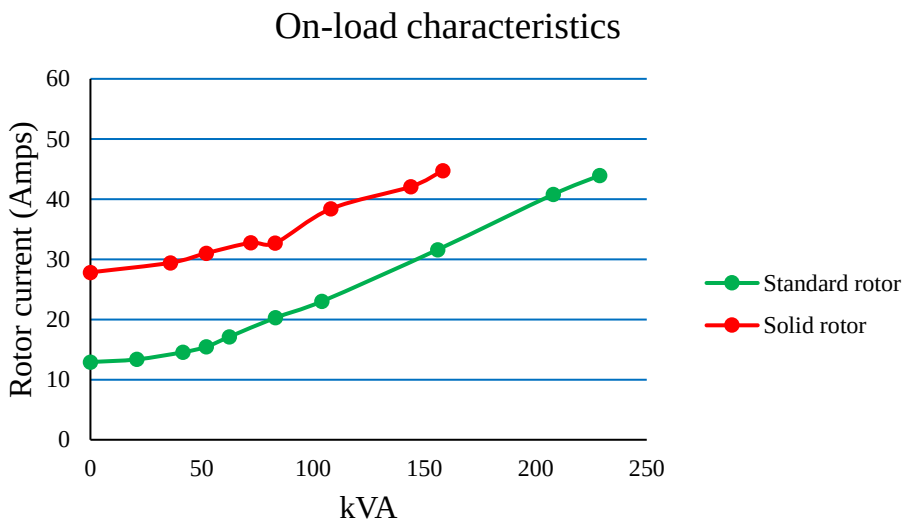


Figure 5-14. The current supplied to the rotor plotted against the output power of the generator. The smooth slope of the standard rotor (in green) shows that the iron of the rotor is not saturated at any point. The slope of the prototype (in red) has a distinct trough where the pole shoes saturate.

In Figure 5-14 the current supplied to the rotor windings is shown plotted against the output kVA. The starting rotor current for the solid rotor is 20 amps higher than for the standard rotor this is due the reluctance of the cast steel to magnetisation requiring a stronger applied magnetic field to produce the same output KVA as the standard rotor. The prototype rotor maintains its requirement for a higher rotor current throughout the test. The standard rotor has a smooth slope as the electrical steel of the core pack is not at saturation so the magnetisation of the rotor is on the linear slope of the magnetisation curve (Figure 3-7). The slope of the prototype shows two distinct stages; the first from 0-72kVA then a trough and a second steeper slope from 83-144kVA. It is clear that the first stage of the prototype's magnetisation (0-72kVA) is dominated by the magnetisation of the Invar 36 pole shoes, therefore it can be stated that from 0-72kVA the slope is due to the pole shoes, which then saturate at 72kVA. After the 72kVA point there is a trough in the slope as the air gap between the rotor and the stator changes from 2mm to 34.5mm. The pole shoes are still supplying the magnetisation up to the 72kVA point but beyond this the current has to rise sharply to increase the magnetic flux over an apparent airgap of 34.5mm.

As the current increases to bridge the apparent airgap the steel of the rotor saturates far more rapidly than if the pole shoe was in an unsaturated state.

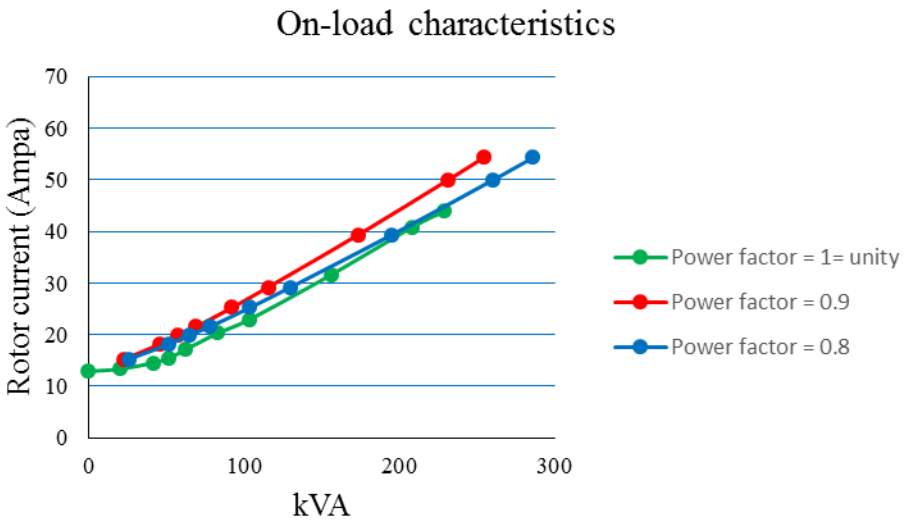


Figure 5-15. The current supplied to the standard rotor plotted against the output power of the generator. The three different power factors are shown with the increase in current required as the power factor moves further from unity.

In Figure 5-15 the amount of current required to magnetise the rotor to produce the desired generator output (kVA) in shown. The current is required to increase as the power factor moves further from unity. The slope of the line of best fit remains the same for each power factor indicating that even with a power factor of 0.8 the core material of the rotor is not saturated.

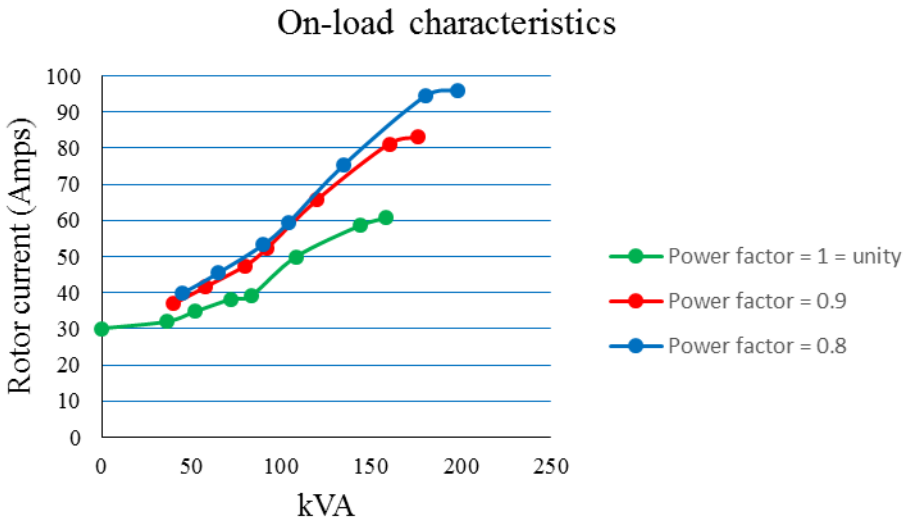


Figure 5-16. The current supplied to the prototype rotor plotted against the output power of the generator. The three different power factors are shown with the increase in current required as the power factor moves further from unity.

In Figure 5-16 the current supplied to the prototype rotor windings plotted against the generators output current is shown. As the power factor decreases the current to the rotor windings increases. The plot of unity demonstrates two distinct stages are less noticeable at 0.9 and 0.8 power factor plots but are being masked by the already higher applied current to the rotor windings.

5.2.1.1 Discussion of the on-load characteristics

The results for the testing of the prototype show that the rotor's pole shoes saturate magnetically earlier than the steel of the main rotor body. At this stage no further on-load testing was carried out at the CGT test centre.

Transients are instantaneous changes in the load applied to the output of the generator. These instantaneous changes in applied load cause the rotor to slow. As the rotor must operate at 1500rpm to produce a 50Hz output the prime mover is forced to increase the torque on the rotor shaft to maintain the rotor's speed. This is a mechanical change in response to a nearly instantaneous electrical change, and it takes fractions of a second for the prime mover to increase the torque. In these fractions of a second the pole shoes of the rotor have large instantaneous currents induced into them.

The saturation of the pole shoes at 72kW shows that no eddy currents can be induced in the saturate poles shoes after this point. The concept of using poles shoes which have a lower saturation than the main body of the rotor is shown to have value however the Invar 36 has saturated too early to allow demonstration of the reduced heating empirically.

5.2.2 Open circuit characteristics (OCC)

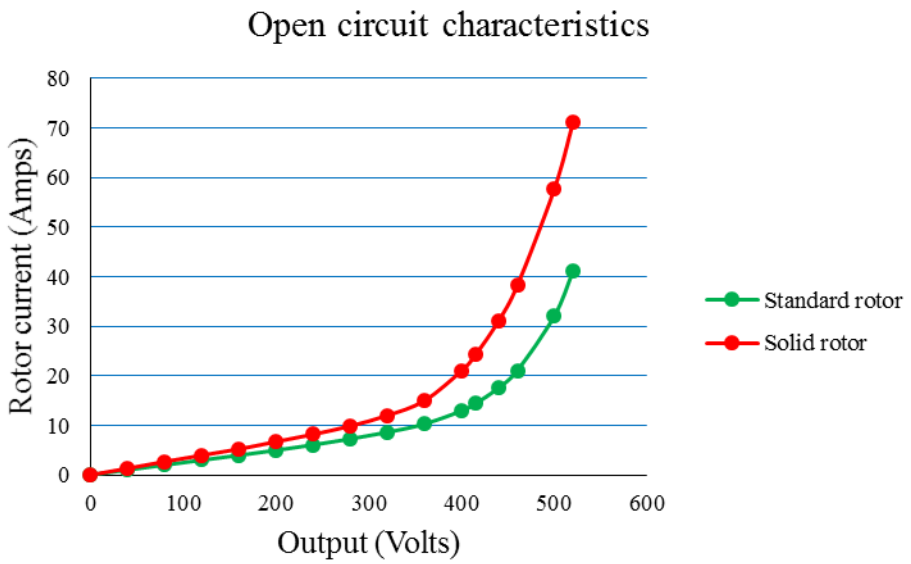


Figure 5-17. The current supplied to the rotor and the resultant voltage generated in the stator of the standard rotor (in green) and the prototype (in red).

In Figure 5-17 a graph plotting the current, which produces the electromagnetic field for the rotor, against the output voltage of the generator is shown. As the output voltage increases from zero to 320 volts the difference between the standard and prototype rotors current is stable. After the output voltage passes 320 volts the difference between the currents increases sharply.

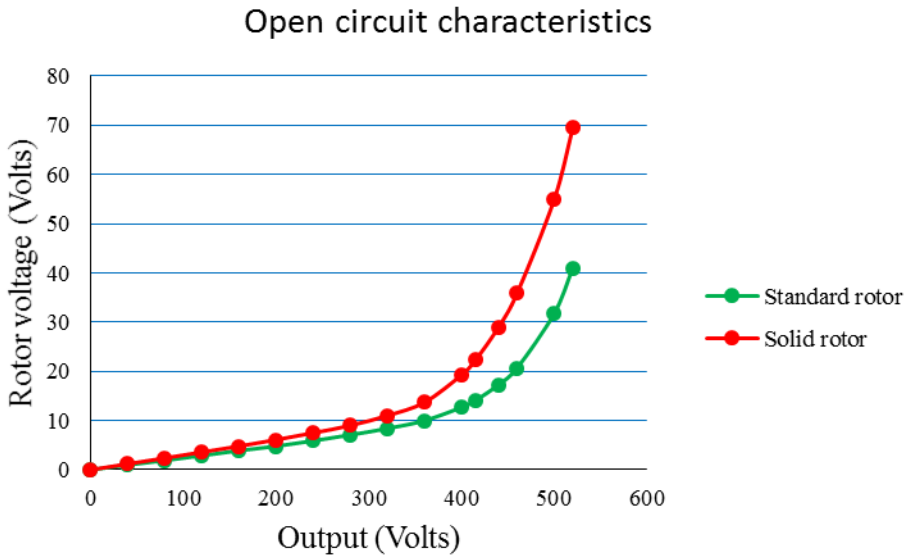


Figure 5-18. The voltage supplied to the rotor and the resultant voltage generated in the stator in the standard rotor (in green) and the prototype (in red).

In Figure 5-18 a graph plotting the voltage, which produces the electromagnetic field for the rotor, against the output voltage of the generator is shown. The difference between the voltages stays stable until the output voltage increases to 320 volts after which the voltage required to increase the output voltages increases sharply.

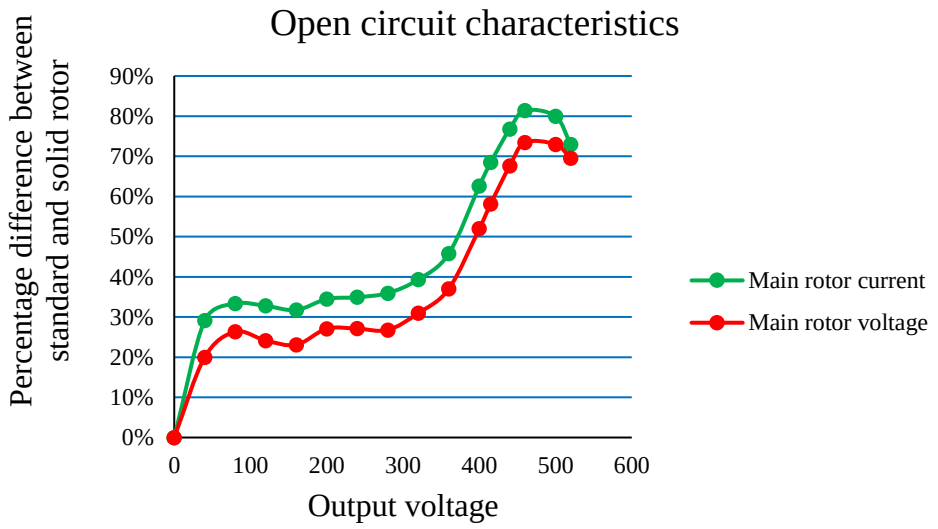


Figure 5-19. The percentage increase of the rotor current (in green) and voltage (in red) between the standard rotor and the solid rotor.

In Figure 5-19 the percentage increase between the standard and prototype rotor's currents and voltages is shown. The increase in current and voltage required for the prototype to match the output power of the standard rotor stays within 30-40% for the current and 20-30% for the voltage until the output voltage reaches 320 volts, after 320 volts both the voltage and the current differences increase in a linear manner until 440 volts output where the percentage differences between the currents is 80% and the voltages 70%. At this point the rotor core is saturated so no increase in output is obtained by increasing the rotor current and voltage. This graph shows the point at which the pole shoes saturate, from 320 volts onwards the current and voltage have to increase at a much sharper rate to compensate for the increase in the apparent airgap. It also shows the point at which the rotor core material saturates, it should be noted that the core material saturates earlier than it should as the field strength has to increase to cross the apparent air gap created by the saturated pole shoes.

5.2.2.1 Discussion of the open circuit characteristics

Figure 5-17, Figure 5-18, and Figure 5-19 show that the differences between standard and prototype current and voltage increase sharply as the output voltage reaches 320 volts. The sharp rise in current and voltages can be explained by the pole shoes reaching magnetic saturation. The aim of the prototype is to show that by careful selection of pole shoe material this saturation point can be manipulated to saturate at the operating magnetisation of the rotor.

5.2.3 Short circuit characteristics (SCC)

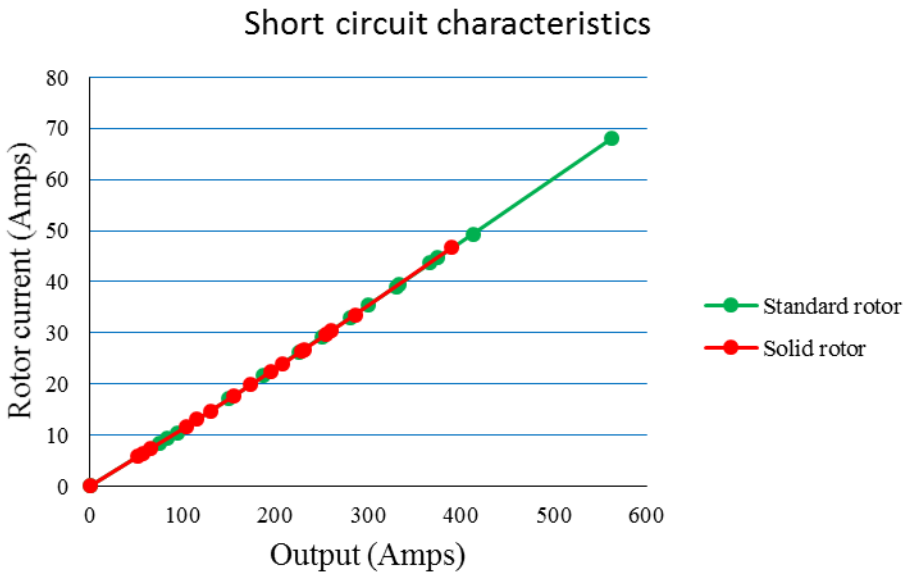


Figure 5-20. The current supplied to the rotor is plotted against the current produced by the generator when the output terminals are shorted together. The green line is the standard rotor and the red line is the prototype rotor.

In Figure 5-20 a graph which plots the current supplied to the field windings against the current produced when the output terminals are short circuited is shown. During the SCC test the iron of the generator is not driven to saturation so the graphs are linear in nature. The standard rotor, represented by the green line, is able produce a higher output current, from the generator, than the prototype rotor as it is run up to 260kVA output power compared to the

prototype rotors 180kVA which was stopped due to thermal loading concerns.

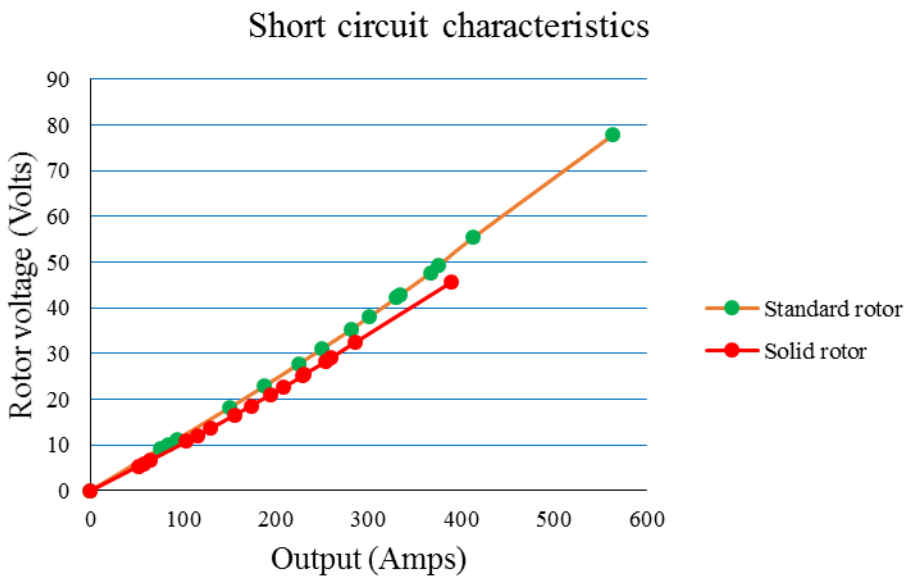


Figure 5-21. The voltage supplied to the rotor is plotted against the current produced by the generator when its output terminals are shorted together. The green line represents the standard rotor and the red the prototype.

In Figure 5-21 a graph which plots the voltage supplied to the field windings against the output current produced when the output terminals of the generator are short circuited is shown. The standard rotor, in green, is able to produce a higher output current than the prototype rotor, in red, due to the higher rating of the standard rotor when compared to the prototype.

5.2.3.1 Discussion of the short circuit characteristics

Figure 5-20 and Figure 5-21 show that the standard and prototype rotor produce the same output current for the same rotor current and voltage. The standard rotor can produce a larger output current than the prototype rotor can produce. The difference between the two rotor's ability to produce a high output current is due to the higher output rating of the standard rotor, at 260kVA, to the prototype's 180kVA. If the test had been carried out on the prototype assuming the full output power of the standard rotor the results would have continued to match as the SCC does not saturate the magnetic material of the rotor.

5.2.4 Magnetisation curve

The no-load testing of the generator results in two sets of graphs (Figure 5-18,Figure 5-19,Figure 5-20, and Figure 5-21) that can be used to define the magnetisation characteristics of the complete generator. The standard method used to represent these two separate graphs is to plot them on a single plot with two y-axes. The left hand axis presents the output voltage and the right hand axis presents the output current. The units of the y-axes can be either in the units measured: for example the output voltage in 40 volt intervals; or as per unit (P.U). The per unit is the measured quantity divided by the rated output of the generator.

Example:

$$x = \frac{z}{y}$$

Where:

$z = Point\ at\ which\ measurement\ was\ taken$

$y = Output\ of\ alternator$

$x = per\ unit\ value$

So if a measurement was taken at 40 volts and the output voltage of the generator is 400 volts then:

$$x = \frac{40}{400} = 0.1\ Per\ Unit\ value$$

The advantage of using per unit values is that a direct comparison of the two rotors is possible despite the differing output powers for the tests.

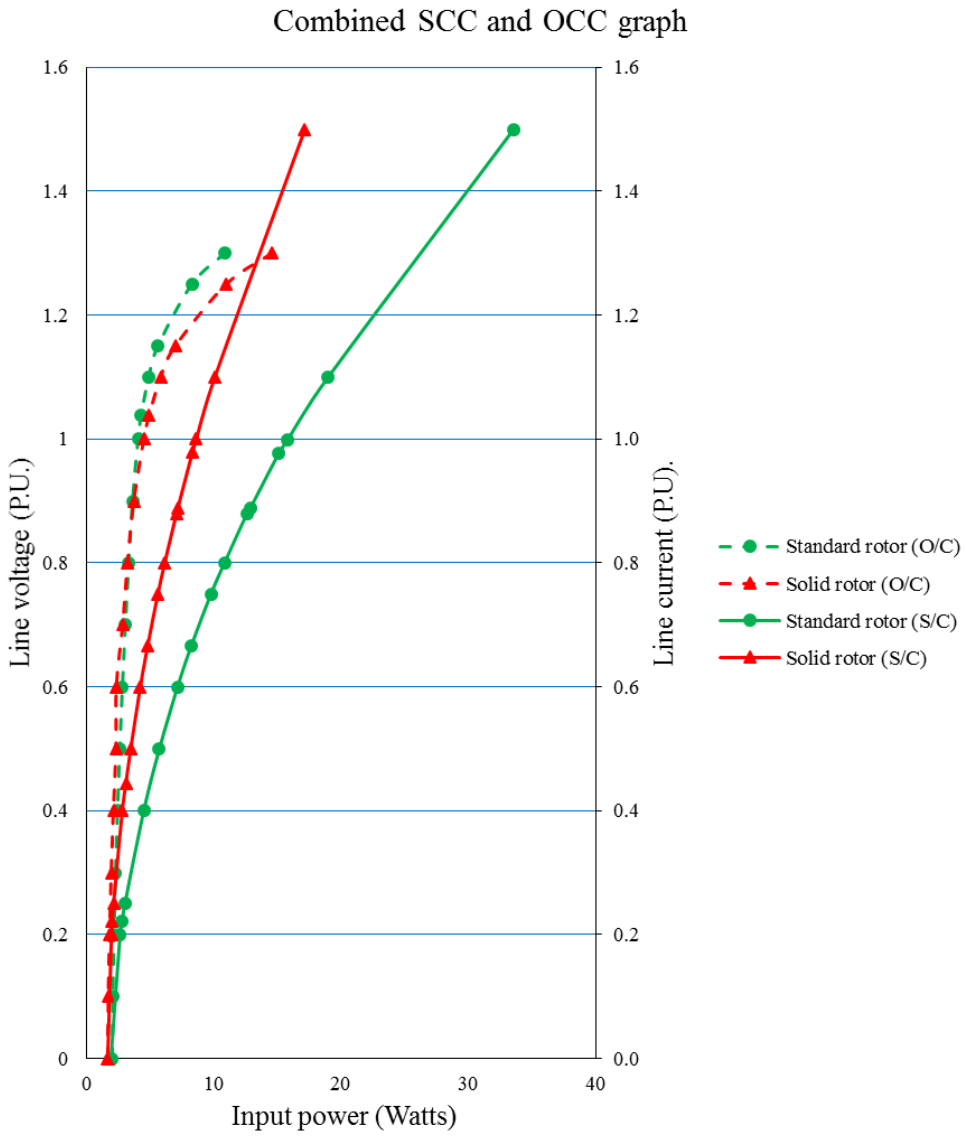


Figure 5-22. The magnetisation curve of both the standard rotor, in green, and the prototype rotor, in red. The OCC of the prototype rotor can be seen to saturate at a lower output voltage, line voltage, than the standard rotor.

The OCC and SCC are displayed on a single graph (Figure 5-22). The saturation of the pole shoes on the prototype rotor results in the OCC plot for the prototype reaching saturation sooner than if the pole shoes were constructed from the same steel that makes up the prototype rotor.

The SCC of the prototype shows that a higher current in the rotor windings is required to match the current output of the standard rotor.

5.2.5 Losses

The losses from the generator are calculated from the measurements taken from the generator under test.

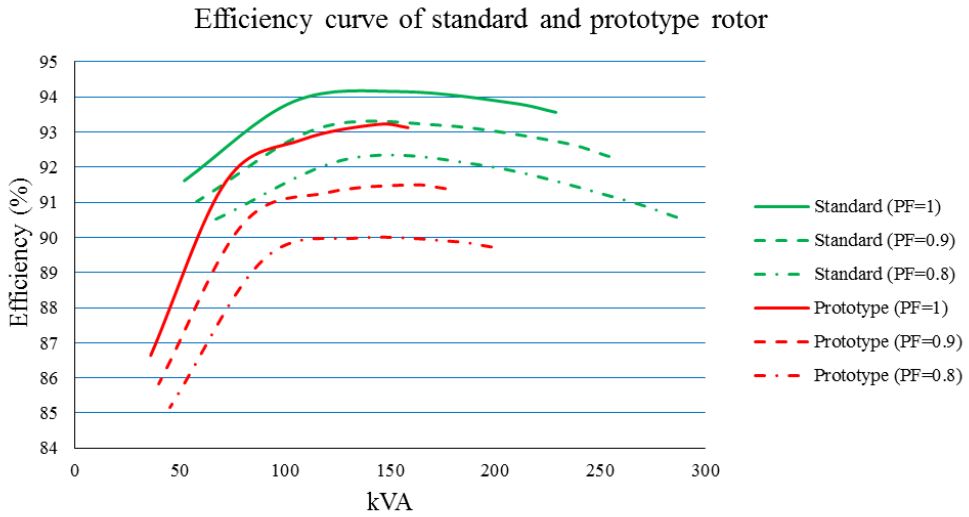


Figure 5-23. The efficiency curve of the generator equipped with a standard (in green) and prototype rotor (in red). The initial efficiency of the prototype rotor is lower than the efficiency of the standard rotor. The change in power factor results in a drop in efficiency for both rotors.

In Figure 5-23 the efficiency of the generator with both the standard and prototype rotor is shown with three different power factors. The prototype rotor has a lower initial efficiency than the standard rotor, however as the output kVA of the generator is increased the difference in efficiency of the two rotors moves towards parity. The prototype rotor was tested to 180kVA so it is unknown if the parity with the standard rotor continues at higher kVA outputs.

5.2.5.1 Discussion of losses

The increased losses of the prototype at the lower output kVAs is due to the increase in iron losses, which are due to the lower magnetisation of the cast A1 grade steel when compared to the M700-65A electrical steel. Once the rotor is magnetised however the losses of the rotor stabilise to match those of the standard rotor. To fully understand the losses the early saturation of the Invar 36 pole shoes needs to be discounted by changing the Invar 36 pole shoes for steel pole shoes. This would allow the rotor to run at 260kVA to give a direct comparison of the losses of the solid rotor verses the standard rotor.

5.2.6 Further testing (University of Nottingham)

5.2.6.1 Open circuit comparison

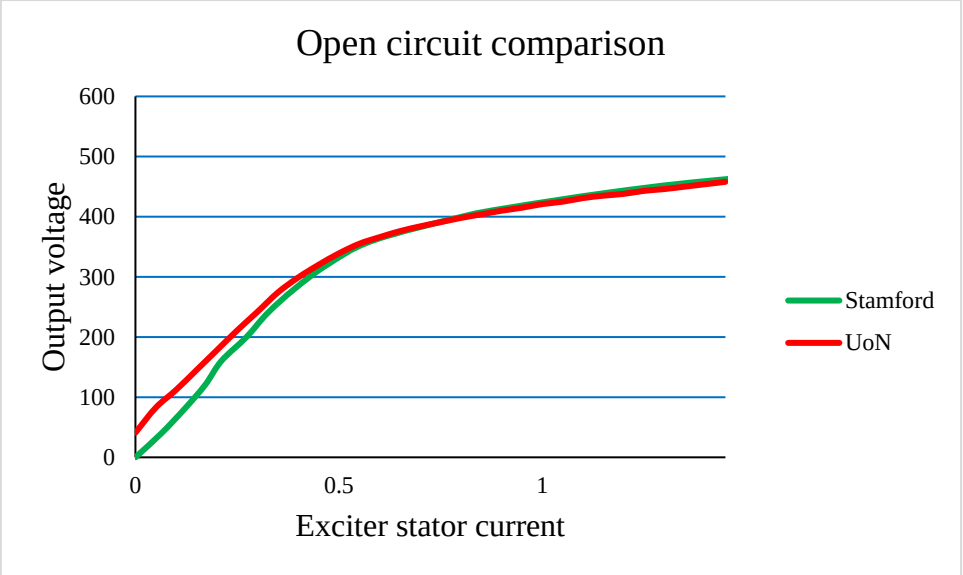


Figure 5-24. A graph showing the OCC of the prototype rotor from data collected at Cummins Stamford test facility and the UoN test facility.

In Figure 5-24 the OCC of the prototype rotor is shown from data collected at Cummins Stamford test facility and the UoN test facility. The OCC collected at the UoN shows that initially the test apparatus at the UoN showed a greater output voltage than the Stamford data. As no current was flowing in the exciter stator the only way an output voltage can be recorded is if the rotor has residual magnetisation from the testing carried out at Stamford. The testing at Stamford saturated the poles shoe and the rotor core material, due to the high coercivity of the materials that make up the prototype rotor some residual magnetisation is to be expected with the rotor acting as a weak permanent magnet. As the exciter stator current reaches 0.5 amps the residual magnetisation of the rotor is no longer a factor and the test apparatus of Stamford and the UoN produce the same results. Indicating that the test apparatus has the same level of sensitivity.

5.2.6.2 Short circuit comparison

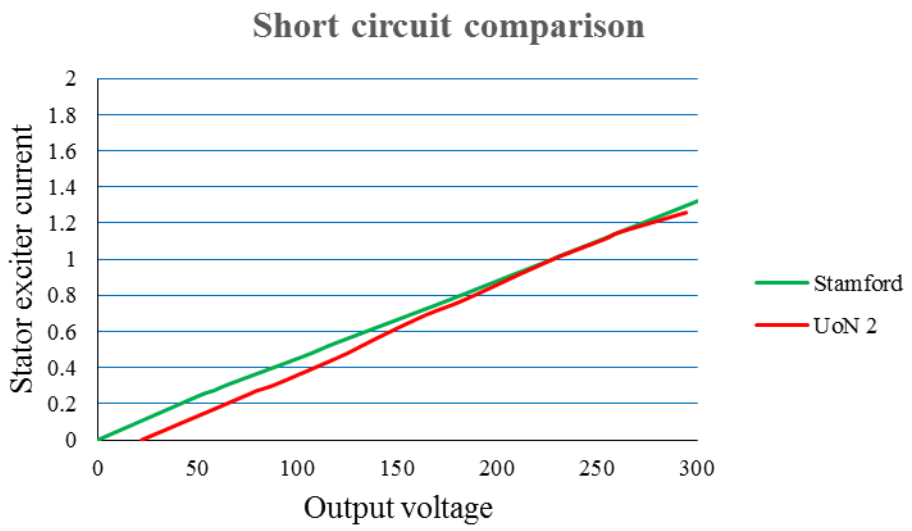


Figure 5-25. A graph showing the SCC of the prototype rotor from data collected at Cummins Stamford test facility and the UoN test facility.

In Figure 5-25 the SCC of the prototype as measured by the Stamford test facility and UoN test facility. The initial output voltage data from the UoN shows that the magnetised rotor is producing an output voltage without any current in the exciter stator. After the exciter current reaches one amp the two graphs match.

5.2.6.3 Discussion of the cross-platform calibration

Both Figure 5-24 and Figure 5-25 both show that the rotor has retained some magnetisation from the tests carried out at Stamford. The magnetisation of the rotor skews the results for the rotor making it produce an output voltage despite no current flowing in the exciter. Once the initial effects of the magnetised rotor are superseded by the increasing current in the exciter stator the data for both test apparatus matches very closely.

.

5.2.7 Results (thermal)

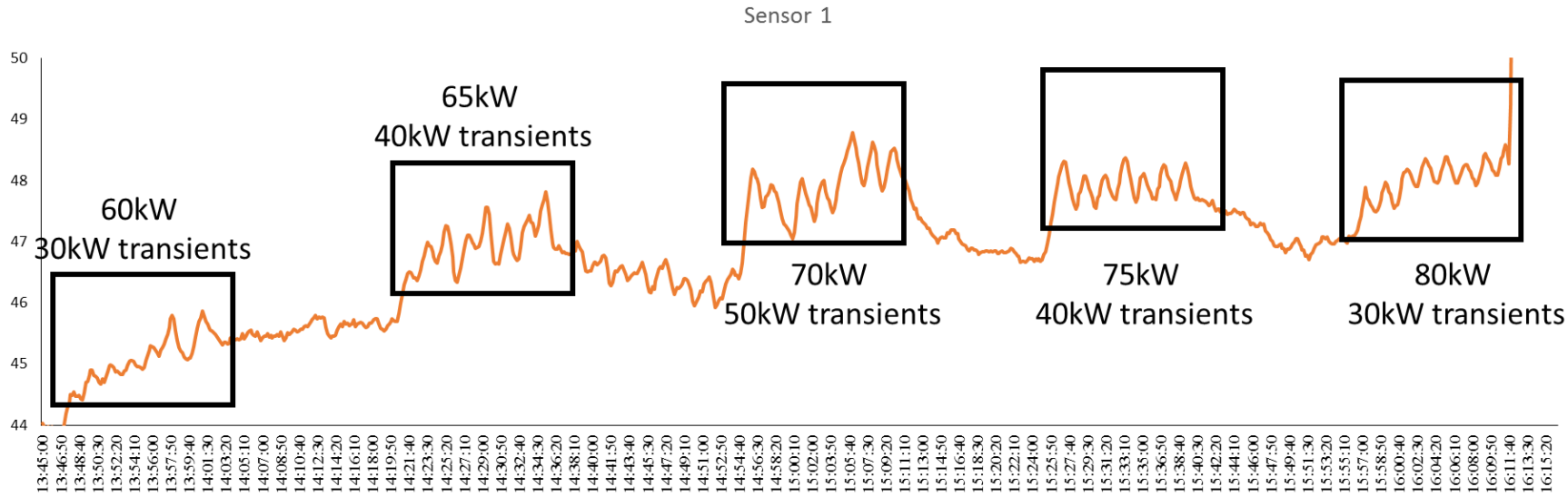


Figure 5-26. Graph of the temperature of the rotor during 5 kW increases in output power and different transient loading

In Figure 5-26 a graph of the temperature of the rotor with the stepped increasing load is shown. Only one of the sensors outputs was recorded due to the cables of the other three sensors being damaged during setup. During testing the load bank developed a fault where it would switch off briefly during testing causing the data to be distorted. The data from the graph is not usable because the load bank repeatedly thermally tripping out causing what should be identical spikes, as the extra load is applied, to become irregular spikes. In periods where no spikes were intended the load banks dropping out caused further spikes that prevented the rotor from reaching near steady state.

5.2.7.1 Discussion of results (thermal)

The graph shown in Figure 5-26 cannot be used to confirm the capability of the pole shoes to block eddy current inducing harmonics and transients for three main reasons.

- The load bank drop outs are distorting the data
- Only one of the four sensors is functional
- The heating of the rotor has not reached a steady state

After reviewing the data shown in Figure 5-26 and discussion with thermal testing experts it was determined that to identify thermally if the pole shoes are reducing eddy currents it is necessary to produce a baseline thermal characterisation of the rotor.

To do this the following procedure was implemented.

- Run the generator at an output power of 55kW for 45 minute
- Increase the output to 60kW for 15 minutes
- Reduce output power to 55kW for 15 minutes
- Increase the output to 65kW for 15 minutes
- Reduce output power to 60kW for 15 minutes
- Increase the output to 70kW for 15 minutes

- Reduce output power to 65kW for 15 minutes
- Increase the output to 75kW for 15 minutes
- Reduce output power to 70kW for 15 minutes
- Increase the output to 80kW for 15 minutes
- Reduce output power to 75kW for 15 minutes

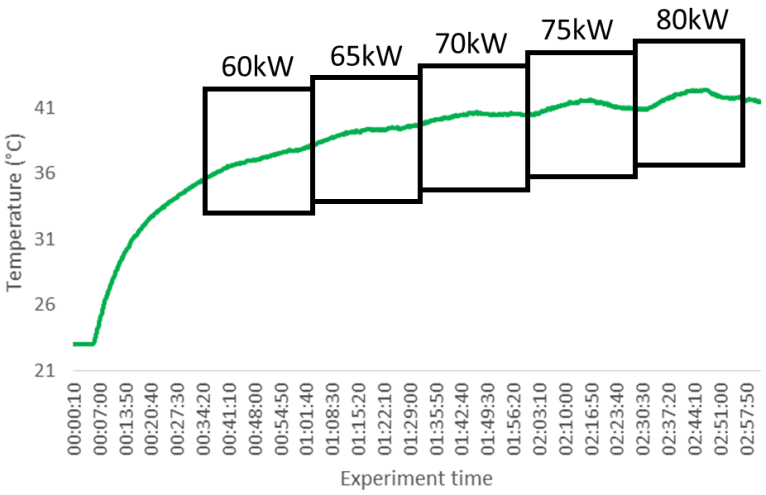


Figure 5-27. The baseline testing of the rotor shows that the temperature increases as a result of the increasing applied load.

In Figure 5-27 the baseline testing of the rotor shows that the changes in rotor temperature for an increasing load are slight. As can be seen from Figure 5-27 the rotor has not reached a thermal steady state. The increase in temperature, due to increasing load, cannot reliably be separated from the rotor temperatures rise until steady state is reached. However the main problem for determining the heating of the rotor is the difference in temperature of the rotor at 60kW, in Figure 5-26 the temperature of the rotor is 44°C while in the baseline testing in Figure 5-27 the rotors temperature is 38°C. The difference in temperature is 6°C, this is much higher than the temperature differences in the baseline testing, in Figure 5-26 and Figure 5-27, as loading is increased.

The thermal testing of the rotor at output powers as low as 80kW results in the changes in temperature being too small to be able to say with confidence that they are the result of the blocking of harmonics and transients. The use of thermal testing to confirm the shield capability of the lower saturation pole shoes is not viable at such low output powers.

5.3 Conclusions

The testing of the cast steel rotor shows that the current and voltage required to obtain the same field strength as the standard rotor will be 30% and 40% higher respectively. This is expected due to the lower permeability of the A1 normalised steel used to cast the rotor. The use of the annealing heat treatment could reduce the current and the voltage, in the field windings, based upon the higher permeability of the annealed A1 grade steel, annealed at a cooling rate of 4.5°C/min, shown in Figure 5-28. The change in performance cause by applying the annealing heat treatment is difficult to quantify without the construction of a second prototype. It would result in a lower voltage and current in the rotor windings but by how much is not currently possible to determine.

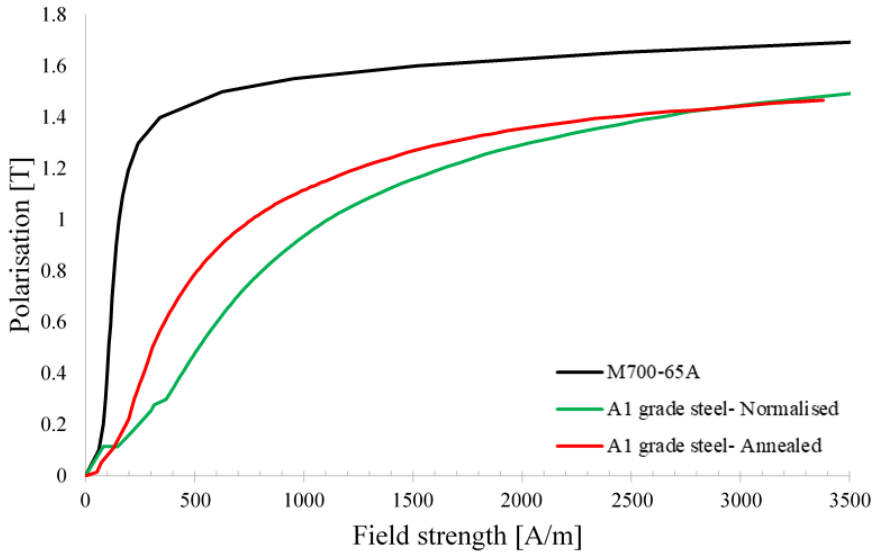


Figure 5-28. The absolute B-H curve of the electrical steel used in current rotor production alongside the A1 grade in both its normalised and annealed states.

Further testing of other cast steels would find other steels which can reduce the required current and voltage increases further. Electrical steel has a microstructure that is refined using annealing processes that cannot be applied to cast steels as the cross-sectional area of the cast part is too large to allow such fine microstructure control throughout. However, electrical steels have between 3.5%wt - 6.5%wt Si added to help reduce induced eddy currents. As the aim of this work is to block the induced eddy currents the steel used to produce the cast rotor will have a higher Fe content and so will have more ferromagnetic Fe than electrical steels.

The effect of a material with lower saturation magnetisation, than the body of the rotor, to produce pole shoes has been shown to increase the apparent air gap between the rotor pole face and the stator. This is the most effective method to stop transients and harmonics from heating of the pole faces. In the prototype under test the Invar 36 saturated at 72kW the reduction in heating from harmonics was not apparent at 185kW as the very high currents and voltages caused heating in the field windings that raised the temperature of the rotor cancelling out the reduction in the heating from transients and harmonics. From a materials science perspective it is clear that a magnetically saturated material will not be influenced by induced eddy currents.

This chapter has shown the limitations of cast steel rotors when compared to the current rotor. The inability of the A1 grade cast steel to match the performance of the electrical steel based rotor would require a reduction in the power density of the rotor or an increase in the size of the rotor to produce the same output power as the current rotor. The use of a better performing cast steel would produce a rotor capable of matching or exceeding the current rotor however none of the samples tested in Chapter 4 were capable of this. The testing of more grades of cast steel will enable a steel with a higher permeability to be found that enables a rotor with a better magnetic performance than the prototype.

The performance data produced in this chapter has been passed onto the UoN electrical machine modelling group to enable a model of the performance of a solid rotor to be accurately modelled so future DC material properties can be simulated without the need for another prototype.

This chapter has also shown that the use of a material with lower saturation magnetisation can be used to shield the pole faces from heating due to transients and harmonics. The testing carried out in this chapter has shown that if the saturation point of the pole shoes is too low the current and voltages in the field winding will need to increase sharply to bridge the apparent air gap the saturated material has created. It was therefore necessary to match the saturation point with the operating magnetisation of the rotor. The next chapter will investigate how this can be accomplished using additive manufacturing methods to produce a coating with tailorable DC magnetic properties.

6 Laser cladding of Ni-Fe soft magnetic alloy

6.1 Introduction

The use of laser cladding to produce a soft magnetic material is a key component of a solid cast steel rotor. The impossibility of defining a single “sweet spot” that the generator normal operates at makes the use of a single material to protect the main rotor body from transients and harmonics impractical. Instead the use of a series of coatings with slight compositional variations, that produce different saturation magnetisations, is required. The production of a graduated coating is outside the scope of this work as the amount of work to validate this concept is large enough to form a PhD thesis on its own. The first step in the concept of a graduated magnetic shield is to determine if laser cladding can produce a thick (>10mm) coating of an intermetallic Ni-Fe powder. To be considered a success the deposited coating must have DC magnetic characteristics that match a commercially available alloy with a similar composition to ASTM A753 - 08(2013) [135]. As stated in Section 3.3.1 the material selected for laser cladding was a permalloy 80 type alloy this was selected due to its characteristic very high initial permeability. For a laser clad permalloy 80 coating to be shown to be functional it must have a B-H curve that matches or exceeds the performance of permalloy 80 sample produced conventionally in a vacuum induction furnace and hot rolled into bar stock. The composition of the powder for laser cladding and the bar stock is matched as closely as possible.

6.2 Results

The testing procedure and the data processing methods are the same as those laid out in Section 3.1.2 and Section 4.2.1 respectively. Each sample was tested three times and the samples normalised to the field strength. The polynomial equation allowed the datasets to be compared providing the standard deviation of the data..

6.2.1 Steel substrate

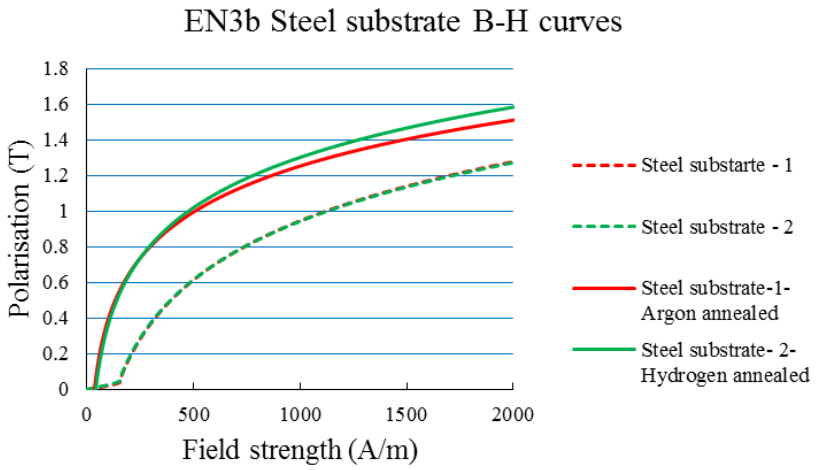


Figure 6-1. A graph of the DC magnetic performance of theEN3b steel substrate samples 1 and 2 before annealing. The DC performance after annealing is also shown.

In Figure 6-1 the EN3b steel has its DC magnetic performance shown before annealing is applied and afterwards. The pre-annealing magnetic performance of the substrate show that initial permeability of the steel is very low until 200A/m field strength is reached and then the permeability increases smoothly until saturation. Both of the non-annealed samples have a saturation magnetisation of $1.5T_{@3500A/m}$. The effect of Ar annealing of the steel substrate shows an increase in both initial permeability and saturation magnetisation, the saturation magnetisation has increased by 4%. The H annealing shows an increase in permeability that is greater than that of the Ar annealing, as shown in Figure 6-3, the H annealing improves the saturation magnetisation of the steel by 5%.

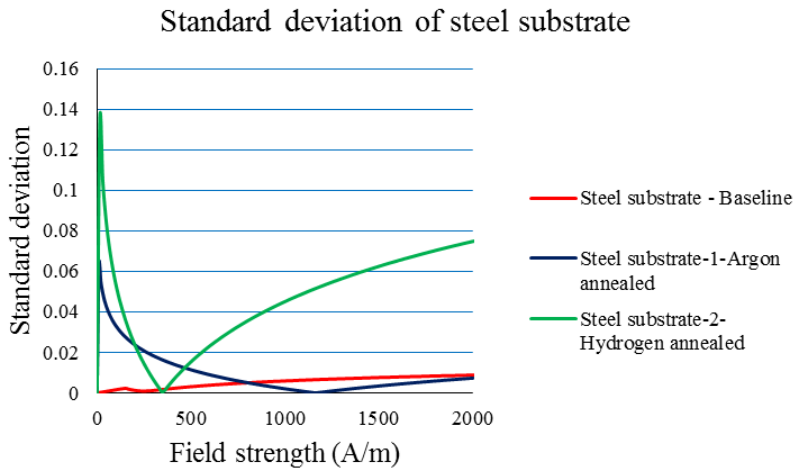


Figure 6-2. A graph showing the standard deviation of the datasets used to produce Figure 6-1.

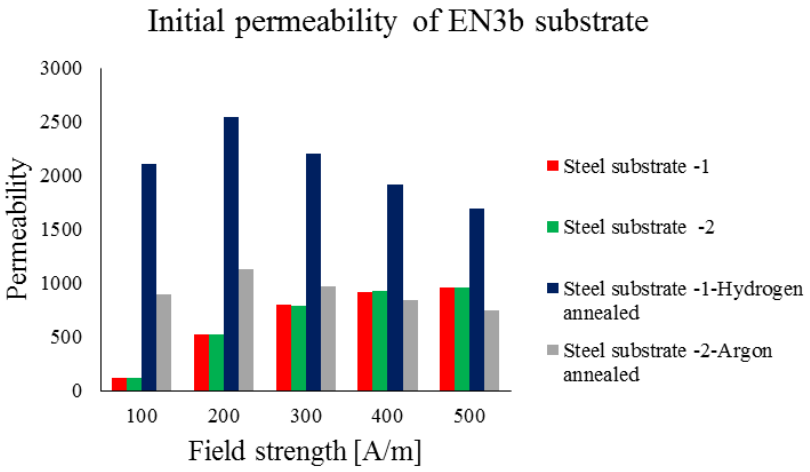


Figure 6-3. A graph of the initial permeability of the steel substrate as the field strength is increased to 500 A/m. The initial permeability of the samples changes after annealing and both annealed samples show an increase in permeability when compared to the non-annealed state until 500 A/m is reach then the permeability of the Ar annealed sample drops below that of the non-annealed.

In Figure 6-3 a graph that shows the initial permeability of the steel samples is shown. The initial permeability of non-annealed steel is very low as the steel initially resists magnetisation after 200A/m is reached the steel begins to magnetise and the permeability increases. Both of the annealed samples begin to magnetise as soon as the magnetic field is applied and have higher initial permeability.

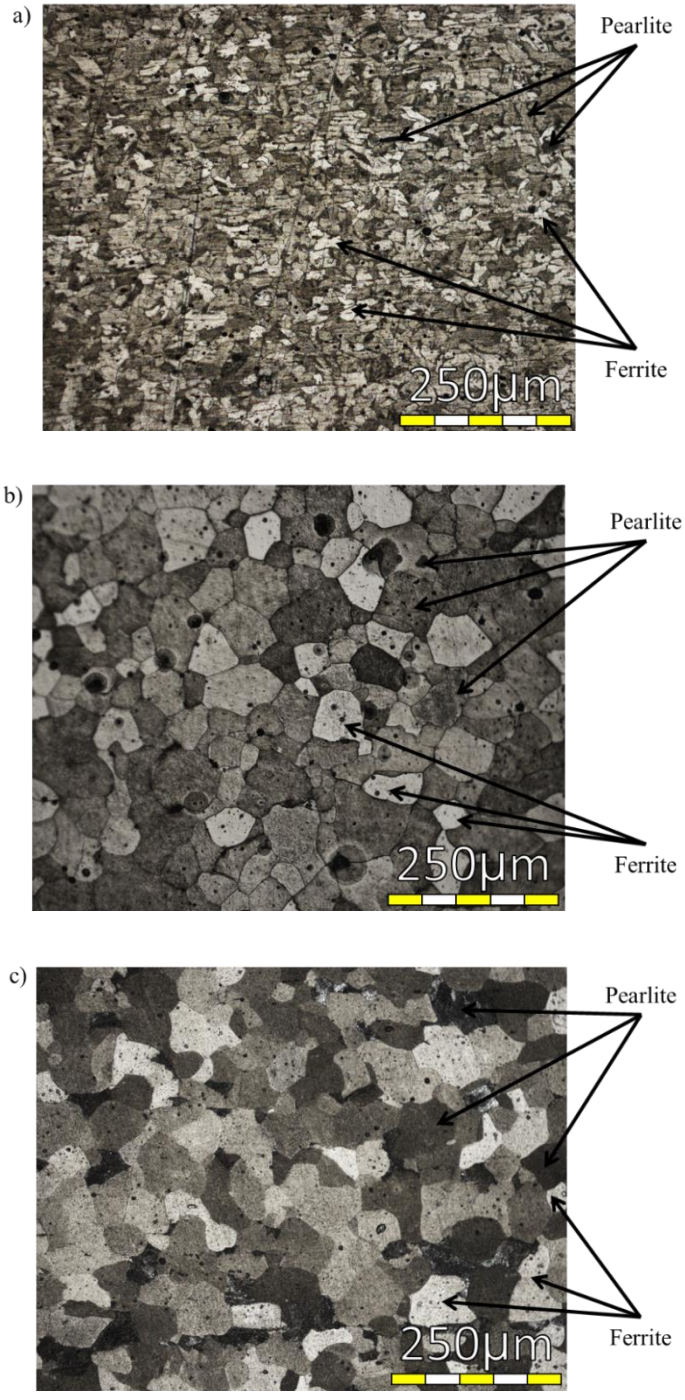


Figure 6-4. Images of the microstructure of the steel substrate (a) with no heat treatment applied (b) with H annealing applied, and (c) with Ar annealing applied.

In Figure 6-4 images of the microstructure of the steel are shown. Figure 6-4. (a) shows the microstructure in a non-annealed state, the microstructure is uniform

with large amounts of fine pearlite and lesser amounts of ferrite. Figure 6-4. (b) is the steel after H annealing, the crystal size has increased, and the grain boundaries are clearly defined. Figure 6-4. (c) is the steel after Ar annealing the crystal size has increased and visually appears to be the same size as the H annealed sample. The grain boundaries of the argon sample are not as clearly defined as in the H annealed image. The change in grain boundaries in the Ar and H annealed microstructures is indicative of the H annealed sample having thinner (more defined) grain boundaries resulting in better coupling between the magnetic domains when a magnetic field is applied. The single biggest contribution to magnetic performance is the crystal grain size. In AC applications there is a trade-off between larger grains giving a higher permeability but an increase in coercivity, therefore greater iron losses. In a DC applications the coercivity is less important so the larger the crystal size the better the magnetic performance, until the point where the number of magnetic domains, within a large crystal, are orientated in a different direction to the applied magnetic field cause resistance to magnetisation. This can be overcome with the use of magnetic annealing of the material [125].

6.2.2 Deposited permalloy

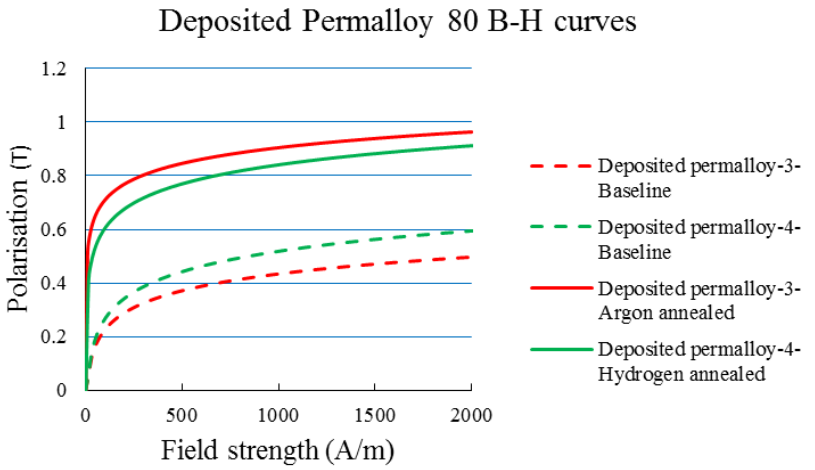


Figure 6-5. A graph of the permeability of the deposited permalloy before and after annealing. Both annealing process result in the characteristically sharp initial permeability of permalloys however the Ar annealed sample has a much higher saturation magnetisation point when compared to the H annealed sample.

In Figure 6-5 the DC permeability of the deposited permalloy before and after annealing is shown. The initial permeability of the non-annealed samples is the same until 0.2T where deposited permalloy -3 begins to saturate. After annealing the deposited alloy obtains the characteristically high initial permeability of permalloy. The H annealing process has increased the saturation magnetisation by 11% whilst the Ar annealing process has increased it by 36%.

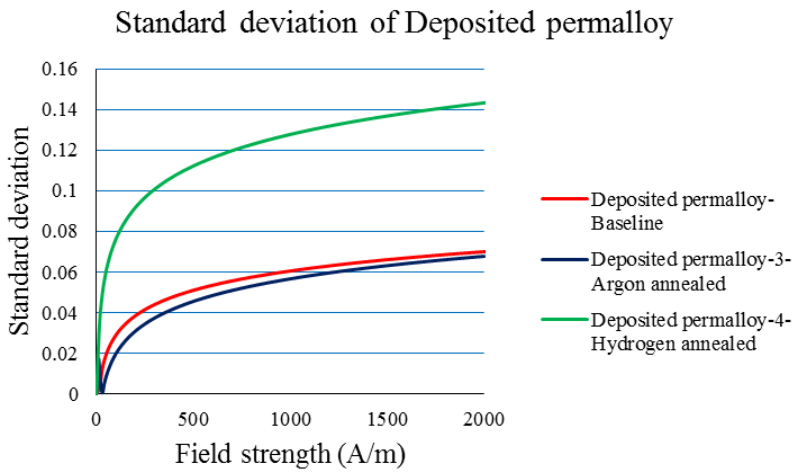


Figure 6-6. A graph showing the standard deviation of the datasets used to produce Figure 6-5

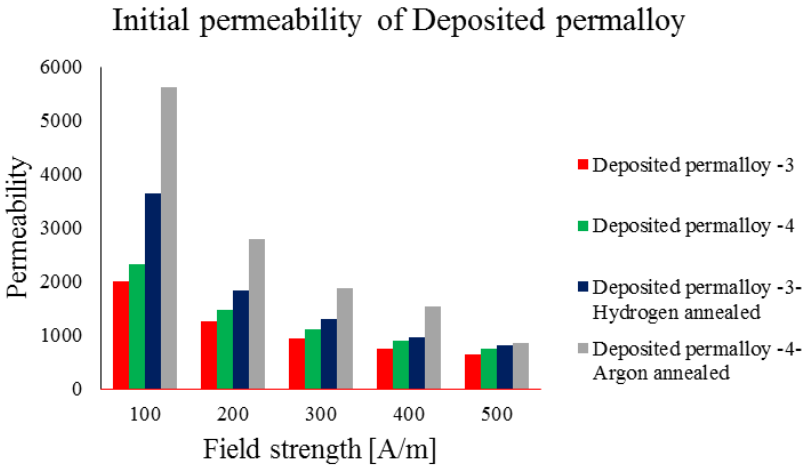


Figure 6-7. A graph of the initial permeability of the deposited permalloy as the field strength is increased to 500 A/m. The initial permeability of the samples changes after annealing and both annealed samples show an increase in permeability when compared to the non-annealed state. The Ar annealed sample shows a much higher permeability when compare to the H annealed sample.

In Figure 6-7 the initial permeability of the non-annealed and annealed samples is shown. The permeability of the non-annealed samples is low when compared to the annealed samples. The differences between the Ar and H anneal samples initial permeability is much clearer than in Figure 6-5. The rapid saturation of both annealed samples can be seen in the decrease in permeability for both samples after 100A/m. The initial permeability of the annealed samples is such that the permeability is already reaching saturation before 100A/m is reached.

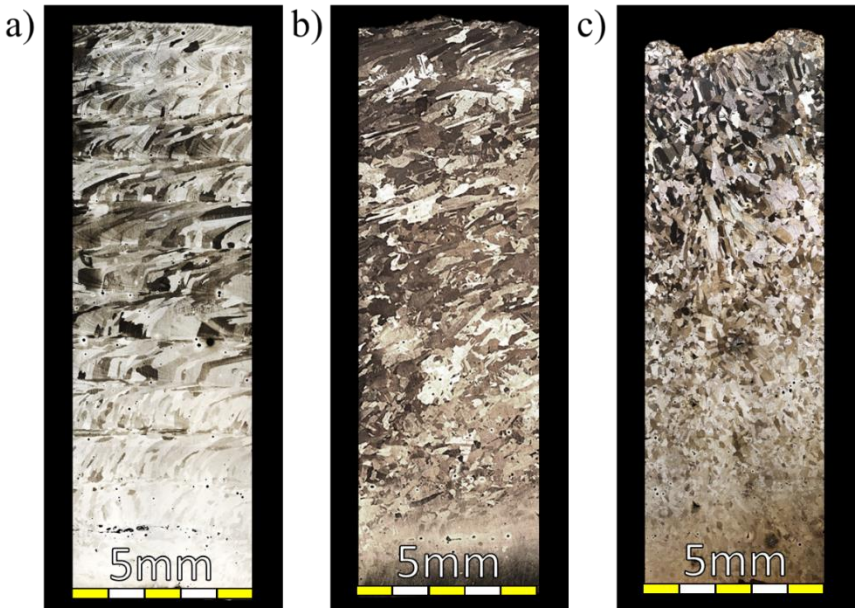


Figure 6-8. Images of the microstructure of the deposited permalloy (a) with no heat treatment applied (b) with H annealing applied, and (c) with Ar annealing applied.

In Figure 6-8 images of the microstructures of the laser clad permalloy are shown. Figure 6-8. (a) shows the microstructure of the deposited permalloy with no heat treatment applied. The layers of deposited material are clearly visible in the image but there are columnar crystals that have grown through the layer boundaries as the layer being deposed remelts part of the previously deposited layer. Figure 6-8. (b) shows the deposited permalloy H annealed sample. The layers are no longer visible in the microstructure as recrystallization has occurred. The crystal size appears smaller than for the non-annealed sample.

Figure 6-8. (c) shows the microstructure of the Ar annealed sample the microstructure has undergone recrystallization, the crystal size of the annealed sample appears smaller than either the non-annealed sample or the H annealed sample. The layers of deposited material are no longer visible

6.2.3 Permalloy clad steel

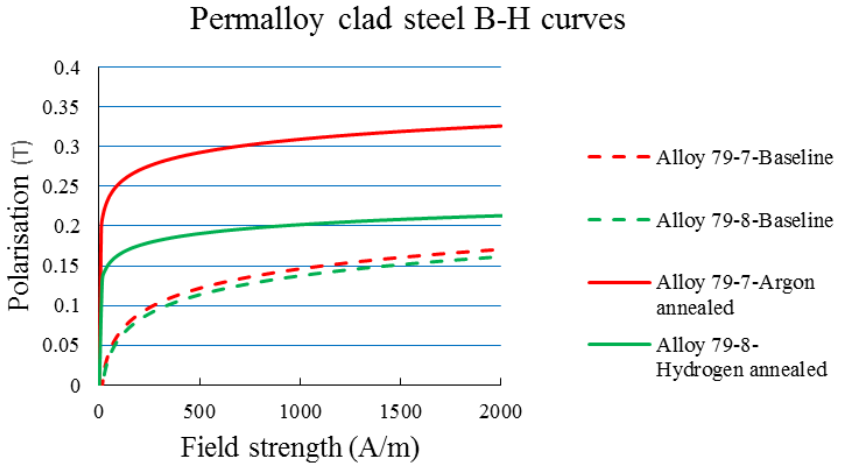


Figure 6-9. A graph of the permeability of the permalloy clad steel before and after annealing. Both the non-annealed samples have low initial permeability and a very low saturation magnetisation. Once annealed both samples show an increase in both initial permeability and saturation magnetisation.

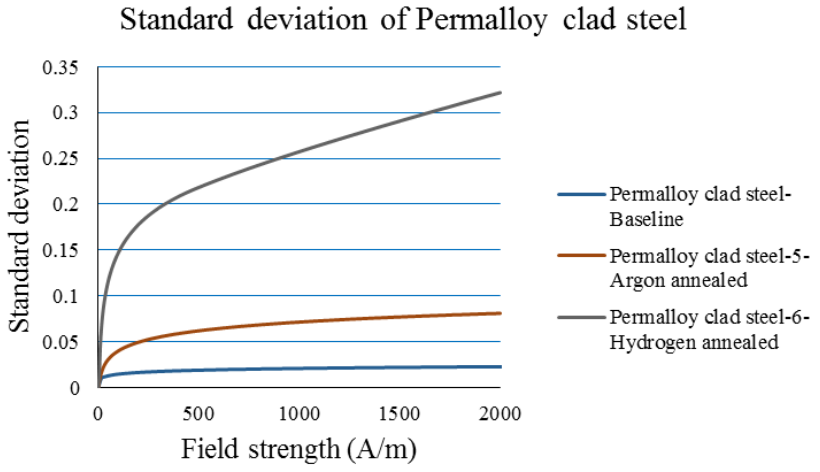


Figure 6-10. A graph showing the standard deviation of the datasets used to produce Figure 6-9

In Figure 6-9 the DC permeability of the permalloy clad steel is shown before and after annealing has taken place. The magnetic performance of both of the non-annealed samples is very similar with the saturation magnetisation of permalloy clad steel -5 being the same as permalloy clad steel -6 (0.19T at 3500A/m). The H annealing process resulted in an increase of the initial permeability and the saturation magnetisation increasing by 110%. The Ar annealing process resulted in an increase in saturation magnetisation of 78% and an increase in the initial permeability. At this point it is worth noting that annealing in H has improved the magnetic properties for both samples that are partially (permalloy clad steel) or completely composed (steel substrate) of EN3b steel. In the deposited permalloy the Ar annealing increased the magnetic performance more than the H annealing. This will be explored further in Section 6.4.

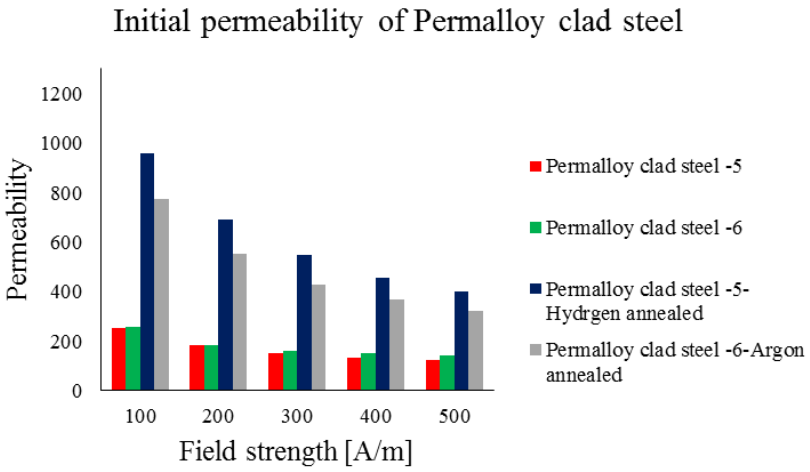


Figure 6-11. A graph of the initial permeability of the permalloy clad steel as the field strength is increased to 500 A/m. The initial permeability of the non-annealed samples improve by both H annealing and Ar annealing. The H annealing process improves the permeability of the permalloy clad steel more than the Ar annealing.

In Figure 6-11 the initial permeability of the non-annealed and annealed samples is shown. The non-annealed samples have nearly identical initial permeabilities. The H annealed sample has the highest permeability of the annealed samples but the difference between the two annealed samples reduces as the field strength increases.

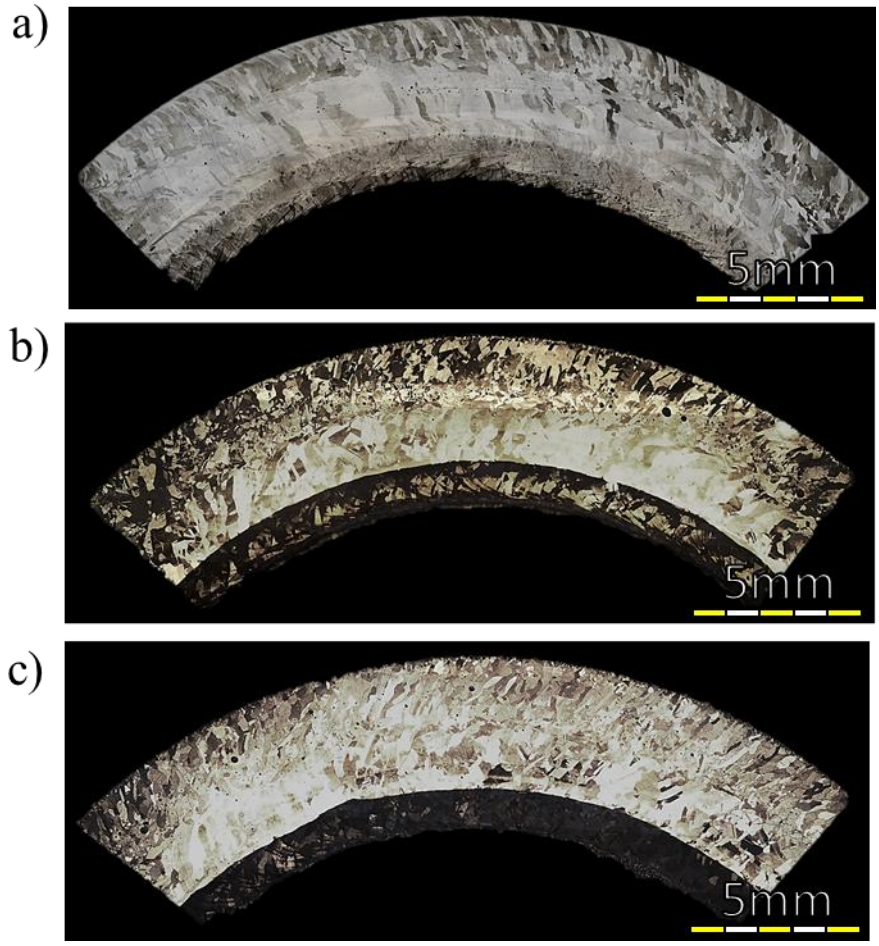


Figure 6-12. Images of the microstructure of the permalloy clad steel substrate (a) with no heat treatment applied (b) with H annealing applied, and (c) with Ar annealing applied.

In Figure 6-12 the permalloy coating, which was applied to the steel substrate is shown. The steel substrate has been corroded by the etchant and is not visible. Figure 6-12. (a) shows the clad steel before annealing the layering of deposited material is shown but is not as clear as in Figure 6-8. (a) this is due to the residual heat in the cylinder being higher than in the deposited block. Figure 6-12. (b) shows the permalloy clad steel after H annealing The microstructure is more uniform than in the non-annealed sample but the crystals appear smaller than those of the non-annealed sample. Figure 6-12 (c) shows the Ar annealed permalloy clad steel the microstructure is more uniform than the non-annealed sample and the crystals appear smaller than the H annealed samples.

All the samples show column crystals in the in the permalloy coating, not just towards the outer edge as in the deposited permalloy samples. The residual heat in the cylinder during cladding was higher allowing large columnar crystals to grow throughout the microstructure of the coating

A band of darker material can be seen in the first two deposited layers on each sample (very bottom of each image) of the deposited permalloy. This is due to the residual heat of the cylinder being so high that the Ar retaining bag melted allowing air into contact with the clad material causing some oxidation. It could be suggested that the over etching of the two layers of deposited material is due to mixing of the steel substrate with the deposited permalloy. This is not the case as there are no dark areas in the first two layers in the deposited permalloy samples (Figure 6-8. (a), Figure 6-8. (b), and Figure 6-8. (c).

6.2.4 Alloy 79

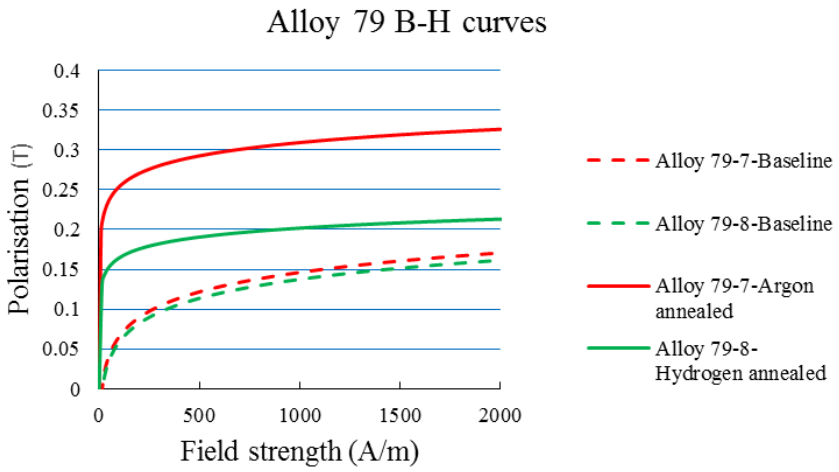


Figure 6-13. A graph of the permeability of Alloy79 before and after annealing. Both the non-annealed samples have low initial permeability and a very low saturation magnetisation. Once annealed both samples show an increase in both initial permeability and saturation magnetisation, with the Ar annealed sample having a higher magnetic saturation.

In Figure 6-13 the DC permeability of Alloy 79 is shown before and after annealing. The two non-annealed samples have initial permeabilities that on average are no more than 3% different while the saturation magnetisation are both $0.16T_{@3500A/m}$.

Once annealed the performance of both samples increases, with the characteristically high permeability of permalloy shown in both samples. The saturation magnetisation of the H annealed sample the same as before it was annealed. The Ar annealed sample has a saturation magnetisation that is 70% higher than before it was annealed.

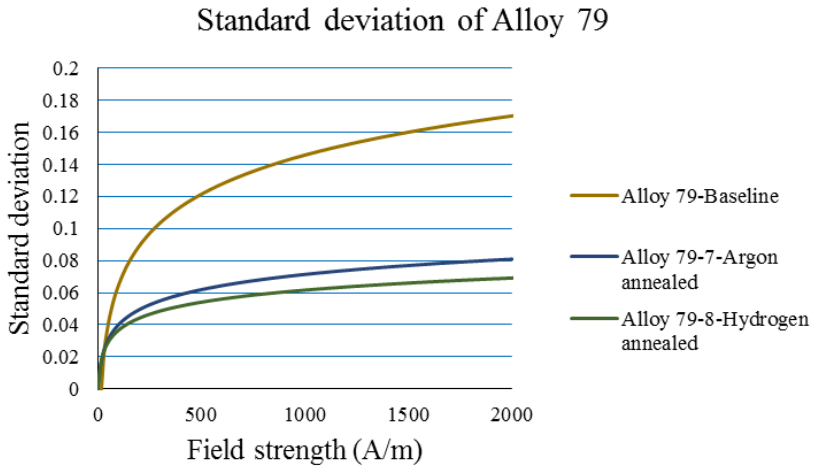


Figure 6-14. A graph showing the standard deviation of the datasets used to produce Figure 6-13

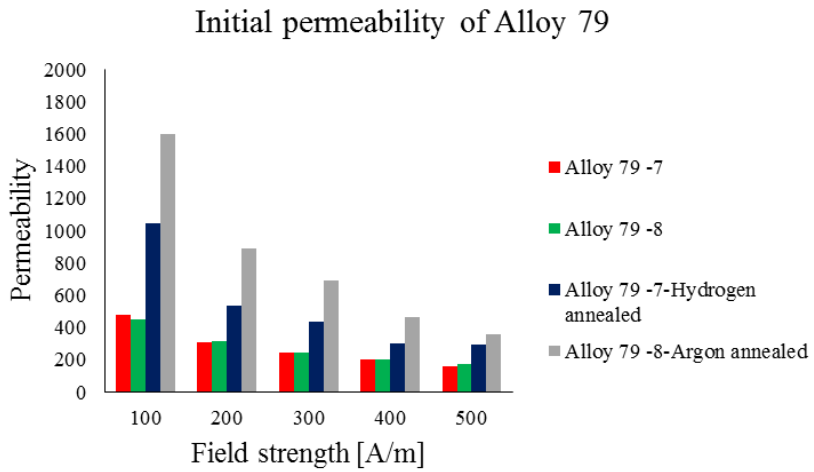


Figure 6-15. A graph of the initial permeability of Alloym79 as the field strength is increased to 500 A/m.. The initial permeability of the non-annealed samples improve by both H annealing and Ar annealing. The Ar annealing process improves the permeability of the Permalloy clad steel more than the H annealing.

In Figure 6-15 the initial permeability of the non-annealed and annealed samples is shown. Both of the non-annealed samples are within 3% of each other. After annealing the permeabilities are higher but as Permalloy reaches saturation by 100A/m the alloy has already reached saturation as can be seen in the decreasing permeability.

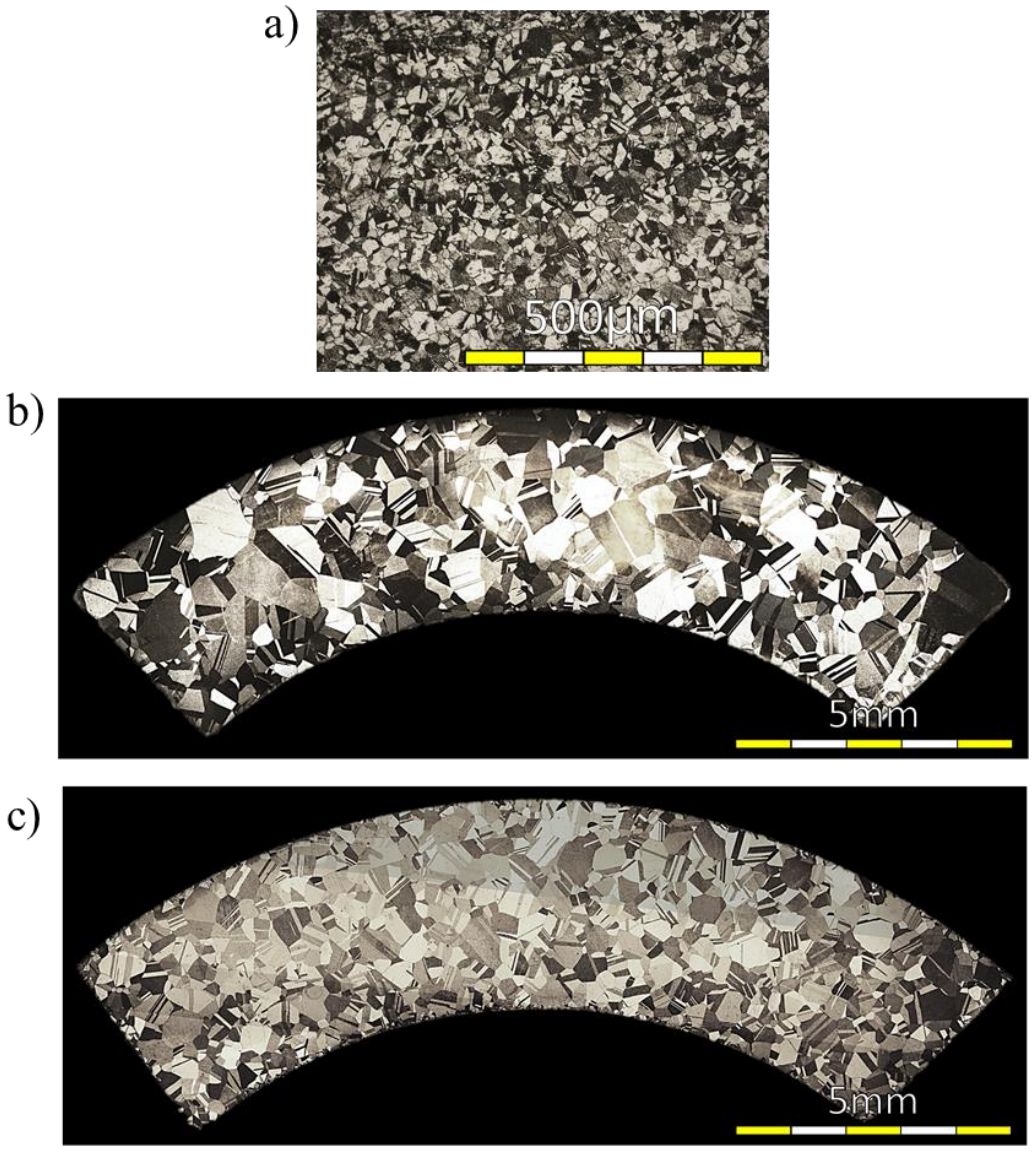


Figure 6-16. Images of the microstructure of Alloy 79 (a) with no heat treatment applied (b) with H annealing applied, and (c) with Ar annealing applied.

In Figure 6-16 the microstructure of Alloy 79 before and after annealing is shown. Figure 6-16. (a) shows the microstructure of the alloy with no heat treatment applied.

Figure 6-16. (b) shows the microstructure of the H annealed sample, it is also uniform in appearance but the crystals are significantly larger than the non-annealed sample, requiring a change in the scale of magnification for the microstructure to be visible. Figure 6-16 (c) shows the Ar annealed samples microstructure, the crystals in the Ar annealed sample are smaller than those of the H annealed sample.

6.3 Discussion

Steel substrate

The improvement in the magnetic performance of the steel shown in Figure 6-1 and Figure 6-3 is predominantly the result of the crystal grain growth cause by the annealing process. The similar crystal size for the H and Ar rules out grain size as the primary reason for the higher permeability of the H annealed sample [141]. The similar crystal sizes for both the Ar and H annealed samples indicate that the higher permeability of the H annealed sample is due to a reduction in impurities (both interstitial and at grain boundaries). As the primary difference between the annealing atmospheres is that Ar is inert and H is reactive it can be seen that as the samples of steel were annealed in their respective atmospheres the impurities (both interstitial and at grain boundaries) in both samples diffuse to the surface. In an Ar atmosphere the impurities concentrate at the surface but do not precipitate off the sample, so as the sample cools the impurities are drawn back into the sample to achieve equilibrium. In the H annealed sample the impurities can react with the H atmosphere and precipitate out of the sample. The reduction in interstitial impurities and impurities at the grains boundaries improved the magnetic performance of the H annealed sample and the reduction in impurities at the grain boundaries can be seen in Figure 6-4. (b) as better defined boundaries between crystals.

Deposited permalloys

Permalloy is known for its very high initial permeability [142] the two non-annealed samples do not show this characteristic.

The microstructure images show that the Ar annealed sample has a smaller crystal size than the H annealed sample and has the highest initial permeability and the highest saturation magnetisation. The H annealed sample has visibly larger crystal size than the Ar annealed sample yet preforms worst in terms of permeability and saturation magnetisation. This work suggests that this is due to the high solubility of H in Ni-Fe alloys. The H diffuses into the alloy [93] during the annealing process [143] and places the Fe-Ni crystals under strain [144] so the microstructure of the H annealed sample is placed under strain whereas the Ar annealed sample has no additional strain, due to Ar inability to diffuse into the sample, during annealing and therefore preforms better than the H annealed sample. An increase in H interstitially could would also increase pinning sites within the crystal reducing magnetic performance.

Permalloy clad steel

The permalloy clad steel has a very low saturation magnetisation and a low initial permeability. While annealing in either Ar or H increases both of these the annealed material still has a poor performance. The layer of oxide formed by the melting of the Ar retaining plastic shroud has caused a reduction in the performance of the clad steel as the higher levels of oxides, carbides, nitrides trapped in the first layers of deposited permalloy result in an increase in pinning sites between magnetic domains reducing the magnetic performance of the material. As with the steel substrate sample the use of H annealing improves the magnetic performance of the permalloy clad steel more than Ar annealing does.

Alloy 79

Alloy 79 has a low initial permeability and a low saturation point. The Ar annealed alloy saturates at $0.16T_{@3500}$ in its non-annealed state and $0.28T_{@3500A/m}$ once annealed. H annealing has less impact on the saturation point (0.9% improvement) compared to a 70% improvement due to the Ar annealing.

The crystals of the Ar sample are smaller than the crystals in the H annealed sample yet it has a higher saturation magnetisation and a higher permeability. The saturation of the $Fe\text{-}Ni_3$ crystals with H could explain the poor performance of the H annealed sample as its crystal structure would be placed under strain by the diffusion of H into it during the cooling stage of the annealing process. The increase in interstitial H would also increase pinning sites reducing magnetic performance.

The use of either annealing atmospheres improved the magnetic performance of all the samples. The Ar annealing improved the performance of the deposited permalloy and Alloy 79 samples more than the H annealing atmosphere. The H annealing atmosphere improved the magnetic performance of samples containing steel, Permalloy clad steel and steel substrate, more than the Ar annealing atmosphere. Hydrogen diffuses more easily in steel than in permalloys [145] this is due to the steels BCC crystal structure [146] but H is three times more soluble in permalloy than in steel [147]. The high temperature of the H annealing process would provide sufficient activation energy for atomic H to diffuse into both the steel and the permalloy. However the low solubility of H in steel may have resulted in the H being precipitated out of the sample during the cooling stage of the annealing process. The high solubility of H in permalloys could result in the H remaining in the $Fe\text{-}Ni_3$ crystal structure creating pinning sites that reduce the magnetic performance of the permalloy and placing the crystal under strain, further reducing its magnetic performance. When annealing in Ar the impurities, such as O, N, S, C, are not removed from the material so as the material cooled they diffused back into the bulk of the sample to reach a state of equilibrium.

This resulted in the Ar annealed samples containing the same level of impurities they had before annealing but having an improved microstructure, hence improved magnetic performance. In the H annealing process some of the atomic H could have diffused into the samples and in the steel samples they precipitated back out during cooling as H is not very soluble in steel.

In the permalloy samples the higher solubility of H would result in an increase of interstitial impurities of H, even though the level of O, N, S, C may have decreased, the H would disrupt the lattice structure reducing the magnetic performance of the permalloy when compared to the Ar annealed permalloy sample.

6.4 Conclusions

This chapter has shown that laser cladding, can deposit soft magnetic materials that match or exceed the magnetic performance of commercially available materials. Thick (>10mm) laser clad coatings are simple to produce and have all the traditional advantages of additive manufacturing. The advantages for the production of magnetic shielding on pole shoes are; that the bonding between the coating and the substrate is stronger than any mechanical bonding technique; and the ability to alter composition of the alloy during deposition; and the reduction in material required as the coating is only applied to the areas where it is needed. The "as deposited" permalloy was shown to have better magnetic performance with either a H or Ar annealing stage. Argon annealing had the largest impact on the magnetic performance of the deposited permalloy.

The laser clad samples had a stronger response to the applied magnetic field than the commercially supplied samples, this can be attributed to the anisotropic nature of the laser clad samples. Whilst the commercial alloy was isotropic the laser clad alloy showed columnar grain growth which produces a preferred axis of magnetisation. If the poles shoes of the rotor were clad in a Ni-Fe alloy the clad layers should be build up so that the direction of magnetisation is in-line with the columnar grain growth. Due to the larger surface area of a pole shoe, when

compared to the deposited block for sample manufacture, the residual heat in the pole shoe will be less, this will restrict the growth of grains between deposited layers reducing the anisotropic nature of the deposited coating.

The clad permalloy, once annealed, showed the characteristic very high initial permeability expected of a high Ni content permalloy.

The laser clad material showed a stronger response to an applied field than the commercially available alloys upon those composition it was based. Laser cladding of Ni-Fe alloys is capable of matching and, depending on magnetisation direct exceeding the permeability and saturation magnetisation of the commercially produced alloy.

The bond to the substrate was not tested during this work however laser cladding produces a metallurgical bond between the substrate and deposited material. The metallurgical bond is stronger than the bond produced by the use of fasteners to hold down thin sheets of material. The bond strength is the same as if the materials were bonded using ultrasonic consideration.

7 Conclusions and future work

7.1 Conclusions

This work set out a methodology to radically simplify the manufacture of the rotor. The difficulty of this was to match the performance of any prototype with the current performance of the CGT state of the art rotor. There are two fundamental requirements that any new rotor must meet: the same power output as the current rotor, and the ability to deal with transient and harmonic induced eddy currents in the pole faces.

The use of casting to produce the prototype rotor added significant limiting factors to the matching of the power output of the current rotor. The lack of knowledge of the DC magnetic characteristics of cast steels in the literature resulted in the first stage of this work being based around the testing of common sand cast steels. The advantages of a simple casting method is that the type of cast steel used can be any one of hundreds of available grades or a bespoke composition to obtain the best magnetic performance. In this thesis ten different grades of steel were tested for their DC magnetic properties. These ten steels were selected on the basis of the grades available at the foundry that had been selected to cast the prototype rotor. Further testing of more grades of cast steel would result in better performance of the prototype rotor. The additional complication of the application of heat treatments to the cast steel increases the breadth of work required significantly.

Within the steels that were tested considerable variation was found in their B-H curves. The content of impurities such as C alone did not separate the best performing steels from the worst. The addition of alloying metals altered the steels microstructure and affected its magnetic performance. The changes in the steel's DC magnetic performance after heat treatments were applied showed that the use of carefully controlled heat treatments can improve the performance of the steel significantly, and therefore reduce the gap between the prototype rotor and the standard rotor.

Once the best performing steel had been found, the design for the rotor had to be finalised. At this stage the choice between producing a rotor that differed radically in design from the current standard rotor and one that matched the standard rotor design had to be made. The greater flexibility in typology that casting and machining offer was offset by the need to be able to compare the results with the standard rotor and also using the test data to produce a magnetic model of the solid rotor that would allow the application of materials with different DC magnetic properties. If the typology of the prototype rotor was altered, the change in performance due to the DC properties of the cast steel would be impossible to differentiate from the changes in performance due to a different typology. The decision was made to retain the current typology of the rotor but to allow the pole faces of the rotor to be remove. The use of Invar 36 pole shoes showed that the saturation of the pole shoes (at 72kW) created an increase in apparent air gap between the rotor pole faces and the stator that forced a sharp increase in voltage and current required to produce an increase in field strength. When the pole shoes saturate it is not possible to induce eddy current within them as the magnetic fields created by transients and harmonics cannot influence a saturated material. The early saturation of the Invar 36 pole shoes stops the prototype rotor from obtaining its maximum output power.

The use of direct energy deposition (DED) additive manufacturing techniques, in this instance laser cladding, was investigated to determine its capability to produce thick coatings of a Ni-Fe alloy called permalloy. Permalloy has a characteristically very high initial permeability, an annealed laser clad sample obtained the very high initial permeability so laser cladding can produce soft magnetic Ni-Fe alloys. The "as deposited" laser clad samples did not show very high initial permeability as their microstructure was distorted by the residual stress inherent in the laser cladding process. The laser clad samples were annealed in H and Ar atmospheres to determine which atmosphere was best suited to producing a microstructure that allowed a very high initial permeability.

Once annealed both the H and Ar annealed samples showed the high initial permeability of permalloy but the Ar annealed sample produced a higher permeability and a higher saturation magnetisation.

This thesis has shown that the performance of a cast rotor is always limited by the DC permeability of the cast steel, but with so many grades of steel available more testing of the available grades is required before the question of whether a cast rotor can match the performance of a standard rotor can be answered. The use of Invar 36 pole shoes shows the effect of using a lower saturation magnetisation material on the pole faces will have and highlights the flaw of using a single material to produce the pole shoes. The use of laser cladding can mitigate this flaw, as it allows layers of differing composition to be laid onto a steel substrate.

This thesis is based upon three critical knowledge gaps:

- The magnetic characteristics of a range of cast steels with and without heat treatments applied
- The performance of a solid rotor when compared to the conventional lamination based rotor
- The use of laser cladding to produce a soft magnetic coating on a steel substrate

This body of work substantially fills in these knowledge gaps with:

- The testing of cast steels with and without applied heat treatments and an optical examination of the effects of the heat treatments on the microstructure and how this effects the magnetic properties of the steel. From this work it can be seen that the use of sand casting of steel rotors is not going to be able to match the performance of the currently used electrical steel.

- The design of a cast steel rotor with low saturation pole shoes. Testing of the rotor and comparison with the lamination based rotor. The capability of lower saturation pole shoes to increase the apparent air gap was proven. An increased air gap results in a decrease in induced eddy currents on the pole faces so it can be inferred that the lower saturation pole shoes results in a reduction in induced eddy currents
- The use of laser cladding techniques to produce a soft magnetic alloy that reproduces the characteristic very high initial permeability of a permalloy alloy was shown to perform better than the commercially available conventionally produced alloy.

7.2 Future work

7.2.1 Material selection for main rotor body

A methodology has been shown which allows testing of the DC magnetic properties of cast steel with various heat treatments applied. The application of this methodology to more grades of cast steel will allow a narrowing of the gap between the magnetic performance of a cast steel rotor and the standard rotor. The use of sand casting results in a high content of carbon and sulphur impurities in the steel. Sand casting cannot produce the same quality of steel as that used in electrical steel, however the use of vacuum induction melting would result in a reduced level of impurities..

7.2.2 Proposed further testing of the rotor

At present the UoN test facilities are not capable of removing a rotor from its housing, although this is a capability that is intended to be added in the near future. Without the capability to remove the rotor it is not possible to replace the damaged RTDs or change the Invar 36 pole shoes for steel pole shoes. CGT have this capability in their factory but are unable to use it for prototype machines as it would disrupt the flow of their production line.

Once the UoN gains the capability to remove the rotor from its housing further testing of the prototype rotor becomes possible.

The use of Invar 36 pole shoes has limited the output power of the generator. The use of steel poles shoes would allow the true maximum output power of the generator to be determined.

To ensure safety whilst testing the load should be increased from the current 180kW rating in 15kW steps and allowed to reach steady thermal state. Once steady state has been achieve the generator should be stopped and the thermal data checked to ensure that the rotor is not exceeding 180°C. If the rotors temperature is below 180°C the load can be increased by 15kW.This would continue until the maximum rating for the generator is reached

7.2.3 Concept for a multilayer magnetically shielding pole shoe

Laser cladding deposited a coating onto a substrate, in the case of a pole shoe the substrate should be a material that has similar magnetic properties to the material that makes up the pole body. In the case of the cast rotor a pole shoe made of the same A1 grade cast steel would be suitable. However sand casting a block of A1 steel to act as a substrate would not be cost effective. Instead the use of a bright drawn mild steel which is available in multiple thicknesses makes a more cost effective way to provide a substrate for the laser cladding process.

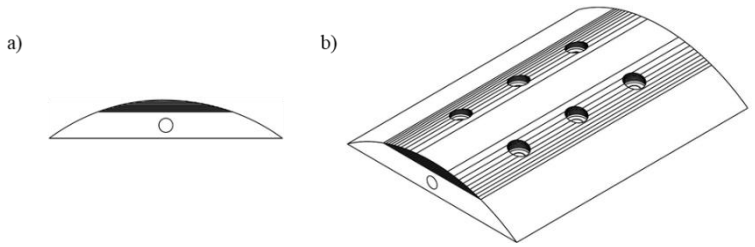


Figure 7-1. A design concept of a multilayer pole shoe with laser clad layers with differing ratios of Ni/Fe in each layer. The differing ratios would result in different saturation magnetisations for each layer producing a graduated magnetic shield on the pole face.

In Figure 7-1 a design concept for a graduated magnetic shield is shown. By changing the ratios of Ni/Fe the saturation pint of each layer could be tailored to protect the rotor from induced eddy currents at predetermine output powers.

7.2.4 Overall concept for next generation salient pole rotor

The use of cast steel, to produce a solid salient pole rotor is limited by the inhomogeneity of the steels microstructure. The variation in a cast steels microstructure results in a reduction in the magnitude of the materials B-H curve. The use of heat treatments improves the magnitude of the B-H curve but adds additional cost to the manufacture of the rotor.

The next generation of a solid salient pole rotor prototype should separate the rotor shaft and core pack. This would allow the use of billet steel, that has a homogeneous microstructure the magnitude of the B-H curve will be larger reducing the increase in voltage and current required to match the current rotors performance. By separating the rotor core pack and the shaft production other casting methods can be used to reduce the impurity levels of the steel. The combination of lower impurity levels and a more homogeneous microstructure will produce a rotor core that has better magnetic performance than the prototype produce for this thesis. The author suggested that the rotor core pack be split into equal parts along its longitudinal axis. These four parts could then be cut into 50mm long blocks the blocks can be produced using the casting method with the lowest levels of impurities associated with it such as vacuum induction melting. The 50mm long blocks could be built up into multiple different core lengths allowing the production of any of the current models of the HC4 type alternator.

The use of laser cladding to produce layers of soft magnetic material onto the face of a pole shoe allows the main body of the rotor to be shielded from induced eddy currents. The layers of deposited soft magnetic material must be laid down so the layers are built in the direction of the magnetic field.

The deposited material is highly anisotropic in nature due to the columnar crystal growth that occurs during the laser cladding process. The use of soft magnetic laser clad coatings allows the possibility of a graduated magnetic shield to protect the rotor from induced eddy currents. Before the composition of the layers can be determined the key points that the alternator operates at need to be experimental derived. Once these are known the testing of different compositions of alloys can be undertaken to find the required composition and layer depth for each layer of the magnetic shield.

References

[1] Y. X. and Z. T. Wenping Cao, “Advances in Wind Power,” 21-Nov-2012. [Online]. Available: http://www.intechopen.com/books/advances-in-wind-power/wind-turbine-generator-technologies. [Accessed: 29-Oct-2014].

[2] *BS EN 60404-4:1997+A2:2008 - Magnetic materials. Methods of measurement of d.c. magnetic properties of magnetically soft materials*. 1997.

[3] “Standard Practice for Sampling and Procurement Testing of Magnetic Materials.” ASTM International, 2012.

[4] A. H. Morrish, “The Magnetic Field,” in *The Physical Principles of Magnetism*, Wiley-IEEE Press, 2001, pp. 1–30.

[5] B. D. Cullity and C. D. Graham, “Diamagnetism and Paramagnetism,” in *Introduction to Magnetic Materials*, Wiley-IEEE Press, 2009, pp. 87–114.

[6] R. M. Bozorth, “Concepts of Ferromagnetism,” in *Ferromagnetism*, Wiley-IEEE Press, 1978, pp. 1–13.

[7] B. D. Cullity and C. D. Graham, “Antiferromagnetism,” *Introduction to Magnetic Materials*. Wiley-IEEE Press, pp. 151–173, 2009.

[8] B. D. Cullity and C. D. Graham, “Ferrimagnetism,” in *Introduction to Magnetic Materials*, Wiley-IEEE Press, 2009, pp. 175–195.

[9] Cogent Power Ltd, “M700-65A properties,” *Electrical Steel Non Oriented Fully Processed*. [Online]. Available: file:///E:/Aaran/EngD/Documents/Documents/EngD/Year 2/EngD project/Papers/Cogent Power Ltd.pdf. [Accessed: 14-Apr-2015].

[10] E. Della Torre, *Physics of Magnetism*. Wiley-IEEE Press, 1999.

[11] A. H. Morrish, “The Magnetization of Ferromagnetic Materials,” in *The Physical Principles of Magnetism*, Wiley-IEEE Press, 2001, pp. 332–431.

[12] J. Pyrhonen, T. Jokinen, and V. Hrabovcova, *Wiley: Design of Rotating Electrical Machines* -, 2nd ed. Wiley, 2009.

[13] J. R. Brauer, “Reluctance Method,” in *Magnetic Actuators and Sensors*, Wiley-IEEE Press, 2006, pp. 29–38.

[14] T. Marcic, G. Stumberger, and B. Stumberger, “Analyzing the Magnetic Flux Linkage Characteristics of Alternating Current Rotating Machines by Experimental Method,” *Magnetics, IEEE Transactions on*, vol. 47, no. 9. pp. 2283–2291, 2011.

[15] B. D. Cullity and C. D. Graham, “Magnetic Anisotropy,” in *Introduction to Magnetic Materials*, Wiley-IEEE Press, 2009, pp. 197–239.

[16] R. E. Matick, “Skin EffectNormal and Anomalous,” in *Transmission Lines and Communication Networks:An Introduction to Transmission Lines, High-frequency and High-speed Pulse Characteristics and Applications*, Wiley-IEEE Press, 1995, pp. 93–152.

[17] A. Hughes and B. Drury, “Synchronous and Brushless Permanent Magnet Machines and Drives BT - Electric Motors and Drives (Fourth Edition),” Boston: Newnes, 2013, pp. 281–313.

[18] K. Habib and H. Wenzel, “Exploring rare earths supply constraints for the emerging clean energy technologies and the role of recycling,” *J. Clean. Prod.*, vol. 84, pp. 348–359, Dec. 2014.

[19] L. Zhou, Y. Wu, W. Geng, Z. Zhang, and C. Liu, “Comparative study on concentrated-windings permanent magnet synchronous machines with different rotor structures for aircraft generator application,” *Electr. Mach. Syst. (ICEMS), 2015 18th Int. Conf.*, pp. 1246–1251, 2015.

[20] S. Mouty and C. Espanet, “Development of permanent magnet generators to integrate wind turbines into electricity transmission and distribution networks A2 - Bessède, Jean-Luc BT - Eco-Friendly Innovation in Electricity Transmission and Distribution Networks,” Oxford: Woodhead Publishing, 2015, pp. 243–262.

[21] B. Hague, “The shape of pole-shoe required to produce a sinusoidal distribution of air-gap flux density,” *Electr. Eng. J. Inst.*, vol. 62, no. 335, pp. 921–929, 1924.

[22] P. Rasilo, A. Belahcen, and A. Arkkio, “Effect of Rotor Pole-Shoe Construction on Losses of Inverter-Fed Synchronous Motors,” *IEEE Trans. Ind. Appl.*, vol. 50, no. 1, pp. 208–217, 2014.

[23] E. W. Kimbark, “Damper Windings and Damping,” in *Power System Stability*, Wiley-IEEE Press, 1995, pp. 214–246.

[24] E. M. Johnson and C. P. Holder, “The design of high-speed salient-pole a.c. generators for water-power plants,” *Proc. IEE - Part II Power Eng.*, vol. 99, no. 71, pp. 479–493, 1952.

[25] M. Liwschitz-Garik, “Harmonics of the Salient-Pole Synchronous Machine and Their Effects. Part I. MMF Harmonics Produced by the Armature and Damper Winding [includes discussion],” *Trans. Am. Inst. Electr. Eng. Part III Power Appar. Syst.*, vol. 75, no. 3, p. 1, 1956.

[26] M. J. Melfi, J. Ikäheimo, and R. Lawrence, “A comparison of current motor technologies appropriate for petroleum and chemical applications,” in *Petroleum and Chemical Industry Technical Conference (PCIC), 2012 Record of Conference Papers Industry Applications Society 59th Annual IEEE*, 2012, pp. 1–8.

[27] G. Klempner and I. Kerszenbaum, “Generator Design and Construction,” in *Handbook of Large Turbo-Generator Operation and Maintenance*, John Wiley & Sons, Inc., 2008, pp. 39–119.

[28] C. Danielsson and C. Sadarangani, “Experimental determination of the parameters for a salient rotor synchronous machine with and without pole screens,” *Electr. Mach. 2008. ICEM 2008. 18th Int. Conf.*, pp. 1–6, 2008.

[29] D. Ogilvie, S. Ratchev, C. Gerada, and S. Grace, “Proposed methodology to combine design concept and manufacturing process selection for distributed wound stator cores,” in *2015 IEEE International Electric Machines & Drives Conference (IEMDC)*, 2015, pp. 1305–1311.

[30] F. Dreher and N. Parspour, “Reducing the cogging torque of PM Transverse Flux Machines by discrete skewing of a segmented stator,” *Electr. Mach. (ICEM), 2012 XXth Int. Conf.*, pp. 454–457, 2012.

[31] E. L. Kaiser, P. J. Savagians, and P. J. Savagian, “Method of manufacturing segmented stator cores.” Google Patents, 03-Jan-2013.

[32] B. Bickel, J. Franke, and T. Albrecht, “Manufacturing cell for winding and assembling a segmented stator of PM-synchronous machines for hybrid vehicles,” *Electric Drives Production Conference (EDPC), 2012 2nd International*. pp. 1–5, 2012.

[33] B. D. Chamberlin and C. Ramey, “Segmented stator assembly for hybrid or electric type vehicle traction motor, has isolators serially connected by interlocks to form cavity closed along assembly axial length and electrically insulating lamination segments from conductors.” Chamberlin B D; Ramey C; Remy Technologies Llc.

[34] J. Brettschneider, R. Spitzner, and R. Boehm, “Flexible mass production concept for segmented BLDC stators,” in *Electric Drives Production Conference (EDPC), 2013 3rd International*, 2013, pp. 1–8.

[35] *The Electricity Safety, Quality and Continuity Regulations 2002*. Queen's Printer of Acts of Parliament.

[36] A. von Meier, "Generators," in *Electric Power Systems:A Conceptual Introduction*, Wiley-IEEE Press, 2006, pp. 85–126.

[37] E. Dlala, A. Belahcen, J. Pippuri, and A. Arkkio, "Interdependence of Hysteresis and Eddy-Current Losses in Laminated Magnetic Cores of Electrical Machines," *IEEE Trans. Magn.*, vol. 46, no. 2, pp. 306–309, 2010.

[38] E. Lamprecht, M. Hoemme, T. Albrecht, and Ieee, "Investigations of Eddy Current Losses in Laminated Cores Due to the Impact of Various Stacking Processes," *2012 2nd Int. Electr. Drives Prod. Conf.*, 2012.

[39] "Principles of Electric Generators," in *Synchronous Generators, Second Edition*, CRC Press, 2015, pp. 13–69.

[40] P. Chrin, M. David, P. Maussion, J. Saint-Michel, E. Fournier, and L. Bun, "Modeling iron, mechanical and rotor copper losses in induction machine with the design of experiments," in *IECON 2014 - 40th Annual Conference of the IEEE Industrial Electronics Society*, 2014, pp. 729–735.

[41] R. D. Vecchio, "The calculation of eddy current losses associated with rotating magnetic fields in thin laminations," *IEEE Trans. Magn.*, vol. 18, no. 6, pp. 1707–1709, 1982.

[42] G. Bertotti, "General properties of power losses in soft ferromagnetic materials," *IEEE Trans. Magn.*, vol. 24, no. 1, pp. 621–630, 1988.

[43] A. J. Clerc and A. Muetze, "Measurement of stator core magnetic degradation during the manufacturing process," *IEEE Trans. Ind. Appl.*, vol. 48, pp. 1344–1352, 2012.

[44] B. D. Cullity and C. D. Graham, "Hard Magnetic Materials," in *Introduction to Magnetic Materials*, Wiley-IEEE Press, 2009, pp. 477–504.

[45] Y. L. Sun *et al.*, “The phase and microstructure analysis of Alnico magnets with high coercivity,” *J. Magn. Magn. Mater.*, vol. 379, pp. 58–62, Apr. 2015.

[46] Z. CHEN, “Global rare earth resources and scenarios of future rare earth industry,” *J. Rare Earths*, vol. 29, no. 1, pp. 1–6, Jan. 2011.

[47] D. D. Rao, “MagWeb,” *World’s Largest Database of Soft Magnetic Materials*, 2018. [Online]. Available: http://magweb.us/consultancy/.

[48] B. D. Cullity and C. D. Graham, “Soft Magnetic Materials,” in *Introduction to Magnetic Materials*, Wiley-IEEE Press, 2009, pp. 439–476.

[49] P. Beckley, *Electrical Steels for rotating machines*, 1st ed. The Istitute of Electrical Engineers, 2002.

[50] A. Sonboli, M. R. Toroghinejad, H. Edris, and J. A. Szpunar, “Effect of deformation route and intermediate annealing on magnetic anisotropy and magnetic properties of a 1wt% Si non-oriented electrical steel,” *J. Magn. Magn. Mater.*, vol. 385, pp. 331–338, Jul. 2015.

[51] J. Liu, Y. Sha, K. Hu, F. Zhang, and L. Zuo, “Formation of Cube and Goss Texture After Primary Recrystallization in Electrical Steels,” *Metall. Mater. Trans. A*, vol. 45, no. 1, pp. 134–138, 2014.

[52] S. Habermehl, D. C. Jiles, and C. M. Teller, “Influence of heat treatment and chemical composition on the magnetic properties of ferromagnetic steels,” *Magn. IEEE Trans.*, vol. 21, no. 5, pp. 1909–1911, 1985.

[53] T. Sohmura and F. E. Fujita, “The effect of hydrogen on the magnetic properties of Fe-Ni base Invar alloys,” *J. Phys. F Met. Phys.*, vol. 10, no. 4, pp. 743–754, Apr. 1980.

[54] J. Steel, “Soft-magnetic materials in large turbo-alternators,” *Magnetics, IEEE Transactions on*, vol. 10, no. 2. pp. 151–154, 1974.

[55] H.-Y. Song *et al.*, “Effect of hot rolling reduction on microstructure, texture and ductility of strip-cast grain-oriented silicon steel with different solidification structures,” *Mater. Sci. Eng. A*, vol. 605, pp. 260–269, 2014.

[56] J.-T. Park and J. A. Szpunar, “Effect of initial grain size on texture evolution and magnetic properties in nonoriented electrical steels,” *J. Magn. Magn. Mater.*, vol. 321, no. 13, pp. 1928–1932, 2009.

[57] H.-T. Liu *et al.*, “Fabrication of high permeability non-oriented electrical steels by increasing 〈001〉 recrystallization texture using compacted strip casting processes,” *J. Magn. Magn. Mater.*, vol. 374, pp. 577–586, Jan. 2015.

[58] “Special-Purpose Nickel Alloys,” *ASM Spec. Handb. Nickel, Cobalt, Their Alloy.*, 2000.

[59] F. Bloch, T. Waeckerle, and H. Fraisse, “The use of iron-nickel and iron-cobalt alloys in electrical engineering, and especially for electrical motors,” in *2007 Electrical Insulation Conference and Electrical Manufacturing Expo*, 2007, pp. 394–401.

[60] “London Metals Exchange.” [Online]. Available: http://www.lme.com/. [Accessed: 19-Jul-2016].

[61] D. C. Jiles, “Recent advances and future directions in magnetic materials,” *Acta Mater.*, vol. 51, no. 19, pp. 5907–5939, Nov. 2003.

[62] P. Beckley, *Chapter 6 - Range of Materials*. Institution of Engineering and Technology, 2002.

[63] G. Zu, X. Zhang, J. Zhao, Y. Cui, Y. Wang, and Z. Jiang, “Analysis of the microstructure, texture and magnetic properties of strip casting 4.5wt.% Si non-oriented electrical steel,” *Mater. Des.*, vol. 85, pp. 455–460, Nov. 2015.

[64] H.-Z. Li, H.-T. Liu, Z.-Y. Liu, H.-H. Lu, H.-Y. Song, and G.-D. Wang, “Characterization of microstructure, texture and magnetic properties in twin-roll casting high silicon non-oriented electrical steel,” *Mater. Charact.*, vol. 88, pp. 1–6, Feb. 2014.

[65] “Metastable Iron-Carbon (Fe-C) Phase Diagram.” [Online]. Available: http://www.calphad.com/iron-carbon.html. [Accessed: 18-Jan-2017].

[66] F. Bertinelli, F. Fudanoki, T. Komori, G. Peiro, and L. Rossi, “Production of Austenitic Steel for the LHC Superconducting Dipole Magnets,” *IEEE Trans. Appl. Supercond.*, vol. 16, no. 2, pp. 1773–1776, 2006.

[67] G. Krauss, “Pearlite,Ferrite, and Cementite,” in *Steels - Processing, Structure, and Performance*, ASM International, 2005.

[68] V. I. Razumovskiy and G. Ghosh, “A first-principles study of cementite (Fe3C) and its alloyed counterparts: Structural properties, stability, and electronic structure,” *Comput. Mater. Sci.*, vol. 110, pp. 169–181, 2015.

[69] D. C. Jiles, “Magnetic properties and microstructure of AISI 1000 series carbon steels,” *J. Phys. D. Appl. Phys.*, vol. 21, no. 7, p. 1186, 1988.

[70] H. Kikuchi, F. Ito, T. Murakami, and K. Takekawa, “Relationship Between Magnetic Properties and Hardness and Its Effect on Recovery and Recrystallization in Cold-Rolled Steel,” *IEEE Trans. Magn.*, vol. 51, no. 11, pp. 1–4, 2015.

[71] V. . Gavriljuk, “Decomposition of cementite in pearlitic steel due to plastic deformation,” *Mater. Sci. Eng. A*, vol. 345, no. 1–2, pp. 81–89, Mar. 2003.

[72] A. Sumner, G. Chris, B. Neil, and A. Clare, “Controlling DC permeability in cast steels,” *J. Magn. Magn. Mater.*, 2016.

[73] N. P. Zhetvin, L. N. Podvoiskii, A. I. Paisov, and E. P. Kapustina, “Heat treatment of low-carbon magnetic core steel,” *Met. Sci. Heat Treat. Met.*, vol. 2, no. 11, pp. 595–598, 1960.

[74] A. Ramazani, S. Kazemiabnavi, and R. Larson, “Quantification of ferrite-martensite interface in dual phase steels: A first-principles study,” *Acta Mater.*, vol. 116, pp. 231–237, Sep. 2016.

[75] G. Krauss, “Martensite in steel: strength and structure,” *Mater. Sci. Eng. A*, vol. 273–275, pp. 40–57, Dec. 1999.

[76] J. W. Byeon and S. I. Kwun, “Magnetic Evaluation of Microstructures and Strength of Eutectoid Steel,” *Mater. Trans.*, vol. 44, no. 10, pp. 2184–2190, 2003.

[77] G. Thomas, “Retained austenite and tempered martensite embrittlement,” *Metall. Trans. A*, vol. 9, no. 3, pp. 439–450, 1978.

[78] H. K. D. H. Bhadeshia and J. W. Christian, “Bainite in steels,” *Metall. Trans. A*, vol. 21, no. 3, pp. 767–797, 1990.

[79] J. S. M. Pedrosa, S. da C. Paolinelli, and A. B. Cota, “Influence of initial annealing on structure evolution and magnetic properties of 3.4% Si non-oriented steel during final annealing,” *J. Magn. Magn. Mater.*, vol. 393, pp. 146–150, Nov. 2015.

[80] R. Ranjan, D. Jiles, and P. Rastogi, “Magnetic properties of decarburized steels: An investigation of the effects of grain size and carbon content,” *IEEE Trans. Magn.*, vol. 23, no. 3, pp. 1869–1876, 1987.

[81] J.-S. Chen, C. Yu, and H. Lu, “Phase stability, magnetism, elastic properties and hardness of binary iron nitrides from first principles,” *J. Alloys Compd.*, vol. 625, pp. 224–230, 2015.

[82] Y. Jirásková, S. Havlíček, O. Schneeweiss, V. Peřina, and C. Blawert, “Characterization of iron nitrides prepared by spark erosion, plasma nitriding, and plasma immersion ion implantation,” *J. Magn. Magn. Mater.*, vol. 234, no. 3, pp. 477–488, 2001.

[83] Z. Janjušević, Z. Gulišija, S. Radosavljević, and Z. Aćimović, “A contribution to study of processes on the steel cast–sand mould contact surface during casting,” *Mater. Lett.*, vol. 45, no. 5, pp. 235–240, Sep. 2000.

[84] “Designing for investment casting.” [Online]. Available: http://machinedesign.com/basics-design/designing-investment-casting. [Accessed: 27-Apr-2015].

[85] G. Y. Chin and J. H. Wernick, “Chapter 2 Soft magnetic metallic materials,” 1980, pp. 55–188.

[86] S. Khaple and R. G. Baligidad, “Effect of Melting Process on the Microstructure and Mechanical Properties of Fe--7 wt{%} Al Alloy,” *Trans. Indian Inst. Met.*, vol. 65, no. 1, pp. 57–61, 2012.

[87] K. Jenkins and M. Lindenmo, “Precipitates in electrical steels,” *J. Magn. Magn. Mater.*, vol. 320, no. 20, pp. 2423–2429, 2008.

[88] R. N. Nelsen, “The effects of atmosphere on decarburizing of magnetic steels,” *1985 EIC 17th Electrical/Electronics Insulation Conference*. pp. 255–256, 1985.

[89] J. Bennett, “Effects of Heat Treatment Variations on Surface Conditions of Iron-Nickel Alloys and the influence on Mercury Switch Behavior,” *IEEE Transactions on Components, Hybrids, and Manufacturing Technology*, vol. 3, no. 1. pp. 172–180, 1980.

[90] G. Zu, X. Zhang, J. Zhao, Y. Cui, Y. Wang, and Z. Jiang, “Analysis of the microstructure, texture and magnetic properties of strip casting 4.5 wt.% Si non-oriented electrical steel,” *Mater. Des.*, vol. 85, pp. 455–460, Nov. 2015.

[91] J. J. Sidor, K. Verbeken, E. Gomes, J. Schneider, P. R. Calvillo, and L. A. I. Kestens, “Through process texture evolution and magnetic properties of high Si non-oriented electrical steels,” *Mater. Charact.*, vol. 71, pp. 49–57, 2012.

[92] V. P. Ramunni, T. D. P. Coelho, and P. E. V de Miranda, “Interaction of hydrogen with the microstructure of low-carbon steel,” *Mater. Sci. Eng. A*, vol. 435–436, pp. 504–514, 2006.

[93] M. B. Djukic, V. S. Zeravcic, G. Bakic, A. Sedmak, and B. Rajicic, “Hydrogen Embrittlement of Low Carbon Structural Steel,” *Procedia Mater. Sci.*, vol. 3, pp. 1167–1172, 2014.

[94] J. Lufrano, P. Sofronis, and H. K. Birnbaum, “Modeling of hydrogen transport and elastically accommodated hydride formation near a crack tip,” *J. Mech. Phys. Solids*, vol. 44, no. 2, pp. 179–205, Feb. 1996.

[95] R. A. Oriani and P. H. Josephic, “Equilibrium and kinetic studies of the hydrogen-assisted cracking of steel,” *Acta Metall.*, vol. 25, no. 9, pp. 979–988, Sep. 1977.

[96] M. L. Martin, J. A. Fenske, G. S. Liu, P. Sofronis, and I. M. Robertson, “On the formation and nature of quasi-cleavage fracture surfaces in hydrogen embrittled steels,” *Acta Mater.*, vol. 59, no. 4, pp. 1601–1606, Feb. 2011.

[97] Subcommittee: F42.91, “ASTM ISO/ASTM52900 Standard Terminology for Additive Manufacturing – General Principles – Terminology.” ASTM International, 2017.

[98] W. E. Frazier, “Metal Additive Manufacturing: A Review,” *J. Mater. Eng. Perform.*, vol. 23, no. 6, pp. 1917–1928, Jun. 2014.

[99] B. Zhang, N.-E. Fenineche, H. Liao, and C. Coddet, “Microstructure and Magnetic Properties of Fe–Ni Alloy Fabricated by Selective Laser Melting Fe/Ni Mixed Powders,” *J. Mater. Sci. Technol.*, vol. 29, no. 8, pp. 757–760, 2013.

[100] B. Zhang, N.-E. Fenineche, L. Zhu, H. Liao, and C. Coddet, “Studies of magnetic properties of permalloy (Fe–30%Ni) prepared by {SLM} technology,” *J. Magn. Magn. Mater.*, vol. 324, no. 4, pp. 495–500, 2012.

[101] B. Zhang, N.-E. Fenineche, H. Liao, and C. Coddet, “Magnetic properties of in-situ synthesized FeNi3 by selective laser melting Fe-80%Ni powders,” *J. Magn. Magn. Mater.*, vol. 336, pp. 49–54, 2013.

[102] J. O. Obielodan, “Fabrication of Multi-Material Structures Using Ultrasonic Consolidation and Laser-Engineered Net Shaping,” 2010.

[103] C. Y. Kong, R. C. Soar, and P. M. Dickens, “Optimum process parameters for ultrasonic consolidation of 3003 aluminium,” *J. Mater. Process. Technol.*, vol. 146, no. 2, pp. 181–187, 2004.

[104] D. Herzog, V. Seyda, E. Wycisk, and C. Emmelmann, “Additive manufacturing of metals,” *Acta Mater.*, vol. 117, pp. 371–392, 2016.

[105] L. E. Murr *et al.*, “Fabrication of Metal and Alloy Components by Additive Manufacturing: Examples of 3D Materials Science,” *J. Mater. Res. Technol.*, vol. 1, no. 1, pp. 42–54, 2012.

[106] A. Schoppa and P. Delarbre, “Soft Magnetic Powder Composites and Potential Applications in Modern Electric Machines and Devices,” *IEEE Trans. Magn.*, vol. 50, no. 4, pp. 1–4, Apr. 2014.

[107] I. W. Donaldson, “Care needed to select the right SMC materials and processes,” *Met. Powder Rep.*, vol. 59, no. 11, pp. 30–33, Dec. 2004.

[108] H. Shokrollahi and K. Janghorban, “Soft magnetic composite materials (SMCs),” *J. Mater. Process. Technol.*, vol. 189, no. 1–3, pp. 1–12, Jul. 2007.

[109] M. Xu, J. Li, J. Jiang, and B. Li, “Influence of Powders and Process Parameters on Bonding Shear Strength and Micro Hardness in Laser Cladding Remanufacturing,” *Procedia CIRP*, vol. 29, pp. 804–809, 2015.

[110] T. M. Yue and T. Li, “Solidification Behaviour and the Evolution of Microstructure in the Laser Cladding of Aluminium on Magnesium Substrate,” *Mater. Trans.*, vol. 48, no. 5, pp. 1064–1069, 2007.

[111] T. L. Starr, K. Rafi, B. Stucker, and C. M. Scherzer, “Controlling phase composition in selective laser melted stainless steels,” *Power (W)*, vol. 195, p. 195, 2012.

[112] M. N. Ahsan, A. J. Pinkerton, R. J. Moat, and J. Shackleton, “A comparative study of laser direct metal deposition characteristics using gas and plasma-atomized Ti–6Al–4V powders,” *Mater. Sci. Eng. A*, vol. 528, no. 25–26, pp. 7648–7657, Sep. 2011.

[113] A. Alagheband and C. Brown, “Plasma Atomization goes commercial,” *Met. Powder Rep.*, vol. 53, no. 11, pp. 26–28, 1998.

[114] S. Hisano and K. Saito, “Research and development of metal powder for magnetic recording,” *J. Magn. Magn. Mater.*, vol. 190, no. 3, pp. 371–381, 1998.

[115] H. Zhao, Z. Zhu, C. Xiong, X. Xu, and Q. Lin, “The effect of transverse magnetic field treatment on wave-absorbing properties of FeNi alloy powders,” *J. Magn. Magn. Mater.*, p. -, 2016.

[116] W. Xie, E. Polikarpov, J.-P. Choi, M. E. Bowden, K. Sun, and J. Cui, “Effect of ball milling and heat treatment process on MnBi powders magnetic properties,” *J. Alloys Compd.*, vol. 680, pp. 1–5, 2016.

[117] Q. Fang *et al.*, “The structure and magnetic properties of Sm–Fe–N powders prepared by ball milling at low temperature,” *J. Magn. Magn. Mater.*, vol. 410, pp. 116–122, 2016.

[118] M. Persson, B. Chalmers, A. Mulki, R. Carlson, N. Sadowski, and L. O. Grander, “New manufacturing methods for electric motors using different soft magnetic material combinations,” *2012 2nd Int. Electr. Drives Prod. Conf.*, vol. 1995, no. 4, pp. 1–7, Oct. 2012.

[119] “BS 3100 -:1991 Specification for steel castings for general engineering purposes.” .

[120] S. W, “Bh curve and iron loss measurements for magnetic materials,” Adelaide, 2008.

[121] Handbook Committee, “ASM Handbook, Materials Characterizations,” pp. 299–308.

[122] E. Girault *et al.*, “Metallographic Methods for Revealing the Multiphase Microstructure of TRIP-Assisted Steels,” *Mater. Charact.*, vol. 40, no. 2, pp. 111–118, Feb. 1998.

[123] G. F. Vander Voort, “Etching isothermally treated steels,” *Heat Treat. Prog.*, vol. 1, no. 2, pp. 25–32, 2001.

[124] X. Liu, “Microstructural Characterisation of Pearlitic and Complex Phase Steels Using Image Analysis Methods,” The University of Birmingham, 2014.

[125] B. Gehrmann, “Nickel–iron alloys with special soft magnetic properties for specific applications,” *J. Magn. Magn. Mater.*, vol. 290–291, pp. 1419–1422, Apr. 2005.

[126] “ISO 1302:1992 - Technical drawings -- Method of indicating surface texture.” [Online]. Available: https://www.iso.org/standard/5883.html. [Accessed: 21-Mar-2017].

[127] M. R. Shah and S. B. Lee, “Optimization of Shield Thickness of Finite Length Rotors for Eddy Current Loss Minimization,” *Conf. Rec. 2006 IEEE Ind. Appl. Conf. Forty-First IAS Annu. Meet.*, vol. 5, pp. 2368–2373, 2006.

[128] L. Zhu, L. Luo, Y. Wu, and J. Cheng, “Microstructure and tribological properties of laser clad Ni-Ag/Tic composite coating,” *J. Wuhan Univ. Technol. Sci. Ed.*, vol. 29, no. 2, pp. 242–245, Apr. 2014.

[129] J. Dutta Majumdar, R. Galun, B. . Mordike, and I. Manna, “Effect of laser surface melting on corrosion and wear resistance of a commercial magnesium alloy,” *Mater. Sci. Eng. A*, vol. 361, no. 1–2, pp. 119–129, Nov. 2003.

[130] D. D. Gu, W. Meiners, K. Wissenbach, and R. Poprawe, “Laser additive manufacturing of metallic components: materials, processes and mechanisms,” *Int. Mater. Rev.*, vol. 57, no. 3, pp. 133–164, 2012.

[131] C. V Mikler *et al.*, “Laser additive processing of Ni-Fe-V and Ni-Fe-Mo Permalloys: Microstructure and magnetic properties,” *Mater. Lett.*, vol. 192, pp. 9–11, 2017.

[132] S. Acquaviva *et al.*, “Pulsed laser deposition of Co- and Fe-based amorphous magnetic films and multilayers,” *Thin Solid Films*, vol. 433, no. 1–2, pp. 252–258, Jun. 2003.

[133] K. Gupta, K. K. Raina, and S. K. Sinha, “Influence of process parameters and alloy composition on structural, magnetic and electrical characteristics of Ni–Fe permalloys,” *J. Alloys Compd.*, vol. 429, no. 1–2, pp. 357–364, 2007.

[134] C.-W. CHEN, “CHAPTER 5 - METALLURGY OF SOFT MAGNETIC MATERIALS BT - Magnetism and Metallurgy of Soft Magnetic Materials,” Elsevier, 1977, pp. 171–367.

[135] “Standard Specification for Wrought Nickel-Iron Soft Magnetic Alloys (UNS K94490, K94840, N14076, N14080).” ASTM International, 2013.

[136] M. Akhtari Zavareh, A. A. D. Mohammed Sarhan, P. Akhtari Zavareh, and W. J. Basirun, “Electrochemical corrosion behavior of carbon steel pipes coated with a protective ceramic layer using plasma and HVOF thermal spray techniques for oil and gas,” *Ceram. Int.*, vol. 42, no. 2, pp. 3397–3406, Feb. 2016.

[137] N. C. Ghosh, H. N. Das, M. A. Gafur, and A. K. M. A. Hossain, “Formation and Magnetic Properties of Nanocrystalline 78.5-permalloy by Mechanical Alloying,” *Procedia Eng.*, vol. 90, pp. 136–139, 2014.

[138] M. Abshinova, “Factors Affecting Magnetic Properties of Fe-Si-Al and Ni-Fe-Mo Alloys,” *Procedia Eng.*, vol. 76, pp. 35–44, 2014.

[139] F. Pfeifer and C. Radeloff, “Soft magnetic Ni-Fe and Co-Fe alloys - some physical and metallurgical aspects,” *J. Magn. Magn. Mater.*, vol. 19, no. 1–3, pp. 190–207, Apr. 1980.

[140] H.-T. Liu *et al.*, “Formation of {001} <510> recrystallization texture and magnetic property in strip casting non-oriented electrical steel,” *Mater. Lett.*, vol. 81, pp. 65–68, Aug. 2012.

[141] C.-K. Hou, “The effects of grain size on the magnetic properties of fully processed, continuous-annealed low-carbon electrical steels,” *IEEE Trans. Magn.*, vol. 32, no. 2, pp. 471–477, 1996.

[142] R. D. Enoch and A. D. Fudge, “High magnetic permeability in Ni-Fe alloys,” *Br. J. Appl. Phys.*, vol. 17, no. 5, p. 623, 1966.

[143] Q. Wu and M. A. Zikry, “Prediction of diffusion assisted hydrogen embrittlement failure in high strength martensitic steels,” *J. Mech. Phys. Solids*, vol. 85, pp. 143–159, Dec. 2015.

[144] H. Naumoski, A. Maucher, and U. Herr, “Investigation of the influence of global stresses and strains on the magnetic properties of electrical steels with varying alloying content and grain size,” *Electric Drives Production Conference (EDPC), 2015 5th International*. pp. 1–8, 2015.

[145] Couderchon, G. and Gautard, D., “Magnetic aging of 80% Ni Mo permalloy,” *J. Phys. IV Fr.*, vol. 08, pp. Pr2–433–Pr2–436, 1998.

[146] R. . Oriani, “The diffusion and trapping of hydrogen in steel,” *Acta Metall.*, vol. 18, no. 1, pp. 147–157, Jan. 1970.

[147] D. S. Dos Santos and P. E. V De Miranda, “Hydrogen diffusivity and solubility in crystalline and amorphous alloys,” *J. Mater. Sci.*, vol. 32, no. 23, pp. 6311–6315, Dec. 1997.

Appendix A

- **Effect of heat treatments on the B-H curve of sample AS1**

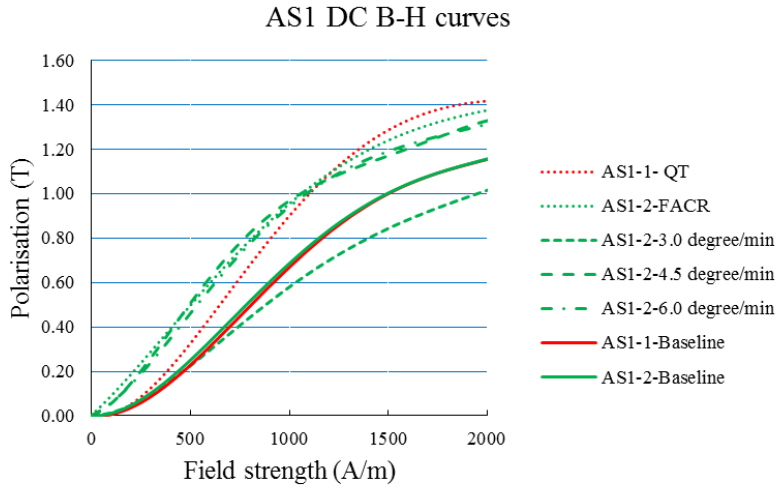


Fig 1. The effect of heat treatments on the B-H curve of a sample of A4 grade steel. The annealed samples all perform better than the normalised sample except the annealed at a cooling rate of 3.0°C/min which has the lowest B-H curve for this sample. The quenched sample initially has a large response to an applied field and then has a reduction in response until 1000A/m than its response increases sharply.

In Fig 1 the effect of heat treatments on the B-H curve of sample AS1 is compared to the normalised sample. The highest permeability is obtained is obtained when the FACR is applied when the applied field strength is below 1250A/m. For higher applied field strengths (>1250A/m) the quenched sample performs better.

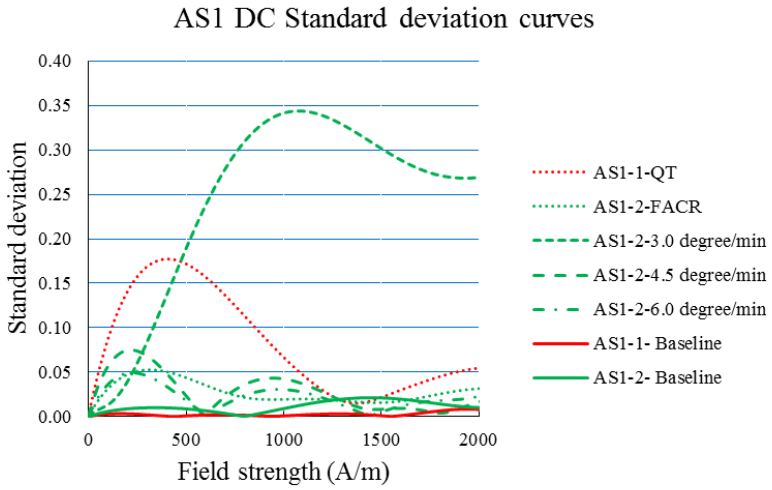


Fig 2. The standard deviation of the data for the B-H curves for sample AS2

In Fig 2 the standard deviation of the datasets for sample AS1 is shown the lowest values of deviation occur at the knee points at the start of the magnetisation curve and at the end of the linear section of the magnetisation curve. The dataset with the largest deviation is the annealed at a cooling rate of 3.0 degrees/min.

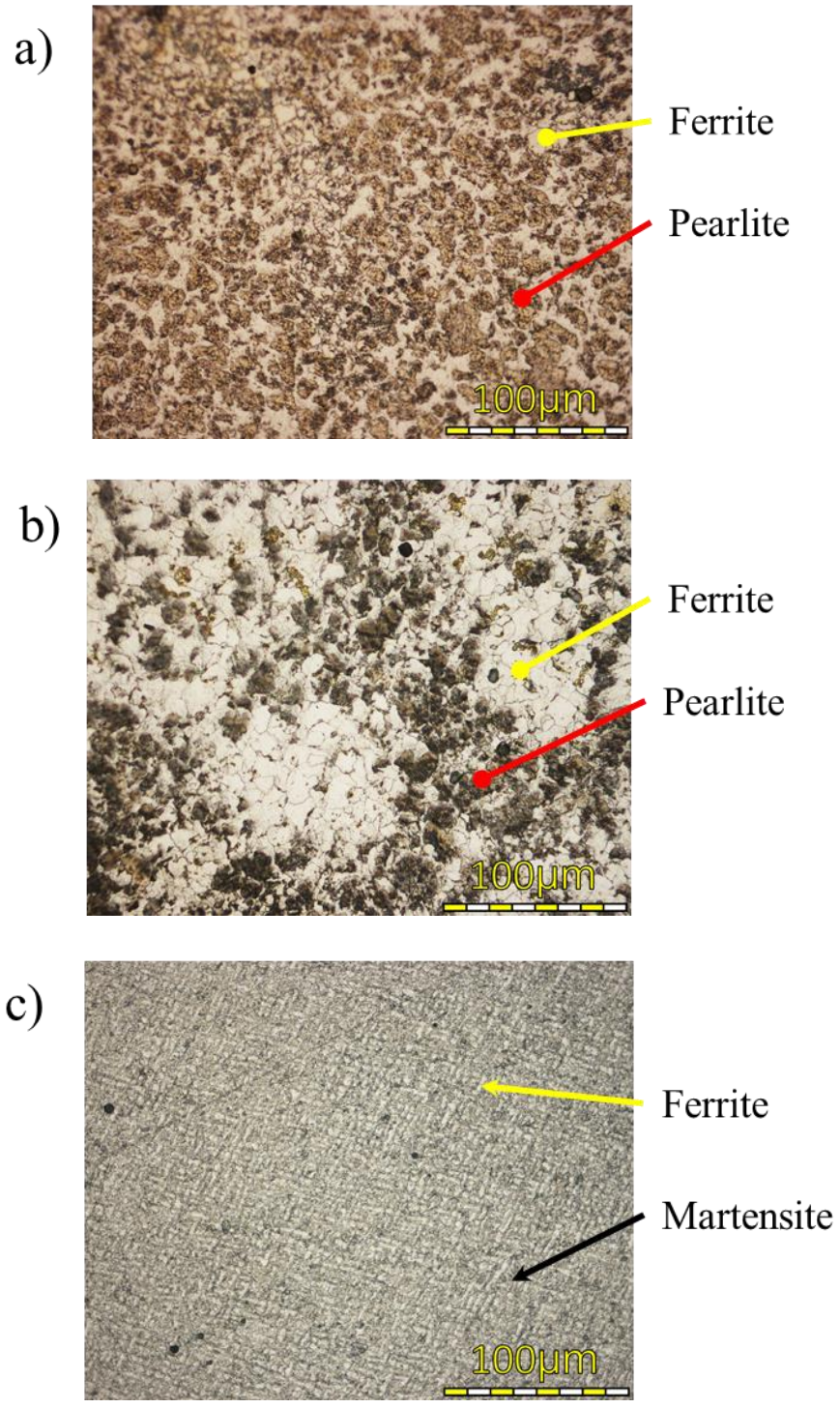


Fig 3. (a) image of the ferrite/pearlite microstructure of the normalised A4 grade steel, (b) image of ferrite/pearlite microstructure of the annealed A4 grade steel, (c) image of the ferrite/martensite microstructure of the quenched A4 grade steel.

Fig 3, (a) shows the microstructure of the normalised sample, the majority of the images crystals are pearlite. The low volume of ferrite crystals present in the microstructure further reduces the permeability of the normalised sample. Fig 3**Error! Reference source not found.** (b) is an image of the FACR sample. The microstructure has undergone a significant change due to the slower cooling rate. The crystals are larger than in Fig 3(a), resulting in fewer grain boundaries which gives a stronger response to an applied field. The pearlite appears to have changed form a cross between course and fine pearlite to only fine pearlite. The ferrite crystals also appear more uniformly white when compared with the greyer coloured ferrite in Fig 3 (a). The combination of larger ferrite crystals and less cementite inclusions in the ferrite and a uniform fine pearlite has resulted in the annealed sample having a large response to an applied magnetic field than the normalised sample.

Fig 3 (c) shows the quenched sample's image. This sample has a very fine microstructure that contains a large volume of fine ferrite crystals separated by martensite crystals. The large number of strongly ferromagnetic ferrite and less strongly ferromagnetic martensite results in a B-H curve which is higher than the annealed sample once the field strength reached 1000A/m and the martensites initial resistance to magnetisation is overcome.

- **Effect of heat treatments on the B-H curve of sample AS2**

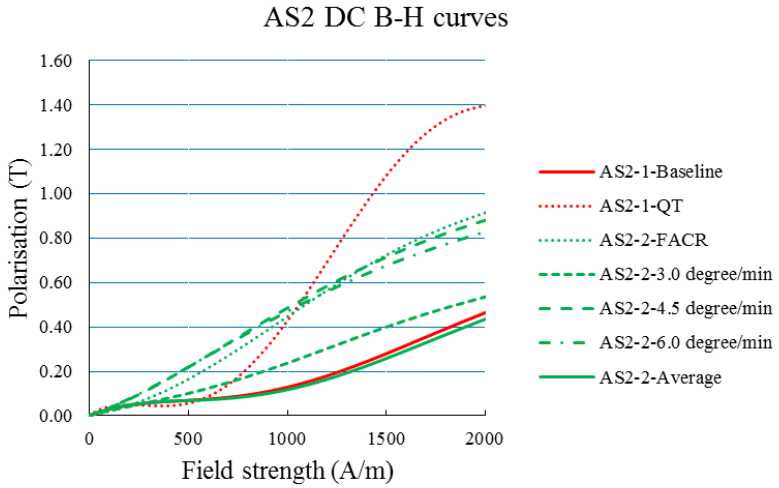


Fig 4. The effect of heat treatments on the permeability of a sample of BT3 grade steel. The best performing sample in terms of B-H curve is the quenched sample. The annealed samples all show a higher B-H curve apart from the annealed at a cooling rate of 3.0°C/min which has a similar B-H curve to the normalised sample.

In Fig 4 the effect of heat treatments on the B-H curve of sample AS2 is compared to the normalised sample. The largest B-H curve is obtained by quenching after the field strength rises above 750A/m. The normalised sample has a low B-H curve when compared to all but the 3.0°C/min annealing cooling rate.

For the annealed samples the best cooling rate the FACR, however the quenched samples significantly out performs any of the annealing cooling rates especially once the field strength rises above 750A/m

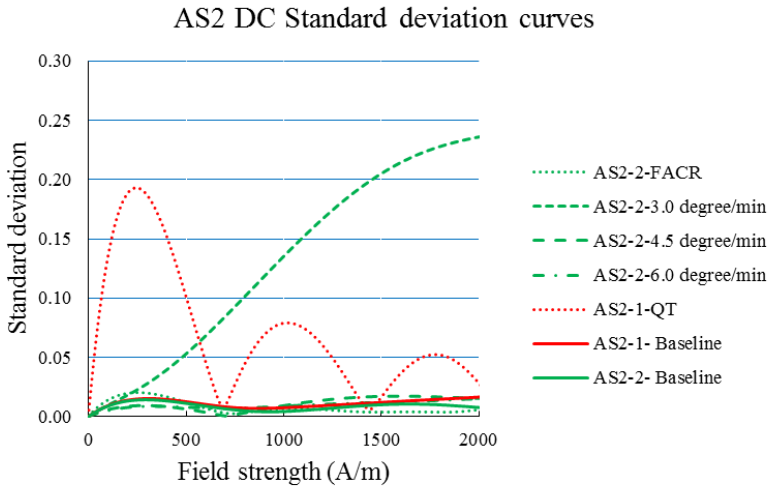


Fig 5. The standard deviation of the data for the B-H curves for sample AS2

In Fig 5 the standard deviation of the datasets for sample AS2 is shown the lowest values of deviation occur at the knee points at the start of the magnetisation curve and at the end of the linear section of the magnetisation curve. The dataset with the largest deviation is the annealed at a cooling rate of 3.0 degrees/min.

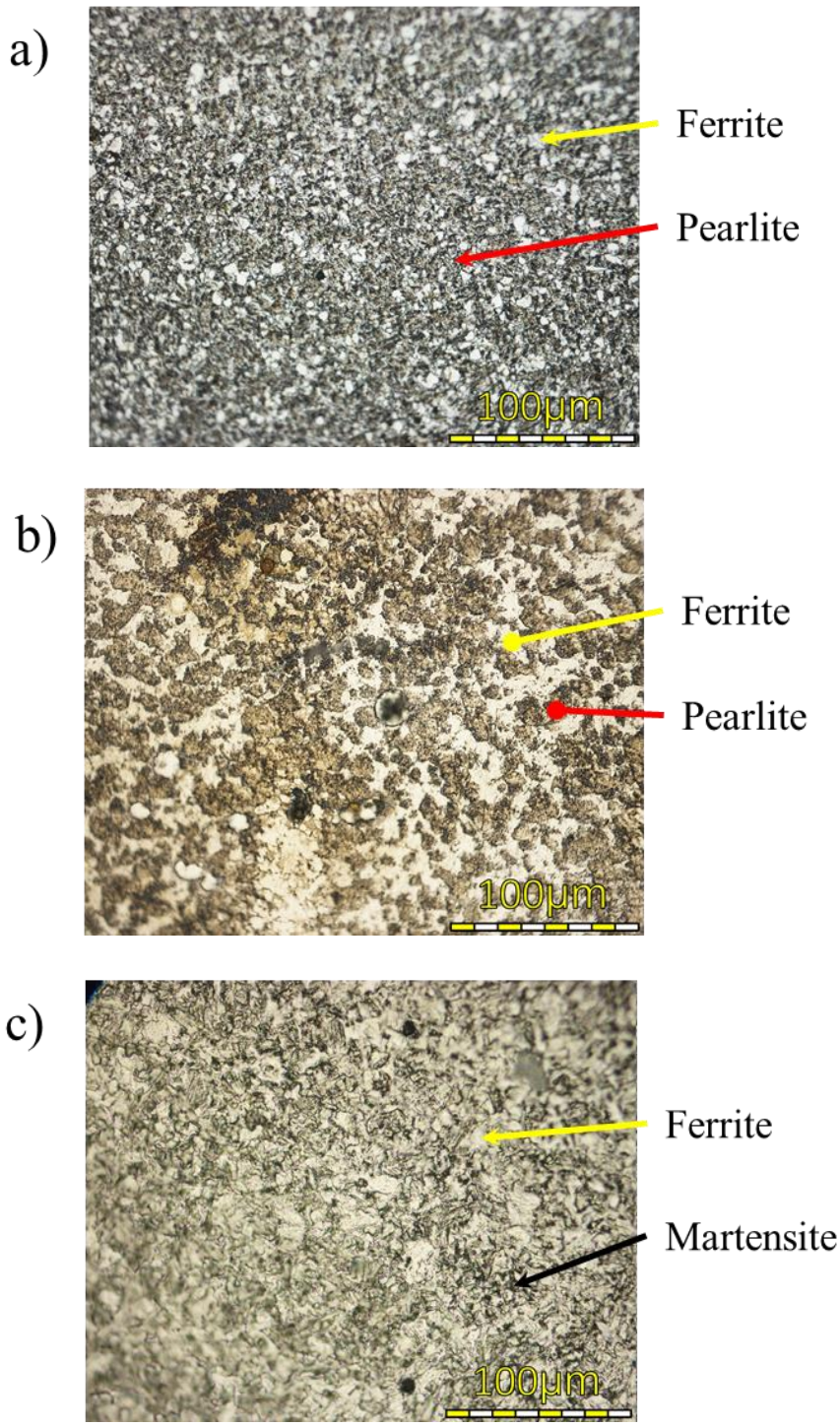


Fig 6 (a) image of the ferrite/pearlite microstructure of the normalised BT3 grade steel, (b) image of ferrite/pearlite microstructure of the annealed BT3 grade steel, (c) image of the ferrite/martensite microstructure of the quenched BT3 grade steel.

Fig 6 (a) shows the microstructure of the normalised sample, it has a large volume of coarse pearlite and small amounts of ferrite crystals resulting in a low permeability. Fig 6 (b) shows the microstructure of the FACR sample. The pearlite and ferrite crystals are larger than in Fig 6 (a) resulting in a higher B-H curve than the normalised sample. Fig 6Error! Reference source not found. **(**c) shows the microstructure of the quenched sample, the crystal size is similar to the annealed sample, however the quantity of martensite and ferrite means the B-H curve is higher than for both the annealed and normalised sample once the field strength overcomes the martensites resistance to magnetisation.

- **Effect of heat treatments on the B-H curve of sample AS3**

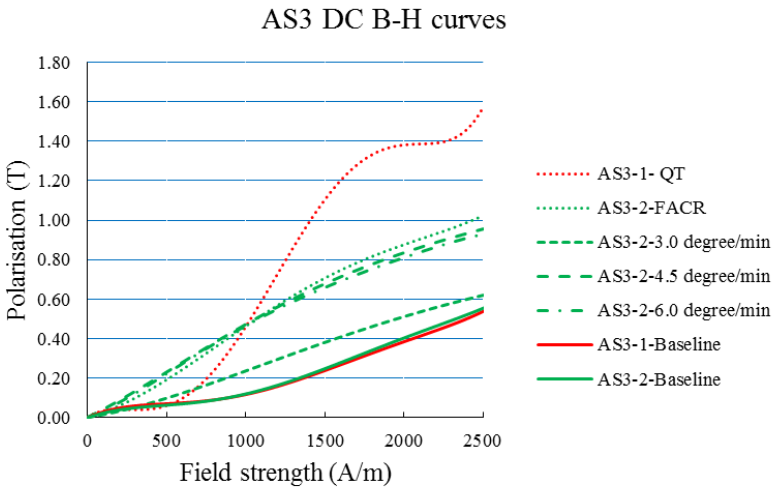


Fig 7. The effect of heat treatments on the B-H curve of a sample of BT1 grade steel. The best preforming samples are those that are annealed at cooling rates of 4.5°C/min, 6.0°C/min, and FACR until the field strength reaches 1000A/m. At this point the annealed at 3.0°C/min cooling rate and the quenched sample overtake all of the other samples in terms of performance. The best preforming sample, after 1000A/m is the annealed at a cooling rate of 3.0°C/min.

In Fig 7 the effect of heat treatments on the B-H curve of sample AS3 is compared to the normalised sample. The highest B-H curve, before the field strength reaches 1000A/m, are the annealed samples with cooling rates of 4. .5°C/min, 6.0°C/min, and FACR. After a field strength of 1000A/m is reached the best performing sample becomes the annealed at a cooling rate of 3.0°C/min. The next biggest improvement in B-H curve height is from quenching. The worst performing sample is the normalised sample. The other annealing process have a similar effect on magnetic performance.

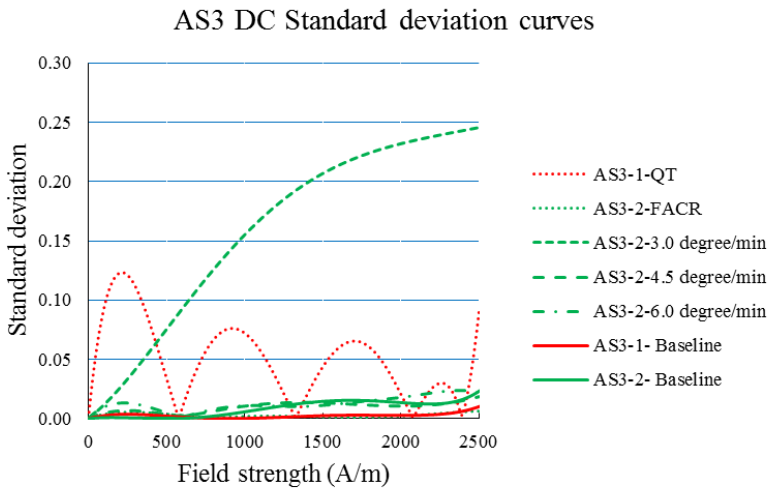


Fig 8. The standard deviation of the data for the B-H curves for sample AS3

In Fig 8 the standard deviation of the datasets for sample AS3 is shown the lowest values of deviation occur at the knee points at the start of the magnetisation curve and at the end of the linear section of the magnetisation curve. The dataset with the largest deviation is the annealed at a cooling rate of 3.0 degrees/min.

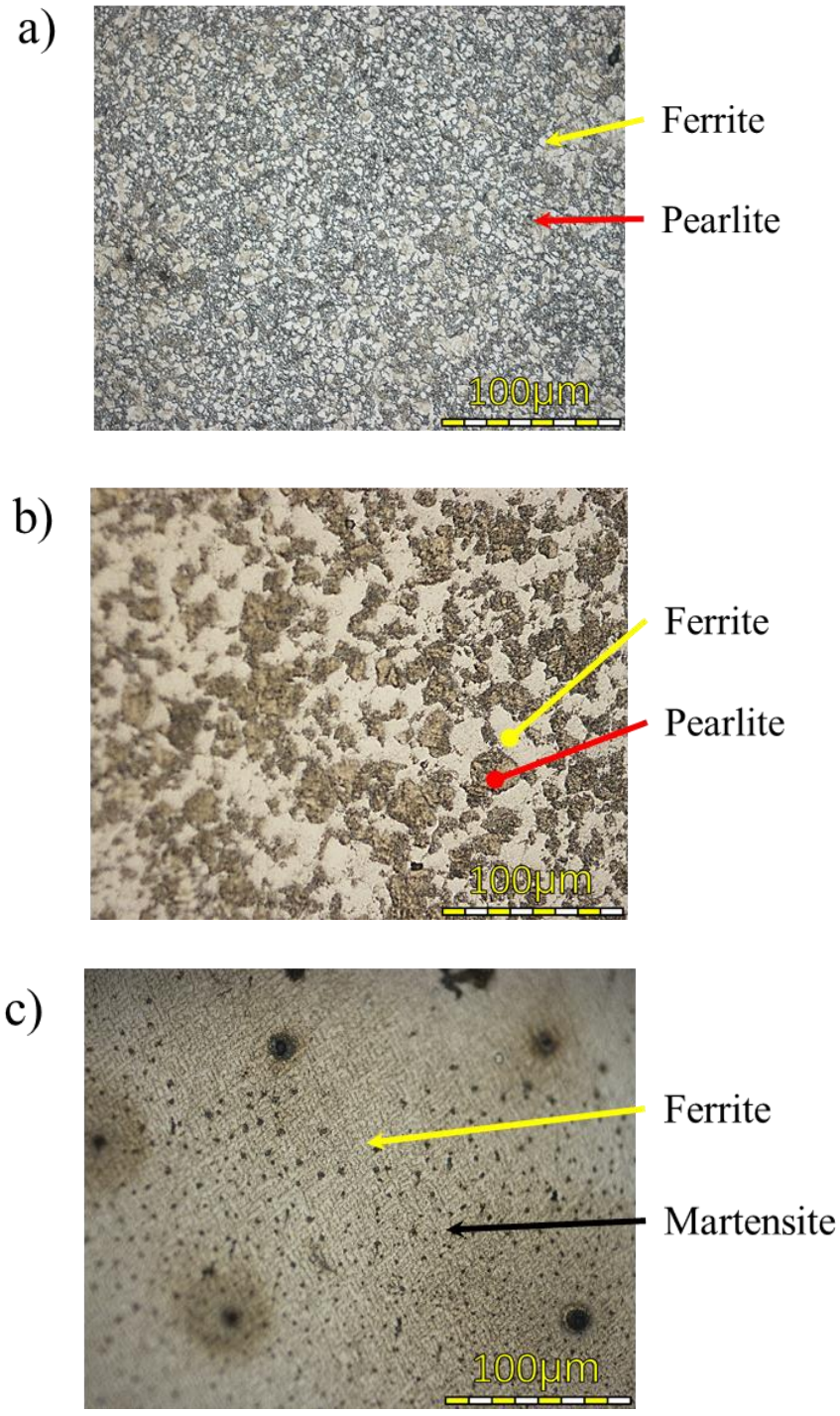


Fig 9. (a) image of the ferrite/pearlite microstructure of the normalised BT1 grade steel, (b) image of ferrite/pearlite microstructure of the annealed BT1 grade steel, (c) image of the ferrite/martensite microstructure of the quenched BT1 grade steel.

In Fig 9 (a) the microstructure of the normalised samples is shown to be a coarse pearlite with small ferrite crystals. The small crystal size of the pearlite and ferrite result in the low B-H curve of the normalised sample. Fig 9 (b) shows the microstructure after annealing, when compared to Fig 9**Error! Reference source not found.** (a) the fine pearlite and ferrite crystals are much larger resulting in the increased permeability. Fig 6 (c) shows a very fine martensite microstructure with small ferrite crystals that result in a high B-H curve once the martensites initial resistance to magnetisation is overcome.

- **Effect of heat treatments on the B-H curve of sample AS5**

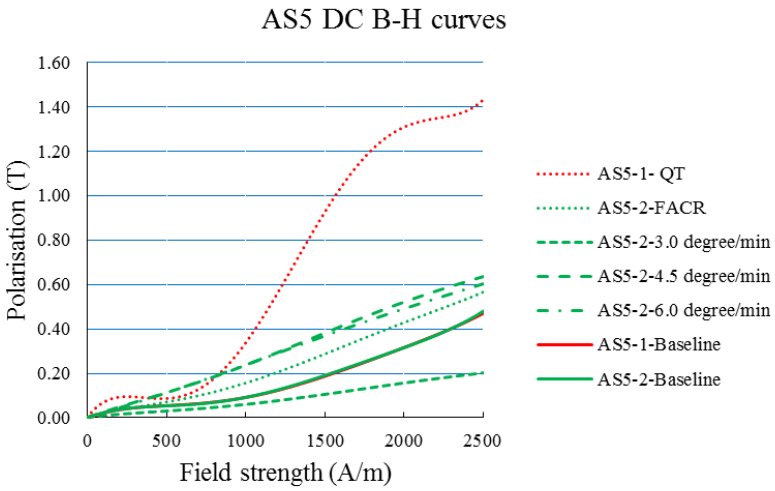


Fig 10. The effect of heat treatments on the B-H curve of a sample of P310 grade steel. The best performing sample is the quenched. The annealed samples all perform better than the normalised sample, except the annealed at a cooling rate of 3.0°C/min.

InFig 10. The effect of heat treatments on the B-H curve of a sample of P310 grade steel. The best performing sample is the quenched. The annealed samples all perform better than the normalised sample, except the annealed at a cooling rate of 3.0°C/min. Fig 10 the effect of heat treatments on the B-H curve of sample AS5 is compared to the normalised sample. The highest B-H curve is obtained by the quenching heat treatment. Annealing produced the three highest increases with only the cooling rate of 3.0°C/min preforming worse than the normalised sample.

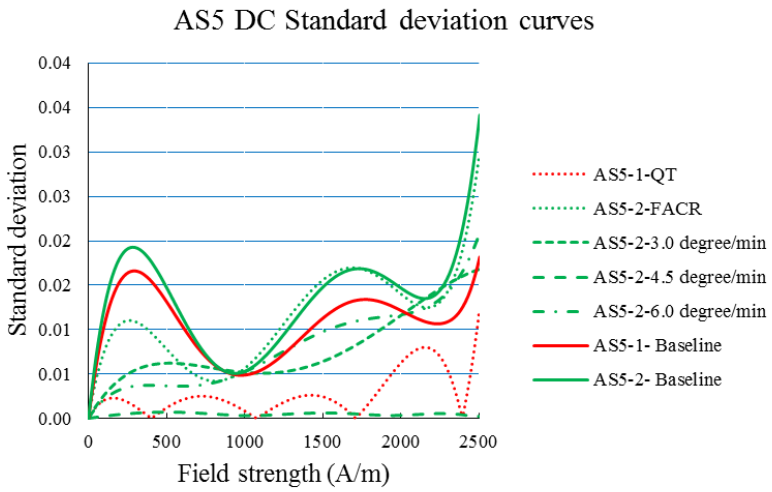


Fig 11. The standard deviation of the data for the B-H curves for sample AS5

In Fig 8Fig 11 the standard deviation of the datasets for sample AS5 is shown the lowest values of deviation occur at the knee points at the start of the magnetisation curve and at the end of the linear section of the magnetisation curve. The dataset with the largest deviation is the FACR sample.

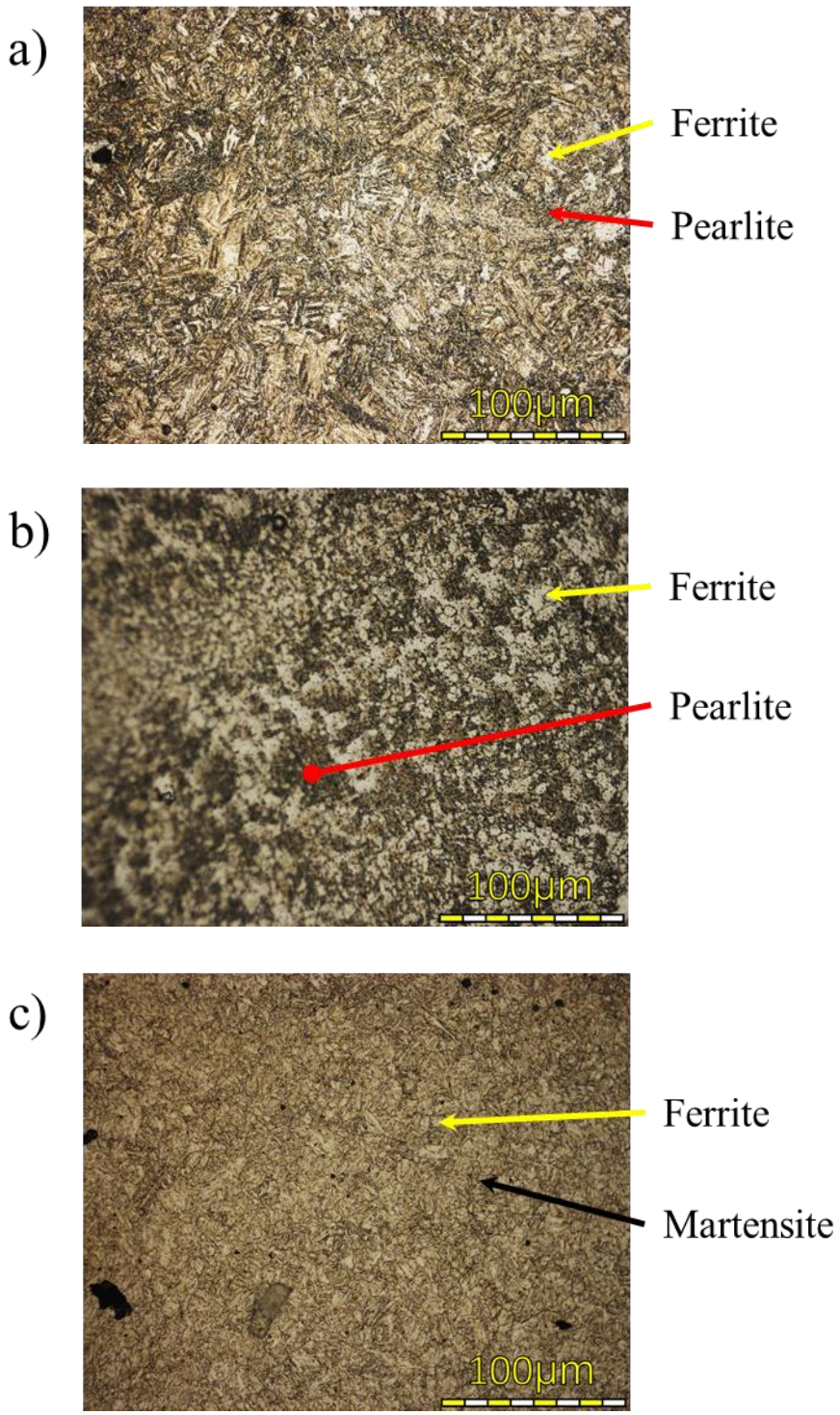


Fig 12 (a) image of the ferrite/pearlite microstructure of the normalised P310 grade steel, (b) image of ferrite/pearlite microstructure of the annealed P310 grade steel, (c) image of the ferrite/martensite microstructure of the quenched P310 grade steel.

Fig 12 (a) shows the microstructure of the normalised sample, it has a coarse pearlite structure with few ferrite crystals resulting in low permeability. Fig 12 (b) shows the microstructure of the FARC sample. Its microstructure has a mix of fine and coarse pearlite with more ferrite crystals than in the quenched sample (Fig 12.a). This is the cause of the slight improvement in its B-H curve. The high pearlite content of the normalised and annealed samples means that the number of pinning sites are very high reducing the size of the B-H curve. Fig 12 (c) shows the microstructure of the quenched sample. The structure has few ferrite crystals and is almost entirely made up of martensite crystals. Martensite is more strongly ferromagnetic than coarse pearlite due to the reduction in pinning sites, this results in the quenched sample having a much higher permeability

- **Effect of heat treatments on the B-H curve of sample AS6**

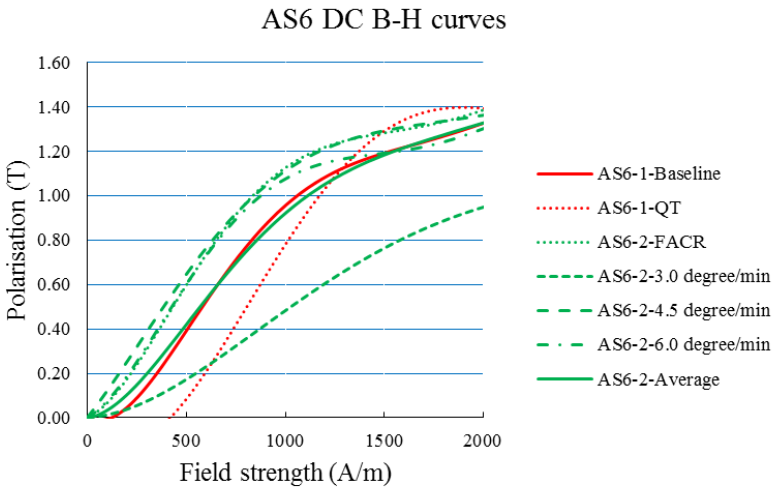


Fig 13. The effect of heat treatments on the B-H curve of a sample of A2 grade steel. The annealed, at a cooling rate of 4.5°C/min has the highest permeability followed by all of the other annealed samples except annealed at a cooling rate of 3.0°C/min which has the lowest B-H curve of all the samples. The normalised sample has a B-H curve that closely matches that of the annealed samples. The quenched sample, once resistance to magnetisation is overcome at 750A/m, has a steeper B-H curve than any of the other heat treatments.

In Fig 13 the effect of heat treatments on the B-H curve of sample AS6 is compared to the normalised sample. The highest B-H curve is obtained by annealing with a cooling rate of 4.5°C/min, the lowest is given by annealing at a cooling rate of 3.0°C/min. Quenching produces a low initial polarisation response but after 750A/m the rate of response increases rapidly. At 2500 A/m the quenched sample is comparable to all of the other heat treatments except annealing at 3.0°C/min.

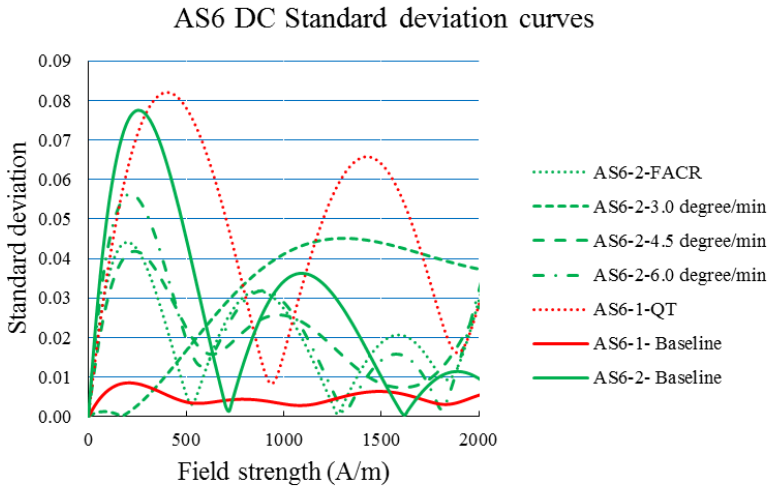


Fig 14. The standard deviation of the data for the B-H curves for sample AS6

In Fig 8Fig 14 the standard deviation of the datasets for sample AS6 is shown the lowest values of deviation occur at the knee points at the start of the magnetisation curve and at the end of the linear section of the magnetisation curve. The dataset with the largest deviation is the FACR sample.

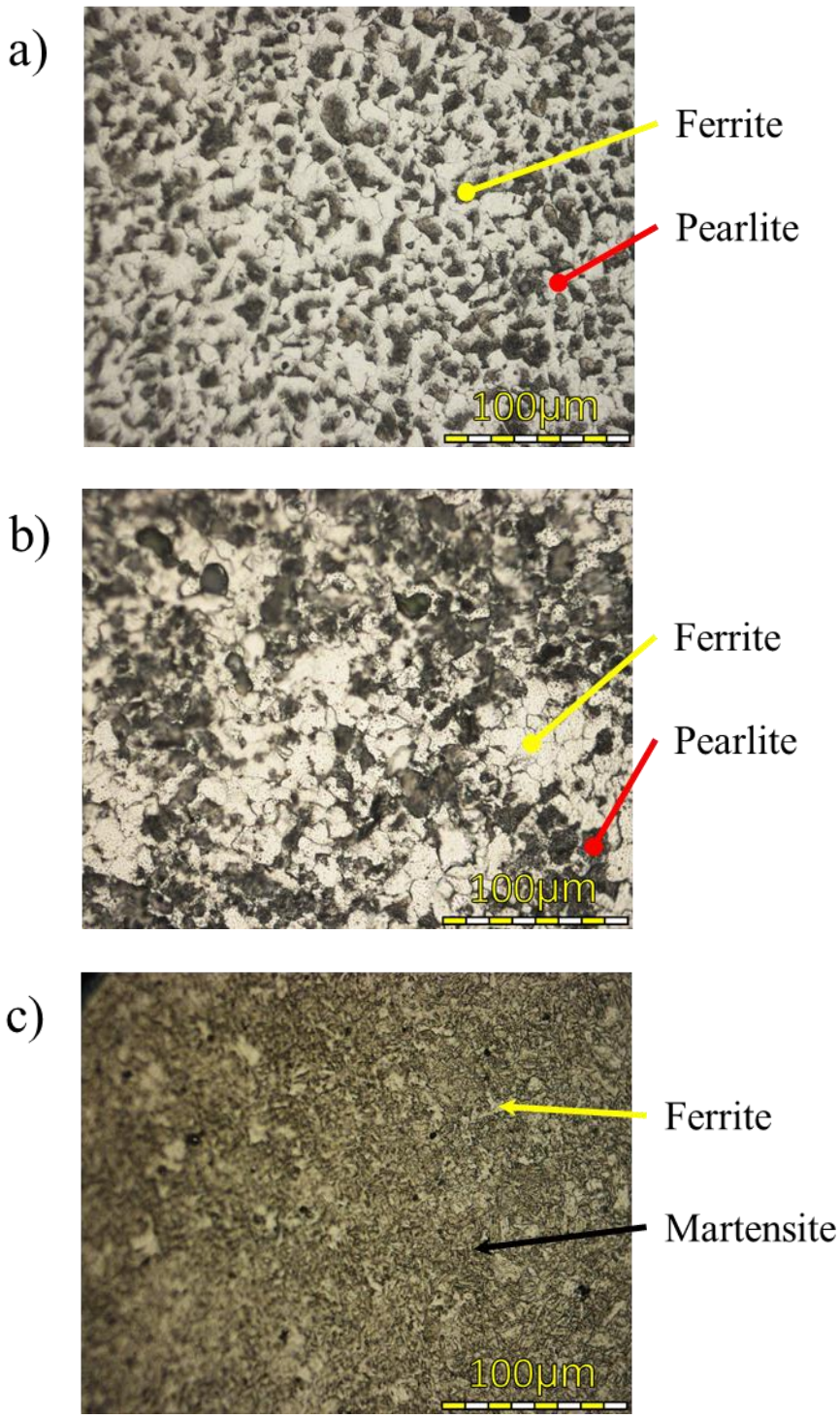


Fig 15 (a) image of the ferrite/pearlite microstructure of the normalised A2 grade steel, (b) image of ferrite/pearlite microstructure of the annealed A2 grade steel, (c) image of the ferrite/martensite microstructure of the quenched A2 grade steel.

Fig 15 (a) shows the microstructure of the normalised sample, the structure consists of fine pearlite and ferrite. The structure of the normalised samples looks similar to that shown for sample AS4 in its normalised state (Figure 4-9.b). Fig 12.(b) shows the microstructure of the annealed sample. The crystals are larger than in the normalised sample and the ferrite appears to contain less cementite inclusions. The larger crystal size reduces grain boundaries increasing the B-H curve, whist the reduction in inclusions reduces pinning sites which also increase the height of the B-H curve. Fig 12.(c) has a martensitic structure with small ferrite crystals present as a result of the tempering. The martensitic structure is slower to respond to an applied field but once it responds the polarisation increases rapidly.

- **Effect of heat treatments on the B-H curve of sample AS7**

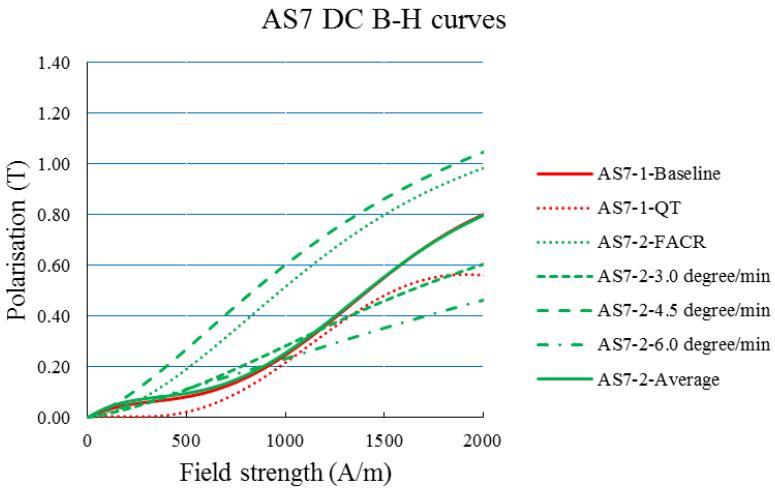


Fig 16. The effect of heat treatments on the B-H curve of a sample of MSS013 grade steel. The sample with the highest B-H curve is the annealed at a cooling rate of 4.5°C/min. The normalised sample has a higher B-H curve than two of the annealed samples, whilst the quenched sample has very low initial response that increase rapidly after the field strength reaches 1000A/m.

In Fig 16 the effect of heat treatments on the B-H curve of sample AS7 is compared to the normalised sample. The highest B-H curve is obtained by annealing at a cooling rate of 4.5°C/min. Annealing at a cooling rate of 3.0°C/min and 6.0°C/min both result in a lower permeability than the normalised sample, as does quenching. The 4.5°C/min and FACR cooling rate increase the B-H curve whereas the 6.0°C/min results in a decrease in polarisation response.

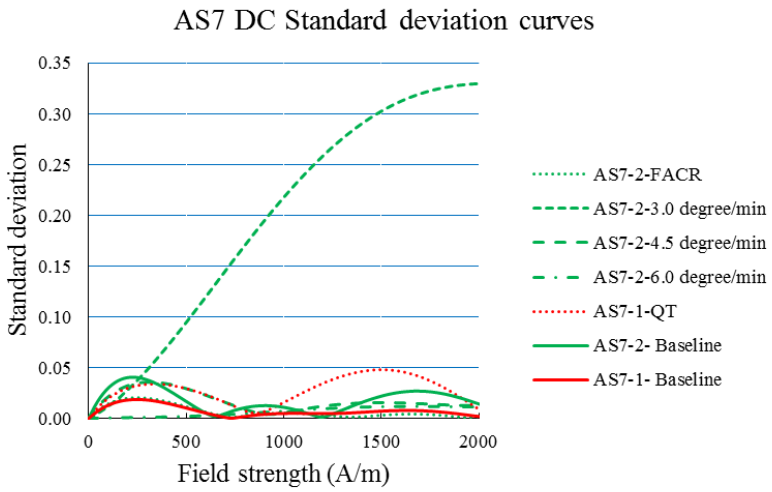


Fig 17. The standard deviation of the data for the B-H curves for sample AS7

In Fig 8Fig 17 the standard deviation of the datasets for sample AS7 is shown the lowest values of deviation occur at the knee points at the start of the magnetisation curve and at the end of the linear section of the magnetisation curve. The dataset with the largest deviation is the FACR sample.

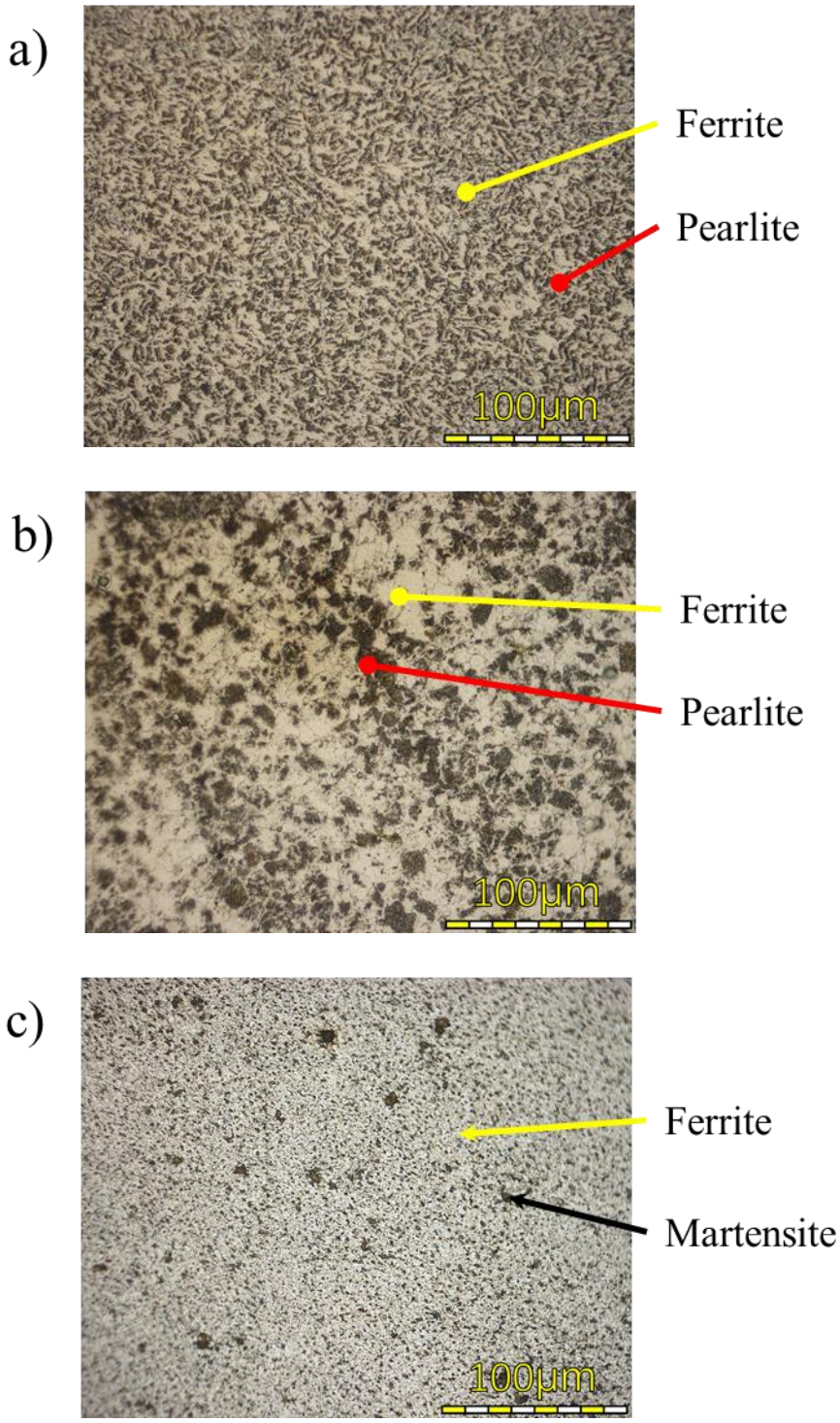


Fig 18 (a) image of the ferrite/pearlite microstructure of the normalised MSS013 grade steel, (b) image of ferrite/pearlite microstructure of the annealed MSS013 grade steel, (c) image of the ferrite/martensite microstructure of the quenched MSS013 grade steel.

Fig 18.(a) shows the microstructure of the normalised sample, it has a mixture of fine pearlite and small ferrite crystals. Fig 18 (b) shows the microstructure of the FACR sample. It has a comparable mixture of fine pearlite and ferrite as Fig 18.(a), but the crystal size is larger. This results in a higher B-H curve than the normalised sample. In Fig 18 (c) the quenched samples microstructure is shown, it shows a large amount of small ferrite crystals with small martensite crystals. The small crystal size and the lack of large ferrite crystals reduces the samples performance.

- **Effect of heat treatments on the B-H curve of sample AS9**

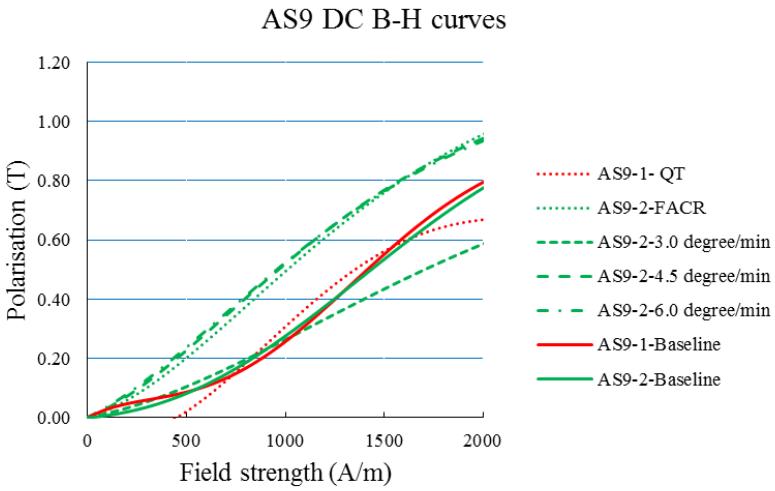


Fig 19. The effect of heat treatments on the B-H curve of a sample of P330 grade steel. The annealed samples with cooling rates of 4.5°C/min, 6.0°C/min, and FACR have a very similar-H response. The annealed at a cooling rate of 3.0°C/min has the lowest B-H curve. The quenched sample does not show the initial resistance to magnetisation that the other steel samples have shown and does not have a sharp increase in polarisation response as the field strength increases.

In Fig 19 the effect of heat treatments on the B-H curve of sample AS9 is compared to the normalised sample. The highest B-H curve is obtained by three of the annealing cooling rates: 4.5°C/min, 6.0°C/min, and FACR which produce near identical improvements in polarisation response when compared to the normalised sample. The 3.0°C/min cooling rate produces a reduction in response as does quenching (after 1500A/m).

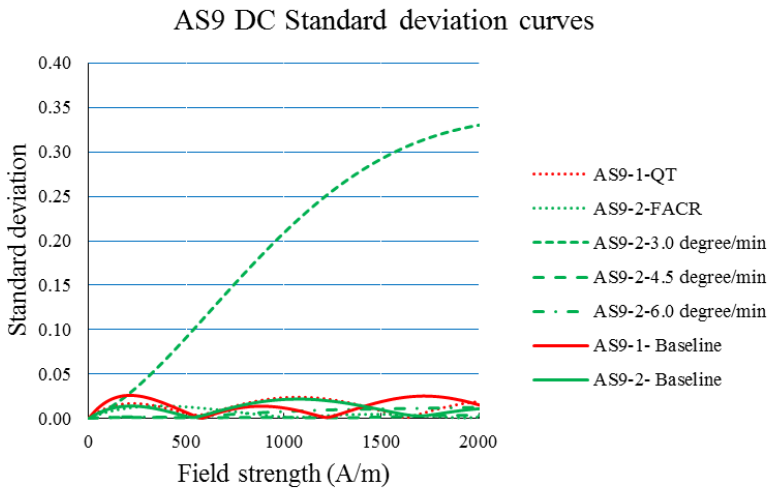


Fig 20. The standard deviation of the data for the B-H curves for sample AS9

In Fig 8Fig 20 the standard deviation of the datasets for sample AS9 is shown the lowest values of deviation occur at the knee points at the start of the magnetisation curve and at the end of the linear section of the magnetisation curve. The dataset with the largest deviation is the annealing at 3.0 degrees/min.

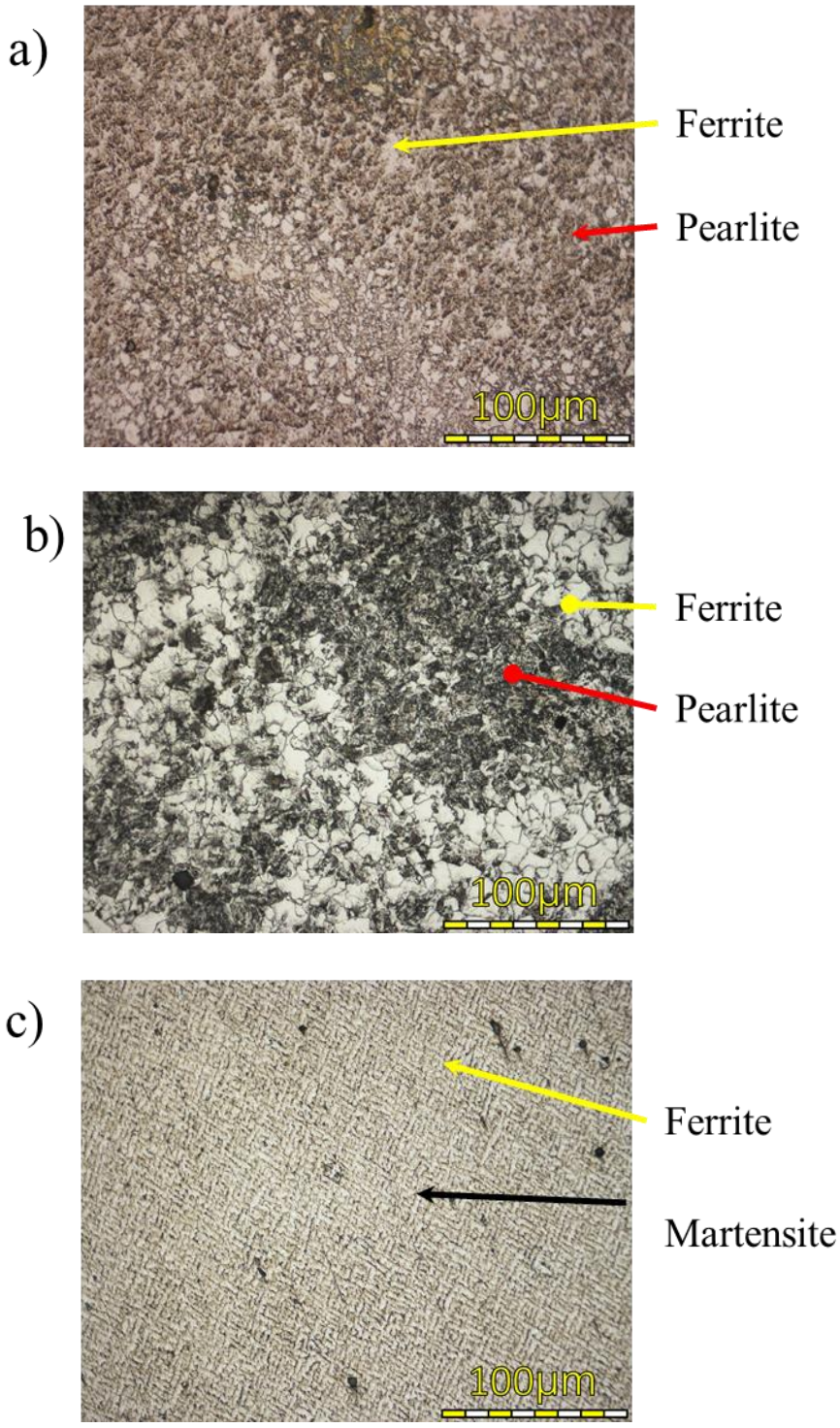


Fig 21 (a) image of the ferrite/pearlite microstructure of the normalised P330 grade steel, (b) image of ferrite/pearlite microstructure of the annealed P330 grade steel, (c) image of the ferrite/martensite microstructure of the quenched P330 grade steel.

Fig 21**Error! Reference source not found.**.(a) shows the normalised samples microstructure, it comprises of coarse pearlite and a few ferrite crystals. Fig 21 (b) shows the annealed sample's microstructure, it shows fine pearlite with ferrite crystals The increase in performance from the normalised to the annealed sample is due to the increase in ferrite and the larger crystal size. Fig 21 (c) shows the quenched sample's microstructure which shows a fine martensite structure with small ferrite crystals.

- **Effect of heat treatments on the B-H curve of sample AS10**

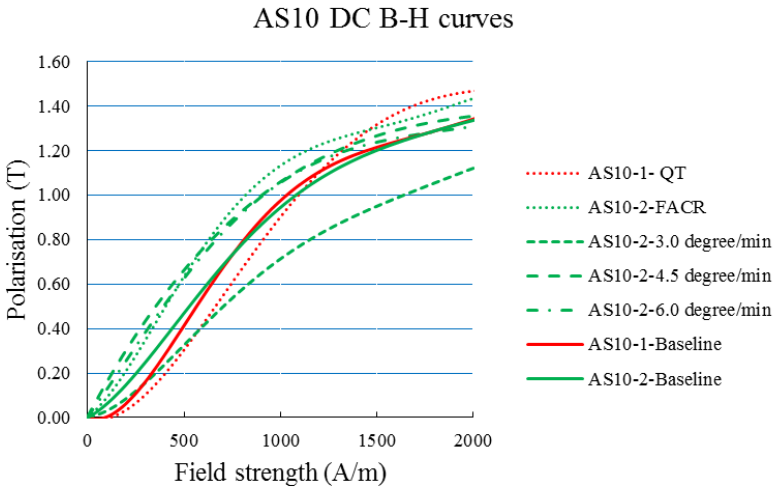


Fig 22. The effect of heat treatments on the B-H curve of a sample of A2 grade steel. Up until the field strength reaches 1500A/m three annealed samples (cooling rates of 4.5°C/min, 6.0°C/min, and FACR) have the highest B-H curves. After 1500A/m the quenched sample has the highest B-H curve. The annealing at 3.0°C/min cooling rate has the lowest B-H curve below that of the normalised sample.

In Fig 22 the effect of heat treatments on the B-H curve of sample AS10 is compared to the normalised sample. The highest B-H curve is obtained by all the annealing heat treatments, bar the 3.0°C/min cooling rate which results in a reduction in the B-H curve. The quenched sample overtakes the annealed samples, in terms of polarisation response increase, after 1500A/m.

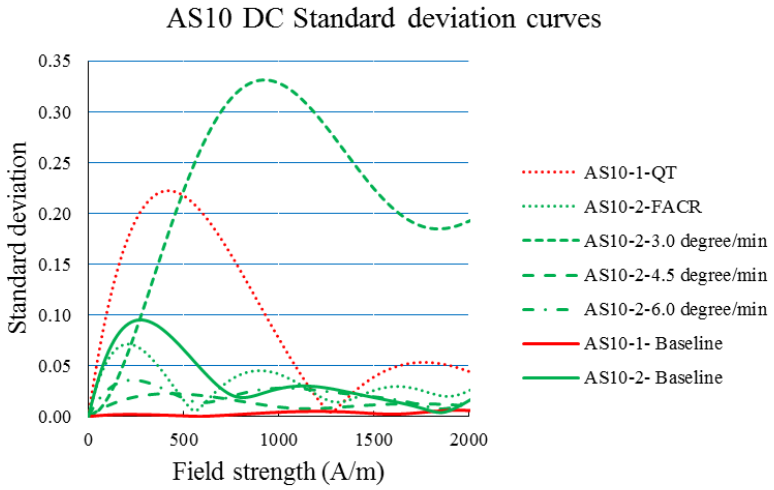


Fig 23. The standard deviation of the data for the B-H curves for sample AS10

In Fig 8Fig 23 the standard deviation of the datasets for sample AS10 is shown the lowest values of deviation occur at the knee points at the start of the magnetisation curve and at the end of the linear section of the magnetisation curve. The dataset with the largest deviation is the annealing at 3.0 degrees/min.

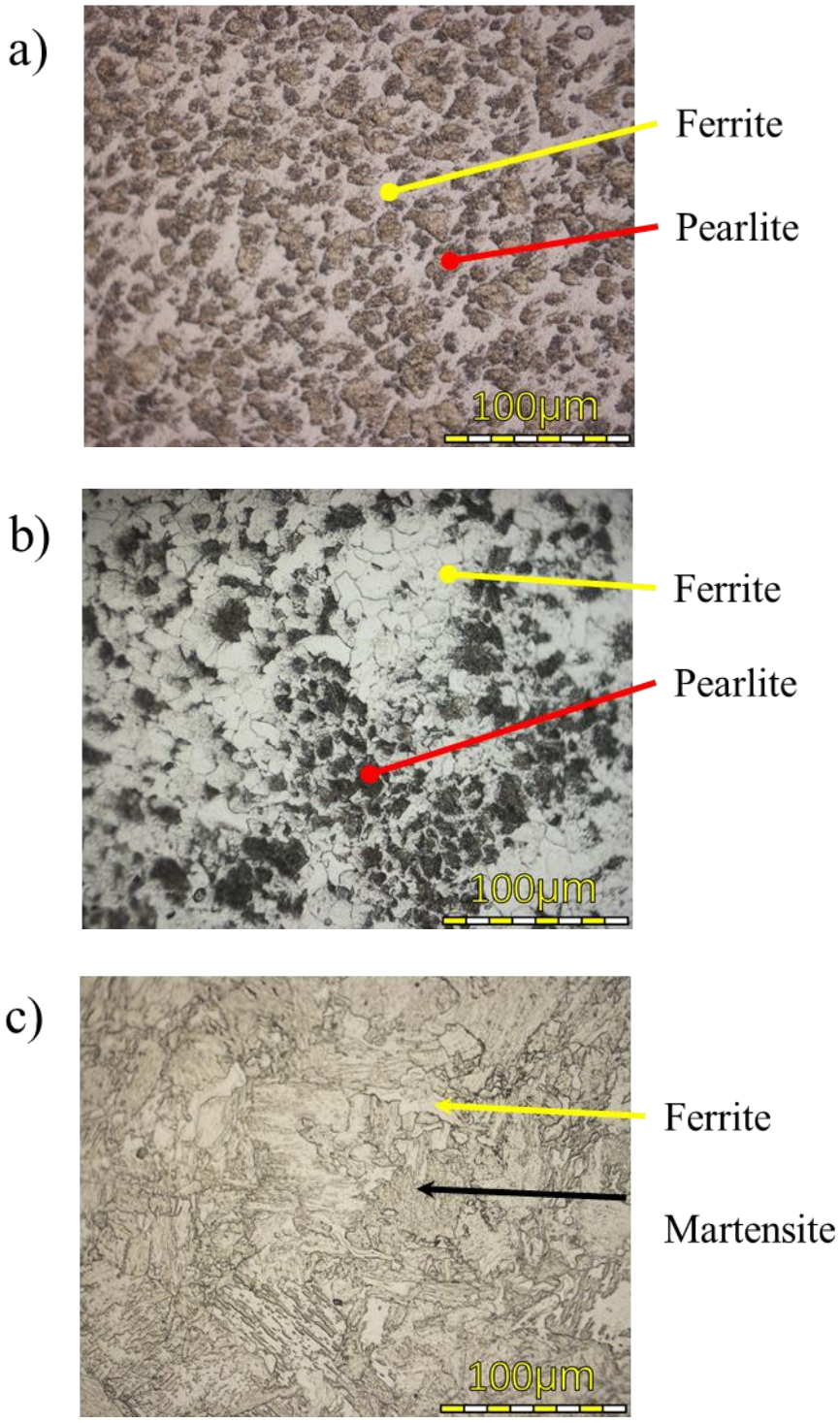


Fig 24 (a) image of the ferrite/pearlite microstructure of the normalised A2 grade steel, (b) image of ferrite/pearlite microstructure of the annealed BT3 grade steel, (c) image of the ferrite/martensite microstructure of the quenched A2 grade steel.

Fig 24 (a) shows that the normalised sample is dominated by a fine pearlite microstructure with large amounts of ferrite crystals. Fig 24 (b) shows that annealing the sample has resulted in a finer pearlite structure with larger concentrations of ferrite, this has resulted in a higher B-H curve than the normalised sample. Fig 24 (c) shows the quenched sample's microstructure consists of large crystals of both martensite and ferrite. The martensite is the reason behind the initially low B-H curve of the quenched sample but once the applied field has increased sufficiently it overcomes the martensites initial reluctance to polarisation.

- **Effect of heat treatments on the B-H curve of sample AS12**

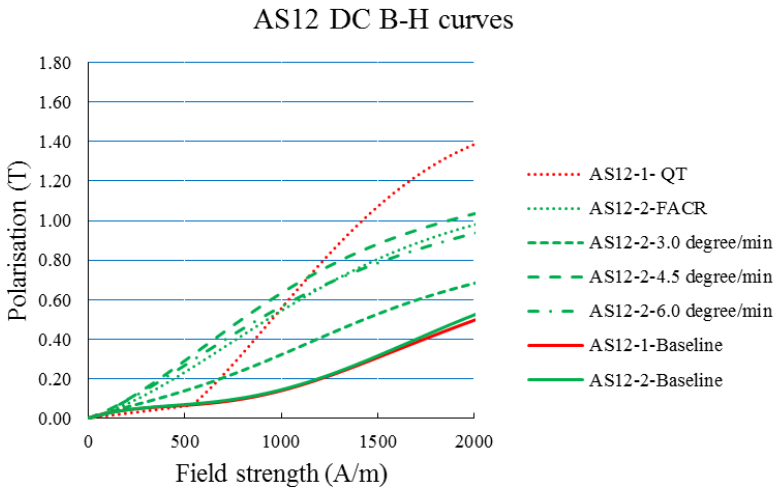


Fig 25. The effect of heat treatments on the permeability of a sample of BT2 grade steel. Until the field strength reaches 1500A/m the sample with the highest permeability is annealed at a cooling rate of 4.5°C/min. After the field strength reaches 1500A/m the quenched sample has the highest permeability. The normalised sample has the lowest permeability with the annealed at a cooling rate of 3.0°C/min showing only a slight improvement on the normalised sample.

In Fig 25 the effect of heat treatments on the B-H curve of sample AS12 is compared to the normalised sample. The highest B-H curve is obtained before 1500A/m by annealing with a cooling rate of 4.5°C/min. After 1500A/m the quenched sample has a higher B-H curve than any of the annealing heat treatments.

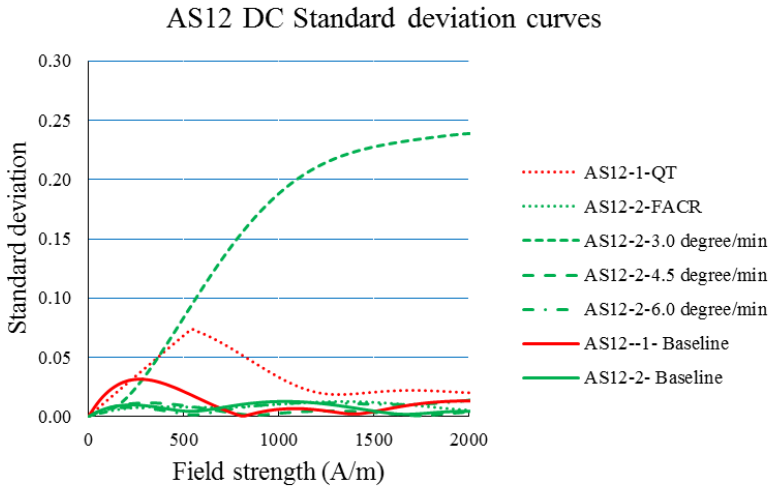


Fig 26. The standard deviation of the data for the B-H curves for sample AS12

In Fig 8Fig 26 the standard deviation of the datasets for sample AS10 is shown the lowest values of deviation occur at the knee points at the start of the magnetisation curve and at the end of the linear section of the magnetisation curve. The dataset with the largest deviation is the annealing at 3.0 degrees/min.

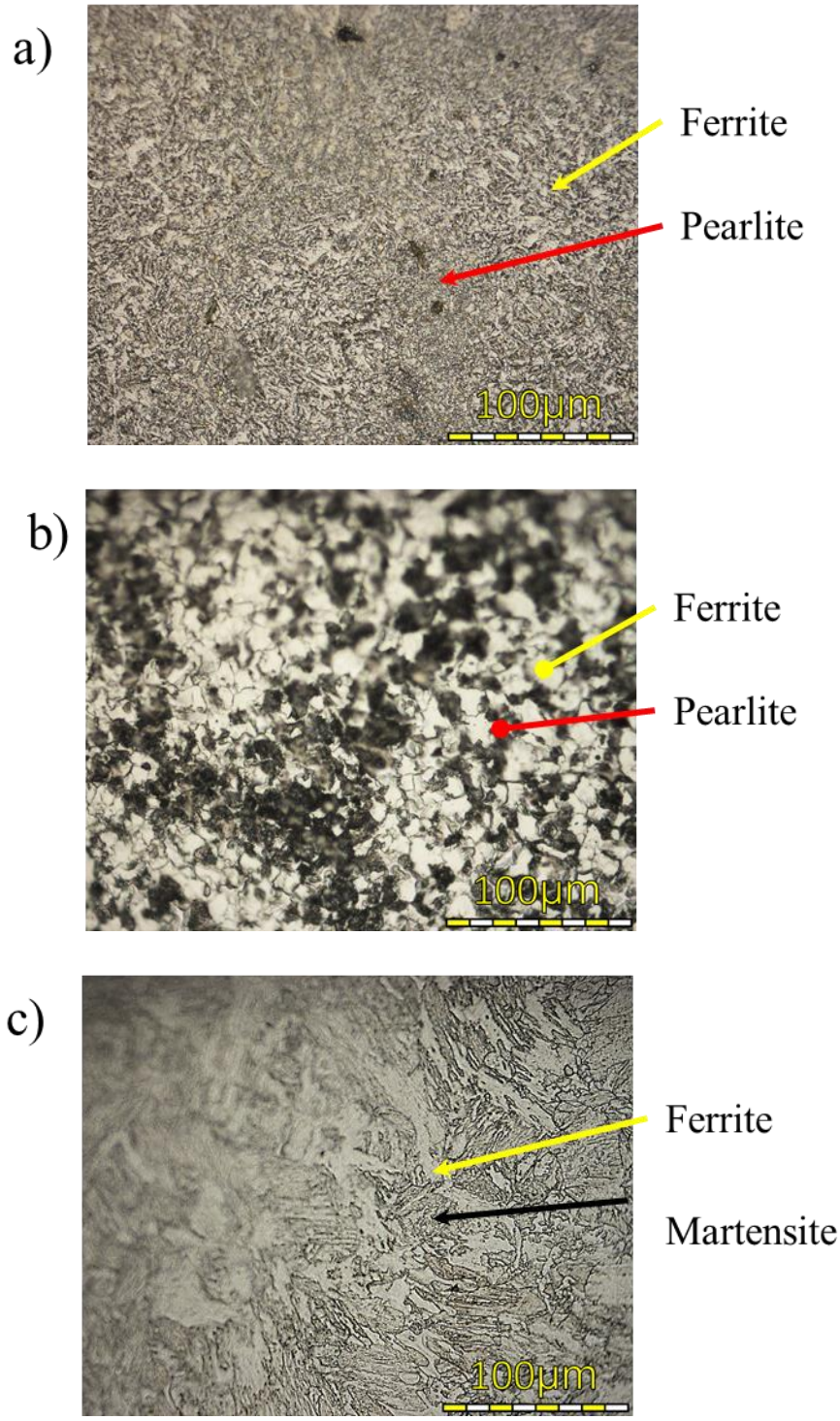


Fig 27 (a) image of the ferrite/pearlite microstructure of the normalised BT2 grade steel, (b) image of ferrite/pearlite microstructure of the annealed BT2 grade steel, (c) image of the ferrite/martensite microstructure of the quenched BT2 grade steel.

Fig 27 (a) shows the normalised sample's microstructure consists of coarse pearlite with few ferrite crystals. The crystal sizes of the coarse pearlite and ferrite combined with the large amount of coarse pearlite resulted in the low polarisation response. Fig 27.(b) shows the microstructure of the annealed sample, it comprises of fine pearlite and ferrite crystals that are larger than those found in the normalised samples. The combination of larger crystal size and more ferrite crystals results in the higher B-H curve of the annealed sample when compared to the normalised sample. Fig 27 (c) shows the microstructure of the quenched sample. The structure consists of large martensite and ferrite crystals. The larger crystal size and better ferromagnetic performance of martensite, when compared to pearlite, results in the quenched sample performing better than either the normalised sample or the annealed sample once the applied field strength has reached 1500A/m.

Appendix B

Calculation of forces on pole shoe retention bolts

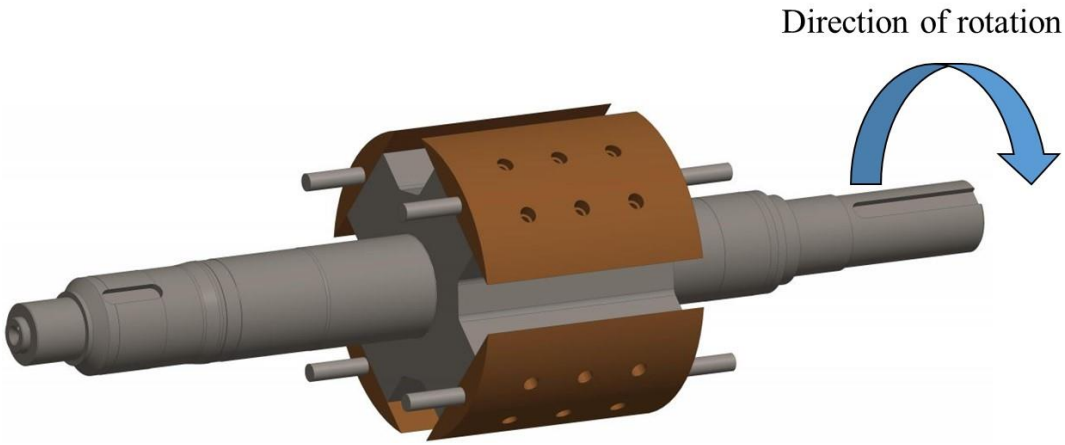


Fig. 1. The direction of rotation of the rotor and pole shoe assembly.

In Fig. 1 an image of the assembled rotor with the direction of rotation is shown. When calculating the force on the pole shoe retaining bolts the total mass of the load held in place by the retaining bolts needed to be calculated.

The 3D computer aided design (CAD) model gives the volume of the pole shoes:

$$Volume = 1189943mm^3 = 1.189943cm^3 = 0.00119m^3$$

The datasheets for the alloy that will be used to produce the pole shoes (Invar 36) state the density of the alloy as:

$$Density\ of\ Invar\ 36\% = 8055\ kg/m^3$$

The mass of the pole shoes can then be calculated as:

$$Mass = Density\ (kg/m^3) x\ Volume\ (m^3)$$

$$Mass = 8055\ x\ 0.00119$$

$$Mass = 9.58545\ kg$$

The mass of the pole shoe itself is only one part of the load on the retaining bolts, the second part is the weight of the copper field windings. From datasheets provided by CGT the overall weight of the field windings is 36.4kg.

Each of the four poles shoes shares a quarter of this weight so the mass of copper per pole shoe is:

$\frac{36.4}{4} = 9.1\ k$

So the total mass of each individual pole shoe and copper winding is:

$9.58545 + 9.1 = 18.68545\ kg\ \ or\ 18.7 kg\ to\ 3\ sig\ figs$

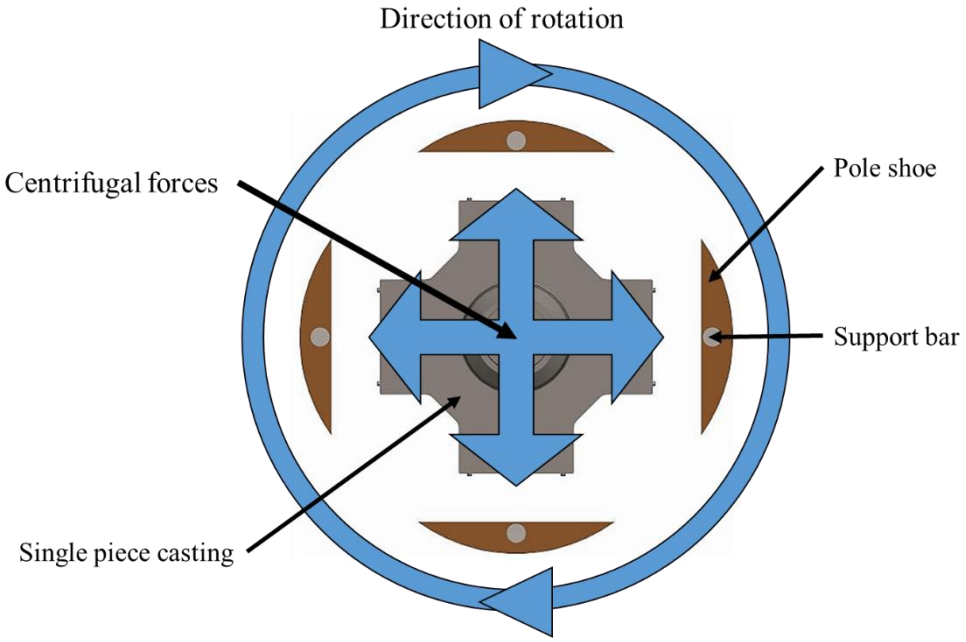


Fig. 2. The direction of rotation with the centrifugal forces on pole shoes shown

Fig. 2. shows the direction of rotation and the direction of the centrifugal forces acting on the pole shoes.

The maximum speed of rotation that the rotor was subjected to is 2700 rpm which occurred during testing. The operational speed is 1500rpm for 50 Hz output and 1800rpm for 60 Hz.

Centrifugal forces can be calculated form the following equation.

$Centrifugal\ force = M\omega^2 r$

Where:

$M = Mass$

$\omega = angular\ speed = \left(\frac{2700}{60}\right) = 45\ \therefore \frac{1}{45} = 0.022 \therefore \omega = \frac{2\pi}{0.022} = 285.6\ rad/s$

$r = 0.1515m\ radius\ of\ the\ main\ cast\ rotor\ body$

$Centrifugal\ force = 18.7x(285.6)^2 x\ 0.1515$

$Centrifugal\ force = 231084.4\ N\ or\ 231\ kN\ per\ pole\ shoe$

Each pole shoe has six bolts used to secure the pole shoe to the rotor body and to counterbalance the centrifugal forces experienced by the pole shoes and copper windings.

$Force\ on\ each\ retaining\ bolt = \frac{231}{6}$ =38.5kN

Now that the force that each retaining bolt experiences has been calculated it is possible to confirm that the selected bolts are strong enough to retain the poles shoes. If M10 x1.25P bolts with a length of 45mm are used, 27.5mm of the bolts thread will be engaged with the cast rotor body. The holes for the retention bolts in the pole shoes are 17.5mm deep (after recessed hole for bolt head) and are unthreaded. From manufactures datasheets the use of high strength 12.9 alloy bolts results in the breaking force of the bolt being 74kN. As each bolt is subjected to a maximum force (during testing) of 39kN the safety factor of the bolts is:

$\frac{74}{39} = 1.8$

So for the limited duration test speed of 2700rpm the bolts can withstand 1.8x the expected force. The operating speed of the rotor is 1500rpm at 50 Hz and 1800rpm at 60 Hz. If the for centrifugal force is calculated using these operating speeds, the maximum force on the retaining bolts becomes 12kN and 17kN respectively.

The safety factor for normal operating speed are therefore:

50Hz = $\frac{74}{12} = 6 =$ meaning the retaining bolts can resist forces six times the operating forces

60Hz = $\frac{74}{17} = 4 =$ meaning the retaining bolts can resist forces four times the operating forces

By calculation it has been shown that the bolts retaining the pole shoes are strong enough to withstand the centrifugal forces from the spinning rotor.

It was then necessary to calculate the force required to pull the bolts out of the casting, good fastener design practice is to have the bolt break before it pulls out of the casting. The mechanical properties of the A1 cast steel that comprises the main rotor body was given by the fabrication company and are shown in Table I.

Table I. Mechanical composition of A1 grade cast steel

Mechanical properties		
Tensile strength N/mm^2	**Yield N/mm^2**	**Elongation %**
506	300.7	27.5

The force required to pull out the retaining bolt is termed the shear strength and is calculated by the following equation:

$F = rAth$

Where

$F = Shear\ strength$

$r = Shear\ strength\ of\ material$

$r = 0.5\ x\ Tensile\ strength\ (506N/mm^2)$

$r = 253MPa$

$Ath = Thread\ shear\ area$

$Ath = 0.5\pi d_0 L_e$

$d_0 = (d_2 + d_3)/2$

$d_2 = 9.188 - From\ manufactures\ data\ sheets$

$d_3 = 8.779 - From\ manufactures\ data\ sheets$

$d_0 = 8.98375$

$L_e = 27.5 - Length\ of\ engagment$

$Ath = 0.5\pi(8.98375)(27.5)$

$Ath = 388.07mm^2$

The force required to pull-out the bolt is

$F = 253x388.07$

$F = 98181N\ or\ 98kN$

So, from this calculation it is clear that the force required to pull out the bolt from the casting is larger than the force required to break the bolt (74kN). These calculations show that the selected M10x1.25P x 45mm length bolts with an engagement into the casting of 27.5mm provides a connection between the cast rotor and the pole shoes that is strong enough to counteract the effects of centrifugal force during the rotors operation.

Calculation of forces on the support bars

The second amendment from the conventional rotor is the removal of support bars that go through the length of the core pack. The supports bars, for the prototype, are produced out of EN19 alloy (also known as 709M40) which has the mechanical properties shown in Table II.

Table II. Mechanical composition of EN19 bar stock

Mechanical properties		
Tensile strength N/mm^2	**Yield N/mm^2**	**Elongation %**
850-1000	700	9

The stress placed upon the support bars is not directly offset by the retention bolts, so the thread of the support bar has to take the entire loading of the supported copper windings and the weight of the support bars themselves across its threads cross-sectional area (Fig. 3. Forces acting on the support bars (with high stress areas circled)).

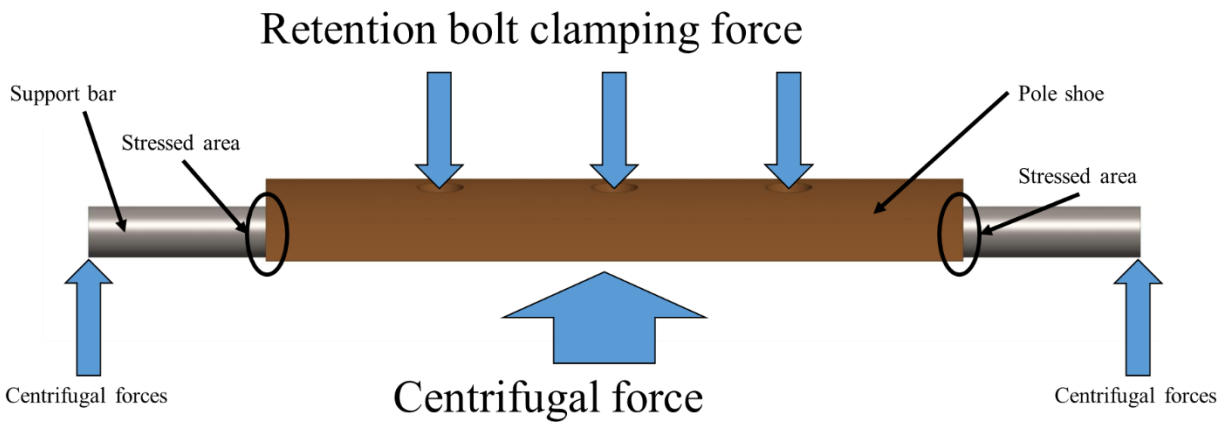


Fig. 3. Forces acting on the support bars (with high stress areas circled)

The thread of the support bar was chosen to be an M14x2P, with a 27.5mm engagement within the pole shoe. This sized thread was selected because it was the

largest thread that could be drilled into the pole shoe whilst maintaining a wall thickness of at least 3mm from the bottom face of the pole shoe.

The stress on the support bar needed to be calculated to ensure that the support bar would not snap under the centrifugal force of testing and operation.

The 3D CAD model gives the volume of the support bars as:

$Volume = 25633.4mm^3 = 0.25633cm^3 = 0.000025633m^3$

The datasheets for the alloy that will be used to produce the supports (EN19) state the density of the alloy as:

$Density\ of\ EN19 = 7850kg/m^3$

The mass of the supports can then be calculated as:

$Mass\ (kg) = Density\ (kg/m^3) x\ Volume\ (m^3)$

$Mass = 7850\ x\ 0.000025633$

$Mass = 0.2g$

The 3D CAD model shows the mass of the unsupported copper for each support is:

$Mass\ of\ unsupported\ copper = 2.5kg$

The total mass of the support and the copper is:

$Total\ mass = 2.5 + 0.2$

$Total\ mass = 2.7kg$

Using the mass of the unsupported copper in the centrifugal force calculation yields a total force on the support of:

$Centrifugal\ force = 2.7x(285.6)^2x\ 0.1515$

$Centrifugal\ force = 33365N\ or\ 34kN$

Unlike the 12.9 alloy bolts used to retain the pole shoes, the breaking force for the thread machined into the bar stock to produce the support bars cannot be obtained from look up tables. The ultimate tensile stress of EN19 has been obtained from the

supplier's data tables and is the lowest value for EN19. The tensile stress area has been taken from manufacturer's datasheets of supplied thread types. The force required to break the bolt can be calculated by:

$$Force\ required\ to\ break\ bolt = Ultimate\ tensille\ strength\ (UTS) x\ tensile\ stress\ area\ (As)$$

$$Force\ required\ to\ break\ bolt = 850 * 115.44$$

$$Force\ required\ to\ break\ bolt = 98124N\ or\ 98kN$$

The breaking force for the support thread is 98kN whiles the maximum applied load is 34kN this gives a safety factor of:

$$\frac{98}{34} = 2.9$$

As with the safety factor on the pole shoe retaining bolts, the 2.9 safety factor of the support bars thread is for the limited duration testing speed of 2700rpm. For normal operation of 1500rpm for 50Hz and 1800rpm for 60Hz the force on the support bar thread reduces to 10kN and 15kN respectively.

$$50Hz = \frac{98}{10} = 9.8\ safety\ factor$$

$$60Hz = \frac{98}{15} = 6.5\ safety\ factor$$

The previous calculations show that the support bar's M14x2P thread is capable of supporting the weight of the copper windings that are not supported by the pole shoes themselves.